Hybrid Silicon Nanophotonic Devices: Enhancing Light Emission, Modulation, and Confinement

Thesis by
Ryan Morrow Briggs

In Partial Fulfillment of the Requirements
for the Degree of
Doctor of Philosophy

California Institute of Technology
Pasadena, California
2011

(Defended May 13, 2011)

To Hannah.

Acknowledgements

With immense gratitude, I first acknowledge my advisor, Professor Harry Atwater, for his support, encouragement, and enthusiasm. Harry is the source of an incredible number of great ideas and visionary scientific contributions, but he also allows his students to own their thesis work in a way that fosters personal and professional growth. Looking back on the past five years, I realize that I would not have had my graduate school experience be any other way. To this day, Harry amazes me with his ability to deeply understand ideas and immediately expand on them with his pithy insights, but he also amazes me with his genuine regard and concern for other people, particularly the members of his group at Caltech. I am eager to see how Harry, his research group, and his entrepreneurial ventures will continue to impact the world in the years to come.

I am also extremely grateful to Professors Oskar Painter, Julia Greer, Amnon Yariv, and Bill Goddard for serving on my candidacy and thesis committees. It is an honor, but also a humbling experience, to prepare a thesis knowing that it will be examined by individuals who are eminent experts in their fields, and I thank them for their time and input.

Within the Atwater group, I must first thank Ken Diest for teaching me how to survive in the lab, figuratively and perhaps literally. Having worked in computational materials science before arriving at Caltech, it was Ken who took the time to show me what it means to be a diligent, careful, and intuitive experimentalist, and I have tried to follow his lead. As is truly characteristic of Ken, he has also been very generous with his time by reading through this thesis and providing many valuable comments. I also thank Robb Walters and Domenico Pacifici for introducing me to experimental optics when I began in the Atwater group. Their input and example was extremely helpful as I began to give shape to my thesis work. I must also particularly thank Gerald Miller for being my brother in arms, as it were, in the fight to make high-efficiency erbium-doped materials. Gerald and I attempted what seems like a countless number of strategies to develop robust and consistent films for waveguide-

integrated light sources. No other aspect of my work at Caltech required as many failed attempts to get a few decent results, but I look back on the experience with a certain fondness, largely because I had Gerald as as a dedicated colleague and good-humored friend along the way.

A little over a year ago, Jonathan Grandidier started as a postdoc in the Atwater group and introduced me to dielectric-loaded surface-plasmon waveguides, and our discussions blossomed into the integration of those devices with the silicon waveguides I had been previously fabricating. In both his scientific and personal dealings, Jonathan is one of the most deliberate and principled people I know, and I am grateful to have worked with him. I have also recently had the pleasure of working with Jim Fakonas, who as a second-year graduate student brings a level of creativity and penetrating insight to research that is typically reserved for much more experienced scientists. I am also very grateful to Jim for his useful comments on this thesis. I have also been fortunate to have the opportunity to work with Stan Burgos and Eyal Feigenbaum. Stan and Eyal helped me collect NSOM measurements on my surface-plasmon waveguide devices, and we have since worked together to experimentally realize their exciting designs for plasmonic metamaterials and resonant waveguide networks. I have thoroughly enjoyed and benefitted from my interactions with Stan and Eyal, and I look forward to seeing the great work that I am certain they will continue to produce in the years to come.

I also wish to acknowledge the people outside the Atwater group with whom I published work during my time at Caltech. Mike Shearn, then a student of Professor Axel Scherer, worked with me to develop an initial pattern-transfer process for fabricating SOI waveguides, and I have since valued his friendship and input on matters scientific and otherwise. After developing the theoretical framework for analyzing spontaneous emission enhancement in silicon slot waveguides presented in this thesis, Harry and I discovered that Young Chul Jun and Professor Mark Brongersma at Stanford University were analyzing similar structures. Ultimately, we submitted a paper together, with Young Chul taking the lead. I am grateful to Young Chul, first of all, for using his different method to corroborate and bring additional insight to the calculations

I had performed for slab waveguides, but also for extending the analysis to more experimentally relevant three-dimensional structures using numerical simulations.

I owe thanks to Melissa Archer and Henri Lezec for generously giving their time and expertise to help me obtain TEM images of the wafer-bonded SOI structures I fabricated when I first started at Caltech. Also, I am glad for the opportunity to have made at least a small contribution to the silicon-microwire photovoltaics effort in the Atwater group. In particular, it was a pleasure working with Michael Kelzenberg, Morgan Putnam, Dan Turner-Evans, and Shannon Boettcher, and I am truly inspired by what they have accomplished. I also thank Hansuek Lee and Eric Ostby in Professor Kerry Vahala's group for their help with exploring erbium-doped sol-gel films and for generally sharing their optics expertise.

I consider myself very fortunate to have shared an office with Koray Aydin, Imogen Pryce, and Carrie Hofmann over the last few years, and, for a time before that, with Luke Sweatlock and Julie Biteen. Koray is as prolific a scientist as I have ever seen, and he has been a truly devoted colleague and friend. I am honored to call him my *abi*. Imogen is one of the hardest-working people I know, and her boundless wit has made our time together in the office much more enjoyable. I am also grateful to Imogen for depositing the VO_2 films I used to fabricate the phase-change modulator devices described in this thesis. Having blazed a trail through the materials science graduate program before me, Carrie has consistently been a source of scientific expertise and moral support, and I have learned much from her example. When I began in the Atwater group, I benefitted greatly from the knowledge and input of Luke and Julie, and it has been exciting to see them go on to become experts in their fields.

While at Caltech, I had the opportunity to mentor two wonderful undergraduate researchers. Balthasar Müller assisted me in designing and refining the fabrication process for the SOI waveguides that are the foundation of many of the devices in this thesis. Balthasar is a talented and intuitive physicist, and I am grateful for our enduring friendship. Michael Sushkov originally came to the Atwater group as a high-school senior and returned after his freshman year at Caltech. I have met few people as loyal and kind as Michael, and I have enjoyed seeing him take on the rigors of the Caltech undergraduate program with great skill and aplomb. Michael performed studies on VO_2 films toward developing an electrically driven modulator, and I thank him for collecting optical and electrical measurements for VO_2 deposited on SiO_2, which are included in this thesis.

It has been wonderful being in the Atwater group with my fellow Oredigger, Andrew Leenheer, who is one of the most creative experimentalists I have seen. In addition, I am thankful for having worked with Jen Dionne. She is an inspiring scientist and very kind to have been so encouraging of a younger graduate student. I am also grateful for the opportunity to have worked alongside members of the Atwater group that I have not yet mentioned, including: Jeff Bosco, Dennis Callahan, Chris Chen, Naomi Coronel, Davis Darvish, Mike Deceglie, Rene de Waele, Matt Dicken, Carissa Eisler, Hal Emmer, Vivian Ferry, Mike Filler, Kate Fountaine, Min Jang, Seokmin Jeon, Ugur Karatay, Brendan Kayes, Yousif Kelaita, Greg Kimball, Emily Kosten, Lise Lahourcade, Krista Langeland, Marina Leite, Manav Malhotra, Jeremy Munday, Keisuke Nakayama, Deirdre O'Carroll, Jan Petykiewicz, Andrey Poletayev, Jen Ruglovsky, Matt Sheldon, Faisal Tajdar, Adele Tamboli, Katsu Tanabe, Emily Warmann, and Samantha Wilson.

April Neidholdt and Lyra Haas deserve my deepest gratitude for all they have done to keep the Atwater group functioning smoothly during my time here. Life has been undoubtedly better because of their hard work and friendship. I also thank Pam Albertson, Connie Rodriguez, Rosalie Rowe, Rosie Sanchez, Eleonora Vorobieff, and Mabel Chik.

I have spent countless hours in the Kavli Nanoscience Institute cleanroom during my time at Caltech, and I am grateful to Guy DeRose, Melissa Melendes, Nils Asplund, and Bophan Chhim for making those hours much more enjoyable and productive. I also thank Mary Sikora for keeping the KNI running topside. To Dave Henry, Christos Santis, Derrick Chi, Andrew Homyk, David Brown, and Slobodan Mitrovic, I owe a debt of gratitude for many useful discussions about device fabrication and for generally keeping me company in the cleanroom.

I wish to thank Hongjin Tan for his camaraderie, especially during our first two

years of coursework at Caltech. The many hours spent conquering problem sets with Hongjin were among the most memorable and rewarding of the past five years.

I am very thankful for the generosity of the National Defense Science and Engineering Graduate Fellowship, which provided me with financial support during my first three years at Caltech. Also, I gratefully acknowledge the Air Force Office of Scientific Research for their support of my research through various programs.

Finally, I am eternally grateful to my family for their endless love and encouragement. Mom, Dad, Megan, and Grandma, you have been wonderfully supportive of me throughout this endeavor, and I cannot thank you enough for all that you have done. My lovely wife, Hannah, your patience and understanding are astounding. Thank you for your steadfast love and support. This thesis, like any good I do in the world, is truly a credit to you as much as it is to me.

Ryan M. Briggs
April 2011
Pasadena, CA

Abstract

Silicon has become an increasingly important photonic material for communications, information processing, and sensing applications. Silicon is inexpensive compared to compound semiconductors, and it is well suited for confining and guiding light at standard telecommunication wavelengths due to its large refractive index and minimal intrinsic absorption. Furthermore, silicon-based optical devices can be fabricated alongside microelectronics while taking advantage of advanced silicon processing technologies. In order to realize complete chip-based photonic systems, certain critical components must continue to be developed and refined on the silicon platform, including compact light sources, modulators, routers, and sensing elements. However, bulk silicon is not necessarily an ideal material for many active devices because of its meager light emission characteristics, limited refractive index tunability, and fundamental limitations in confining light beyond the diffraction limit.

In this thesis, we present three examples of hybrid devices that use different materials to bring additional optical functionality to silicon photonics. First, we analyze high-index-contrast silicon slot waveguides and their integration with light-emitting erbium-doped glass materials. Theoretical and experimental results show significant enhancement of spontaneous emission rates in slot structures. We then demonstrate the integration of vanadium dioxide, a thermochromic phase-change material, with silicon waveguides to form micron-scale absorption modulators. It is shown experimentally that a 2-μm long waveguide-integrated device exhibits broadband modulation of more than 6.5 dB at wavelengths near 1550 nm. Finally, we demonstrate polymer-on-gold dielectric-loaded surface-plasmon waveguides and ring resonators coupled to silicon waveguides with 1.0 ± 0.1 dB insertion loss. The plasmonic waveguides are shown to support a single surface mode at telecommunication wavelengths, with strong electromagnetic field confinement at the polymer-gold interface. These three device concepts show that diverse materials can be integrated with silicon waveguides to achieve enhanced light emission, broadband modulation, and strong confinement, all while retaining the advantages of the silicon photonics platform.

Contents

List of Publications

The following publications are directly related to this thesis:

- R. M. Briggs, M. Shearn, A. Scherer, and H. A. Atwater, "Wafer-bonded single-crystal silicon slot waveguides and ring resonators," Appl. Phys. Lett. **94**, 021106 (2009). **(Chapter 3)**
- R. M. Briggs, G. M. Miller, and H. A. Atwater, "Modifying the radiative quantum efficiency of erbium-doped glass in silicon slot waveguides," Proc. of the 6th IEEE International Conference on Group IV Photonics, pp. 223-225 (2009). **(Chapter 4)**
- Y. C. Jun, R. M. Briggs, H. A. Atwater, and M. L. Brongersma, "Broadband enhancement of light emission in silicon slot waveguides," Opt. Express **17**, 7479-7490 (2009). **(Chapter 4)**
- R. M. Briggs, I. M. Pryce, and H. A. Atwater, "Compact silicon photonic waveguide modulator based on the vanadium dioxide metal-insulator phase transition," Opt. Express **18**, 11192-11201 (2010). **(Chapter 5)**
- R. M. Briggs, J. Grandidier, S. P. Burgos, E. Feigenbaum, and H. A. Atwater, "Efficient coupling between dielectric-loaded plasmonic and silicon photonic waveguides," Nano Lett. **10**, 4851-4857 (2010). **(Chapter 6)**

List of Figures

List of Tables

Chapter 1

Introduction

1.1 Silicon as a Photonic Material

Over the past decade, silicon-based photonics has risen from the status of a promising technology to become a standard platform for on-chip optics. The usefulness of silicon as a photonic material for communications and information processing is largely the result of the somewhat separate materials-science histories of fiber-optic and integrated-circuit technologies. Fiber optics for telecommunications has become such an essential component of the modern world that the development of ultra-low-loss glass fibers warranted the Nobel Prize in Physics for Charles Kao in 2009. In the late 1960s, Kao and his coworkers determined that the attenuation of light propagating in fused silica could, in principle, be sufficiently low to enable communication links over many kilometers [1, 2]. This finding led to the subsequent development of silica-based fiber with negligible impurity concentrations and, ultimately, propagation loss below 1 dB/km at near-infrared wavelengths. In particular, high-quality silica fiber exhibits the least attenuation at wavelengths around 1.3 and 1.55 μm, which has established those regions of the electromagnetic spectrum as the standard for optical communications.

During the two decades preceding Kao's pioneering work, Gordon Teal and his coworkers at Bell Labs and Texas Instruments created the framework for growing high-purity single crystals of silicon and germanium for integrated circuits [3]. Ultimately, silicon became the material of choice because of the quality of the thermally oxidized silicon-silica interface for insulating barriers and surface passivation, but also because of unfavorably high intrinsic free-carrier concentrations in germanium devices resulting from that material's smaller bandgap. While the invention of the transistor is one of the defining achievements of the twentieth century (and the topic of another Nobel Prize), the semiconductor electronics industry as we know it today has been made possible by the ability to grow large silicon crystals with astounding levels of perfection.

Given the success of monolithic integration of electronic devices on silicon, it is perhaps natural that silicon would be a candidate material for integrated photonics. Driven by the electronics industry, the technology infrastructure has existed for some time to not only create high-purity silicon in large quantities, but also to pattern silicon devices over large areas with sub-micron feature sizes and remarkably high yield. In addition, because of the technology created to generate, amplify, and detect light at wavelengths near 1.3 and 1.55 μm for fiber-optic communications, there has been an impetus to design on-chip photonic devices that operate in the same part of the electromagnetic spectrum.

In 1986, Soref and Lorenzo published a paper suggesting that silicon is in fact very well suited for guiding and manipulating light at telecommunication wavelengths over chip-scale distances [4]. In particular, the bandgap of silicon is large enough that the optical loss due to absorption in lightly doped single crystals can be significantly less than 1 dB/cm at both 1.3 and 1.55 μm. Furthermore, Soref and his coworkers showed that the injection of charge carriers using integrated electrical structures allows for optical switching due to the dependence of the complex refractive index on free-carrier concentration [5].

While initial efforts in integrated silicon photonics were promising, one additional materials technology has played an important role in moving silicon to the forefront of on-chip optics: namely silicon-on-insulator, or SOI. Soref and others used the small index contrast between a lightly doped silicon epitaxial layer and a highly-doped silicon substrate to confine guided modes. Their epitaxial waveguides were fabricated with cross-sectional dimensions of several microns, which helped minimize modal overlap with the highly absorbing substrate but did not take full advantage of the high degree of confinement made possible by the large refractive index of silicon. Analogous to the advancement of ultra-high-purity silicon crystals, the microelectronics industry has driven the development and large-scale manufacture of SOI wafers with a thin single-crystal silicon device layer isolated from the silicon substrate by an insulating region, which enables improved performance and efficiency of integrated circuits. While many processes have been used to achieve such structures, wafer bonding of silicon wafers with thermally grown SiO_2 bonding layers has emerged as the most scalable method for producing SOI without degrading the quality of the silicon device layer or introducing deleterious interface effects [6, 7]. The high-quality materials and interfaces that are desirable for electrical devices also enable the fabrication of low-loss SOI waveguides that can take advantage of the large index contrast between silicon and silica to achieve high optical confinement with sub-micron lateral dimensions [8].

Today, bonded SOI wafers with SiO_2 buried-oxide (BOX) layers are used in vast quantities by electronics manufacturers around the world, with most of the wafers being produced by Soitec using their Smart Cut^{TM} thin-film exfoliation process [9]. A direct byproduct of the immense scale of SOI manufacturing has been the availability of high-quality, inexpensive SOI substrates for photonics technology development. Consequently, in addition to the advantages of silicon as a high-index, low-loss photonic material at telecommunication wavelengths, there has been a strong economic incentive for exploring silicon for on-chip optics as opposed to more expensive material systems, such as epitaxial III-V compound semiconductors.

1.2 Applications of Silicon Photonics

Two major technology drivers for silicon photonics are fiber-integrated transceivers for local information networking and on-chip optical interconnects for computing [10, 11]. Compared with electrical wires, a general advantage is gained with optical communications by using wavelength-division multiplexing (WDM) to simultaneously transmit many signals through a single optical conduit. The lower cost of silicon processing can potentially enable the wider use of optical communication links for short-range information transfer, where fiber-coupled chip-based silicon photonic devices can be used to construct many of the components necessary for optical transceivers. By comparison, the cost of conventional transceiver components has generally limited fiber-optic communication to longer-distance applications. A prime example of this concept is the 40-Gb/s fiber-coupled transceiver demonstrated by the photonics company Luxtera using components monolithically integrated on a scalable silicon platform [12]. Over even shorter distances on a single silicon chip, silicon waveguides may be able to replace copper interconnects, for example, between cores in computer multiprocessors [13, 14]. Despite the relatively large size of dielectric waveguides and the anticipated delay of optical modulators and detectors, it has been predicted that optical interconnects using WDM can achieve an overall greater bandwidth density than delay-limited electrical interconnects [15].

A less mature but nonetheless compelling application of silicon photonics is chemical and biological sensing. Low-loss SOI waveguides can be used to measure small index changes in the surrounding dielectric environment, which can be correlated to molar concentration. Densmore *et al.* recently demonstrated functionalized SOI-waveguide sensors operating near 1.55 μm wavelength integrated with microfluidic channels [16]. Using a balanced Mach-Zehnder waveguide interferometer to detect changes in effective optical path length, particular proteins delivered through the microfluidic channels were reliably detected at sub-femtogram levels over sub-mm^2 areas. Such sensitivity is comparable to commercial surface-plasmon resonance sensors, but the waveguide-based devices on silicon have the additional potential to be monolithically integrated with routers, detectors, and other components in order to reduce overall system size and cost.

1.3 Limitations of Silicon: The Need for Hybrid Photonic Devices

The transparency and large refractive index of silicon at telecommunication wavelengths along with the scalability of silicon technology make a convincing case for silicon photonics; however, fully realizing the applications just described (and potentially many others) requires more than just passive waveguide components. To achieve monolithically integrated photonic systems will require that light sources, modulators, routers, and detectors all be developed together on the silicon platform. Devising a silicon-compatible light source is considered the most difficult of these challenges. As an indirect-bandgap semiconductor, radiative electronic transitions in crystalline silicon from the conduction band minimum to the valence band maximum require the simultaneous creation or annihilation of a phonon, which is sufficiently improbable that most excited electrons decay by non-radiative processes, even for highly optimized devices [17]. Continuous-wave lasers in silicon have been demonstrated near telecommunication wavelengths using Raman scattering to induce photon emission [18]; however, such devices still require a high-power external optical pump, making them impractical for integrated on-chip systems. Due to the lack of silicon-based light sources, current commercially available silicon photonic systems, including the previously mentioned Luxtera transceiver technology, make use of external III-V compound semiconductor light sources.

Since the initial work of Soref and others, great progress has been made in using electro-optic effects due to free-carrier dispersion to create high-speed silicon-based modulators [14, 19, 20] and wavelength-division multiplexers [21, 22] operating at wavelengths near 1.55 μm. However, even for relatively large variations in free-carrier concentration, changes in the refractive index of silicon are small [5], requiring that devices employ structures such as ring resonators or Mach-Zehnder interferometers to induce significant amplitude modulation by interference. As a result, devices must be significantly larger than a single waveguide and optimal modulation is achieved over a limited span of wavelengths determined by the resonator linewidth or interferometer free-spectral range. Electroabsorption in silicon due to the Franz-Keldysh effect is present at shorter wavelengths (closer to the indirect bandgap energy) [23], but absorption modulation at 1.55 μm is limited for reasonable values of free-carrier concentration, requiring long interaction lengths and, consequently, large devices. It has also been shown that sub-bandgap defect absorption in silicon can be used to generate carriers for fast photodetection at telecommunication wavelengths [24], but interaction lengths of many microns are required for high performance.

Given the limitations of silicon in terms of its optical properties, it may be favorable to explore other materials that can be integrated on the silicon platform in order to push the limits of device performance and miniaturization while still benefitting from the optical confinement, manufacturability, and low cost of SOI. Hybrid devices may require redefining what materials and processes are "CMOS-compatible," but such changes have been effectually accommodated in the past (for example, with high-k gate dielectrics and even copper interconnects). There have in fact already been successful demonstrations of hybrid devices in silicon photonics: in particular, III-V semiconductor lasers bonded to SOI waveguides [25, 26] and deposited [27] or bonded [28] germanium photodetectors and modulators.

Motivated by the success of erbium-doped glass fiber amplifiers for telecommunications [29], there have also been extensive efforts toward doping silicon with erbium, a rare-earth element that can emit at wavelengths near 1.54 μm when in the proper oxidation state [30]. To date, it has been found that the radiative efficiency of erbium in silicon is too low to generate net gain; however, erbium-doped glass cladding layers have been successfully used for optically pumped silicon-based microcavity lasers [31]. Another demonstrated photonic device concept that holds promise for hybrid devices is the silicon slot waveguide structure, which takes advantage of the large index of silicon to tightly confine a propagating optical mode within a low-index nanoscale region in the center of the waveguide [32, 33]. By filling the narrow slot with light-emitting [34] or switchable [35] materials, slot waveguides can leverage favorable optical properties not inherent to silicon itself, while maintaining the benefits of silicon for guiding optical modes.

Finally, waveguides supporting surface-plasmon modes at a metal-dielectric interface can be used to confine light to a surface in order to maximize interaction with a thin dielectric cladding layer and potentially achieve smaller mode volumes than are possible with dielectric waveguides [36, 37]. However, efficient integration of plasmonic structures with silicon photonics and the mitigation of attenuation due to absorption in the metal remain formidable challenges. If these challenges are adequately addressed, propagating surface plasmons can be exploited to enhance the sensitivity of waveguide modes to dynamic material properties such as electrorefraction [38] or thermo-optic effects [39] for switching applications. Furthermore, since a plasmonic mode concentrated at a metal-dielectric interface can be very responsive to changes in optical properties immediately at the metal surface, the integration of plasmonic structures with SOI waveguides has the potential to enable compact, monolithic chemical and biological sensors.

1.4 Scope of This Thesis

This thesis describes three new hybrid device concepts that use materials other than silicon to achieve different optical functionalities on the silicon photonics platform. The chapters are organized as follows:

- **Design and Fabrication of SOI Waveguides:** Chapters 2 and 3 describe the SOI structures that form the foundation of the hybrid devices demonstrated in the rest of the thesis. In Chapter 2, we present calculations of the optical modes supported in SOI waveguides for both single-layer silicon and Si/SiO$_2$/Si slot geometries. We also provide details on the design of surface-relief grating couplers and waveguide ring resonators, which are used to probe the optical characteristics of SOI-integrated devices in subsequent chapters. In Chapter 3, we describe the fabrication and optical characterization of SOI devices, and we present Si/SiO$_2$/Si slot waveguides fabricated by wafer bonding.

- **Enhanced Erbium Emission:** Chapter 4 describes the enhancement of radiative spontaneous emission for infrared emitters embedded in silicon slot waveguides, with applications for waveguide-integrated light sources. Calculations of the local density of optical states for Si/SiO_2/Si slab waveguides are presented, and it is shown that the radiative spontaneous emission rate of an emitter in the low-index slot layer can be enhanced by more than an order of magnitude. Furthermore, the calculations suggest that emission will couple preferentially to guided modes that exhibit high electric-field confinement in the slot. We then describe experiments aimed at measuring the spontaneous emission rate enhancement in slot waveguides with erbium-doped glass slot layers emitting at wavelengths near 1.54 μm. From time-resolved photoluminescence measurements, we determine that the rates of both radiative and non-radiative decay are enhanced for optically excited Er^{3+} in slot structures, resulting in significantly increased emission rates but comparable internal quantum efficiencies for erbium-doped films in slot waveguides compared with emitters in bulk glass.

- **Phase-Change Modulation:** Chapter 5 examines integrated photonics applications of vanadium dioxide, a material that undergoes a reversible insulator-to-metal phase transition accompanied by drastic changes in optical properties. For this first demonstration, the VO_2 phase transition is induced thermally; however, implementations using faster optically or electrically induced switching are discussed. Measurements of the complex refractive index of VO_2 films fabricated by pulsed-laser deposition reveal a shift from a relatively transparent state to a highly absorbing metallic phase at wavelengths near 1.55 μm. We propose a single-pass absorption modulator design based on VO_2-clad SOI waveguides, and we use a SOI ring resonator to probe a 2-μm long VO_2 device exhibiting broadband modulation of more than 6.5 dB at telecommunication wavelengths.

- **Plasmonic Waveguide Integration:** Chapter 6 presents the experimental realization of dielectric-loaded surface-plasmon polariton (DLSPP) waveguides and ring resonators on the SOI platform. We demonstrate insertion loss of 1.0 ± 0.1 dB for 1.55-μm light coupled between SOI waveguides and DLSPP waveguides composed of polymer wires patterned on gold. In addition, average intrinsic quality factors of 180 ± 8 are observed for 10-μm diameter DLSPP ring resonators. It is shown that the DLSPP structures support a single plasmonic mode that is strongly confined to the polymer dielectric cladding, particularly at the gold-polymer interface. Given the coupling efficiencies demonstrated in this study, it is feasible to envision compact plasmonic components becoming part of monolithically integrated on-chip networks without introducing excessive loss.

Chapter 2

Grating-Coupled Silicon-on-Insulator Waveguides

In this chapter, we introduce properties of silicon photonic waveguides that will be referred to throughout the rest of the thesis. While there have been many previous implementations of the concepts described in this chapter, we feel it is instructive to explicitly develop the framework for our particular SOI waveguide platform, which we use to explore novel device concepts in subsequent chapters. We begin with a brief overview of the electromagnetic modes supported in single-layer and slot silicon-on-insulator (SOI) waveguides, followed by a description of surface-relief diffraction gratings, which we employ in experimental measurements to couple light between free space and guided waveguide modes. Finally, we present a few important relations for analyzing waveguide ring resonators, which we use in later chapters to probe the characteristics of fabricated silicon waveguides as well as the the optical properties of thermochromic phase-change material and plasmonic waveguide structures.

2.1 Guided Modes in Single-Layer and Slot Waveguides

We are generally interested in the electromagnetic modes supported at near-infrared wavelengths by a silicon waveguiding layer surrounded by cladding material with a lower refractive index. In particular, we examine devices designed to operate near the optical telecommunications C-band, which covers wavelengths from $\lambda = 1530$ to 1565 nm. The multilayered slot waveguide geometry is considered in detail, where the waveguiding region is composed of two silicon layers surrounding a thin slot layer.

Single-layer waveguides are simply a special case of the slot geometry with a slot-layer thickness of zero.

As seen in Chapter 3, where we describe the fabrication of silicon waveguide devices, commercially available SOI wafers provide an excellent starting point for designing photonic elements. Using SOI, guided modes can be confined vertically within a thin layer of high-refractive-index single-crystal silicon that sits atop a lower-index buried SiO_2 layer. Furthermore, given a relatively low doping concentration, one can perform accurate mode calculations assuming the silicon layer is lossless at wavelengths near 1550 nm. As will be shown here, a slightly more complicated slot waveguide structure allows for greatly enhanced modal confinement, particularly when the slot layer is thin ($<$ 100 nm) and has a refractive index significantly smaller than that of silicon [32]. Large modal confinement within such thin layers opens up exciting opportunities for enhancing the interaction of guided modes with active materials. As a prime example, slot waveguides can be used to significantly modify the spontaneous emission properties of dipole emitters embedded in the slot, which is the topic of Chapter 4.

In addition to the vertical confinement provided by SOI substrates, the silicon device layer can be patterned to form narrow wires or ridges that provide lateral confinement of propagating modes. Silicon waveguides with two-dimensional confinement can be used to direct light to and from other on-chip components while occupying a relative small area, which is the primary function of the SOI waveguides described in Chapters 5 and 6. We specifically consider shallow-ridge SOI waveguides for practical reasons. First, as shown in Section 2.2, patterned diffraction gratings are most effective at coupling light between guided and free-space modes when the grating is partially etched into the silicon device layer. By designing SOI waveguides of the same depth, grating-coupled devices can be fabricated in a single pattern-transfer process, as described in Chapter 3. Second, while bulk losses can be remarkably low in high-quality silicon, the large index contrast between silicon and low-index cladding materials makes SOI waveguides very sensitive to any geometrical imperfections introduced during device fabrication [40]. By minimizing the etched sidewall area, shallow-ridge waveguides have been shown to exhibit reduced scattering-induced propagation loss [41, 42]. Finally, looking forward to integrated opto-electronic devices, the shallow-ridge design allows for lateral electrical access to the SOI waveguiding region.

2.1.1 Mode Calculations

From the electromagnetic theory of light, we express optical modes in terms of their electric and magnetic fields, which obey Maxwell's equations. Assuming the absence of both fixed charge and charge current, Maxwell's equations can be expressed as

$$\nabla \cdot \mathbf{E}(\mathbf{r}, t) = 0 \ , \tag{2.1a}$$

$$\nabla \cdot \mathbf{H}(\mathbf{r}, t) = 0 \ , \tag{2.1b}$$

$$\nabla \times \mathbf{E}(\mathbf{r}, t) + \mu_0 \frac{\partial}{\partial t} \mathbf{H}(\mathbf{r}, t) = 0 \ , \tag{2.1c}$$

$$\nabla \times \mathbf{H}(\mathbf{r}, t) - \epsilon(\mathbf{r}) \ \frac{\partial}{\partial t} \mathbf{E}(\mathbf{r}, t) = 0 \ , \tag{2.1d}$$

where $\mathbf{E}(\mathbf{r}, t)$ and $\mathbf{H}(\mathbf{r}, t)$ are the electric and magnetic fields, respectively, and it is assumed we have non-magnetic materials with the permeability of vacuum, μ_0, and isotropic dielectric constant, $\epsilon(\mathbf{r})$. For monochromatic light with angular frequency ω, we have $\mathbf{E}(\mathbf{r}, t) = \mathbf{E}(\mathbf{r})e^{-i\omega t}$ and $\mathbf{H}(\mathbf{r}, t) = \mathbf{H}(\mathbf{r})e^{-i\omega t}$.[†] Equations 2.1c and 2.1d can then be written as

$$\nabla \times \mathbf{E}(\mathbf{r}) - i\omega\mu_0 \mathbf{H}(\mathbf{r}) = 0 \ , \tag{2.2a}$$

$$\nabla \times \mathbf{H}(\mathbf{r}) + i\omega\epsilon(\mathbf{r}) \mathbf{E}(\mathbf{r}) = 0 \ . \tag{2.2b}$$

[†] It is not strictly rigorous notation to use the vector symbols **E** and **H** for both the time-dependent and time-independent fields, but we do so for simplicity. In this case, as well as for fields with different spatial dependencies, we explicitly write the dependent variables in order to properly identify each function.

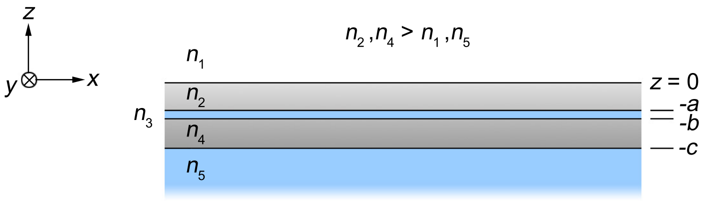

Figure 2.1. Geometry of a general one-dimensional slab silicon-on-insulator slot waveguide.

Taking the curl of the expressions in Eq. 2.2, and assuming that $\epsilon(\mathbf{r})$ is isotropic and piecewise constant, we can obtain the Helmholtz equation in terms of either the electric or magnetic field:

$$\nabla^2\mathbf{E}(\mathbf{r}) + n^2(\mathbf{r})\frac{\omega^2}{c^2}\mathbf{E}(\mathbf{r}) = 0 \; , \tag{2.3a}$$

$$\nabla^2\mathbf{H}(\mathbf{r}) + n^2(\mathbf{r})\frac{\omega^2}{c^2}\mathbf{H}(\mathbf{r}) = 0 \; , \tag{2.3b}$$

where the dielectric constant is related to the refractive index, $n(\mathbf{r})$, as $\epsilon(\mathbf{r}) = \epsilon_0 n^2(\mathbf{r})$, and where ϵ_0 is the permittivity of free space and the speed of light in vacuum is $c = 1/(\mu_0\epsilon_0)^{1/2}$.

The geometry depicted in Fig. 2.1 is an infinite slab with variations in the dielectric constant only along the z-direction. If we consider electromagnetic modes confined to the plane of the slab, the coordinate system can be oriented so that modes propagate along the x-direction with the form $\mathbf{E}(\mathbf{r}) = \mathbf{E}(z)e^{i\beta x}$, where the fields cannot have y-dependence because of translational symmetry. The Helmholtz equation for the electric field then becomes

$$\frac{d^2\mathbf{E}}{dz^2} + (k^2 n^2(z) - \beta^2)\mathbf{E}(z) = 0 \; , \tag{2.4}$$

and similarly for the magnetic field, where $k = \omega/c$ is the free-space wavenumber, which is related to the free-space wavelength by $k = 2\pi/\lambda$.

The z-component of the wavevector in region j with index n_j is

$$k_{jz} = (k^2 n_j^2 - \beta^2)^{1/2} \ , \tag{2.5}$$

which can be either purely real or purely imaginary. We first consider transverse-electric (TE) solutions to Eq. 2.4, where the electric field is oriented along the y-axis, so that $\mathbf{E}(z) = E_y(z)\ \hat{\mathbf{y}}$. The general solution for guided modes can be expressed as

$$E_y(z) = \begin{cases} A_1 e^{ik_{1z}z} & , \ z > 0 \\ A_2 \cos[k_{2z}z] + B_2 \sin[k_{2z}z] & , \ 0 > z > -a \\ A_3 \cos[k_{3z}(z+a)] + B_3 \sin[k_{3z}(z+a)] & , \ -a > z > -b \\ A_4 \cos[k_{4z}(z+b)] + B_4 \sin[k_{4z}(z+b)] & , \ -b > z > -c \\ A_5 e^{-ik_{5z}(z+c)} & , \ z < -c \ , \end{cases} \tag{2.6}$$

where the field decays away exponentially in the cladding regions when the condition

$$\max[n_2, n_4] > \beta > n_1, n_5 \tag{2.7}$$

is satisfied. The mode solution has a total of nine unknown parameters, including the coefficients A_j, B_j and the propagation constant β. From Maxwell's equations, both $E_y(z)$ and its derivative, dE_y/dz, must be continuous at each dielectric interface [43], which, combined with a normalization condition,[‡] allows the unknown parameters to be completely determined. While the solution for a structure with a single waveguiding layer can be written down in a relatively compact form, we used the symbolic solver in *Mathematica* to obtain the transcendental equation that determines β for more complicated multilayer structures. In general, there are multiple values of β that satisfy the condition given in Eq. 2.7, each corresponding to a unique guide mode.

For transverse-magnetic (TM) guided modes, the magnetic field is oriented along

---

[‡] To simply determine β, the normalization condition can be somewhat arbitrary, e.g. $A_1 = 1$. We develop more physically relevant normalization conditions in Chapter 4 in order to determine the relative contribution of guided modes to the total modal density in dielectric slot waveguides.

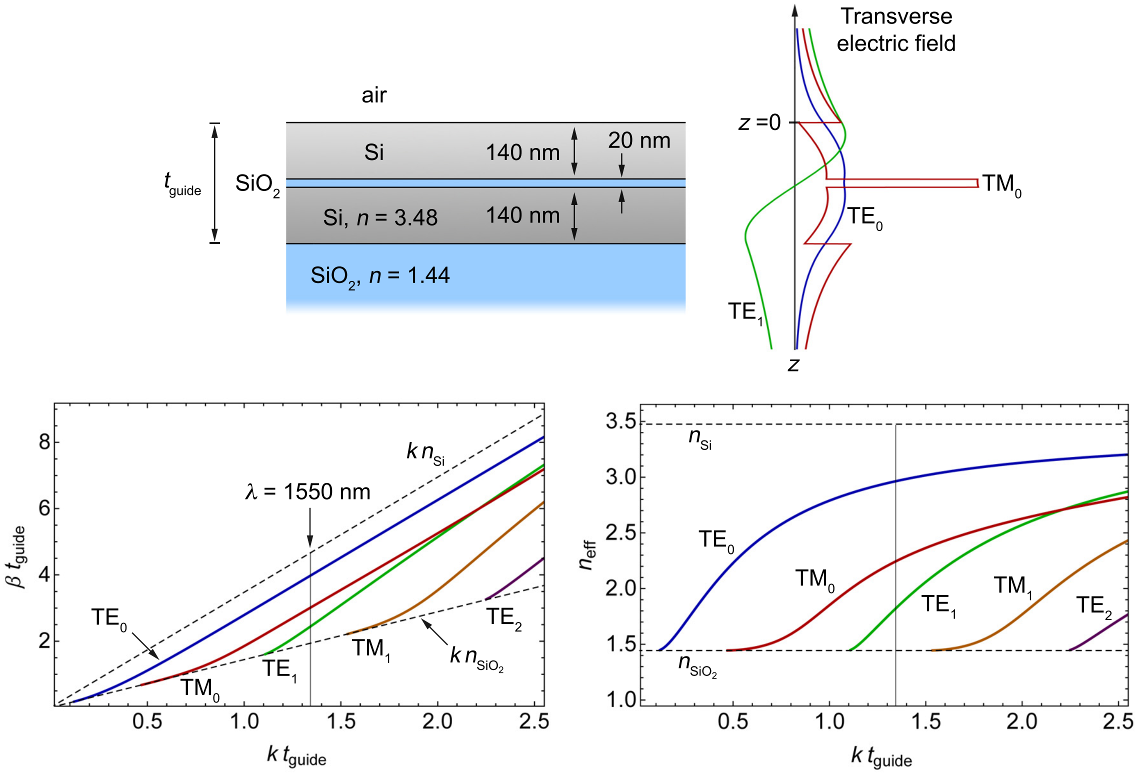

Figure 2.2. Modes supported by a slab silicon slot waveguide with the indicated dimensions. The transverse component of electric field for each mode supported at $\lambda = 1550$ nm is plotted alongside the waveguide geometry. The modal dispersion is plotted for the propagation constant, β, as well as for the normalized propagation constant (effective index), $n_{\text{eff}} = \beta/k$, where $k = 2\pi/\lambda$.

the y-axis, so that $\mathbf{H}(z) = H_y(z)\ \hat{\mathbf{y}}$, where $H_y(z)$ assumes the same general form as the electric field given in Eq. 2.6. However, for TM modes, the magnetic field and the longitudinal component of the electric field, $E_x(z)$, are continuous at the index interfaces, as dictated by Maxwell's equations [43]. From Eq. 2.2b, we have that $E_x(z) = \frac{-i}{\omega\epsilon(z)}\frac{dH_y}{dz}$ and $E_z(z) = \frac{-\beta}{\omega\epsilon(z)}H_y(z)$, so the continuity of $E_x(z)$ means that the magnetic field has a slope discontinuity at the index interfaces proportional to the ratio of the dielectric constants in each medium. Furthermore, the transverse electric field in medium i, near the interface with medium j, has a discontinuity equal to n_j^2/n_i^2.

An example slab silicon slot waveguide is shown in Fig. 2.2, where $n_2 = n_4 = n_{\text{Si}}$, $n_3 = n_5 = n_{\text{SiO}_2}$, and $n_1 = 1$. The value of β was calculated over a range of free-space wavenumbers, k, revealing the modal dispersion for the given layer dimensions. The dispersion relation can also be represented in terms of the normalized propagation constant, or effective modal phase index, $n_{\text{eff}} = \beta/k$. Near $\lambda = 1550$ nm, two TE modes and one TM mode are supported, where the transverse electric field profiles are plotted in the upper-right part of the figure. The modes are identified by their polarization and a subscript indicating the mode order (0 for the fundamental modes). For the TE modes, one can clearly see the continuity of the electric field across the index interfaces, while the TM mode has pronounced discontinuities in the transverse electric field, $E_z(z)$. This illustrates perhaps the most interesting property of silicon slot waveguides with a narrow, low-index slot layer: the TM-mode electric field in the slot is enhanced by a factor of $n_{\text{Si}}^2/n_{\text{slot}}^2$ near the silicon waveguiding layers.

In addition to fostering physical intuition, calculating guided modes in the analytically soluble case of a one-dimensional slab is instrumental to our analysis of spontaneous emission rates in Chapter 4. However, we are also interested in realizing SOI waveguides with both vertical and lateral confinement. For the example shallow-ridge waveguide geometries shown in the top panels of Fig. 2.3, we must solve Eqs. 2.3 in two dimensions, which requires numerical techniques. We used COMSOL Multiphysics, a commercial finite-element method software package, to determine the mode solutions shown in Fig. 2.3. For each mode, the density plots represent the time-averaged power flow in the propagation direction (x), given by

$$P_x = \frac{1}{2}\text{Re}\left\{[\mathbf{E}(y,z) \times \mathbf{H}^*(y,z)] \cdot \hat{\mathbf{x}}\right\} \ , \tag{2.8}$$

where, for clarity in the plots, the power flow is normalized to its maximum value for each mode. Assuming only real permittivities, there is no power flow along the y- or z-directions. The magnitude and orientation of the transverse electric field for the modes in Fig. 2.3 are represented by the arrows, and we note that, while the modes exhibit either dominant TE- or TM-mode character, there is noticeable TE-TM hybridization near the shallow-ridge sidewalls. While the modes supported by waveguides with lateral confinement are not purely TE or TM, it is conventional to

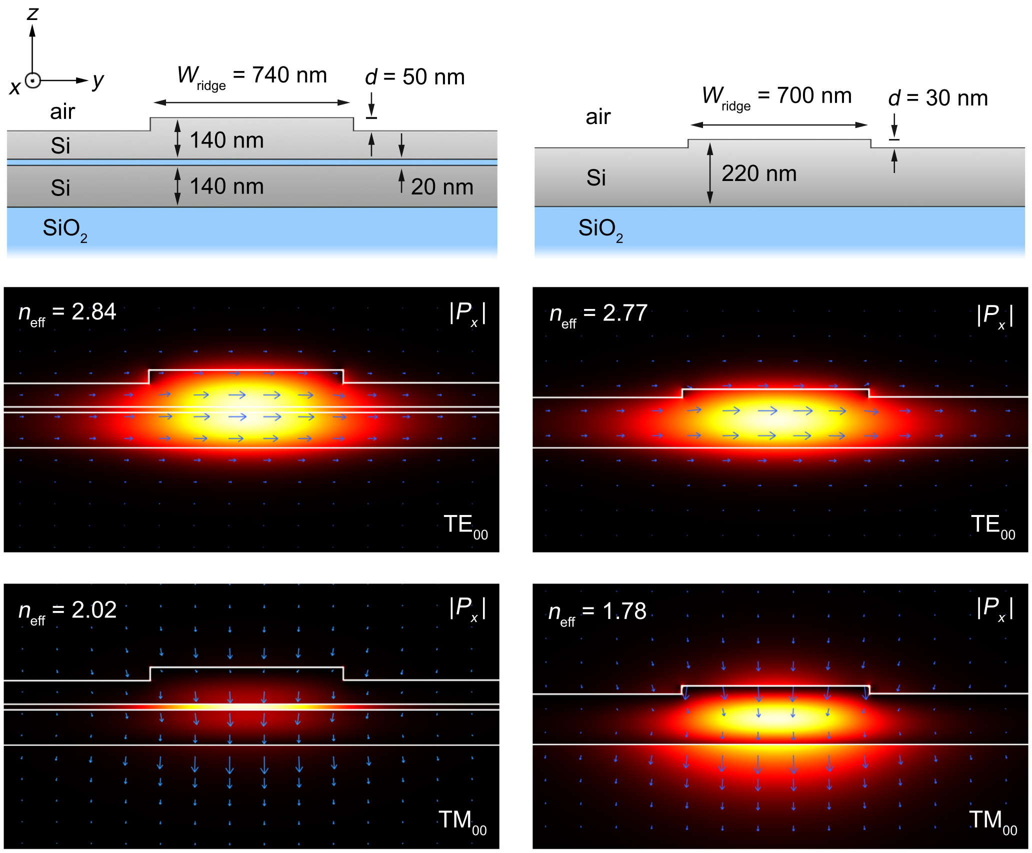

Figure 2.3. Modes supported by shallow-ridge SOI waveguides at $\lambda = 1550$ nm, calculated using the electromagnetic finite-element method in two dimensions. The density plots represent the power in the propagation direction (x), and the arrows indicate the magnitude and orientation of the in-plane (transverse) electric field.

identify them by those labels according to their dominant field polarization. Each mode is identified by a double subscript, indicating that there can be multiple vertical and lateral mode orders.

2.1.2 Modal Group Velocity

Physically, the propagation constant, β, is related to modal phase velocity, v_{p}, where $v_{\mathrm{p}} = \omega/\beta = c/n_{\mathrm{eff}}$. For a monochromatic plane wave propagating in an infinite homogeneous medium, v_{p} is also the group velocity, $v_{\mathrm{g}} = \partial\omega/\partial\beta$, which is equivalent to the speed of energy flow in lossless media. However, even when neglecting any material dispersion in the constituent materials, waveguide modes exhibit dispersion that can lead to different values of v_p and v_g. We define the group index, n_g, as $n_\mathrm{g} = c/v_\mathrm{g} = \partial\beta/\partial k$, which for the waveguide modes calculated in the preceding section can be found from the slope of the dispersion relations in Fig. 2.2. We note that for modes far from cutoff, the dispersion is very nearly linear over narrow ranges of wavelength. Furthermore, the indices of silicon and silica are nearly constant across the C-band; therefore, we neglect higher-order dispersion terms (i.e. group velocity dispersion).

It is often useful to express the group index in terms of the effective index. Neglecting material dispersion, we have

$$n_\mathrm{g} = \frac{d\beta}{dk} = n_\mathrm{eff}(k) + k\frac{dn_\mathrm{eff}}{dk} \ , \tag{2.9}$$

or, in terms of wavelength:

$$n_\mathrm{g} = n_\mathrm{eff}(\lambda) - \lambda\frac{dn_\mathrm{eff}}{d\lambda} \ . \tag{2.10}$$

2.1.3 Leaky TM Modes in Ridge Waveguides

An important additional design consideration for shallow-ridge waveguides is the possibility of leakage from laterally guided modes into slab modes supported in the surrounding slab regions. In particular, for geometries similar to those shown in Fig. 2.3, the effective index of the TM_{00} ridge mode, $n_\mathrm{eff,TM}$, can be less than that of the TE_0 slab mode, $n^\mathrm{slab}_\mathrm{eff,TE}$. Since the slab mode can propagate at any angle, φ, relative to the x-direction in the xy-plane, the modes can couple to one another when $n^\mathrm{slab}_\mathrm{eff,TE}\cos\varphi = n_\mathrm{eff,TM}$, where TM-to-TE mode conversion is facilitated by the ridge sidewalls.

Webster, *et al.* made the insightful observation that the width of the waveguide ridge can be designed so that the TE slab mode in the ridge (with effective index $n^\mathrm{core}_\mathrm{eff,TE}$) interferes destructively with the TE slab mode in the partially etch regions, which minimizes leakage from the laterally confined TM mode [44]. This requires that the phase accumulated by the TE slab mode in the ridge as it traverses the ridge width, W_{ridge}, be an integer multiple of 2π, or, in terms of the free-space wavelength:

$$W_{\text{ridge}} = \frac{m\lambda}{\sqrt{(n_{\text{eff,TE}}^{\text{core}})^2 - (n_{\text{eff,TM}})^2}}, \quad m = 1, 2, 3... \tag{2.11}$$

Values of W_{ridge} fulfilling this condition have been dubbed "magic" widths [42, 45]. In the work reported in this thesis, we designed our SOI ridge waveguides (including the geometries shown in Fig. 2.3) to meet the magic width condition for $m = 1$. Satisfying Eq. 2.11 for $m > 1$, without allowing higher lateral-order modes to be supported in the ridge, requires extremely shallow ridges that are difficult to fabricate and exhibit large bending loss in curved waveguide geometries [41, 44].

2.2 Surface-Relief Grating Couplers

As shown experimentally for fabricated devices in Chapter 3, surface-relief diffraction gratings can be etched into the device layer of a SOI waveguide to facilitate coupling between free-space radiation and guided modes. Ultimately, we wish to interface on-chip devices with fiber-coupled sources and detectors. As described in Chapter 3, this can be accomplished by using grating couplers to diffract light at a specified angle relative to the chip surface, where lensed fibers are positioned at the same angle above the waveguide. To properly design the grating geometry and achieve predictable free-space coupling angles, we seek to understand how a periodic perturbation affects the previously calculated propagating waveguide modes. We use the approximation method laid out by Streifer, *et al.* for both TE modes [46] and TM modes [47], which was initially developed to design Bragg reflectors and distributed-feedback structures for semiconductor lasers.

We consider the general grating geometry shown in Fig. 2.4(a), with a periodic rectangular profile of pitch Λ, tooth width w, and depth d. When a guided mode encounters the grating, the modal propagation constant is affected by the dielectric perturbation, but the grating also diffracts light into modes with different in-plane momentum. If the magnitude of the modified in-plane wavenumber is less than kn_1,

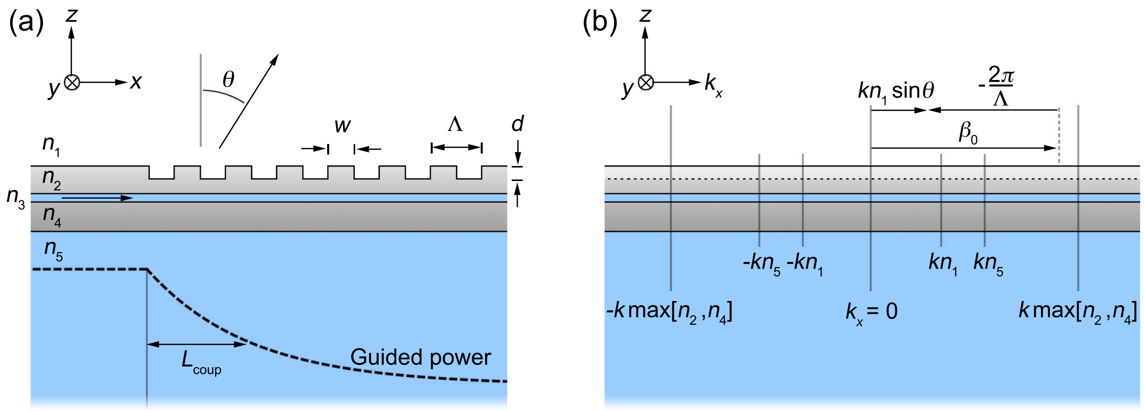

Figure 2.4. Schematic of a SOI-waveguide surface-relief grating coupler assumed to be infinitely broad in the y-direction. (a) As a guided mode propagating along the x-direction encounters the grating, light can be diffracted into unguided modes in the cover and substrate regions, resulting in exponential attenuation of the guided power. (b) This quasi-k-space diagram shows how the guided mode in the grating region, with wavevector β_0, can be diffracted into modes differing in their in-plane momentum by an integer multiple of $2\pi/\Lambda$.

then the mode will radiate into the cover region at a well-defined angle, as depicted in Fig. 2.4(b). We define the coupling angle, θ, relative to the normal of the waveguide surface. Light can of course also be diffracted into radiative modes in the substrate and even into other guided modes, but we focus our analysis on light radiated into the cover region where it can be collected by external optics. Finally, note that while we have created a physical picture of the grating coupler problem in terms of a guided mode being coupled into free space, the out-coupling angle, by symmetry, is equivalent to the in-coupling angle for a given mode.

The interaction of a grating with TE modes will be analyzed first. We consider grating structures that are infinitely wide in the y-direction with the same layer dimensions as the slab waveguide geometry in Fig. 2.1. However, with the addition of the grating, the refractive index is now a function of both x and z. Since the index is periodic in x, it can be represented by a Fourier series:

$$n^2(x,z) = n_0^2(z) + \sum_{\substack{q=-\infty \\ q\neq 0}}^{\infty} C_q(z) e^{2\pi i q x/\Lambda} \ , \tag{2.12}$$

where $n_0^2(z)$ is the $q = 0$ Fourier coefficient, given by:

$$n_0^2(z) = \begin{cases} \frac{wn_2^2+(\Lambda-w)n_1^2}{\Lambda} & , \ 0 > z > -d \\ n_j^2 & , \ \text{otherwise} \ . \end{cases} \tag{2.13}$$

Note that, in the grating region, $n_0^2(z)$ is simply the average dielectric constant. For a rectangular grating profile, the other coefficients in Eq. 2.12 are given by

$$C_q(z) = \begin{cases} \left(\frac{n_2^2-n_1^2}{\pi q}\right) \sin\left(\frac{\pi q w}{\Lambda}\right) & , \ 0 > z > -d \\ 0 & , \ \text{otherwise} \ . \end{cases} \tag{2.14}$$

Setting $C_{q\neq 0} = 0$, the one-dimensional Helmholtz equation can be solved to obtain an initial approximation of the modes supported in the grating waveguide structure. We identify the approximated guided TE-mode solution as $\mathbf{E}_0(z) = E_{y,0}(z)\ \hat{\mathbf{y}}$ with a propagation constant β_0. Equation 2.4 then becomes

$$\frac{d^2\mathbf{E}_0}{dz^2} + (k^2 n_0^2(z) - \beta_0^2)\mathbf{E}_0(z) = 0 \ , \tag{2.15}$$

with solutions of the form

$$E_{y,0}(z) = \begin{cases} A_{1,0}e^{ik_{1z,0}z} & , \ z > 0 \\ A_{d,0}\cos\left[k_{dz,0}z\right] + B_{d,0}\sin\left[k_{dz,0}z\right] & , \ 0 > z > -d \\ A_{2,0}\cos\left[k_{2z,0}(z+d)\right] + B_{2,0}\sin\left[k_{2z,0}(z+d)\right] & , \ -d > z > -a \\ A_{3,0}\cos\left[k_{3z,0}(z+a)\right] + B_{3,0}\sin\left[k_{3z,0}(z+a)\right] & , \ -a > z > -b \\ A_{4,0}\cos\left[k_{4z,0}(z+b)\right] + B_{4,0}\sin\left[k_{4z,0}(z+b)\right] & , \ -b > z > -c \\ A_{5,0}e^{-ik_{5z,0}(z+c)} & , \ z < -c \ . \end{cases} \tag{2.16}$$

The in-plane component of the wavevector for the different modes accessible with the grating is:

$$\beta_m = \beta_0 + \frac{2\pi m}{\Lambda} \ , \ m = 0, \pm1, \pm2... \tag{2.17}$$

where, here, m denotes the grating diffraction order. Then the z-component of the wavevector is given by:

$$k_{jz,m} = (k^2 n_j^2 - \beta_m^2)^{1/2} \ , \tag{2.18}$$

where the grating region is denoted by the index symbol $j = d$, so we have $n_j^2 = n_d^2 = [wn_2^2 + (\Lambda - w)n_1^2]/\Lambda$, for $0 > z > -d$.

For the mode solution given in Eq. 2.16, the TE-mode boundary conditions from Section 2.1 can be used to determine the value of β_0, which can then be inserted into Eq. 2.17 to estimate the in-plane wavenumbers of the diffracted modes. When $-kn_1 < \beta_m < kn_1$, the diffracted mode radiates into the cover region at a coupling angle equal to

$$\theta = \sin^{-1}\left(\frac{\beta_m}{kn_1}\right) . \tag{2.19}$$

If $-kn_5 < \beta_m < kn_5$, the diffracted mode also radiates into the substrate, where we assume it cannot be collected, and if $(k \ \max[n_1, n_5]) < |\beta_m| < (k \ \max[n_2, n_4])$, light can be diffracted into another guided mode, if such a mode exists with a propagation constant equal to β_m. Finally, if $|\beta_m| > (k \ \max[n_2, n_4])$, the diffracted mode must be exponentially decaying in all regions of the waveguide, which, given the boundary conditions, means the mode is zero everywhere. Since only a limited range of values of β_m will result in coupling to a mode characterized by a non-zero solution, there is a finite number of relevant diffraction orders.

Using the approximated values of β_m, we can also estimate the power coupled by the grating per unit length in the propagation direction. For mode solutions corresponding to the m^{th} grating diffraction order, the Helmholtz equation, given the full form of the refractive index given in Eq. 2.12, is

$$\frac{d^2\mathbf{E}_m}{dz^2} + (k^2 n_0^2(z) - \beta_m^2)\mathbf{E}_m(z) = -k^2 \sum_{\substack{q=-\infty \\ q\neq m}}^{\infty} C_{m-q}(z)\mathbf{E}_q(z) \ . \tag{2.20}$$

where $\mathbf{E}_m(z) = E_{y,m}(z)\ \hat{\mathbf{y}}$. Again using the framework laid out by Streifer, *et al.* [46], we define the function:

$$\mathcal{F}_m(z) = -k^2 \sum_{\substack{q=-\infty \\ q\neq m}}^{\infty} C_{m-q}(z)E_{y,q}(z) \ . \tag{2.21}$$

The solution to Eq. 2.20 is then given by

$$E_{y,m}(z) = \begin{cases} A_{1,m}e^{ik_{1z,m}z} & ,\ z > 0 \\ A_{d,m}\cos\left[k_{dz,m}z\right] + B_{d,m}\sin\left[k_{dz,m}z\right] + \mathcal{T}_m(z) & ,\ 0 > z > -d \\ A_{2,m}\cos\left[k_{2z,m}(z+d)\right] + B_{2,m}\sin\left[k_{2z,m}(z+d)\right] & ,\ -d > z > -a \\ A_{3,m}\cos\left[k_{3z,m}(z+a)\right] + B_{3,m}\sin\left[k_{3z,m}(z+a)\right] & ,\ -a > z > -b \\ A_{4,m}\cos\left[k_{4z,m}(z+b)\right] + B_{4,m}\sin\left[k_{4z,m}(z+b)\right] & ,\ -b > z > -c \\ A_{5,m}e^{-ik_{5z,m}(z+c)} & ,\ z < -c \ , \end{cases} \tag{2.22}$$

where

$$\mathcal{T}_m(z) = \frac{1}{k_{dz,m}} \int_0^z \mathcal{F}_m(\xi)\sin\left[k_{dz,m}(\xi - z)\right] \ . \tag{2.23}$$

If the function $\mathcal{F}_m(z)$ is approximated using only the previous solution, $E_{y,0}(z)$, from Eq. 2.16, then

$$\begin{aligned} \mathcal{F}_m(z) &= -k^2 C_m(z)E_{y,0}(z) \qquad (2.24) \\ &= \begin{cases} -k^2\left(\frac{n_2^2-n_1^2}{\pi m}\right)\sin\left(\frac{\pi m w}{\Lambda}\right)\left(A_{d,0}\cos\left[k_{dz,0}z\right] + B_{d,0}\sin\left[k_{dz,0}z\right]\right) & ,\ 0 > z > -d \\ 0 & ,\ \text{otherwise} \ . \end{cases} \end{aligned}$$

Consistent with this approximation, if we also assume that β_0 takes the value obtained from the approximate solution satisfying Eq. 2.15, then all of the coefficients in the solution given by Eq. 2.22 can be determined. For a given TE mode, the time-averaged power lost from the waveguide in the z-direction for the m^{th}-order grating mode is

$$P_{z,m}(z) = \frac{1}{2}\mathrm{Re}\left\{[\mathbf{E}_m(z) \times \mathbf{H}^*_m(z)] \cdot \hat{\mathbf{z}}\right\} = \frac{1}{2}\mathrm{Re}\left\{E_{y,m}(z)\left(\frac{-i}{\omega\mu_0}\frac{dE^*_{y,m}}{dz}\right)\right\} \ . \tag{2.25}$$

At the interface of the waveguide with the cover and substrate regions, the total radiated power per unit length is then [46]

$$P_{\mathrm{rad},m} = \frac{1}{2\omega\mu_0}\mathrm{Re}\left\{(k^2n_1^2 - \beta_m^2)^{1/2}|E_{y,m}(0)|^2 + (k^2n_5^2 - \beta_m^2)^{1/2}|E_{y,m}(-c)|^2\right\} \ . \tag{2.26}$$

Note that $P_{\mathrm{rad},m}$ in this form represents a relative value since $E_{y,m}(0)$ was never explicitly normalized with respect to power. By normalizing the radiated power per unit length to the power propagating in the guided mode, we obtain

$$\frac{1}{L_{\mathrm{coup}}} = \frac{\sum_m P_{\mathrm{rad},m}}{\frac{\beta_0}{2\omega\mu_0}\int_{-\infty}^{\infty}|E_{y,0}(z)|^2\, dz} \ , \tag{2.27}$$

where L_{coup} is the $1/e$ propagation length of the guided mode in the grating region. In general, multiple diffraction orders can contribute to the attenuation of the guided power, but only when $|\beta_m| < kn_1$ and/or $|\beta_m| < kn_5$.

Figure 2.5 shows an example calculation for the TE$_0$ mode supported by a silicon slot waveguide structure with a grating etched into the top silicon device layer. For the indicated pitch of $\Lambda = 660$ nm, only the $m = -1$ diffraction order results in coupling to radiative modes in the cover and substrate regions at a wavelength of $\lambda = 1550$ nm. The top panel shows the normalized power per unit length radiated into the cover and substrate regions as a function of the grating depth, d. As described in Chapter 3, we interface our fabricated grating coupled devices to lensed fiber focusers with a focused spot size on the order of 10 μm. Since the coupling length should

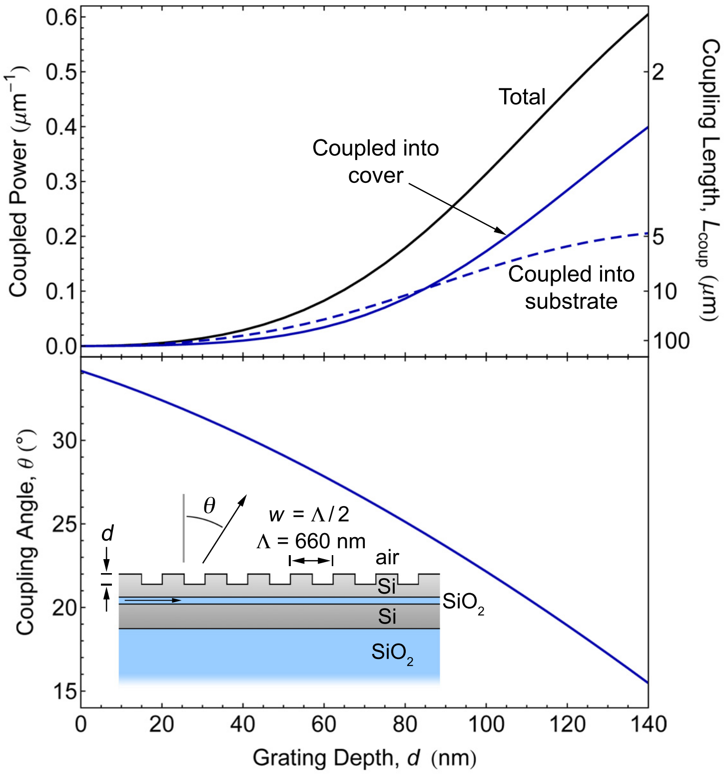

Figure 2.5. Normalized power coupled per unit length and coupling angle for a silicon slot waveguide grating coupler as a function of grating depth at $\lambda = 1550$ nm, plotted for the TE$_0$ waveguide mode. The waveguide is assumed to have 140-nm thick silicon layers and a 20-nm SiO$_2$ slot, and, due to the $m = -1$ diffraction order, power is coupled into the cover region (air) at an angle θ, and also into the SiO$_2$ substrate. The coupling length, L_{coup}, represents the propagation distance over which the guided power is attenuated to $1/e$ of its initial value.

be comparable to the spot size for efficient coupling [48], we see that the grating depth should be less than 100 nm. The lower panel in Fig. 2.5 shows the calculated coupling angle, θ, for the same range of grating depths, which was determined from the approximated guided mode solution using Eq. 2.19. For grating depths less than d =100 nm, the coupling angle is between 20° and 35° off-normal, which is easily accessible using free-space optics.

For TM modes, the coupling angle can be determined by an approximation method similar to the one used for TE modes. However, when Eq. 2.15 is cast in terms of the magnetic field, the zeroth-order Fourier coefficient of the index becomes [47]

$$n_0^2(z) = \begin{cases} \left(\frac{w}{n_2^2} + \frac{(\Lambda - w)}{n_1^2}\right)^{-1} \Lambda & , \ 0 > z > -d \\ n_j^2 & , \ \text{otherwise} . \end{cases} \tag{2.28}$$

The approximated propagation constant, β_0, can then be determined using the TM-mode boundary conditions identified in Section 2.1.

Figure 2.6 shows the TE_0 and TM_0 coupling angles calculated for the same grating geometry considered in Fig. 2.5, except that the grating depth is held fixed at $d =$ 50 nm, and the pitch is varied. At a pitch of $\Lambda = 660$ nm, the $m = -1$ diffraction order results in a TM_0-mode coupling angle of $\theta \sim -30°$, significantly different than the TE_0-mode coupling angle of $\theta \sim +30°$. The next accessible diffraction order, $m = -2$, does not result in coupling into the cover region for smaller values of the pitch. While it is not explicitly shown in the figure, a pitch of $\Lambda = 660$ nm also does not result in coupling into the higher-index substrate.

The example geometry in Fig. 2.6 illustrates a few of the key design principles for surface-relief grating couplers on SOI. First, gratings can take advantage of the unique phase velocities of TE and TM modes to facilitate *selective* coupling. We can design the pitch and depth of a grating to produce coupling angles for unique modes that are significantly different from one another, but both accessible using free-space optics. In Chapter 3, we present an experimental configuration that takes advantage of selective coupling by allowing adjustments in the angle of excitation and collection relative to the waveguide surface. Second, the grating pitch can be made sufficiently small such that radiative modes are accessible by only one diffraction order: $m = -1$. While the same coupling angles can be accessed with higher diffraction orders by increasing the pitch, the coupled power is then split between multiple radiative modes, making the coupling efficiency for any one diffraction order less efficient.

In subsequent chapters, we present fabricated grating-coupled waveguides with varying geometries. The grating couplers for these devices were all designed using the framework described here by simply modifying the form of the mode solutions to account, for example, for a higher-index cover layer of finite thickness or the absence of a slot region. The approximations made in this section result in some error in

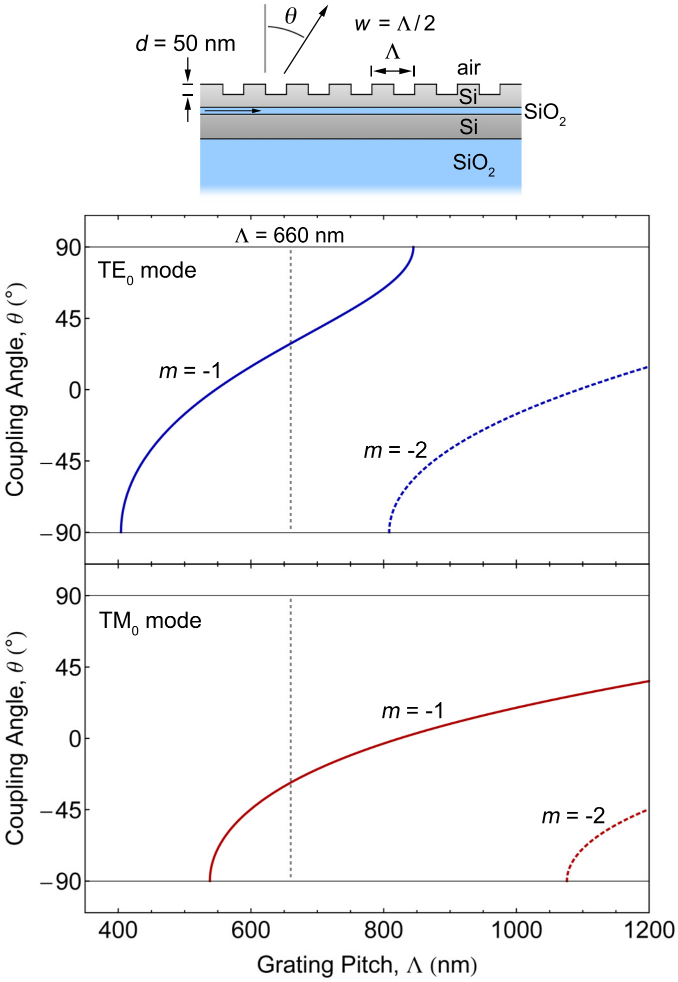

Figure 2.6. Coupling angles for the TE_0 and TM_0 guided modes in a silicon slot waveguide grating coupler as a function of grating pitch at $\lambda = 1550$ nm. The waveguide layer thicknesses are taken to be the same as the structure shown in Fig. 2.5, but with a fixed grating depth of $d = 50$ nm. At a grating pitch of $\Lambda = 660$ nm, only the $m = -1$ diffraction order couples into radiative modes, and the coupling angles for the TE_0 and TM_0 modes are approximately $+30°$ and $-30°$, respectively.

the predicted coupling angles compared with the experimental values; however, for the relatively shallow grating geometries shown here, we never observed this error to be more than a few degrees, which can be compensated for by slightly varying the experimental excitation/collection angle.

2.3 Ring Resonators

Throughout this thesis, we use waveguide ring resonator cavities as a tool to characterize fabricated waveguide structures. Figure 2.7 shows a general schematic of a SOI ridge-waveguide resonator coupled to a grating-coupled bus waveguide. While the modes supported by a curved waveguide are certainly different than those supported by a straight one, we assume the cross-sectional field profiles are the same. For the SOI rings we explore experimentally in Chapters 3 and 5, and even for the plasmonic rings in Chapter 6, this approximation is found to be acceptable based on the agreement between measured values of the modal group index and values calculated assuming the mode propagates in a straight line. Furthermore, the experiments reveal coupling to TE and TM modes of a single radial order, indicating that, in contrast to many disk resonator geometries (see, e.g., Borselli *et al.* [49]), no additional modes are excited within the interior region of the resonator.

Another concern with curved waveguides, particularly when dealing with the shallow-ridge SOI structures considered here, is radiation loss due to bending. We employed the effective index method laid out by Marcuse to estimate the bending loss using the calculated modal effective index [50]. For a 220-nm thick SOI ridge with an etch depth of 30 nm, the estimated propagation loss due to bending quickly exceeds 10 dB/cm as the bending radius is decreased below 100 μm, which, as will be shown in the next chapter, is significantly larger than the typical attenuation due to all other sources of loss. To be conservative, we typically fabricated rings with a bending radius of 200 μm, which, for an etch depth of 30 nm, results in an estimated bending loss below 10^{-2} dB/cm for TE modes and even lower for TM modes at wavelengths near $\lambda = 1550$ nm.

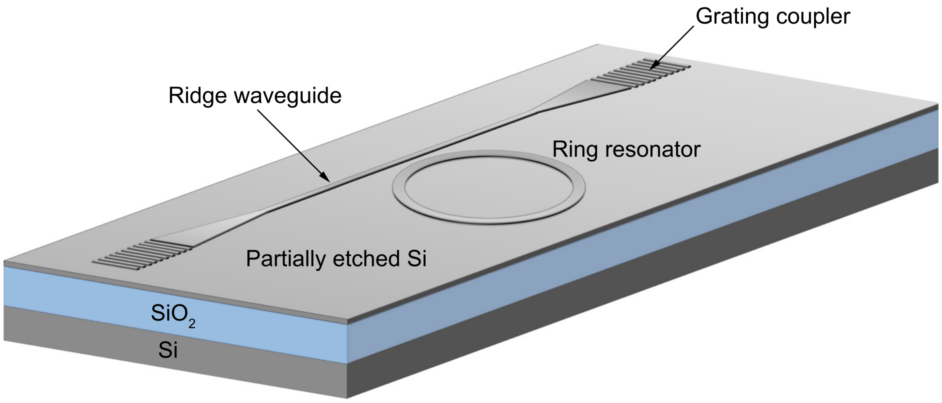

Figure 2.7. Schematic of a grating-coupled SOI waveguide and ring resonator. The straight bus waveguide acts as a directional coupler for exciting resonant modes in the ring.

2.3.1 Coupling to Cavity Modes

In an infinitely long straight waveguide, there is a spectral continuum of modes; however, the ring resonator geometry imposes the constraint that a circulating mode must be phase matched to itself after an integer number of round trips, which leads to discrete azimuthal mode orders in the ring resonator spectrum. Since we use straight through-port waveguides as evanescent couplers to direct light into and out of ring resonators, we need to know how the properties of the ring are manifested in the transmission spectrum of the bus waveguide. Yariv derived a general expression for the transmission past a resonator, T, in terms of the round-trip phase accumulated in the ring, δ, the field coupling parameter, $t = |t|e^{i\phi}$ (where ϕ accounts for additional phase accumulation caused by the evanescent coupler), and the round-trip fraction of the field intensity that is not lost to attenuation in the ring, a [51]:

$$T = \frac{a^2 + |t|^2 - 2a|t|\cos(\delta - \phi)}{1 + a^2|t|^2 - 2a|t|\cos(\delta - \phi)} \ . \tag{2.29}$$

Independent of the coupler, the phase accumulation in one round trip is $\delta = \beta L_\mathrm{c} = 2\pi n_\mathrm{eff} L_\mathrm{c}/\lambda$, where L_c is the round-trip distance around the resonator cavity. Since n_eff is generally a function of wavelength, the transmission spectrum for a through-port waveguide coupled to ring is thus

$$T(\lambda) = \frac{a^2 + |t|^2 - 2a|t|\cos\left(\frac{2\pi n_{\mathrm{eff}}(\lambda)L_{\mathrm{c}}}{\lambda} - \phi\right)}{1 + a^2|t|^2 - 2a|t|\cos\left(\frac{2\pi n_{\mathrm{eff}}(\lambda)L_{\mathrm{c}}}{\lambda} - \phi\right)} \ . \tag{2.30}$$

As was alluded to earlier, resonances in the ring occur when phase matching is satisfied, which corresponds to the condition

$$\frac{2\pi n_{\mathrm{eff}}(\lambda_m)L_{\mathrm{c}}}{\lambda_m} - \phi = 2\pi m, \quad m = 1, 2, 3... \tag{2.31}$$

where m is the azimuthal mode order, λ_m is the wavelength of the m^{th}-order resonance, and we assume that ϕ is not significantly dependent on wavelength. In the absence of gain ($a < 1$), the wavelengths λ_m correspond to minima in the transmission spectrum, and a and $|t|$ together determine the width and depth of the transmission dips centered at each minimum. By fitting the experimentally measured transmission spectra for fabricated ring resonators, with a, $|t|$, and ϕ taken as fitting parameters, we can determine the attenuation per unit length in the ring as $\alpha_{\mathrm{prop}} = -2\ln(a)/L_{\mathrm{c}}$ and the round-trip loss due to coupling as $l_{\mathrm{coup}} = -2\ln|t|$. We note that a and $|t|$ are interchangeable in Eq. 2.30, but one can design the bus-ring coupling gap to be sufficiently large so that losses are dominated by attenuation in the ring, in which case we have $a < |t|$ (corresponding to an *under-coupled* resonator).

The general result given by Eq. 2.30 is used to analyze small-diameter plasmonic ring resonators in Chapter 6; however, for shallow-ridge SOI resonators with a typical diameter of 400 μm, the azimuthal mode order for resonances near $\lambda = 1550$ nm is in excess of 1000. Consequently, instead of fitting multiple azimuthal orders, we analyze single resonances to determine the attenuation due to propagation loss and coupling.

Consider a resonance of arbitrary azimuthal order occurring at a wavelength λ_0. Since the coupling-induced phase shift, ϕ, is assumed to be constant, we assign it a value of zero for simplicity. If we consider small wavelength deviations, ε, around λ_0 [52], then we have

$$\delta = \frac{2\pi n_{\mathrm{eff}}(\lambda)L_{\mathrm{c}}}{\lambda} \approx \frac{2\pi n_{\mathrm{eff}}(\lambda_0 + \varepsilon)L_{\mathrm{c}}}{\lambda_0^2}(\lambda_0 - \varepsilon) \ , \tag{2.32}$$

where we retain only terms of the lowest-order in ε. If we write a Taylor expansion of $n_{\text{eff}}(\lambda)$ around λ_0, we obtain

$$\delta \approx \frac{2\pi L_{\text{c}}}{\lambda_0^2}(\lambda_0 - \varepsilon)\left[n_{\text{eff}}(\lambda_0) + \varepsilon \frac{dn_{\text{eff}}}{d\lambda}\Big|_{\lambda_0}\right] \approx \frac{2\pi L_{\text{c}}}{\lambda_0^2}\left[(\lambda_0 - \varepsilon)n_{\text{eff}}(\lambda_0) + \varepsilon\lambda_0 \frac{dn_{\text{eff}}}{d\lambda}\Big|_{\lambda_0}\right] , \tag{2.33}$$

which, using the definition of the group index, further simplifies to

$$\delta = \frac{2\pi L_{\text{c}}}{\lambda_0^2}\left[\lambda_0 n_{\text{eff}}(\lambda_0) - \varepsilon n_{\text{g}}(\lambda_0)\right] . \tag{2.34}$$

Then we have

$$\begin{aligned} \cos\delta = \cos\left(\frac{2\pi n_{\text{eff}}(\lambda_0)L_{\text{c}}}{\lambda_0}\right)\cos\left(\frac{2\pi\varepsilon n_{\text{g}}(\lambda_0)L_{\text{c}}}{\lambda_0^2}\right) \\ - \sin\left(\frac{2\pi n_{\text{eff}}(\lambda_0)L_{\text{c}}}{\lambda_0}\right)\sin\left(\frac{2\pi\varepsilon n_{\text{g}}(\lambda_0)L_{\text{c}}}{\lambda_0^2}\right) , \end{aligned} \tag{2.35}$$

which, given the phase-matching condition in Eq. 2.31, is simply

$$\cos\delta = \cos\left(\frac{2\pi\varepsilon n_{\text{g}}(\lambda_0)L_{\text{c}}}{\lambda_0^2}\right) = 1 - \frac{1}{2}\left(\frac{2\pi\varepsilon n_{\text{g}}(\lambda_0)L_{\text{c}}}{\lambda_0^2}\right)^2 + \cdots \tag{2.36}$$

Finally, keeping only the first two terms in the cosine series expansion and inserting the result into Eq. 2.29, we obtain

$$T(\lambda) = \frac{(t-a)^2 + (2\pi n_{\text{g}}L_{\text{c}})^2 at\frac{(\lambda-\lambda_0)^2}{{\lambda_0}^4}}{(1-at)^2 + (2\pi n_{\text{g}}L_{\text{c}})^2 at\frac{(\lambda-\lambda_0)^2}{{\lambda_0}^4}} . \tag{2.37}$$

Since Eq. 2.37 is valid only for an isolated resonance and for small values of $|\lambda - \lambda_0|$, we use it to model resonances with a linewidth, $\delta\lambda$, that is significantly smaller than both the mode spacing, $\Delta\lambda$, and the resonant wavelength, λ_0. In addition, the wavelength dependence of the group index can be neglected since n_{g} is approximately constant over narrow ranges of wavelength. Finally, because we do not explicitly account for the coupling-induced phase shift, ϕ, we take the parameter t to be real.

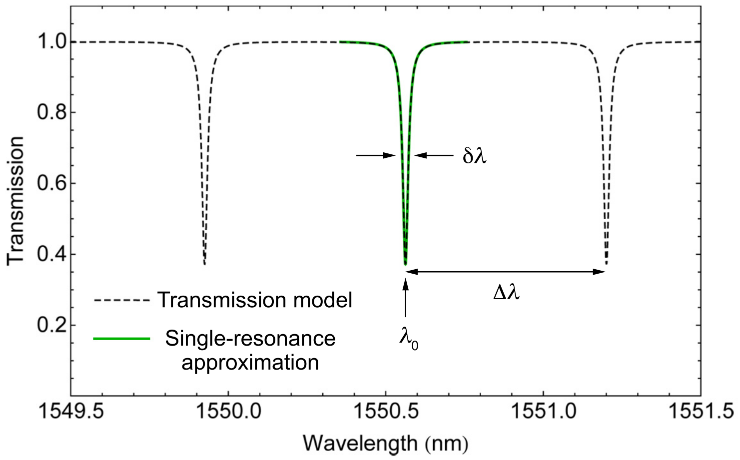

Figure 2.8. Predicted transmission spectrum for a through-port bus waveguide coupled to a 400-μm diameter ring resonator assuming propagation loss and coupling parameters $a = 0.92$ and $|t| = 0.98$ and dispersive modal effective index, $n_{\text{eff}}(\lambda) = 3 - (0.5\ \mu\text{m}^{-1})\lambda$. The dashed black curve represents the spectrum given by Eq. 2.30, and the solid green curve is the approximated spectrum for a single resonance given by Eq. 2.37 assuming small wavelength deviations around λ_0.

Figure 2.8 shows an example transmission spectrum for a bus waveguide coupled to a large-diameter ring resonator, predicted using Eq. 2.30. The single-resonance approximation given by Eq. 2.37 is also plotted, showing the excellent agreement for resonances fulfilling the conditions $\delta\lambda << \lambda_0$ and $\Delta\lambda << \lambda_0$.

2.3.2 Cavity Free-Spectral Range

The mode spacing between resonator modes, or the free-spectral range (FSR), is a useful parameter because it allows the modal group index to be estimated from measured resonator transmission spectra. Consider the phase difference between two adjacent resonances:

$$\frac{2\pi n_{\text{eff}}(\lambda_{m+1})L_{\text{c}}}{\lambda_{m+1}} - \frac{2\pi n_{\text{eff}}(\lambda_m)L_{\text{c}}}{\lambda_m} = 2\pi\ . \tag{2.38}$$

Assuming the modal effective index is approximately linear over the FSR, where the FSR is defined as $\Delta\lambda = \lambda_m - \lambda_{m+1}$, we have $n_{\text{eff}}(\lambda_{m+1}) \approx n_{\text{eff}}(\lambda_m) - \Delta\lambda(dn_{\text{eff}}/d\lambda)_{\lambda_m}$. The phase difference between resonances can then be expressed as

$$\frac{2\pi\left[n_{\mathrm{eff}}(\lambda_m) - \lambda_m \frac{dn_{\mathrm{eff}}}{d\lambda}\Big|_{\lambda_m}\right] L_{\mathrm{c}}\Delta\lambda}{\lambda_{m+1}\lambda_m} = \frac{2\pi n_{\mathrm{g}} L_{\mathrm{c}}\Delta\lambda}{\lambda_{m+1}\lambda_m} = 2\pi \ , \tag{2.39}$$

which, assuming $\Delta\lambda << \lambda_m$, gives the result:

$$\Delta\lambda \approx \frac{\lambda_m^2}{n_{\mathrm{g}} L_{\mathrm{c}}} \ . \tag{2.40}$$

2.3.3 Resonance Quality Factor

The quality factor, or Q factor, of a resonator is defined in terms of the ratio of the energy stored in the resonator, $\mathcal{E}$, and the rate of energy dissipation:

$$Q = \frac{\omega\mathcal{E}}{d\mathcal{E}/dt} \ . \tag{2.41}$$

In a passive resonator, the energy decay rate is identified as the inverse of the cavity lifetime, τ_{c}, where $d\mathcal{E}/dt = -\mathcal{E}/\tau_{\mathrm{c}}$. For a cavity length (ring-resonator circumference, in this case) of L_{c}, the cavity lifetime is related to the round-trip fractional loss, l, by the group velocity, so that

$$Q = \omega\tau_{\mathrm{c}} = \frac{\omega n_{\mathrm{g}} L_{\mathrm{c}}}{cl} = \frac{2\pi n_{\mathrm{g}} L_{\mathrm{c}}}{\lambda l} \ . \tag{2.42}$$

When a resonator has a Lorentzian spectral response, the Q factor is related to the power-spectrum full-width at half maximum, $\delta\omega$, by [43]

$$Q = \frac{\omega}{\delta\omega} \approx \frac{\lambda}{\delta\lambda} \ , \tag{2.43}$$

where the last approximation is valid when $\delta\lambda << \lambda$. These relations will prove useful in the analysis of fabricated ring resonator devices in subsequent chapters.

Chapter 3

Waveguide Fabrication and Testing

We realized grating-coupled silicon-on-insulator (SOI) waveguides using electron-beam lithography and reactive-ion etching. Using a custom-built waveguide testing setup, fabricated devices were characterized by spectrally resolved transmission measurements at infrared wavelengths near $\lambda = 1550$ nm. This chapter describes the device pattern transfer process and provides an overview of the performance of the waveguides and ring resonators that form the foundation of the hybrid devices described in Chapters 5 and 6. In the last section, we report on multilayer silicon slot waveguides and ring resonators fabricated by wafer bonding.

3.1 Fabricating Grating-Coupled SOI Ridge Waveguides

A typical array of grating-coupled SOI waveguide devices is shown in the optical microscope image in Fig. 3.1. Each device consists of a ring resonator evanescently coupled to through-port and drop-port waveguides, which are terminated with diffraction gratings that allow light to be redirected between free space and the modes of the waveguides. The gratings are made relatively large in order to efficiently capture light from an incident laser beam with a spot size on the order of 10 μm, and light is funneled into the sub-micron-wide single-mode waveguides using gradual tapers. The devices were defined by etching away ~ 30 nm of silicon from the 220-nm thick device layer of an SOI chip, where the waveguides and grating teeth were protected from the etch by a lithographically patterned mask. By starting with high-quality

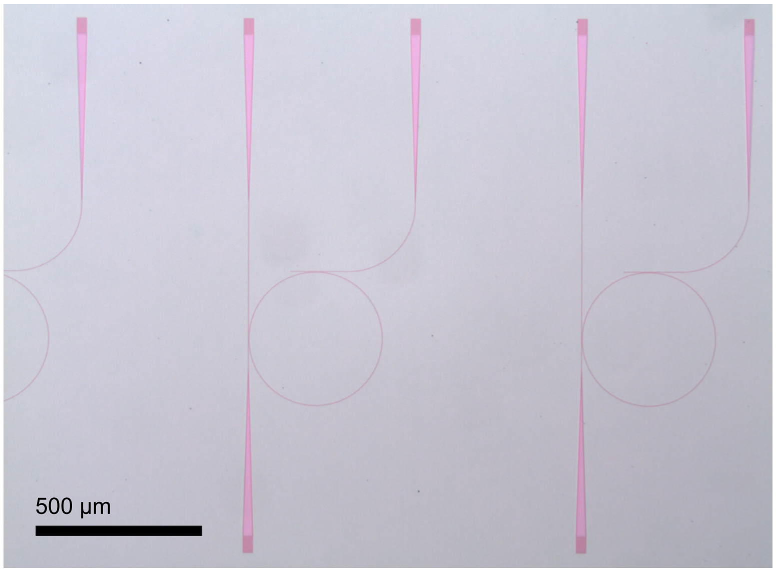

Figure 3.1. Optical microscope image of a patterned array of grating-coupled silicon-on-insulator waveguides and ring resonators.

SOI material, the propagation losses observed in our fabricated devices are largely due to imperfections introduced during the pattern-transfer process.

Figure 3.1 illustrates the utility of the grating-coupler scheme for on-chip device testing, namely that complete devices can be contained within a limited area on the chip surface and can consequently be arrayed in two dimensions. This is in contrast to edge-coupled devices with waveguides extending to the edge of the chip, which, when pattered on a single photonic layer, are topologically constrained to a one-dimensional array. Another advantage of grating-coupled devices is that the chip does not require further cleaving or edge polishing to accommodate end-fire coupling. In many cases, the waveguides and grating couplers can even be fabricated simultaneously in a single pattern-transfer process.

The advantages of grating couplers are particularly useful in a research setting, where devices are often tested one at a time and only need to be coupled to external sources and detectors for the duration of a measurement. For high-volume development and commercial applications, chips must interfaced with external optical fibers in a more robust and parallelized fashion. For their silicon photonics technology platform, researchers at IBM have developed a fixed, multi-channel chip-fiber interface using nanotapers [53] and spot size converters, with demonstrated insertion loss below 1 dB [54]. Another advantage of end-fire coupling is spectral bandwidth: by relying on diffraction to redirect light, grating couplers are inherently wavelength selective. Nevertheless, the grating bandwidth of the devices demonstrated here is large enough to avoid adversely affecting most measurements, but it does become a nuisance when characterizing broad plasmonic resonances, as described in Chapter 6.

3.1.1 SOI Source Material

For all the waveguide structures reported in this thesis, we began with commercially available SOI wafers from SOITEC, with either a 2- or 3-μm buried-oxide (BOX) layer separating the silicon substrate from the thin single-crystal silicon device layer. For the waveguide geometries we fabricated, the BOX layer thickness was found to be sufficient to prevent modes propagating in the device layer from significantly coupling into the substrate. We used wafers with p-type Si(001) device layers that were lightly doped with a boron concentration of $\sim 10^{15}$ cm^{-3}. The bulk losses in lightly doped SOITEC SOI are low enough that, as shown by Borselli *et al.*, the waveguide propagation loss near $\lambda = 1550$ nm is dominated by surface absorption and surface scattering caused by fabrication-induced roughness [55]. We used SOI with a device-layer thickness of 220 nm for single-layer waveguide devices; however, in some cases (such as with the multilayer wafer-bonded devices described in Section 3.4), we began with 250-nm thick device layer that was subsequently thinned by partially oxidizing the silicon layer, and the oxide was removed with hydrofluoric acid (HF). Prior to patterning samples, SOI samples were cleaved by hand from the full wafers and then rinsed in deionized (DI) water and blown dry with N_2 to remove debris generated during the cleaving process.

3.1.2 Electron-Beam Lithography

To form partially etched ridge structures, device patterns were first lithographically defined in ma-N 2403 negative tone resist (Micro Resist Technology). Prior to spin coating and baking the resist, SOI samples were cleaned in acetone and isopropanol and rinsed in DI water. The native oxide was then removed from the top silicon surface with a 10-s etch in buffered HF (Transene Buffer HF Improved), followed by another rinse in DI water and drying in N_2. Finally, samples were baked at 180 °C on a hotplate for at least 5 min to evaporate water from the surface. This cleaning and baking process was found to be essential for consistent resist wetting and adhesion. Resist was spun onto the SOI samples at 3000 rpm for 30 s, resulting in a film approximately 300-nm thick, followed by baking on a hotplate at 90 °C for 75 s.

Spin-coated ma-N 2403 resist layers were patterned using a 100-kV Leica EBPG 5000+ electron-beam lithography system with a typical pattern resolution and beam-step size of 5 nm, an electron dose of 260 μC/cm^2, and a beam current of 1 to 2 nA. The EBPG 5000+ tool has a sample stage with laser-interferometer positioning, allowing for devices to be written across multiple fields of view without measurable stitching errors. The unexposed resist was dissolved away in tetramethylammonium hyroxide-based ma-D 525 developer (Micro Resist Technology), leaving behind the exposed waveguide and grating features.

3.1.3 ICP Reactive-Ion Etching of Silicon

The resist patterns were transferred into the underlying silicon using inductively coupled plasma (ICP) reactive-ion etching. We used an Oxford Instruments Plasmalab System 100 ICP 380 chamber with a liquid nitrogen-cooled sample stage designed to accommodate 150-mm (6-in) diameter wafers, a 5-kW ICP generator operating at 2 MHz, and a sample-stage electrode with a 600-W RF generator operating at 13.56 MHz. Our small samples were attached to 150-mm silicon carrier wafers using a dab of Fomblin perfluorinated polyether vacuum fluid.

At first, we used a C_4F_8/SF_6 "pseudo-Bosch" etching process with low DC bias to define partially etched silicon structures. In this process, fluorine generated by the plasma ionization of the source gases etches the silicon by forming volatile silicon compounds [56, 57]; however, at low bias, some of the C_4F_8 polymerizes on the silicon surface to create a fluorocarbon passivation layer [58]. Under the correct conditions, polymerized C_4F_8 does not accumulate on the horizontal sample surfaces (normal to

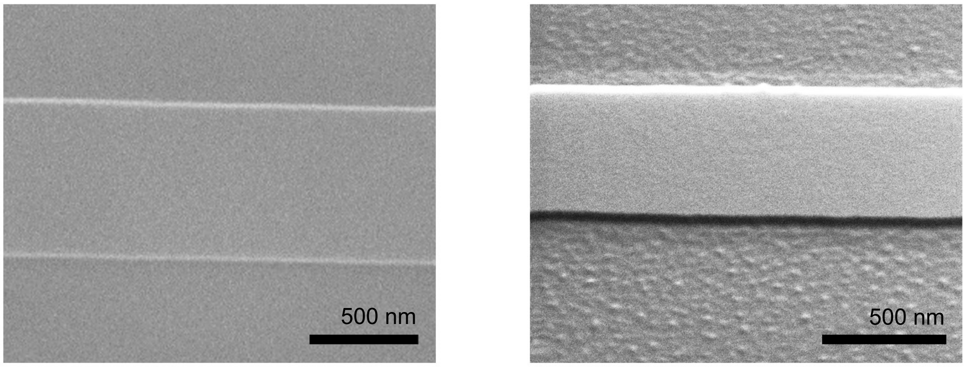

Figure 3.2. Partially etched silicon waveguide structures fabricated using a C_4F_8/O_2 etch process (left) and a C_4F_8/SF_6 etch process (right). The C_4F_8/SF_6 process creates unwanted roughness on the exposed silicon surfaces. Both structures were stripped of resist and cleaned prior to imaging. The image on the right was collected with the sample tilted at 45°, making the waveguide edge more visible.

the direction of ion bombardment) but merely slows the etch rate, while the vertical sidewalls created during the etch remain passivated. The end result is directional etching that can be tuned to achieve an almost perfectly vertical etch profile [59].

To create shallow-ridge waveguides with etch depths of 50 nm or less, the verticality of the sidewalls is less essential than achieving a slow, controllable etch rate. In practice, the conditions under which we could achieve an etch rate below 10 nm/s also resulted in roughened horizontal surfaces, as shown with the partially etched silicon waveguide in the right panel in Fig. 3.2. We hypothesize that the texture on the partially etched silicon is a result of localized C_4F_8 polymerization, which leads to an non-uniform etch rate over the silicon surface.

Ultimately, we developed a plasma etching process without SF_6, where fluorine ions were generated from the C_4F_8 source gas, which resulted in a slower silicon etch rate and smoother partially etched surfaces. By increasing the forward power to the sample-stage electrode and adding O_2, we achieved silicon etch rates of $\sim$ 2 nm/s and were able to prevent accumulation of polymerized C_4F_8. The scanning electron micrograph in the left panel of Fig. 3.2 shows a 30-nm etched silicon ridge formed by this C_4F_8/O_2 etch process, where there is no perceptible difference in the roughness between the protected silicon ridge and the surrounding partially etched surfaces.

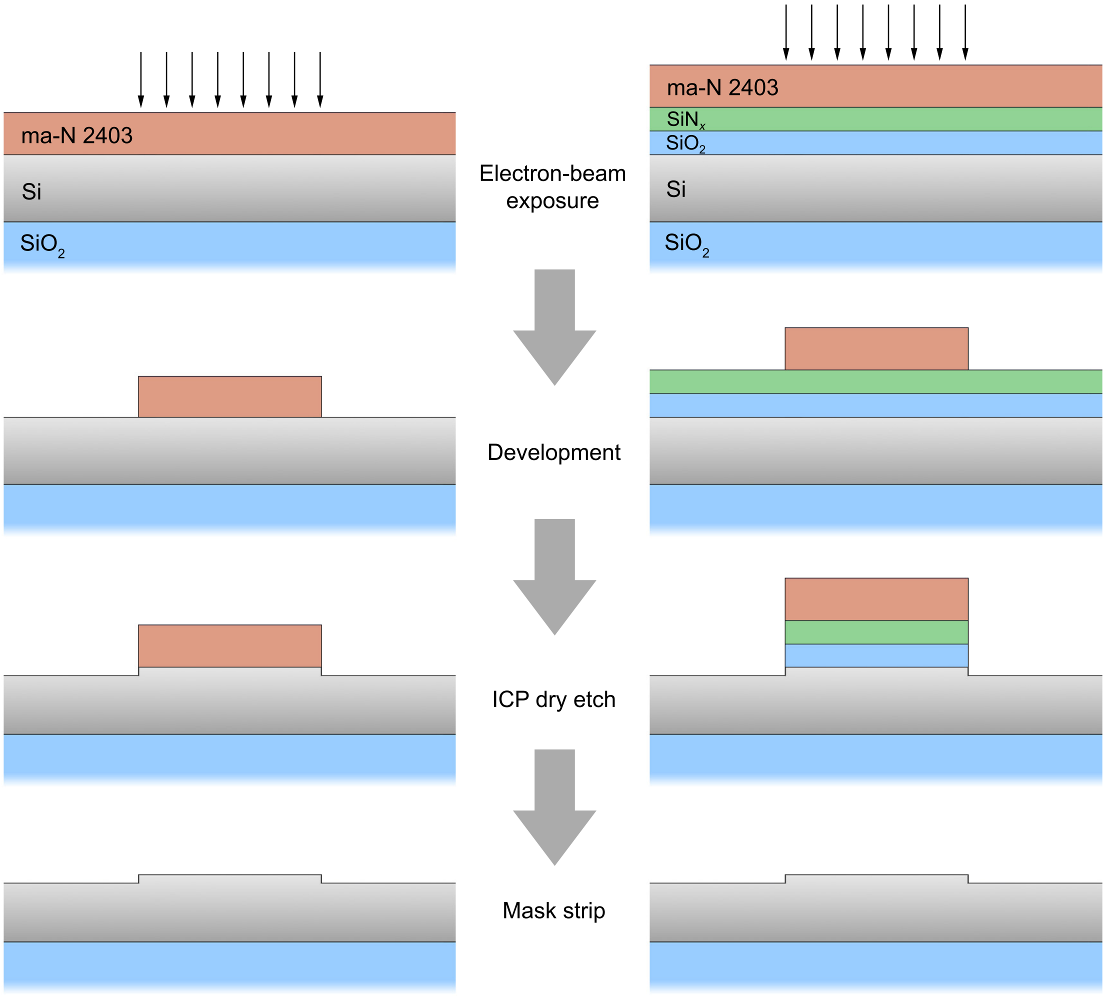

Figure 3.3. Process flow for fabricating waveguide structures using electron-beam lithography and dry etching. A single-layer resist process was implemented (left), as well as a dielectric hardmask process designed to reduce mask erosion and improve pattern fidelity (right).

The parameters of both the pseudo-Bosch and C_4F_8/O_2 plasma etching processes are detailed in Appendix A.

After the samples were etched, the resist was removed, along with any residual polymer from the etch process, using either an O_2 plasma clean (see Appendix A) or a more involved wet-chemical cleaning process. For the latter process, samples were cleaned in a 3:1 Piranha solution of H_2SO_4 and 30 % H_2O_2 at 100 °C, etched in buffered HF, and finally rinsed and dried. For samples etched with C_4F_8/O_2 using a simple resist mask, we never consistently observed higher losses for waveguides cleaned using the O_2-plasma process compared with devices cleaned in the Piranha solution. The pattern-transfer process flow is shown in Fig. 3.3.

For some samples, the patterned ma-N 2403 resist was hard baked in a convection oven at 100 °C for 5 min in order to improve its etch resistance. In addition, a few samples were heated above 140 °C to reflow the resist in an attempt to remove small-scale edge roughness. However, for the shallow-etched structures described here, we observed no significant decrease in waveguide loss after either hard baking or reflowing the resist, suggesting that waveguide roughness is predominantly etch-induced and that mask erosion is not significantly reduced by high-temperature baking.

We also fabricated samples that were patterned with resist after first being coated with 50 nm of SiO_2 and 50 nm of SiN_x using plasma-enhanced chemical vapor deposition (PECVD) in an Oxford Instruments Plasmalab System 100 PECVD, as shown in Fig. 3.3. The dielectric film deposition processes are described in Appendix A. The C_4F_8/O_2 etch process was used to etch through the SiN_x and SiO_2 hardmask layers as well as $\sim$ 30 nm of the underlying SOI device layer. After removing the deposited dielectric layers with HF, cleaning the sample in Piranha solution, and performing a final HF etch, rinse, and dry, the waveguide devices were observed to have losses nearly a factor of two lower than devices patterned by the C_4F_8/O_2 etch process with just a resist mask. This result suggests that mask erosion during etching is indeed responsible for a significant portion of the observed waveguide loss, and that erosion can be reduced with an intermediate hardmask layer.

A completed device is shown in Fig. 3.4 along with the critical parameters of the waveguide and grating structures. The particular chip represented in the micrographs was fabricated using the hardmask process with C_4F_8/O_2 etching, resulting in excellent pattern fidelity and smooth etched surfaces.

3.2 Fiber-Coupled Waveguide Test Platform

To couple light through grating-coupled SOI waveguides, we constructed a testing platform with a fiber-coupled New Focus 6428 Vidia Swept external-cavity infrared

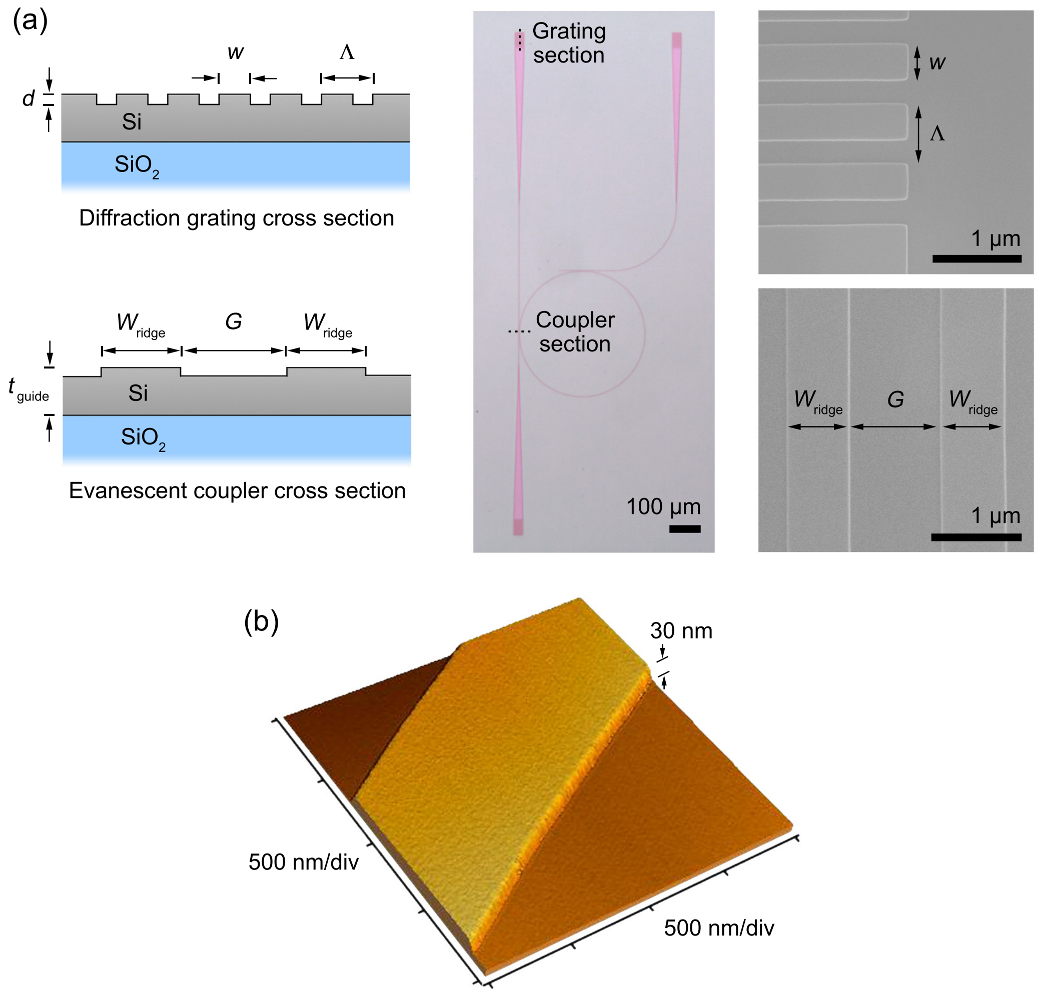

Figure 3.4. (a) Grating-coupled SOI waveguide device fabricated by electron-beam lithography and C_4F_8/O_2 etching. The particular device shown in the normal-incidence scanning electron micrographs on the right has a grating pitch of $\Lambda = 685$ nm with a grating tooth width of $w = 400$ nm. The bus waveguides are coupled to the 400-μm diameter ring resonator across a coupling gap of $G = 1\ \mu$m, and the bus and ring waveguides have a width of $W_{\text{ridge}} = 720$ nm. Both the gratings and the waveguides were defined in a single etch step with an etch depth of $d \approx 30$ nm, and the total silicon device layer thickness is $t_{\text{guide}} = 220$ nm. (b) Atomic-force microscope image of a SOI ridge with a 30-nm etch depth.

diode laser and a pair of identical input/output lensed fiber focusers, as shown in Fig. 3.5. The laser is tunable over wavelengths from $\lambda = 1500$ to 1575 nm, but can only be operating at full power between $\lambda = 1520$ to 1570 nm. The pigtail focusers (OZ Optics) each consist of a connectorized single-mode optical fiber integrated with an aspheric lens pair designed for a 12.4-mm working distance and a spot size of approximately 10 μm. Between the laser and the input focuser, an in-line polarization controller was used to control the polarization at the input grating. From the output fiber, light was coupled into either a calibrated InGaAs power meter or a 10-MHz InGaAs photoreceiver (New Focus 2053FC) connected to a 500-MHz oscilloscope. For spectrally resolved measurements, the laser wavelength was swept linearly at a rate of 10 nm/s or slower, resulting in sub-picometer detector-limited wavelength resolution using the photoreceiver, and the oscilloscope was triggered using the sweep-sync output from the Vidia laser.

The lensed fiber focusers were mounted to rotation stages atop precision translation stages, allowing the focusers to be positioned above the SOI gratings and rotated eucentrically to access a variety of grating coupling angles, θ. Positive coupling angles could be achieved with the configuration represented in Fig. 3.5, while negative coupling angles were accessible by focusing the output focuser onto the input grating and vice versa. The long working distance of the fiber focusers allowed access to a relatively wide range of positive and negative coupling angles, which provided the flexibility to adjust the wavelength corresponding to maximum grating-coupling efficiency.

The focusers were roughly aligned to the grating couplers by connecting the focuser fibers (one at a time) to a fiber-coupled 635-nm alignment laser. The red laser spot could then be imaged with a color camera attached to a zoom lens mounted above the sample stage. Figure 3.5(c) is a captured image from the zoom-lens camera showing the alignment laser trained on the through-port output grating of a waveguide device. Once the focusers were each roughly aligned to the appropriate grating, the fibers were connected to the infrared laser and detector, and fine adjustments were made to maximize the waveguide transmission.

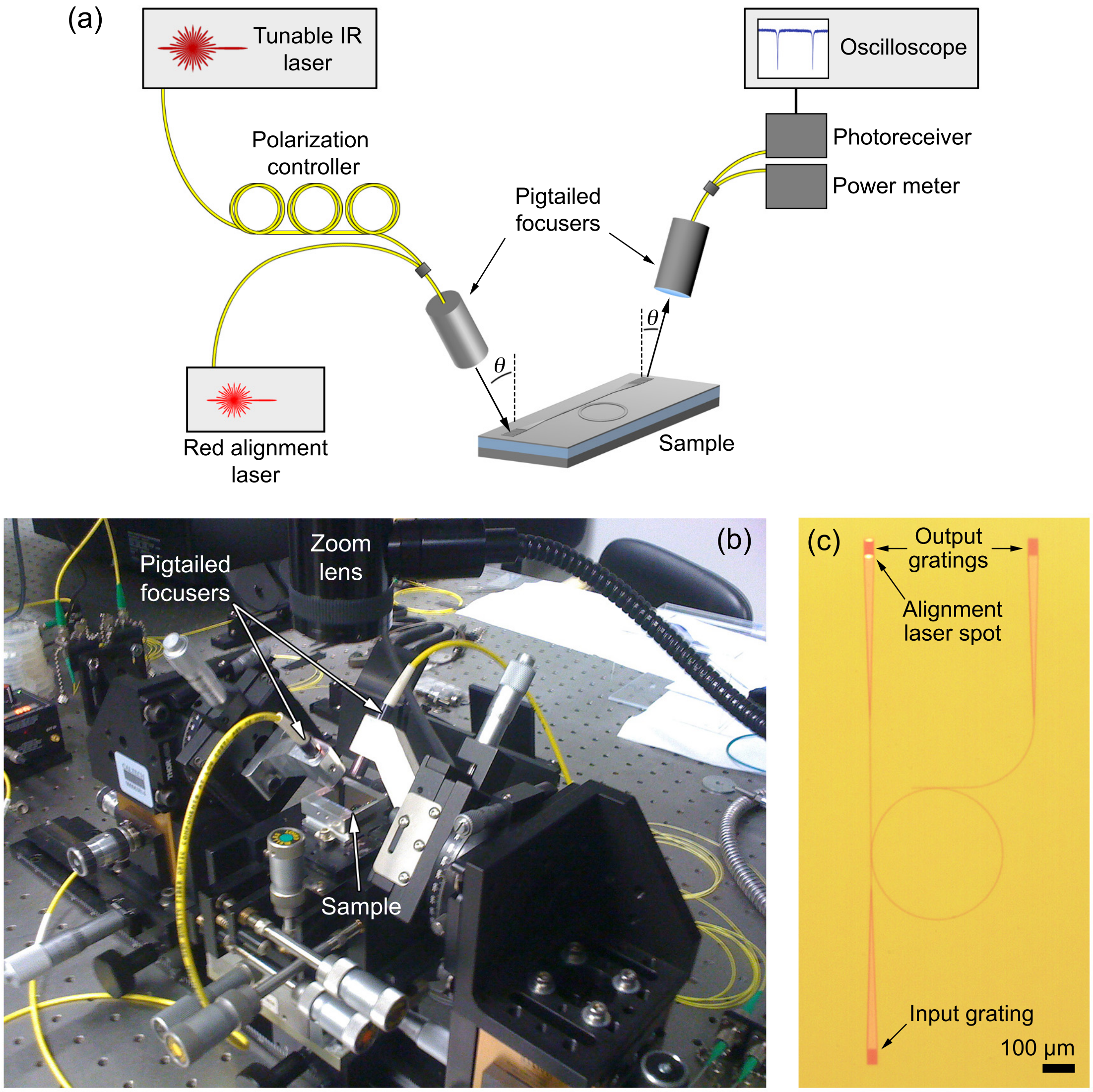

Figure 3.5. Waveguide testing setup implementing long-working-distance fiber-pigtailed focusers for coupling light into grating-coupled devices. (a) Control of the input polarization and coupling angle allows selective coupling to different modes in the same device. (b) The focusers are trained on the grating couplers using rotation and translation stages. (c) The optical image collected through the zoom lens above the sample shows the beam from the red alignment laser, which can be connected to either the input or output focuser, trained on the through-port output grating of a SOI ring resonator device.

The observed coupling efficiency using the waveguide test setup varied between samples due primarily to variations in the grating-coupler etch depth; however, we were generally interested in spectral linewidth measurements from a single device and/or differences in transmission between devices on the same sample with nominally identical gratings. Nevertheless, to provide an estimate of the grating coupling efficiency, we give the example of the device shown in Fig. 3.6, which has an etch depth of $d = 30$ nm, a silicon device layer with thickness $t_{\mathrm{Si}} = 220$ nm, and a 560-nm thick cover layer of polymethylmethacrylate (PMMA) resist with an index of 1.49 near $\lambda = 1550$ nm. For a laser power of 2.5 mW at the input-focuser fiber and a wavelength of $\lambda = 1550.2$ nm (off resonance for both TE- and TM-polarized ring resonator modes), the measured through-port transmission using the calibrated power meter was 56 μW at the optimized TM-mode coupling angle and 70 μW at the optimized TE-mode coupling angle. This corresponds to a total fiber-to-detector loss of 16.5 dB for TM modes and 15.5 dB for TE modes. The per-grating coupling efficiency is thus at least 15%, since we have neglected the loss in the focusers (estimated at 0.6 dB per focuser by OZ Optics) and propagation loss in the waveguides and tapered transitions.

We note that impressive work has been done to demonstrate highly optimized SOI-waveguide grating couplers with measured coupling efficiencies up to 69%, but these structures include fabrication-intensive metal back reflectors and utilize a direct fiber-to-grating interface [60]. For certain research applications, there are advantages to using moderately efficient, but simpler, structures with the long working-distance, adjustable-angle interface described here. Foremost among these advantages is the ability to *selectively* couple to different modes in the same device simply by adjusting the grating coupling angle, as will be demonstrated in the next section.

3.3 SOI Waveguide Device Measurements

In Fig. 3.6, we have analyzed fabricated SOI waveguides by investigating the response of a 400-μm diameter SOI ring resonator evanescently coupled to a straight

SOI through-port waveguide across a 1-μm gap. With an etch depth of $d = 30$ nm, a ridge width of $W_{\text{ridge}} = 735$ nm, and a 560-nm PMMA cover layer, the waveguide cross section supports just the fundamental TE and TM modes near $\lambda = 1550$ nm. Furthermore, the width was chosen to meet the "magic-width" condition [44] described in Chapter 2, so that TM-mode leakage loss is minimized at $\lambda = 1550$ nm. Finally, the ring diameter is large enough that bending losses are negligible [41, 50].

By scanning the input wavelength through the bus waveguide with the testing setup described above, we observe coupling to resonant modes supported by the ring corresponding to the sharp dips in the transmission. For diffraction-grating coupling angles of $\theta = +26°$ and $-26.5°$, we see coupling to either TE or TM resonator modes, respectively, confirming that the gratings allow for selective coupling to just one polarization due to the distinct modal phase velocities. We can verify the identity of the resonator modes based on their free-spectral range (FSR), which is also different for the two modes because of their unique dispersion. The transmission spectra also show the typical bandwidth of the grating couplers, which leads to the relatively broad envelope with a typical spectral full-width at half maximum of 20 to 30 nm.

As seen in the TM-mode transmission spectrum in the top panel of Fig. 3.6, obtained at a coupling angle of $\theta = -26.5°$, the extinction ratio for the SOI ring-resonator modes is largest near $\lambda = 1550$ nm, where the magic-width condition is satisfied. The loaded resonator quality factor for the resonance centered at $\lambda_0 = 1549.493$ nm is $Q = 94{,}000$. By accounting for coupling loss, the intrinsic quality factor due to propagation loss, Q_{int}, can be determined. The high-resolution transmission spectrum, $T(\lambda)$, shown in the top inset of Fig. 3.6, was fit to the form given in Section 2.3:

$$T(\lambda) = \frac{(t-a)^2 + (2\pi n_{\text{g}} L_{\text{c}})^2 at \frac{(\lambda-\lambda_0)^2}{{\lambda_0}^4}}{(1-at)^2 + (2\pi n_{\text{g}} L_{\text{c}})^2 at \frac{(\lambda-\lambda_0)^2}{{\lambda_0}^4}} \ , \tag{3.1}$$

where the circumference of the SOI ring is $L_{\text{c}} = 400\pi$ μm, n_{g} is the modal group index, and a and t are fitting parameters accounting for attenuation due to propagation loss and coupling, respectively, where $a < t$ for an undercoupled resonator. The fit shown

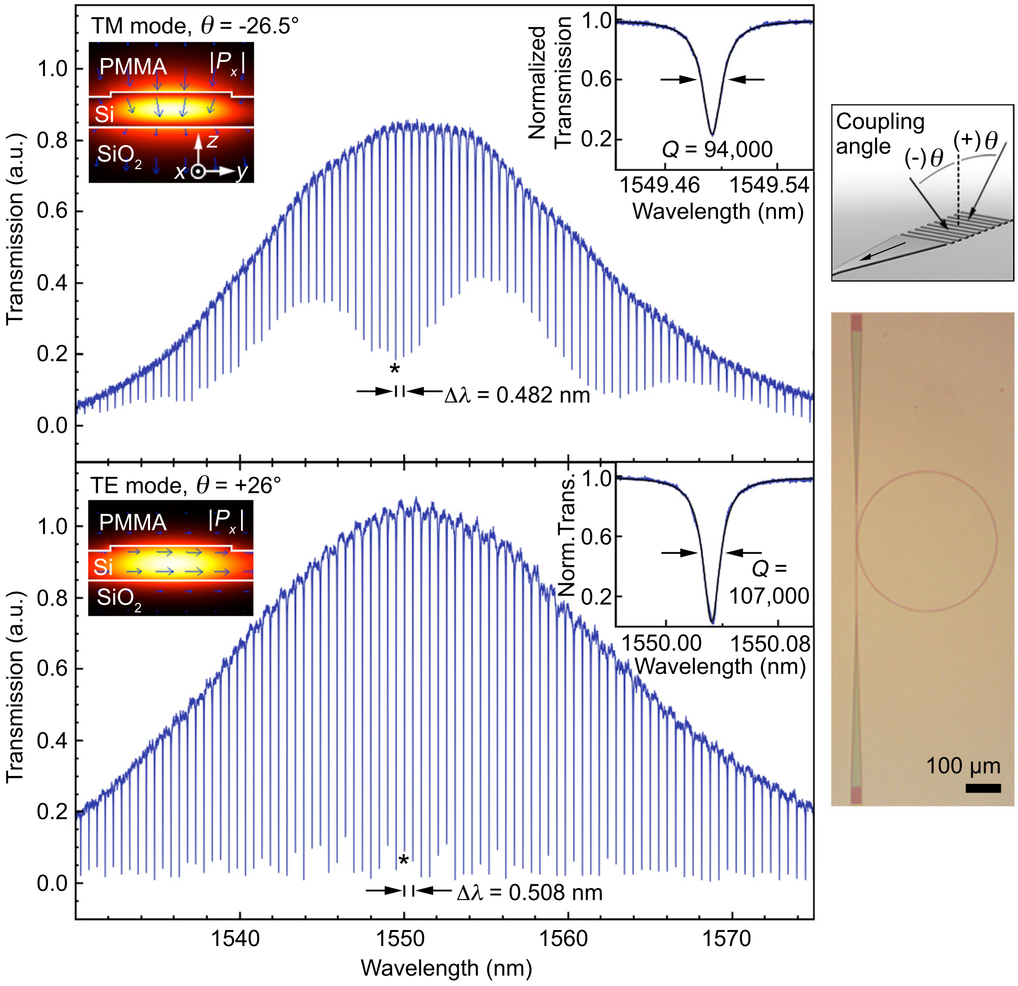

Figure 3.6. TM- and TE-mode transmission spectra collected at different grating coupling angles, θ, from a 400-μm diameter ring resonator with a PMMA cover layer (shown in the optical micrograph). The TM-mode transmission spectrum in the upper panel was collected at an angle of $\theta = -26.5°$, and the inset shows a high-resolution wavelength scan at the indicated resonance along with the loaded quality factor obtained from the fitted curve shown in black. The lower panel shows the transmission spectrum for the same device where light was selectively coupled to the TE-polarized waveguide mode at a grating coupling angle of $\theta = +26°$. The calculated power profiles are shown for each mode, where the arrows indicate the direction and magnitude of the in-plane electric field.

in the top inset of Fig. 3.6 corresponds to $a = 0.923$ and $t = 0.973$. The round-trip fractional loss, independent of coupling, is $l_{\mathrm{prop}} = -2\ln(a)$, resulting in an intrinsic quality factor of $Q_{\mathrm{int}} = 2\pi n_{\mathrm{g}} L_{\mathrm{c}}/(\lambda_0 l_{\mathrm{prop}}) = 126{,}000$, where the group index, $n_{\mathrm{g}} = 3.96$, can be obtained from the FSR, $\Delta\lambda$, by the relation $n_{\mathrm{g}} \approx \lambda_0^2/(\Delta\lambda L_{\mathrm{c}})$, since $\Delta\lambda << \lambda_0$. From the fitted value of a, the TM-mode propagation loss is estimated to be $\alpha_{\mathrm{prop}} = l_{\mathrm{prop}}/L_{\mathrm{c}} = 1.28\ \mathrm{cm}^{-1}$, or 5.5 dB/cm.

The TE-mode transmission spectrum for the same device is shown in the lower panel of Fig. 3.6, where the TE-polarized bus-waveguide mode was accessed selectively using a coupling angle of $\theta = +26°$. The TE resonator modes are distinguishable from the TM modes because of their distinct FSR and the absence of wavelength dependence in the extinction ratio. The TE-mode group index near $\lambda = 1550$ nm is $n_{\mathrm{g}} = 3.76$, significantly smaller than the TM-mode group index. Accounting for coupling loss, the TE-mode propagation loss is 3.7 dB/cm.

In Fig. 3.7, we show the TE-mode transmission spectrum for a device with the same geometry as the one shown in Fig. 3.4, which has both a through-port waveguide and a drop-port waveguide. As expected, light is only coupled into the drop-port when optical power is dropped into the ring on resonance. At each wavelength where the through-port spectrum (which is offset vertically in the figure for clarity) exhibits a transmission dip, the drop-port spectrum shows a transmission peak. Furthermore, both transmission spectra show that the maximum grating coupling efficiency is observed to be fairly close to $\lambda = 1550$ nm at a coupling angle of $\theta = 30°$, which was the intended coupling condition using the approximation method described in Chapter 2.

The through-port spectrum in Fig. 3.8 was collected from a device on a chip fabricated using the hardmask process described in Section 3.1, which produced devices with the highest-Q TE-mode resonances we observed on our waveguide platform. Since this device had both a through-port and a drop-port with identical coupling gap, G, the fitted value of the field attenuation parameter, a, represents loss due to both attenuation in the ring and coupling losses at the drop-port; therefore, we have $a \to at$ [51] . The fit shown for the resonance at $\lambda_0 = 1550.544$ nm corresponds to $a = 0.962$ and $t = 0.987$, so the intrinsic quality factor is $Q_{\mathrm{int}} = 2\pi n_{\mathrm{g}} L_{\mathrm{c}}/(\lambda_0 l_{\mathrm{prop}}) =$

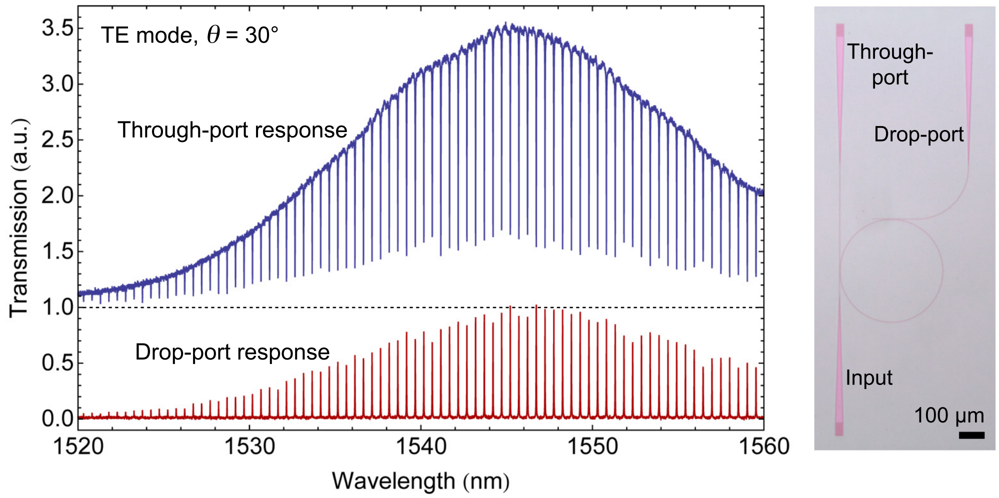

Figure 3.7. TE mode transmission spectra collected from through-port and drop-port waveguides coupled to a 400-μm diameter SOI ring resonator. The transmission dips in the through-port spectrum (offset vertically for clarity) align with the peaks in the drop-port spectrum, and the envelope of both spectra is a result of the grating-coupler spectral response.

374,000, where $l_{\text{prop}} = -2\ln(a/t)$, $n_{\text{g}} = 3.77$, and L_{c} is again 400π μm. The coupling quality factor is $Q_{\text{coup}} = 2\pi n_{\text{g}} L_{\text{c}}/(\lambda_0 l_{\text{coup}}) = 734{,}000$, where the coupling loss per round-trip around the resonator is $l_{\text{coup}} = -2\ln(t)$. The TE-mode waveguide propagation loss is $\alpha_{\text{prop}} = -2\ln(a/t)/L_{\text{c}} = 0.41$ cm^{-1}, or 1.8 dB/cm.

Since other researchers have reported on wider, shallower ridge structures with propagation losses four to five times lower than the values observed here [41, 42], we hypothesize that the TE-mode loss in our structures largely arises from the mode interacting with roughness at the waveguide edges. Borselli *et al.* showed that loss due to surface absorption and bulk defects in lightly doped SOI is significantly lower than the loss values reported here [49, 55], suggesting that the attenuation in our devices is dominated by surface scattering caused by fabrication-induced roughness. Furthermore, for the range of laser powers used here, we observed no evidence of power-dependent spectral shifts in the ring resonances, indicating that the loss is not dominated by absorption, which would lead to thermally induced refractive index changes in the silicon.

For TM modes, the highest-Q resonator modes we observed were for devices with

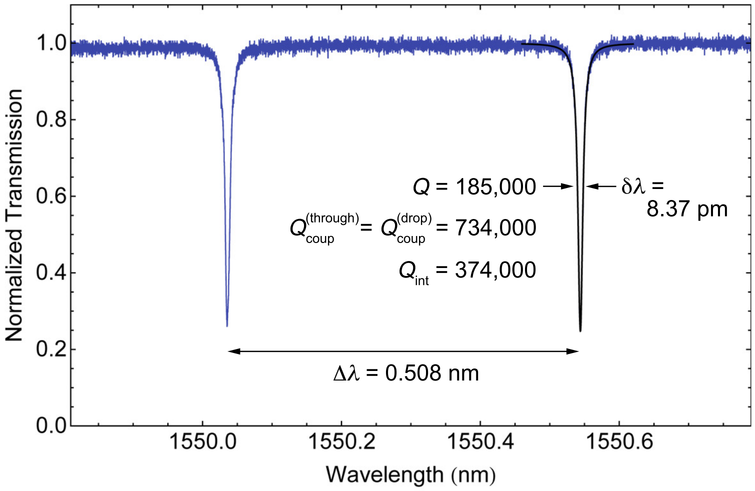

Figure 3.8. Through-port transmission spectrum showing high-Q TE-mode resonances of a SOI ring fabricated using the hardmask pattern transfer process. The black fitted curve overlaying the resonance at $\lambda_0 = 1550.544$ nm corresponds to a resonance linewidth of $\delta\lambda = 8.37$ pm, and a total loaded quality factor of $Q \approx \lambda_0/\delta\lambda = 185,000$. The intrinsic quality factor, Q_{int}, was obtained by accounting for the resonator losses due to the identical through- and drop-port couplers.

a PMMA cover layer, as shown in Fig. 3.6; however, even meeting the magic-width condition, the TM-mode loss was not as low as the typical TE-mode loss. This is consistent with the observations of Pafchek, *et al.*, and is attributed to bending-radius dependence in the radiation-canceling effect responsible for the magic-width phenomenon [42]. Overall, despite the loss induced by scattering and TM-mode radiation leakage, the waveguides and resonators demonstrated here are of sufficient quality for the device applications realized in Chapters 5 and 6.

3.4 Wafer-Bonded Slot Waveguide Devices

Before moving on to hybrid devices that integrate non-silicon materials onto the silicon photonics platform, we describe the fabrication of silicon slot waveguides and ring resonators using room-temperature wafer bonding of SOI. Devices were fabricated with a 25-nm SiO_2 slot layer, and after removing the silicon substrate and buried oxide from one side of the bonded structure, grating-coupled waveguides and ring resonators were partially etched into the $Si/SiO_2/Si$ device layers. The ring resonators were measured to have loaded Q factors of 42,000 for the TE mode, corresponding to a propagation loss of 15 dB/cm, and 13,000 for the leaky TM mode, corresponding to a propagation loss of 44 dB/cm.

As described in Chapter 2, silicon slot waveguides can exhibit high TM-mode field confinement in a narrow slot, particularly when the slot layer is composed of a lower-index material. For active photonics applications, switchable [35] or light-emitting [61] materials can be integrated into the slot to maximize modal overlap with a small volume of active material, and the silicon layers can facilitate electrical injection [34]. While vertical slot waveguides in SOI have been demonstrated [33, 62], it is difficult to fill the high-aspect ratio slot using conventional thin-film deposition processes. Consequently, the fabrication of structures in a horizontal configuration could be more adaptable to applications where a deposited active slot material is to be used. The wafer bonding technique we present here can be used to fabricate horizontal slot waveguides with deposited amorphous or polycrystalline active materials but also with single-crystal silicon (c-Si) top and bottom waveguiding layers. While there have been recent demonstrations of slot waveguides with silicon top layers composed of deposited polycrystalline [63] and amorphous [45] silicon top layers, there are applications where the superior optical and electrical properties of c-Si are desired.

3.4.1 Wafer Bonding and Back-Etching of SOI

We used a room-temperature covalent wafer bonding process to transfer the silicon device layer of a SOI sample onto a second SOI sample with a thin SiO_2 slot layer in between, as shown in Fig. 3.9. The resulting layered structure has c-Si layers both above and below the slot. Although the devices presented here are passive, an active silica-based slot layer could be deposited prior to bonding in order to fabricate a variety of active devices.

To fabricate wafer-bonded slot waveguides, we began with SOI wafers with a 3-μm BOX layer and a 250-nm thick, lightly doped p-type silicon device layer that was thinned to approximately 140 nm using wet thermal oxidation and buffered HF etching. The wafers have a manufacturer-specified three-standard-deviation thickness

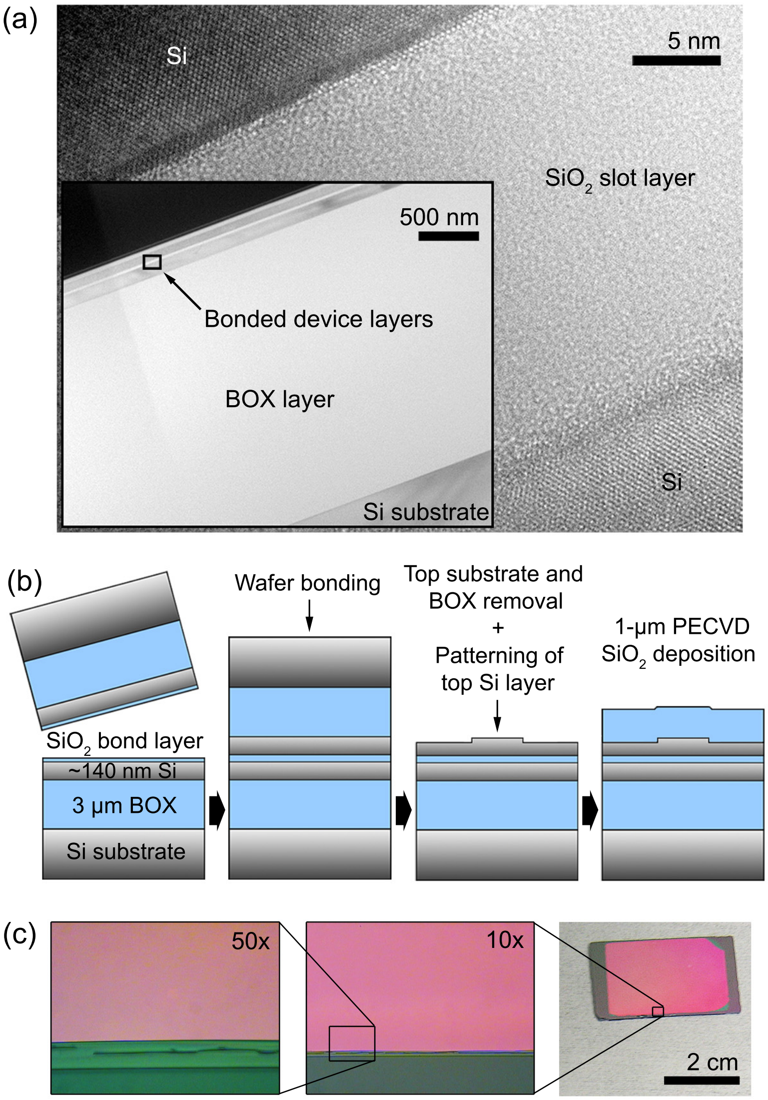

Figure 3.9. (a) Cross-sectional TEM of a wafer-bonded and back etched structure showing the Si/SiO$_2$/Si device layers on a 3-μm thick BOX layer. The high-magnification inset shows the single-crystal silicon waveguide layers above and below the amorphous SiO$_2$ slot. (b) The schematic of the fabrication process flow depicts the bonding, back-etching, and pattern transfer process used to fabricate waveguides and ring resonators. (c) Optical micrographs of a bonded and back-etched sample. The pink-colored film is the multilayered wafer-bonded region and the surrounding dark regions are the silicon substrate of the bottom SOI wafer, which was partially etched during removal of the top SOI substrate.

variation of 20 nm for the Si device layer; however, we measured variations of less than 5 nm over relevant device areas. A thin thermal oxide bonding layer was grown using dry oxidation. Cleaved pieces of the wafers were then prepared and bonded using a process adapted from Tong, *et al.* [64]. Specifically, the pieces were cleaned in a modified RCA solution of 1:0.2:5 H_2O_2:NH_4OH:H_2O, rinsed in DI water, and dipped in 1:200 HF:H_2O for 10 s. The samples were then baked at 250 °C, cleaned again in the RCA solution, and treated in an O_2 plasma at 400 W with an O_2 pressure of 115 mTorr. Following a brief dip in a solution of 28 to 30% NH_4OH in water and drying in N_2, the samples were placed in contact with light pressure. After being left in contact at room temperature for at least 24 h, the samples were observed to be securely bonded; however, to further increase the bond strength, the samples were also annealed in a quartz clamping fixture at 1100 °C in a N_2 ambient.

The silicon substrate on one side of the bonded structure was removed using a combination of mechanical lapping and etching in a 20% KOH solution at 90 °C. Figure 3.10 shows photographs of the lapping process using a Logitech PM5 lapping/polishing system. Bonded samples were attached three at a time to a glass plate with bonding wax and mounted to the vacuum chuck on a 3-in. wafer polishing jig, as shown in Fig. 3.10(a). The jig was then used to compress the samples against a cast-iron lapping plate. As shown in Fig. 3.10(a), the lapping plate was rotated while an aqueous slurry containing 9-μm diameter alumina particles was dispensed onto the plate's surface. The thicknesses of the bonded samples were measured periodically while they were still attached to the glass plate. Once $\sim$ 500 μm of material had been removed from the originally 625-μm thick top silicon substrate, the samples were detached from the glass plate and placed in the heated KOH solution to remove the remaining silicon material. The KOH solution also etched the bottom silicon handle; however, several hundred micrometers of material still remained by the time the top silicon handle was completely removed. Finally, the top BOX layer was removed by etching in buffered HF. Optical images of a bonded and back-etched sample are shown in Fig. 3.9.

A lamella from a completed sample was extracted by focused-ion beam milling

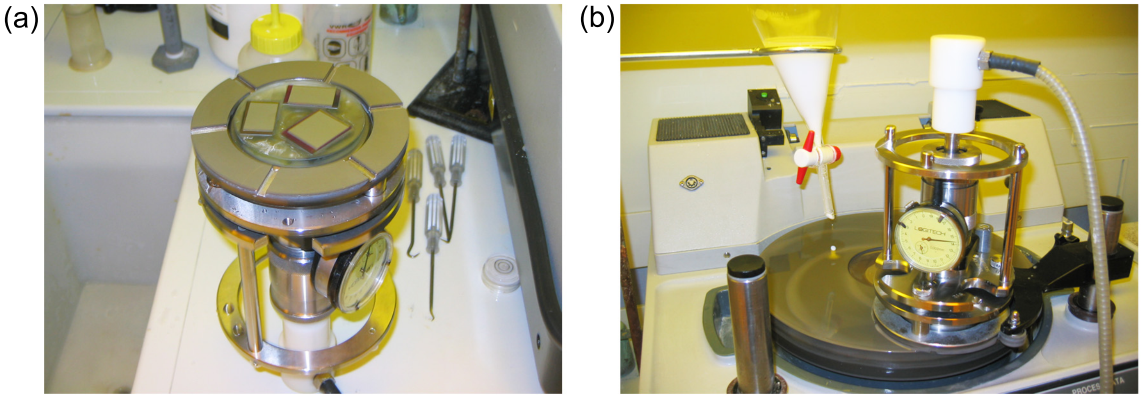

Figure 3.10. Polishing/lapping system used for mechanical removal of the top silicon substrate from wafer-bonded SOI samples. (a) Samples were attached three at a time to a 3-in. diameter glass plate and mounted to a polishing jig. (b) The samples were compressed against a rotating cast-iron lapping plate as aqueous alumina-particle slurry was dispensed onto the plate's surface.

and characterized with high-resolution transmission electron microscopy (TEM), as shown in Fig. 3.9(a). The observed layer dimensions agree with those determined by spectroscopic ellipsometry (given in Fig. 3.12) to within ±2 nm, and the silicon layers are clearly single-crystalline, as indicated by the appearance of lattice fringes in TEM.

3.4.2 Patterning Grating-Coupled Waveguides and Resonators

Ring resonators with grating-coupled through- and drop-ports were fabricated using electron-beam lithography and the C_4F_8/SF_6 pseudo-Bosch reactive-ion etching process described in Section 3.1. The gratings were designed for a depth of 50 nm in order to match their characteristic coupling and the actual etch depth was determined to be 58 nm using ellipsometry. A waveguide width of 800 nm was chosen in order to ensure that only the lowest-order TE and TM modes would be supported. The final cross-sectional waveguide geometry is shown in Fig. 3.11, along with the power profiles of the TE and TM modes at $\lambda = 1550$ nm calculated using the finite-element method in COMSOL.

The resonator device layout is shown in Fig. 3.12 along with scanning-electron micrographs of the etched structures. The gratings are 30 μm wide and 50 μm long

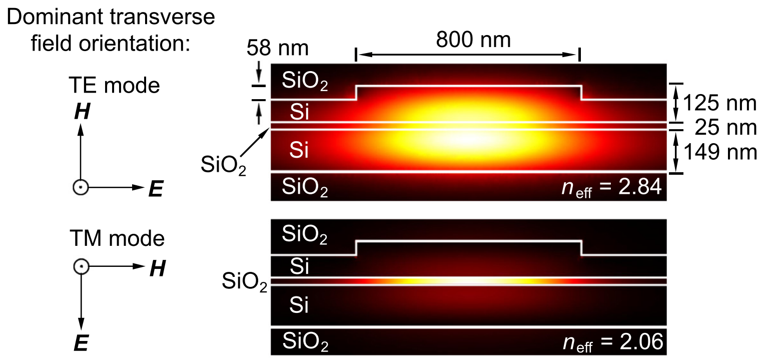

Figure 3.11. Power flow in the propagation direction calculated at $\lambda = 1550$ nm for the TE and TM modes supported by the fabricated slot waveguide geometry.

with a pitch of 660 nm, and 500-μm long linear transitions were pattered between the gratings and the narrower waveguides. Rings were patterned with a large inner diameter of 400 μm to avoid bending loss [50], and 1-μm coupling gaps were defined between the bus waveguides and the rings. Finally, the entire structure was coated with 1 μm of SiO_2 using plasma-enhanced chemical vapor deposition (PECVD).

3.4.3 Wafer-Bonded Waveguide Loss Measurements

Light near λ =1550 nm was coupled selectively into TE and TM modes using the fiber-focuser testing setup. Using the approximation method described in Chapter 2, the ideal coupling angle was calculated to be near 30° off-normal for TE modes and -30° for TM modes, as depicted in the inset in Fig. 3.12(a). The ideal coupling angles were found experimentally to be near 28.5° and -27°, respectively.

Fig. 3.13 shows the through- and drop-port response near 1550 nm for a single device at both the TE- and TM-mode coupling angles. The modes can be distinguished by their characteristic FSR, which, as described in Chapter 2, is related to the group index by $\Delta\lambda \approx \lambda_0^2/(n_{\mathrm{g}} L_{\mathrm{c}})$ when the resonant wavelength, λ_0, is significantly larger than $\Delta\lambda$. COMSOL was used to determine n_{eff} and its derivative with respect to λ for each mode, which gives a calculated value of the group index by the relation $n_{\mathrm{g}} = n_{\mathrm{eff}} - \lambda_0 \left(\frac{\partial n_{\mathrm{eff}}}{\partial \lambda}\right)_{\lambda_0}$. It was found that $n_{\mathrm{g,TE}} = 3.46$ and $n_{\mathrm{g,TM}} = 3.22$ for $\lambda_0 \approx$ 1550 nm, which gives estimated FSR values of $\Delta\lambda_{\mathrm{TE}} = 0.551$ nm and $\Delta\lambda_{\mathrm{TM}} = 0.592$

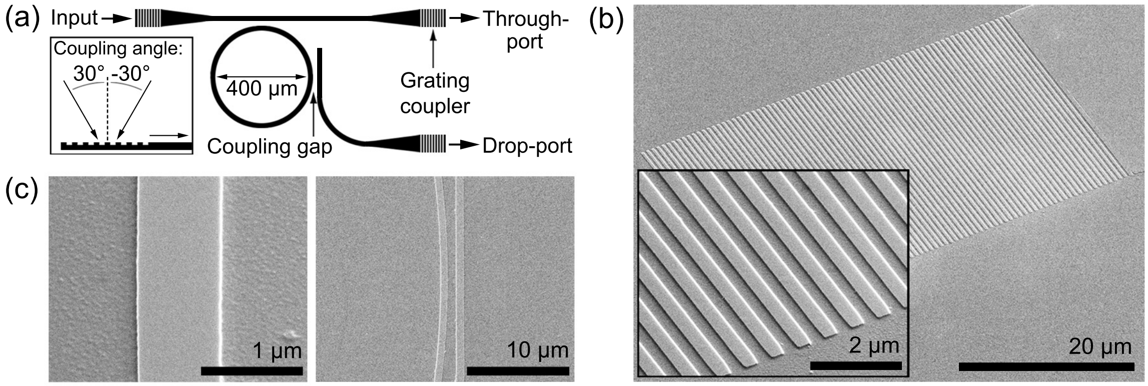

Figure 3.12. (a) Schematic of the ring resonator device layout. (b) Scanning electron micrographs of a fabricated grating coupler with a pitch of 660 nm. (c) Micrograph of one of the directional couplers used to evanescently couple light into a ring resonator, with an edge-to-edge coupling gap of $G = 1$ μm, and a higher-magnification image of the ring waveguide.

nm, in good agreement with the experimental FSR values shown in Fig. 3.13(a). For both polarizations, the calculated FSR is slightly overestimated compared with the experimental values, likely a result of variations in the geometry of the fabricated structure compared with the dimensions used in the calculations.

By fitting Lorentzian functions to the through-port resonances near $\lambda = 1550$ nm, as shown in Fig. 3.13(b), the on-resonance extinction was determined to be 1.2 dB for the TE mode and 0.3 dB for the TM mode, indicating that the resonators are significantly under-coupled and that the loaded Q factor is a fair estimate of the intrinsic Q. As a result of the low coupling to the TM mode, higher gain was used on the photoreceiver to resolve the TM drop-port resonances, resulting in a distorted lineshape. Based on the though-port response, the frequency linewidths of the resonances are 4.6 GHz for the TE mode and 15 GHz for the TM mode, corresponding to Q factors of 42,000 and 13,000, respectively. Given the measured values of n_{g}, the corresponding propagation loss is 15 dB/cm for the TE mode and 44 dB/cm for the TM mode.

The TE-mode loss, while high compared with partially etched single-layer SOI waveguides [41, 65], is likely due in part to the relatively large sidewall depth and residual surface roughness from the C_4F_8/SF_6 etch, as seen in Fig. 3.12(c). We note

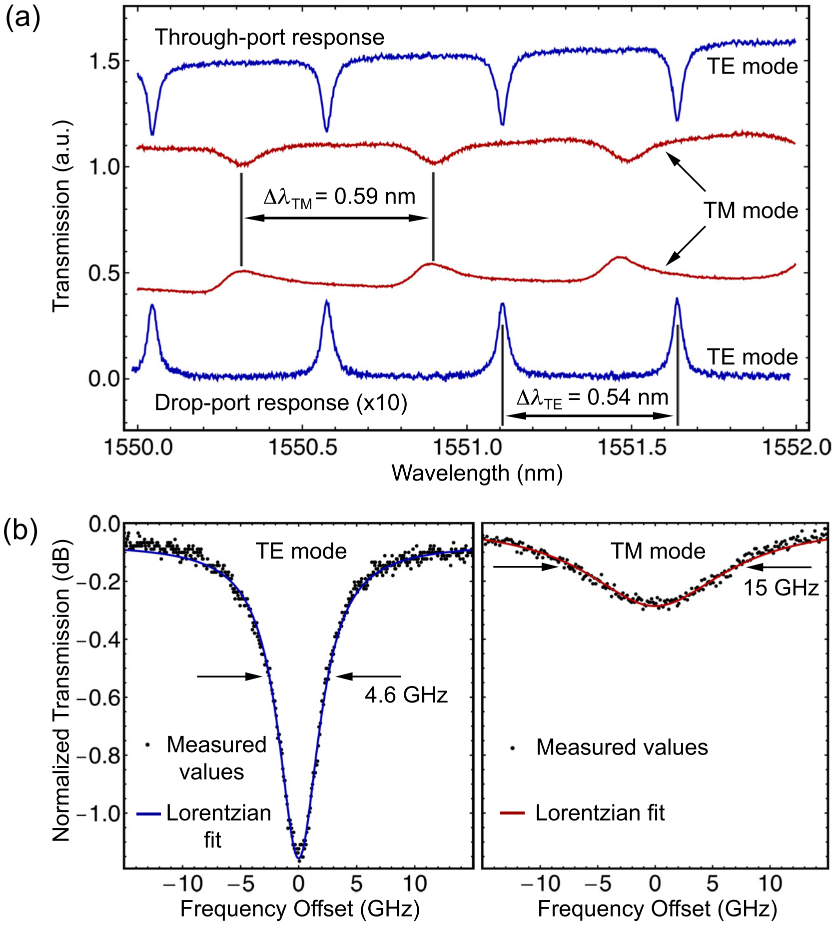

Figure 3.13. (a) Through- and drop-port response of a slot waveguide ring resonator collected at the TE- and TM-mode grating-coupling angles. The TM-mode response curves are offset for clarity. The shape of the drop-port resonances for the TM-mode is distorted due to a higher gain setting on the photoreceiver, but we observe qualitatively that the resonances are spectrally aligned to the through-port resonances. (b) Lorentzian functions were fit to a through-port resonance for each mode to determine the resonance linewidths.

that these devices were fabricated before the improved C_4F_8/O_2 had been developed. Nevertheless, the TE-mode loss is comparable to previously reported fully etched single-layer c-Si waveguides that have not undergone additional smoothing [8, 40]. The TM-mode loss is nearly five times lower than slot waveguides with sputtered silicon waveguiding layers [61], but as much as six times higher than vertical-slot c-Si waveguides [62] and horizontal-slot waveguides with a c-Si bottom layer and a polycrystalline silicon top layer [63]. Shortly after we originally reported the results described here, Pafchek *et al.* reported silicon slot waveguides with a c-Si bottom layer and a deposited amorphous silicon top layer exhibiting TM-mode loss below 2 dB/cm, which is to our knowledge significantly lower than the TM-mode loss reported for any other configuration.

The loss observed for the TM mode is likely due the roughness-induced loss affecting the TE mode but also leakage resulting from incomplete magic-width radiation canceling. The condition for minimal TM-mode leakage for a partially etched structure, given by Eq. 2.11, depends on the confined TM-mode effective index, $n_{\text{eff,TM}}$, which depends on the ridge width and etch depth, and the slab TE-mode effective index in the ridge, $n_{\text{eff,TE}}^{\text{slab}}$ [44]. For our fabricated structures, we find $n_{\text{eff,TE}}^{\text{slab}} = 2.89$ and $n_{\text{eff,TM}} = 2.06$, where the latter value is smaller than originally intended due to imperfect control of the etch depth. The lowest-order magic-width condition therefore corresponds to $W_{\text{ridge}} = 765$ nm, slightly smaller than fabricated dimension of $W_{\text{ridge}} = 800$ nm, which leads to enhanced leakage loss.

It is also conceivable that the bonding process we employed leads to defects at the bond interface that predominantly enhance the TM-mode loss due to the large modal overlap with the slot region. Although slot-layer defects are not clearly visible in the TEM image in Fig. 3.9(a), our low-temperature bonding process introduces hydrogen and nitrogen at the bond interface by terminating the SiO_2 surfaces with OH^- and ${NH_2}^-$ groups [64], which can lead to the formation of absorbing energy levels and structural defects. The post-bonding anneal at 1100 °C was intended to allow the SiO_2 slot layer to flow and consume voids at the bond interface [66], but it is unclear whether defects can be completely removed from the slot layer after it has been encapsulated by the c-Si layers. Future work could explore high-temperature bonding of hydrophobic SiO_2 surfaces in order to eliminate the need for potentially deleterious compounds at the bond interface.

While there are many options to explore toward achieving bonded slot waveguides with lower losses, we believe the results presented here show that wafer bonding is a viable method for integrating a variety of low-index slot materials directly into SOI waveguides. Ultimately, the single-layer and slot waveguides demonstrated in this chapter can be applied to a variety of hybrid photonic device applications. In the rest of this thesis, we will show how silicon waveguide structures can be used to probe and even modify the properties of different materials as well as efficiently deliver light to and from compact on-chip components.

Chapter 4

Enhanced Spontaneous Emission in Silicon Slot Waveguides

The purpose of this chapter is to elucidate the nature of spontaneous emission from dipole emitters embedded in dielectric waveguide structures, and, in particular, silicon slot waveguides. The effect described here is similar to the important Purcell enhancement effect in optical cavities [67], except that the slab waveguide structures we consider are confined in only one direction. Consequently, the electromagnetic mode density does not exhibit wavelength dependence beyond the usual waveguide dispersion, and there is broadband, non-resonant enhancement of spontaneous emission arising from to the local confinement of modes supported by the waveguide. We focus specifically on erbium-doped glass as an optically active slot material because of its prevalence in existing telecommunications technologies [29] as well as its potential applications for on-chip silicon-based light sources [34]. In addition, previous demonstrations of electroluminescence from erbium-doped materials show that it is possible to pump active layers electrically [68, 69], which would eliminate the need for external optical sources. Ultimately, we show that it is possible, using slot waveguides, to enhance the rate and efficiency of spontaneous emission from erbium and also to direct that emission into a particular waveguide mode. These features could allow for broadband spontaneous emission-based light sources to take the place of lasers for on-chip optical applications when coherence is not required.

An understanding of spontaneous emission within structures supporting a continuum of radiative (leaky) modes has existed for some time [70], and the dependence of the spontaneous emission rate on dielectric environment has since been clearly observed for rare-earth emitters exhibiting high internal quantum efficiency [71, 72] and for optically active semiconductor heterostructures [73] and nanocrystals [74]. However, researchers have only relatively recently produced a rigorous theoretical treatment of spontaneous emission from dipoles embedded in a dielectric structure supporting guided modes. Both Khosravi and Loudon [75] and Urbach and Rikken [76] considered the simplest case of a single waveguiding layer surround by lower-index materials, where the latter work corrected a few errors contained in the former. More recently, Robinson, *et al.* constructed a compelling theoretical argument that multilayer slot waveguide structures, due to the extreme confinement of the fundamental TM mode, would result in large spontaneous emission rate enhancement [77]; however, the other modes supported by the slot structure (both guided and radiative) were not explicitly taken into account. Since the total radiative decay rate depends on the character of all modes into which a photon can be emitted, a complete accounting of guided and unguided modes is required to be truly quantitative in predicting spontaneous emission enhancement.

In this chapter, we present calculations and experimental results showing enhanced radiative decay rates for trivalent erbium emitters embedded in multilayer high-index-contrast slot waveguides [78, 79], accounting for all modes and dipole emitter orientations. This study suggests that the radiative spontaneous emission rate of emitters embedded in a low-index slot layer can be enhanced by more than an order of magnitude. For simple one-dimensional slot geometries, only metal-clad waveguides supporting guided surface plasmon modes have been shown to enable significantly larger non-resonant emission enhancement [80, 81, 82]. We point out that, contemporary with the work presented here, Creatore, *et al.* published theoretical [83] and experimental [84] studies on spontaneous emission in silicon slot waveguides. While their work and ours is in good agreement overall, there are differences, particularly in the experiments, where our work hopefully provides additional insight into the practical realization of optically active silicon slot waveguides.

Our work indicates that while spontaneous emission rate enhancement is readily observable for erbium-doped glass embedded in slot waveguides, the effect is as much due to undesirable non-radiative decay processes as increases in the local electromagnetic mode density. Presently, despite attempting many different tacks, successful strategies for overcoming these non-radiative effects have eluded us. Nevertheless, we maintain hope that future experiments can avoid the likely culprits of the observed reduction in radiative quantum efficiency, such as exposure of erbium-doped oxides to reducing environments and high-temperature processing of thermally mismatched films, and allow erbium-doped silicon slot waveguides to live up to the promise of the theoretical calculations.

4.1 The Local Density of Optical States

Spontaneous emission from a quantum emitter in vacuum cannot be understood with classical electrodynamics alone. In the dipole approximation, the part of the Hamiltonian describing the interaction between an electron in a two-level atom and a classical field is proportional to the field amplitude. If the electric field in at least one mode is non-zero, the probability that the electron will be found in a given atomic state evolves over time, resulting in absorption and stimulated emission as energy is transferred to and from the electron. However, if the field amplitude is zero in all modes (and vacuum fluctuations are neglected [85]), the electron will remain in its initial state, even if it was initially excited, so the transition rate goes to zero. To explain *spontaneous* emission, we must therefore account for the quantum mechanical nature of light, where the electromagnetic field is described in terms of photon creation and annihilation operators. In this picture, the atom can couple to any number of available electromagnetic modes, as will be shown below.

In a homogeneous medium, the simplest example of which is the vacuum, there are infinitely many modes, which leads to a vanishingly small probability that energy can be coupled back to an electron once it has been spontaneously emitted into the electromagnetic continuum. However, the rate of the emission process depends on the spectral density of modes, which is dependent on the dielectric environment. Although a dielectric waveguide does support discrete guided modes, the fact that it is an open optical system means that, for an ensemble of dipoles emitting in all directions, the discrete modes coexist with a continuum of leaky modes (described here as *radiative* modes). Fortunately, by adding up the mode densities contributed by all guided and radiative modes, we can calculate the total spontaneous emission rate. As we will show, the mode density very much depends on the dielectric environment around a dipole emitter, resulting in transition rates that can be extremely different than the rate observed in vacuum. Since we are interested in analyzing layered dielectric structures, the mode density is position dependent; therefore, the mode density at the position of an emitter is dubbed the *local density of optical states*, or LDOS.

Even though we consider the quantized electromagnetic field, the average spontaneous emission rate can be related to the classical electric fields of the modes supported within a given structure. Consider a two-level atom with energy eigenstates $|a\rangle$ and $|b\rangle$ and an energy level separation $\hbar\omega_b - \hbar\omega_a = \hbar\omega_0$. We define a space of photon modes identified by the index $\mathbf{k}$, with annihilation and creation operators, $\hat{a}_{\mathbf{k}}$ and $\hat{a}^{\dagger}_{\mathbf{k}}$. The total Hamiltonian for the system is

$$\mathcal{H}_{\text{tot}} = \mathcal{H}_0 + \mathcal{H}_{\text{int}} \ , \tag{4.1}$$

where $\mathcal{H}_0$ has contributions from the atom and the electromagnetic field:

$$\mathcal{H}_0 = \hbar\omega_a \left|a\right\rangle \left\langle a\right| + \hbar\omega_b \left|b\right\rangle \left\langle b\right| + \sum_{\mathbf{k}} \hbar\omega \left(\hat{a}^{\dagger}_{\mathbf{k}}\hat{a}_{\mathbf{k}} + \frac{1}{2}\right) \ . \tag{4.2}$$

We can use the dipole approximation because we are interested in wavelengths of radiation on the order of $\lambda = 1550$ nm, which are much larger than a typical atomic emitter; therefore, the interaction Hamiltonian can be approximated as the electric dipole Hamiltonian [86]

$$\mathcal{H}_{\text{int}} \approx \mathcal{H}_{\text{ED}} = -e\hat{\mathbf{r}}_0 \cdot \hat{\mathbf{E}}(\mathbf{r}, t) \ , \tag{4.3}$$

where e is the fundamental unit of charge, $\hat{\mathbf{r}}_0$ is the electron position operator ($\mathbf{r}_0$ being the position of the electron relative to the core of the atom), and $\hat{\mathbf{E}}(\mathbf{r},t)$ is the electric field operator, given by

$$\hat{\mathbf{E}}(\mathbf{r},t) = i\sum_{\mathbf{k}}\sqrt{\frac{\hbar\omega}{2\epsilon_0}}\left(\mathbf{E}_{\mathbf{k}}(\mathbf{r})\hat{a}_{\mathbf{k}}e^{-i\omega t} - \mathbf{E}^*_{\mathbf{k}}(\mathbf{r})\hat{a}^\dagger_{\mathbf{k}}e^{i\omega t}\right) \ . \tag{4.4}$$

Equation 4.4 sums over all modes assuming harmonically varying fields with frequency ω, where $\mathbf{E}_{\mathbf{k}}(\mathbf{r})$ is the classical electric field of mode $\mathbf{k}$ at the dipole position, $\mathbf{r}$. The classical electric fields obey the orthogonality relation

$$\int_{\text{all space}} \frac{\epsilon}{\epsilon_0}\mathbf{E}_{\mathbf{k}}(\mathbf{r})\cdot\mathbf{E}^*_{\mathbf{k}'}(\mathbf{r})d\mathbf{r} = \delta_{\mathbf{k}\mathbf{k}'} \ , \tag{4.5}$$

and the prefactor in Eq. 4.4 has been chosen so that, by the usual commutation relations for the annihilation and creation operators, the electric field contributes $\hbar\omega/2$ of energy for each photon excited in the field [76]:

$$\int_{\text{all space}} \epsilon\hat{\mathbf{E}}(\mathbf{r},t)\cdot\hat{\mathbf{E}}^*(\mathbf{r},t)d\mathbf{r} = \frac{1}{2}\sum_{\mathbf{k}}\hbar\omega\left(\hat{a}^\dagger_{\mathbf{k}}\hat{a}_{\mathbf{k}} + \frac{1}{2}\right) \ . \tag{4.6}$$

Since the magnetic field contributes an equal amount of energy per photon, a total energy of $\hbar\omega$ is added to (or removed from) the system for every photon that is created (or annihilated), consistent with the electromagnetic field term in Eq. 4.2.

Since $\{|a\rangle, |b\rangle\}$ forms a complete basis for the two-level atom, we can express the position vector for the electron within the atom in terms of the dipole transition matrix elements, $\mathbf{D}_{ab} = e\langle a|\hat{\mathbf{r}}_0|b\rangle$ and $\mathbf{D}_{ba} = e\langle b|\hat{\mathbf{r}}_0|a\rangle$:

$$e\hat{\mathbf{r}}' = e\left(|a\rangle\langle a|\hat{\mathbf{r}}_0|b\rangle\langle b| + |b\rangle\langle b|\hat{\mathbf{r}}_0|a\rangle\langle a|\right) = \mathbf{D}_{ab}|a\rangle\langle b| + \mathbf{D}_{ba}|b\rangle\langle a| \ . \tag{4.7}$$

Then the interaction Hamiltonian becomes

$$\mathcal{H}_{\text{ED}} = -\left(\mathbf{D}_{ab}|a\rangle\langle b| + \mathbf{D}_{ba}|b\rangle\langle a|\right)\cdot\hat{\mathbf{E}}(\mathbf{r},t) \ . \tag{4.8}$$

which, once expanded using Eq. 4.4, consists of four terms in the joint atom-field space. However, the term proportional to the joint-space operator $|a\rangle\langle b|\,\hat{a}_{\mathbf{k}}$ corresponds to the electron losing $\hbar\omega_0$ in energy while a photon is annihilated, and the term proportional to $|b\rangle\langle a|\,\hat{a}^{\dagger}_{\mathbf{k}}$ corresponds to the electron gaining $\hbar\omega_0$ in energy while a photon is created. Since neither of these processes conserve energy, they are considered extremely short-lived according to the time-energy uncertainty principle and can be neglected (the "rotating-wave approximation") [85]. The interaction Hamiltonian is then rewritten as

$$\mathcal{H}_{\text{ED}} = -i\sum_{\mathbf{k}}\sqrt{\frac{\hbar\omega}{2\epsilon_0}}\left(\mathbf{D}_{ab}\cdot\mathbf{E}^{*}_{\mathbf{k}}(\mathbf{r})\,|a\rangle\langle b|\,\hat{a}^{\dagger}_{\mathbf{k}}e^{i\omega t} + \mathbf{D}_{ba}\cdot\mathbf{E}_{\mathbf{k}}(\mathbf{r})\,|b\rangle\langle a|\,\hat{a}_{\mathbf{k}}e^{-i\omega t}\right)\ . \quad (4.9)$$

A renowned result of time-dependent perturbation theory is Fermi's golden rule, which relates the interaction Hamiltonian of an atom-field system to the sponanteous emission rate, Γ, from an initial state, $|i\rangle$, to a final state, $|f\rangle$ [86]:

$$\Gamma = \frac{2\pi}{\hbar^2}|\langle f|\,\mathcal{H}_{\text{ED}}\,|i\rangle|^2\delta(\omega_i-\omega_f)\ . \quad (4.10)$$

For the case at hand, we are concerned with an initial state corresponding to the electron in the excited state of the atom and no excited photons, $|i\rangle = |b,0\rangle$, and a final state corresponding to the electron in the ground state of the atom and a single photon excited in mode $\mathbf{k}$, $|f\rangle = |a,1_{\mathbf{k}}\rangle$. In addition, the initial and final frequencies are simply the frequencies of the atomic excitation and the emitted photon, respectively. Inserting Eq. 4.9 into Eq. 4.10, the second term of $\mathcal{H}_{\text{ED}}$ disappears due to the orthogonality of the atomic states, and we obtain

$$\Gamma = \frac{\pi}{\epsilon_0\hbar}\sum_{\mathbf{k}}|\mathbf{D}_{ab}\cdot\mathbf{E}^{*}_{\mathbf{k}}(\mathbf{r})|^2\omega\delta(\omega_0-\omega)\ . \quad (4.11)$$

The dipole matrix element, $\mathbf{D}_{ab}$, is real and lies parallel to the electron position vector, $\mathbf{r}_0$, so we can write Eq. 4.11 as

$$\Gamma = \frac{\pi}{\epsilon_0 \hbar} |\mathbf{D}_{ab}|^2 \sum_{\mathbf{k}} \left| \mathbf{E}_{\mathbf{k}}(\mathbf{r}) \cdot \frac{\mathbf{r}_0}{|\mathbf{r}_0|} \right|^2 \omega \delta(\omega_0 - \omega) \ , \tag{4.12}$$

where we assume, consistent with the dipole approximation, that $|\mathbf{D}_{ab}|^2$ is a function of the chemical environment immediately surrounding the atomic emitter and is therefore unaffected by any changes in the dielectric environment more than a few angstroms away. Ultimately, Eq. 4.12 states that the spontaneous emission rate for a dipole emitter is a function only of frequency, dipole orientation, and the classical electric field intensity of each mode at the position of the dipole. Equation 4.12 can be written in the following form:

$$\Gamma = \frac{\pi}{\epsilon_0 \hbar} |\mathbf{D}_{ab}|^2 \rho(\mathbf{r}) \ , \tag{4.13}$$

where the LDOS, $\rho(\mathbf{r})$, is defined as

$$\rho(\mathbf{r}) = \sum_{\mathbf{k}} \left| \mathbf{E}_{\mathbf{k}}(\mathbf{r}) \cdot \frac{\mathbf{r}_0}{|\mathbf{r}_0|} \right|^2 \omega \delta(\omega_0 - \omega) \ . \tag{4.14}$$

4.2 Spontaneous Emission in a One-Dimensional Dielectric Stack

A one-dimensional dielectric stack is now considered, where, in general, both guided and radiative modes can be supported. We will follow the formalism laid out by Urback and Rikken for three layer structures [76], but we extend the calculations to consider up to five layers in order to analyze slot waveguides. To be analytically tractable, the analysis here is confined to variations in the dielectric environment in one dimension. A study of spontaneous emission in silicon slot waveguides with confinement in two dimensions can be found elsewhere [78], where the finite-difference time domain method is employed to numerically calculate the LDOS.

The summation over modes in Eq. 4.12 must include the electric fields for discrete guided modes with both TE and TM polarization, while the mode density for the continuum of radiative modes is calculated by integrating over the relevant range of momentum space. More specifically, when an emitter is placed inside a waveguiding structure, some of the light that would normally be emitted into free-space modes will instead be “captured” by the waveguide and forced to propagate in the plane of the waveguide with the modal phase velocity. However, for open dielectric-clad waveguides (as opposed to, e.g., metal-clad waveguides where radiative modes cannot propagate in the cladding), there still exists a range of momenta in the waveguide propagation direction where light can escape the high-index waveguide layer(s) and radiate into the cladding, as depicted schematically in Fig. 4.1. We note that, within the plane of the slab, there are infinitely many guided modes corresponding to every possible azimuthal direction of propagation; however, the symmetry of a dielectric slab allows the problem to be analyzed in one-dimension, in which there is indeed only a finite number of guided modes.

As is explicitly shown in Eq. 4.14, the LDOS varies with dipole emitter orientation; however, since the experiments described later afford no control over the dipole orientation, we assume a physical scenario in which there is a large ensemble of emitters with an isotropic orientation distribution. Then the total LDOS is simply the mean of the LDOS contributions from dipoles oriented in each direction:

$$\rho(z) = \frac{1}{3}\left(\rho_x(z) + \rho_y(z) + \rho_z(z)\right) \ , \tag{4.15}$$

where the LDOS can only be a function of z due to the symmetry of the slab.

Also as a result of the azimuthal symmetry of the dielectric stack, the wavevector, $n\mathbf{k} = k_x\hat{\mathbf{x}} + k_y\hat{\mathbf{y}} + k_z\hat{\mathbf{z}}$, where $k_x^2 + k_y^2 + k_z^2 = k^2n^2$ and $k = \omega/c$, can be expressed in cylindrical coordinates. For the axes depicted in Fig. 4.1, one can define the in-plane propagation constant as $\beta = \left(k_x^2 + k_y^2\right)^{1/2}$, where φ is the azimuthal angle relative to x, and we have $k_x = \beta\cos\varphi$ and $k_x = \beta\sin\varphi$. As derived in detail by Urbach and Rikken [76], but with somewhat clarified notation, the total LDOS can then be expressed in terms of a one-dimensional integral over β for radiative modes and a sum over discrete guided modes:

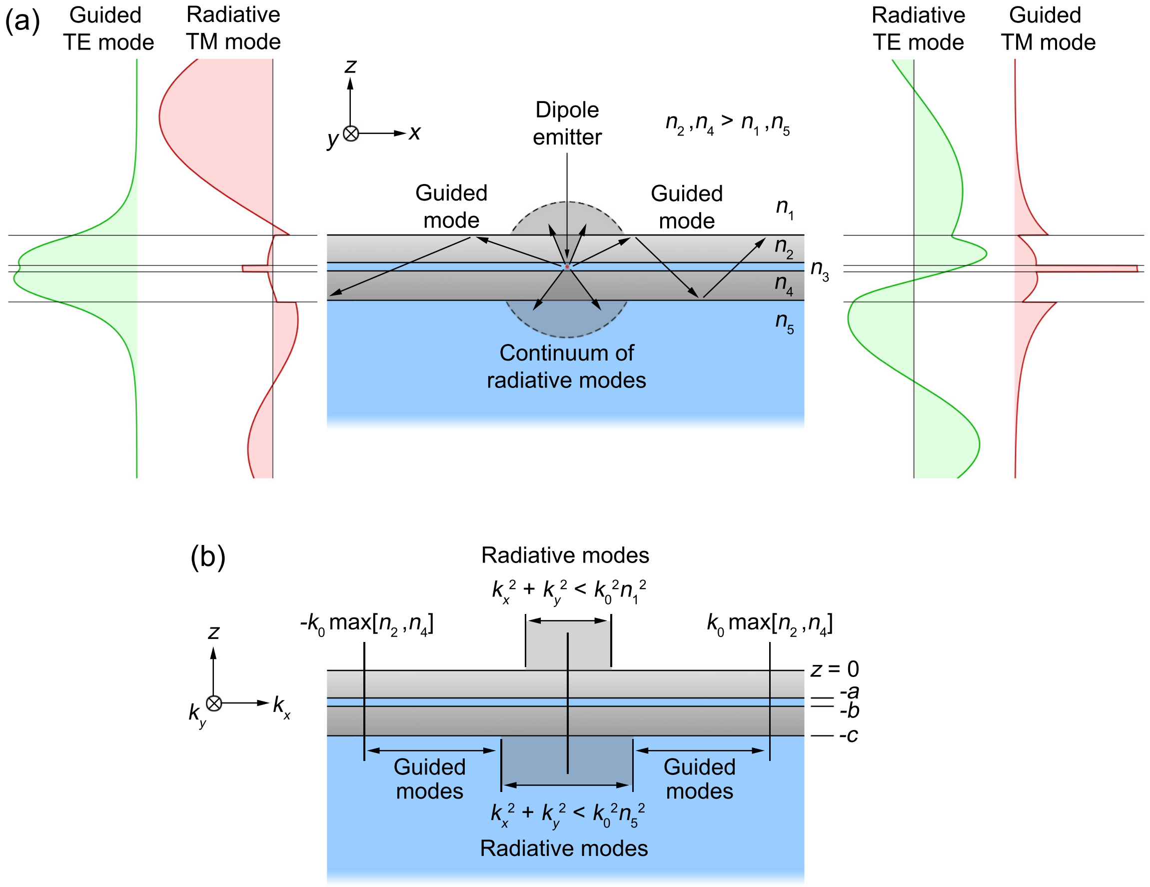

Figure 4.1. Schematic of a dipole emitting into guided and radiative modes in a multilayer slot waveguide with the indicated index of refraction in each layer. (a) Spontaneous emission can couple into a continuum of radiative modes in the cover and substrate layers or to a particular guided mode with a well-defined in-plane propagation constant. The field profiles are representative of the real part of the transverse electric field for modes of the various types. (b) In this quasi-k-space picture, the vertical dimensions of the dielectric stack are shown in real space, while the ranges of the in-plane wavenumber for radiative and guided modes are shown in the horizontal x-direction.

$$\rho(z) = \frac{2\pi}{3}k_0\left[\sum_{\zeta=\text{TE,TM}}\sum_{\mu=1,5}\int_0^{k_0 n_\mu}\left|\mathbf{E}_{\mathbf{k},\zeta,\mu}(z)\right|^2\beta d\beta + \sum_m\left|\mathbf{E}_m(z)\right|^2\beta_m(k_0)\frac{d\beta_m}{dk}\bigg|_{k_0}\right] \tag{4.16}$$

where ζ denotes the polarization of radiative modes, m distinguishes the distinct guided modes of both polarizations, and $k_0 = 2\pi c/\omega_0$ is the vacuum wavenumber corresponding to the atomic transition. The angle φ is taken to be 0 so that the in-plane component of the wavevector is oriented along the x direction, which is equivalent, by symmetry, to any other direction in the xy plane. The complete set of radiative modes is decomposed into those originating from the waveguide cover (medium 1 with index n_1 in Fig. 4.1) and the substrate (medium 5 with index n_5). These modes are distinguished by the label μ, and the integral over β is bounded by the largest possible value of the in-plane wavevector for a radiative mode propagating in each medium, $k_0 n_\mu$. Taking $\mathbf{E}_{\mathbf{k},\zeta,\mu}(\mathbf{r}) = \mathbf{E}_{\mathbf{k},\zeta,\mu}(z)e^{i(k_x x + k_y y)}$, the radiative modes obey the orthogonality relation [76, 87]

$$\int_{\text{all space}}\frac{\epsilon(\mathbf{r})}{\epsilon_0}\mathbf{E}_{\mathbf{k},\zeta,\mu}(\mathbf{r})\cdot\mathbf{E}^*_{\mathbf{k}',\zeta',\mu'}(\mathbf{r})d\mathbf{r} = \delta(k_x - {k_x}')\delta(k_y - {k_y}')\delta(k - k')\delta_{\zeta\zeta'}\delta_{\mu\mu'}\ , \tag{4.17}$$

and the guided modes, $\mathbf{E}_m(\mathbf{r}) = \mathbf{E}_m(z)e^{i(k_x x + k_y y)}$, obey

$$\int_{\text{all space}}\frac{\epsilon(\mathbf{r})}{\epsilon_0}\mathbf{E}_m(\mathbf{r})\cdot\mathbf{E}^*_{m'}(\mathbf{r})d\mathbf{r} = \delta(k_x - {k_x}')\delta(k_y - {k_y}')\delta_{mm'}\ , \tag{4.18}$$

where the modal propagation constant, $\beta_m = \left(k_x^2 + k_y^2\right)^{1/2}$, is indexed by the mode number, m, to emphasize that it assumes discrete values.

4.2.1 LDOS Contribution from Radiative Modes

Although the *intensity* of the electric field is a scalar function of z only, we must treat the fields of the radiative modes as vectors because of the different mode polarizations. First, we define the z-component of the wavevector in medium j with refractive index

n_j as

$$k_{jz} = \left(k^2 {n_j}^2 - {k_x}^2 - {k_y}^2\right)^{1/2} = \left(k^2 {n_j}^2 - \beta^2\right)^{1/2} \ . \tag{4.19}$$

Note that k_{jz} can be imaginary for modes originating in a medium with index n_μ if $n_\mu > n_j$. The transverse polarization vectors for the TE and TM radiative modes are

$$\hat{\mathbf{n}}_{\mathbf{k},\mathrm{TE}} = \sin\varphi\hat{\mathbf{x}} - \cos\varphi\hat{\mathbf{y}} \ , \tag{4.20a}$$

$$\hat{\mathbf{n}}^{\pm}_{\mathbf{k},\mathrm{TM}} = \frac{1}{\left(\beta^2 + |k_{jz}|^2\right)^{1/2}} \left(k_{jz}\cos\varphi\hat{\mathbf{x}} + k_{jz}\sin\varphi\hat{\mathbf{y}} \mp \beta\hat{\mathbf{z}}\right) \ , \tag{4.20b}$$

where the electric field is in the xy-plane for TE modes, but TM modes have an out-of-plane component that can be positive or negative depending on the direction of propagation.

For the general five-layer stack in Fig. 4.1, the electric field for radiative TE modes can be expressed as

$$\mathbf{E}_{\mathbf{k},\mathrm{TE},\mu}(z) = \begin{cases} U^{(1)}_{\mathrm{TE},\mu}\hat{\mathbf{n}}_{\mathbf{k},\mathrm{TE}}e^{ik_{1z}z} + V^{(1)}_{\mathrm{TE},\mu}\hat{\mathbf{n}}_{\mathbf{k},\mathrm{TE}}e^{-ik_{1z}z} & , \ z > 0 \\ U^{(2)}_{\mathrm{TE},\mu}\hat{\mathbf{n}}_{\mathbf{k},\mathrm{TE}}e^{ik_{2z}z} + V^{(2)}_{\mathrm{TE},\mu}\hat{\mathbf{n}}_{\mathbf{k},\mathrm{TE}}e^{-ik_{2z}z} & , \ 0 > z > -a \\ U^{(3)}_{\mathrm{TE},\mu}\hat{\mathbf{n}}_{\mathbf{k},\mathrm{TE}}e^{ik_{3z}z} + V^{(3)}_{\mathrm{TE},\mu}\hat{\mathbf{n}}_{\mathbf{k},\mathrm{TE}}e^{-ik_{3z}z} & , \ -a > z > -b \\ U^{(4)}_{\mathrm{TE},\mu}\hat{\mathbf{n}}_{\mathbf{k},\mathrm{TE}}e^{ik_{4z}z} + V^{(4)}_{\mathrm{TE},\mu}\hat{\mathbf{n}}_{\mathbf{k},\mathrm{TE}}e^{-ik_{4z}z} & , \ -b > z > -c \\ U^{(5)}_{\mathrm{TE},\mu}\hat{\mathbf{n}}_{\mathbf{k},\mathrm{TE}}e^{ik_{5z}z} + V^{(5)}_{\mathrm{TE},\mu}\hat{\mathbf{n}}_{\mathbf{k},\mathrm{TE}}e^{-ik_{5z}z} & , \ z < -c \ . \end{cases} \tag{4.21}$$

For TM modes, the magnetic field is continuous across the index interfaces and oriented along $\hat{\mathbf{n}}_{\mathbf{k},\mathrm{TE}}$. Solving for the electric field by the relation $\mathbf{E}(\mathbf{r}) = \frac{i}{\omega\epsilon(\mathbf{r})}\nabla \times \mathbf{H}(\mathbf{r})$ yields

$$\mathbf{E}_{\mathbf{k},\mathrm{TM},\mu}(z)=\begin{cases}\frac{\left(\beta^2+|k_{1z}|^2\right)^{1/2}n_\mu}{(\epsilon_0/\mu_0)^{1/2}kn_1^2}\left[U^{(1)}_{\mathrm{TM},\mu}\hat{\mathbf{n}}^+_{\mathbf{k},\mathrm{TM}}e^{ik_{1z}z}+V^{(1)}_{\mathrm{TM},\mu}\hat{\mathbf{n}}^-_{\mathbf{k},\mathrm{TM}}e^{-ik_{1z}z}\right],\ z>0\\ \frac{\left(\beta^2+|k_{2z}|^2\right)^{1/2}n_\mu}{(\epsilon_0/\mu_0)^{1/2}kn_2^2}\left[U^{(2)}_{\mathrm{TM},\mu}\hat{\mathbf{n}}^+_{\mathbf{k},\mathrm{TM}}e^{ik_{2z}z}+V^{(2)}_{\mathrm{TM},\mu}\hat{\mathbf{n}}^-_{\mathbf{k},\mathrm{TM}}e^{-ik_{2z}z}\right],\ 0>z>-a\\ \frac{\left(\beta^2+|k_{3z}|^2\right)^{1/2}n_\mu}{(\epsilon_0/\mu_0)^{1/2}kn_3^2}\left[U^{(3)}_{\mathrm{TM},\mu}\hat{\mathbf{n}}^+_{\mathbf{k},\mathrm{TM}}e^{ik_{3z}z}+V^{(3)}_{\mathrm{TM},\mu}\hat{\mathbf{n}}^-_{\mathbf{k},\mathrm{TM}}e^{-ik_{3z}z}\right],\ -a>z>-b\\ \frac{\left(\beta^2+|k_{4z}|^2\right)^{1/2}n_\mu}{(\epsilon_0/\mu_0)^{1/2}kn_4^2}\left[U^{(4)}_{\mathrm{TM},\mu}\hat{\mathbf{n}}^+_{\mathbf{k},\mathrm{TM}}e^{ik_{4z}z}+V^{(4)}_{\mathrm{TM},\mu}\hat{\mathbf{n}}^-_{\mathbf{k},\mathrm{TM}}e^{-ik_{4z}z}\right],\ -b>z>-c\\ \frac{\left(\beta^2+|k_{5z}|^2\right)^{1/2}n_\mu}{(\epsilon_0/\mu_0)^{1/2}kn_5^2}\left[U^{(5)}_{\mathrm{TM},\mu}\hat{\mathbf{n}}^+_{\mathbf{k},\mathrm{TM}}e^{ik_{5z}z}+V^{(5)}_{\mathrm{TM},\mu}\hat{\mathbf{n}}^-_{\mathbf{k},\mathrm{TM}}e^{-ik_{5z}z}\right],\ z<-c\ .\end{cases}\tag{4.22}$$

When written in this general way, Eqs. 4.21 and 4.22 can be expressed in the more compact form:

$$\mathbf{E}_{\mathbf{k},\mathrm{TE},\mu}(z)=U^{(j)}_{\mathrm{TE},\mu}\hat{\mathbf{n}}_{\mathbf{k},\mathrm{TE}}e^{ik_{jz}z}+V^{(j)}_{\mathrm{TE},\mu}\hat{\mathbf{n}}_{\mathbf{k},\mathrm{TE}}e^{-ik_{jz}z}\tag{4.23}$$

for TE modes, and

$$\mathbf{E}_{\mathbf{k},\mathrm{TM},\mu}(z)=\frac{\left(\beta^2+|k_{jz}|^2\right)^{1/2}n_\mu}{(\epsilon_0/\mu_0)^{1/2}kn_j^2}\left[U^{(j)}_{\mathrm{TM},\mu}\hat{\mathbf{n}}^+_{\mathbf{k},\mathrm{TM}}e^{ik_{jz}z}+V^{(j)}_{\mathrm{TM},\mu}\hat{\mathbf{n}}^-_{\mathbf{k},\mathrm{TM}}e^{-ik_{jz}z}\right]\tag{4.24}$$

for TM modes, where it should be understood that the field is a piecewise function with subdomains j. The constants $U^{(j)}_{\zeta,\mu}$ and $V^{(j)}_{\zeta,\mu}$ are completely determined using the appropriate boundary conditions at the dielectric interfaces and by imposing the normalization condition. For modes incident from region 1, the only non-zero component in medium 5 is the one traveling in the negative z direction, so, for both polarizations, $U^{(5)}_{\zeta,\mu=1}=0$. For the incident plane wave, the normalization condition in Eq. 4.17 yields

$$V^{(1)}_{\mathrm{TE},\mu=1}=\frac{1}{(2\pi)^{3/2}}\left(\frac{k}{k_{1z}}\right)^{1/2},\tag{4.25a}$$

$$V^{(1)}_{\mathrm{TM},\mu=1}=\frac{(\epsilon_0/\mu_0)^{1/2}}{(2\pi)^{3/2}}\left(\frac{k}{k_{1z}}\right)^{1/2}.\tag{4.25b}$$

Similarly, for modes incident from region 5, we have $V^{(1)}_{\zeta,\mu=5} = 0$ and

$$U^{(5)}_{\mathrm{TE},\mu=5} = \frac{1}{(2\pi)^{3/2}} \left(\frac{k}{k_{5z}}\right)^{1/2} , \tag{4.26a}$$

$$U^{(5)}_{\mathrm{TM},\mu=5} = \frac{(\epsilon_0/\mu_0)^{1/2}}{(2\pi)^{3/2}} \left(\frac{k}{k_{5z}}\right)^{1/2} . \tag{4.26b}$$

The other $U^{(j)}_{\zeta,\mu}$ and $V^{(j)}_{\zeta,\mu}$ are found, for TE modes, by imposing continuity of the electric field and its first derivative at each dielectric interface and, for TM modes, by imposing continuity of the magnetic field and the in-plane component of the electric field, analogous to the analysis in Chapter 2 for guided modes. Although it is possible to write down these coefficients explicitly, the expressions are very unwieldy for a full five-layer stack. The calculations presented in the following sections have made use of the symbolic solver in *Mathematica* to determine each coefficient in terms of β and n_j.

At this point, we can insert Eqs. 4.23 and 4.24 into the expression for $\rho(z)$ to calculate the LDOS contribution from radiative modes. Since we are primarily interested in the LDOS *enhancement*, it is useful to normalize $\rho(z)$ by the LDOS of an emitter in a homogeneous medium. The well-know result for the spontaneous emission rate in vacuum is [85]

$$\Gamma_{\mathrm{vac}} = \frac{\omega_0^3 |\mathbf{D}_{ab}|^2}{3\pi\epsilon_0\hbar c^3} = \frac{\pi}{\epsilon_0\hbar}|\mathbf{D}_{ab}|^2 \rho_{\mathrm{vac}} , \tag{4.27}$$

where we have defined the vacuum density of optical states, $\rho_{\mathrm{vac}} = k_0^3/(3\pi^2)$. Note that in a homogeneous dielectric with index n_{ref},

$$\Gamma_{\mathrm{ref}} = \frac{\omega_0^3 |\mathbf{D}_{ab}|^2}{3\pi(\epsilon_0 n_{\mathrm{ref}}^2)\hbar(c/n_{\mathrm{ref}})^3} = \frac{\pi}{\epsilon_0\hbar}|\mathbf{D}_{ab}|^2 \rho_{\mathrm{ref}} , \tag{4.28}$$

where

$$\rho_{\mathrm{r}} = \rho_{\mathrm{vac}} n_{\mathrm{ref}} = \frac{k_0^3}{3\pi^2} n_{\mathrm{ref}} . \tag{4.29}$$

In a structure supporting no guided modes, the radiative spontaneous emission rate enhancement relative to an emitter embedded in a homogeneous reference materials is then

$$\frac{\Gamma(z)}{\Gamma_{\text{ref}}} = \frac{\rho(z)}{\rho_{\text{ref}}} = \frac{2\pi^3}{k_0^2 n_{\text{ref}}} \sum_{\mu=1,5} \int_0^{k_0 n_\mu} \left[\left| U^{(j)}_{\text{TE},\mu} e^{ik_{jz}z} + V^{(j)}_{\text{TE},\mu} e^{-ik_{jz}z} \right|^2 + \frac{(\beta^2 + |k_{jz}|^2) n_\mu}{(\epsilon_0/\mu_0) k n_j^2} \left| U^{(j)}_{\text{TM},\mu} e^{ik_{jz}z} + V^{(j)}_{\text{TM},\mu} e^{-ik_{jz}z} \right|^2 \right] \beta d\beta \ . \quad (4.30)$$

We note that the prefactor for the TM-mode part of the integrand in Eq. 4.30 has two terms: the term proportional to β^2 is due to the in-plane electric field component while the term proportional to $|k_{jz}|^2$ is due to the out-of-plane component. Thus, the sum of the TE-mode term and the in-plane TM-mode term represent the LDOS contribution from dipoles oriented in the x- and y-directions, $\rho^{\parallel}(z)$, while the contribution from dipoles along the z-direction, $\rho^{\perp}(z)$, is given by the out-of-plane TM-mode term. We can then explicitly express the LDOS enhancement in terms of contributions from dipoles parallel and perpendicular to the plane of the dielectric interface:

$$\frac{\rho(z)}{\rho_{\text{ref}}} = \frac{\rho^{\parallel}(z)}{\rho_{\text{ref}}} + \frac{\rho^{\perp}(z)}{\rho_{\text{ref}}} \ . \quad (4.31)$$

As an experimentally relevant test structure supporting only radiative modes, a single Si-SiO$_2$ interface is analyzed using the equations outlined above, where the waveguiding layers (regions j = 2, 3, and 4) have zero thickness, as shown in Fig. 4.2. A wavelength of $\lambda_0 = 2\pi/k_0 = 1537$ nm is considered, corresponding to the $^4I_{13/2}$ to $^4I_{15/2}$ transition for Er^{3+} ions embedded in glass (the material system considered experimentally in Section 4.3). The relevant indices are $n_1 = 1.444$ for SiO$_2$ and $n_5 = 3.476$ for silicon.

The integrals in Eq. 4.30 were integrated numerically in *Mathematica* for values of z in 1-nm increments. For $\mu = 5$, there is a singularity in the integrand at $\beta = k_0 n_1$, which is a standard problem when considering modes incident from the higher-index region of geometries with asymmetric cover and cladding layers. By simply

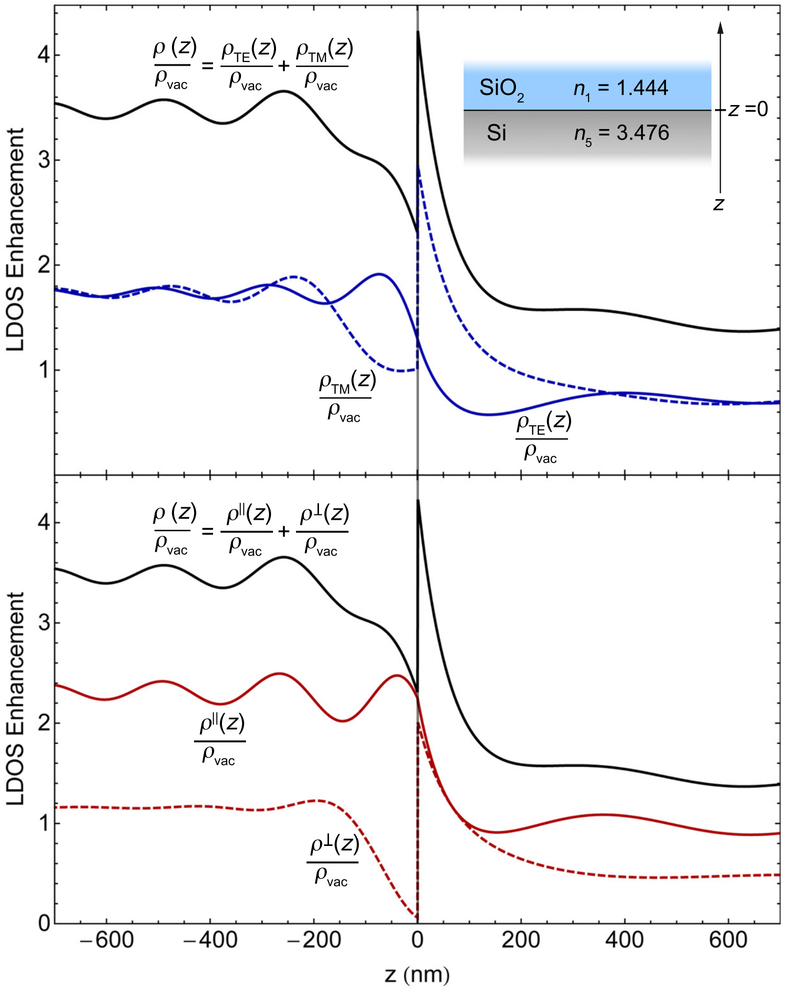

Figure 4.2. Calculated radiative spontaneous emission rate enhancement near a Si-SiO$_2$ interface as a function of dipole emitter position assuming an isotropic distribution of dipole orientations and a free-space emission wavelength of $\lambda_0 = 1537$ nm. In both panels, the total LDOS enhancement is plotted in black. In the upper panel, the fractional contributions from TE- and TM-polarized radiative modes are shown, while the lower panel shows the fractions contributed by dipoles parallel and perpendicular to the interface.

excluding the singularity point in the integration domain, the numerical integration will converge reliably.

Figure 4.2 shows the total LDOS relative to vacuum across the Si-SiO$_2$ interface. Also shown are the fractional contributions from dipoles parallel and perpendicular to the plane of the interface and the contributions from radiative TE and TM modes. Note that the TE contribution is continuous and slope continuous across the interface, while the contribution from dipoles parallel to the interface is continuous, but with a slope discontinuity due to the TM-mode contribution. Perhaps the most striking feature is the discontinuity in the LDOS enhancement due to dipoles perpendicular to the interface, which, very close to the interface, is even higher in the low-index medium than the bulk rate enhancement in the high-index medium. Finally, as expected, the total LDOS tends toward $\rho_{\text{vac}} n_j$ for dipole positions far from the interface.

4.2.2 LDOS Contribution from Guided Modes

The electromagnetic fields for TE- and TM-polarized guided modes in a slot waveguide were already determined in Chapter 2 by using the appropriate boundary conditions at the dielectric interfaces and assuming exponentially decaying fields in the cover and cladding layers. At this point, we simply need to properly normalize the guided modes to obtain their relative contribution to the total LDOS calculated using Eq. 4.16. In their work, Urbach and Rikken [76] explicitly derive the normalization factors for guided modes in a symmetrical three-layer stack, where the refractive index of the cover and substrate are equal. Here, we derive general expressions for normalizing guided modes that can be applied to more complicated geometries.

For Eq. 4.16 to be valid, the guided modes must obey the orthogonality relation in Eq. 4.18. Since the magnetic field contributes an equal amount of energy to the system as the electric field, we have [76, 87]

$$\frac{1}{2}\int_{\text{all space}}\left[\frac{\epsilon(\mathbf{r})}{\epsilon_0}\mathbf{E}_m(\mathbf{r})\cdot\mathbf{E}^*_{m'}(\mathbf{r})+\frac{\mu_0}{\epsilon_0}\mathbf{H}_m(\mathbf{r})\cdot\mathbf{H}^*_{m'}(\mathbf{r})\right]d\mathbf{r}=\delta(k_x-{k_x}')\delta(k_y-{k_y}')\delta_{mm'} \tag{4.32}$$

where the expression on the lefthand side of Eq. 4.32 is proportional to the time-averaged electromagnetic energy density [43]. For a given mode m with a propagation constant β_m, this simplifies to [†]

$$\frac{1}{2}\int_{-\infty}^{\infty}\left[\frac{\epsilon(z)}{\epsilon_0}|\mathbf{E}_m(z)|^2+\frac{\mu_0}{\epsilon_0}|\mathbf{H}_m(z)|^2\right]dz=\frac{1}{(2\pi)^2}\ . \tag{4.33}$$

Again assuming $\varphi = 0$, the time-averaged power flow in the propagation direction (along x) is equal to the energy density multiplied by the modal group velocity, $v_\mathrm{g} = c/n_\mathrm{g}$, where the modal group index is $n_\mathrm{g} = (d\beta_m/dk)_{k_0}$. Thus, we have

$$\begin{aligned}2\pi^2\int_{-\infty}^{\infty}&\left[\frac{\epsilon(z)}{\epsilon_0}|\mathbf{E}_m(z)|^2+\frac{\mu_0}{\epsilon_0}|\mathbf{H}_m(z)|^2\right]dz\\&=\frac{(2\pi)^2(d\beta_m/dk)_{k_0}}{\epsilon_0 c}\int_{-\infty}^{\infty}(\mathbf{E}_m(z)\times\mathbf{H}_m^*(z))\cdot\hat{\mathbf{x}}\ dz=1\ .\end{aligned} \tag{4.34}$$

According to Maxwell's equations, guided TE modes, for which the electric field has only an in-plane component, will be normalized with respect to power when

$$\int_{-\infty}^{\infty}(\mathbf{E}_m(z)\times\mathbf{H}_m^*(z))\cdot\hat{\mathbf{x}}\ dz=\frac{\beta_m}{\mu_0\omega_0}\int_{-\infty}^{\infty}|\mathbf{E}_m(z)|^2dz=1\ , \tag{4.35}$$

and TM modes, for which the magnetic field has only an in-plane component, will be normalized when

$$\int_{-\infty}^{\infty}(\mathbf{E}_m(z)\times\mathbf{H}_m^*(z))\cdot\hat{\mathbf{x}}\ dz=\frac{\beta_m}{\omega_0}\int_{-\infty}^{\infty}\frac{|\mathbf{H}_m(z)|^2}{\epsilon(z)}dz=\frac{\beta_m}{\epsilon_0\omega_0}\int_{-\infty}^{\infty}\frac{|\mathbf{H}_m(z)|^2}{n^2(z)}dz=1\ . \tag{4.36}$$

To conform to the normalization condition given by Eq. 4.33, we must simply divide the power flow normalization factors by $\epsilon_0 v_\mathrm{g}/(2\pi)^2$. Using $\omega_0 = ck_0$, the energy density normalization condition for TE modes becomes

---

[†] As with the normalization of the radiative modes, the factor of 2π for each δ function arises because, e.g. for k_x, $\int_{-\infty}^{\infty} e^{i(k_x-k_x{}')x}dx=\delta\left(\frac{k_x-k_x{}'}{2\pi}\right)=2\pi\delta(k_x-k_x{}')$.

$$(2\pi)^2 \frac{\beta_m (d\beta_m/dk)_{k_0}}{k_0} \int_{-\infty}^{\infty} |\mathbf{E}_m(z)|^2 dz = 1 \ . \tag{4.37}$$

For TM modes, we have

$$(2\pi)^2 \frac{\beta_m (d\beta_m/dk)_{k_0}}{\epsilon_0^2 c^2 k_0} \int_{-\infty}^{\infty} \frac{|\mathbf{H}_m(z)|^2}{n^2(z)} dz = 1 \ , \tag{4.38}$$

where the normalized magnetic field can be used to find the electric field using the relation $\mathbf{E}(\mathbf{r}) = \frac{-i}{\epsilon\omega} \nabla \times \mathbf{H}(\mathbf{r})$. In terms of the (real) transverse component of the electric field, which was found in Chapter 2, the normalization condition becomes

$$(2\pi)^2 \frac{\beta_m (d\beta_m/dk)_{k_0}}{k_0} \int_{-\infty}^{\infty} E_y^2(z) dz = 1 \tag{4.39}$$

for TE modes and

$$(2\pi)^2 \frac{k_0 (d\beta_m/dk)_{k_0}}{\beta_m} \int_{-\infty}^{\infty} n^2(z) E_z^2(z) dz = 1 \tag{4.40}$$

for TM modes, where it is implied that the fields are associated with mode m.

Taking the silicon slot waveguide geometry shown in Fig. 4.3 as an example, we can calculate the properly normalized guided modes and their relative contributions to the spontaneous emission rate enhancement. The dispersion relation for the structure is shown in the top panel of Fig. 4.3, from which the values of β_m and $(d\beta_m/dk)_{k_0}$ can be determined at the Er^{3+} emission wavelength of $\lambda_0 = 2\pi/k_0 = 1537$ nm. The lower panel shows the LDOS contribution for each mode relative to vacuum as a function of position across the interface.

As expected, the TE-mode contributions to the LDOS enhancement are continuous across the dielectric interfaces, while the TM-mode contribution adopts the discontinuities exhibited by the out-of-plane component of the electric field. It is apparent in Fig. 4.3 that the enhancement in the low-index slot layer is due primarily to the fundamental TM mode and can be very substantial. The limits and geometrical dependencies of this enhancement are the subjects of the next section.

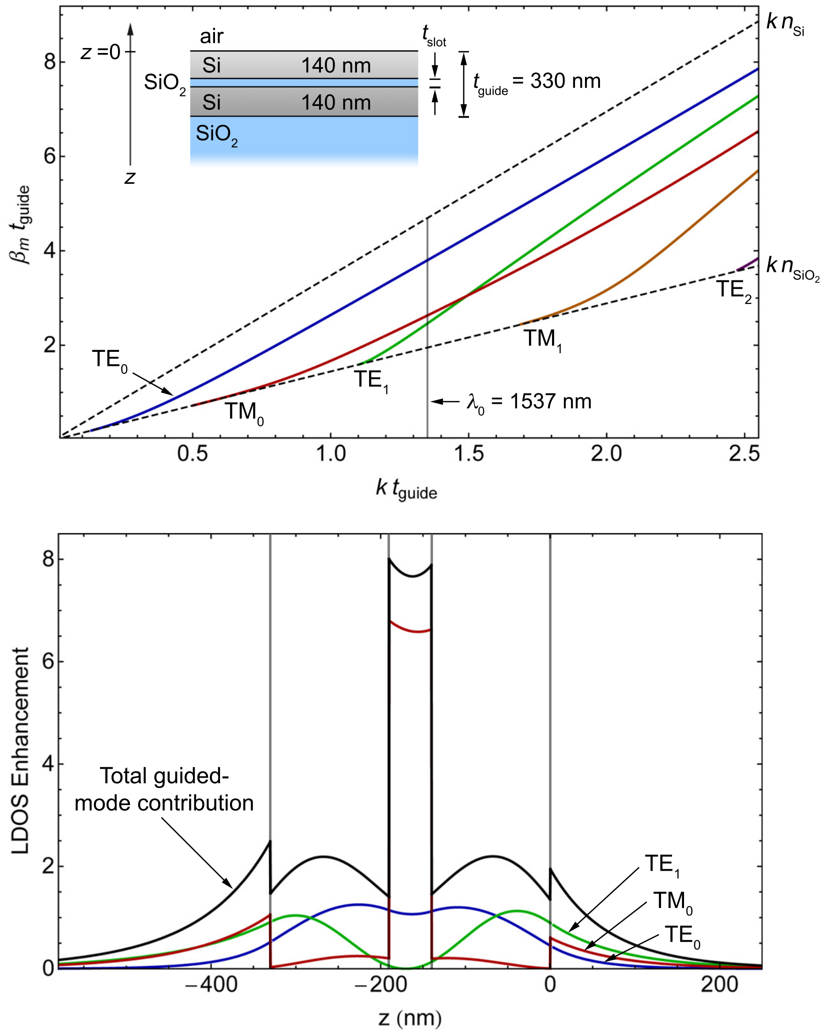

Figure 4.3. LDOS enhancement relative to vacuum due to guided modes in a silicon slot waveguide as a function of dipole emitter position. The top panel shows the dispersion relation for the illustrated geometry, where two TE modes and one TM mode are supported at the Er^{3+} emission wavelength of $\lambda_0 = 1537$ nm. For the same wavelength, the contributions from each mode and the sum of their contributions are shown in the lower panel as a function of dipole position within the dielectric stack.

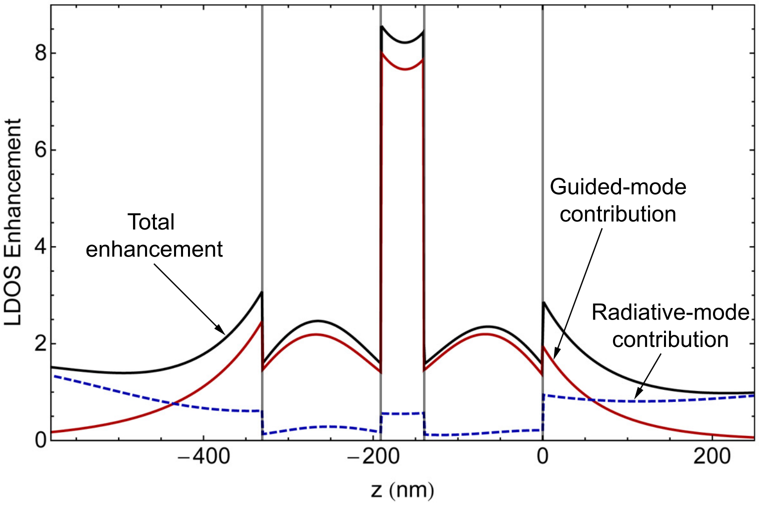

Figure 4.4. Total LDOS enhancement relative to vacuum due to all supported radiative and guided modes in a silicon slot waveguide at the Er^{3+} emission wavelength of $\lambda_0 = 1537$ nm. The structure has the same layer dimensions as the geometry considered in Fig. 4.3.

4.2.3 LDOS Enhancement in Slot Waveguides

Using the mathematical machinery constructed in the preceding sections, we can predict the enhancement of the spontaneous emission rate in any dielectric slot waveguide geometry. Figure 4.4 shows the total LDOS enhancement relative to vacuum for the slot waveguide structure from Fig. 4.3. As expected, the LDOS enhancement away from the waveguiding layers converges toward the bulk values for the cover and substrate, and the radiative modes make a small but not insignificant contribution to the total enhancement in the slot waveguide itself.

For maximum spontaneous emission rate enhancement, the obvious location for an emitter is within the low-index slot layer; however, as shown in Fig. 4.4, there is a slight position dependence of the LDOS enhancement across the slot layer. We wish to consider experimental scenarios in which emitters are distributed throughout the slot layer; therefore, we define the average LDOS within the slot as

$$\rho_{\text{slot}} = \frac{1}{t_{\text{slot}}} \int_{\text{slot}} \rho(z) dz \ , \tag{4.41}$$

where t_{slot} is the slot thickness, and the integration is performed over the extent of the slot layer assuming a uniform dipole distribution. Even in situations where the distribution of emitters has z-dependence (such as with ion-implanted erbium), the z-dependence of ρ within the slot is sufficiently minimal that we define the spontaneous emission rate enhancement in terms of ρ_{slot}.

Figure 4.5 shows the average slot LDOS enhancement, relative to the bulk SiO_2 value, as a function of t_{slot}. Again, for the range of slot thicknesses shown, the total enhancement is largely attributable to the fundamental guided TM mode. As t_{slot} approaches zero, the electric field intensity of the TM mode in the slot becomes large enough to generate a more than 20-fold enhancement of the radiative emission rate, while the LDOS contribution from radiative modes and TE-polarized guided modes remains relatively constant. We consider values of the slot thickness down to $t_{\mathrm{slot}} = 1$ nm, at which point it becomes dubious to assume that the local chemical environment surrounding a dipole emitter would be unaffected by the silicon layers.

Another consequence of the dominance of the fundamental guided TM mode in the total LDOS is that spontaneous emission will preferentially couple into that mode. For the geometry shown in Fig. 4.5, over 90% of emitted photons are expected to be excited in the TM-polarized waveguide mode when t_{slot} is 10 nm or less. Experimental evidence of preferential coupling has been observed for erbium emitters embedded in a silicon slot waveguide, where TM-polarized photoluminescence collected from the end facet of the waveguide was several times more intense than TE-polarized luminescence [61].

In terms of the silicon layer dimensions, the geometry represented in Fig. 4.5 leads to a near-maximal enhancement of LDOS in the slot [78]. If the silicon layers are made thinner, more of the guided-mode electric field resides in the evanescent regions of the cover and substrate, resulting in less overlap with the slot. Conversely, if the silicon layers are made significantly thicker, the guided modes reside more prominently in the silicon layers themselves. The birth of higher-order TM modes does not significantly enhance the overall LDOS primarily because antisymmetric modes will have a node near the slot while symmetric modes will have additional anti-nodes located within the silicon layers. For dielectric slot waveguides, significant enhancement of the LDOS

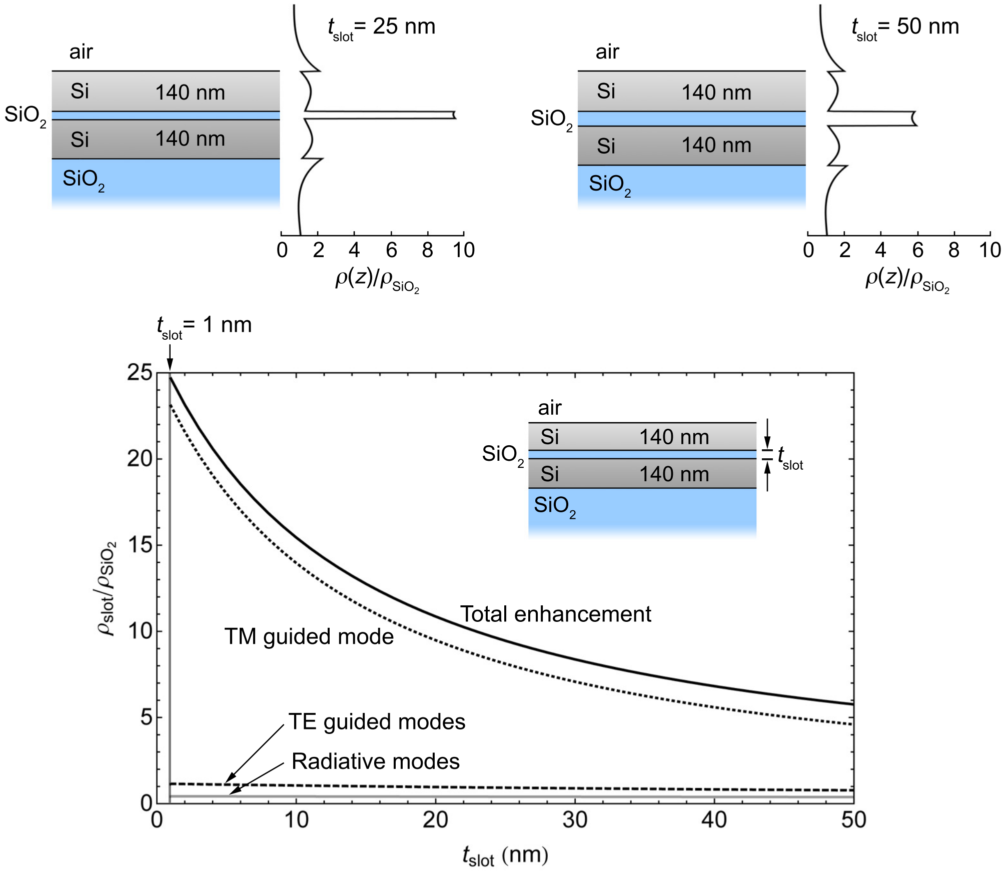

Figure 4.5. Average LDOS enhancement in slot waveguides with SiO$_2$ slots of varying thickness. The total LDOS as well as the contributions from radiative and guided modes relative to the mode density in bulk SiO$_2$ are plotted for a free-space wavelength of $\lambda_0 = 1537$ nm. In the top panels, the LDOS is plotted as a function of dipole position for slot thicknesses of 25 and 50 nm.

beyond that shown in Fig. 4.5 can be achieved only by using higher-index waveguide layers (e.g. amorphous silicon or GaAs) and/or a lower-index slot material.

4.3 Silicon Waveguides with Erbium-Doped Glass Slots

The first excited-state transition of trivalent erbium (Er^{3+}) is resonant with a free-space photon wavelength of 1.54 μm, which lies within the wavelength range where silica is most transparent [88]. For this reason, erbium-doped silica fibers [29] have become ubiquitous in optical signal amplifiers for telecommunications networks and the development of planar chip-based amplifiers has been an extremely active area of photonics research over the past few decades [30, 89, 90, 91, 92, 93]. The lowest-lying energy levels of Er^{3+}, labeled using Russell-Saunders notation, are shown in Fig. 4.6. When incorporated into a host matrix, the lowest-energy vacuum transitions, which occur within the $4f$ orbitals of the erbium electronic structure, are perturbed by the ligands surrounding the Er^{3+} ion, and the levels are split into energy manifolds. However, since the $4f$ electrons are shielded by filled $5s$ and $5p$ orbitals, this degeneracy splitting is minimal and the otherwise parity-forbidden ${}^4I_{13/2}$ to ${}^4I_{15/2}$ transition becomes only weakly allowed. As a result, erbium emission at $\lambda_0 = 1.54$ μm is characterized by a remarkably low radiative rate and a diminutive emission cross section of $\sim 10^{-21}$ cm^2 [88].

The motivation for using erbium-doped glass in structures that facilitate spontaneous emission enhancement is two-fold. First, from a practical standpoint, thin films of erbium-doped glass can be fabricated by ion implantation [30], sputtering [90, 92], or chemical-vapor deposition [94], and the radiative quantum efficiency can be quite high. In addition, there are exciting technological implications surrounding the integration of erbium with on-chip photonic structures that can enhance erbium's feeble emission characteristics. For on-chip device applications where coherence is not required, a light source based on fast and efficient spontaneous emission from Er^{3+} could be useful.

In this section, we report on a representative subset of many experiments that

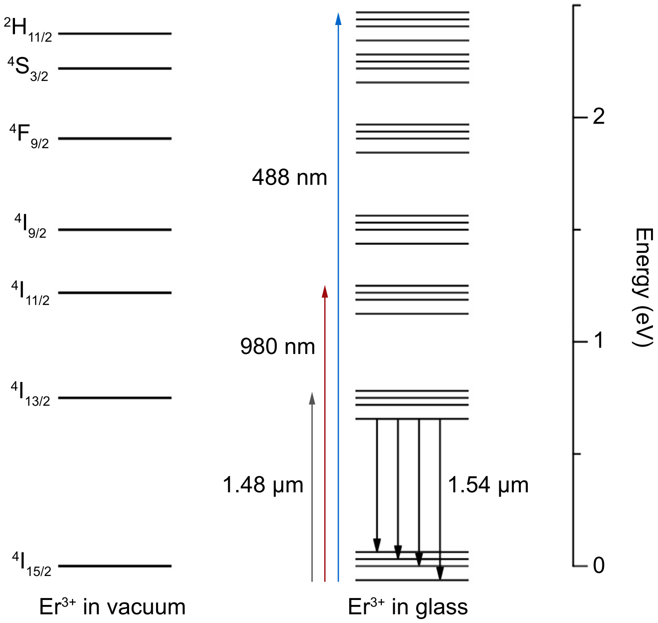

Figure 4.6. Lowest-lying energy levels for an Er^3+ ion in vacuum and in a silica-based glass matrix. In the latter case, Stark shifting induced by the glass matrix results in splitting of the free-ion energy levels. The photon energies associated with typical pump wavelengths are also shown.

were performed in order to observe the spontaneous emission enhancements that were theoretically predicted in Section 4.1 for silicon slot waveguides. Using erbium-doped glass slots, we indeed show enhancement of the Er^{3+} emission rate, but we must distinguish between enhancement of the rate at which photons are emitted and the rate at which energy is lost along other pathways. We therefore take the total decay rate to be [72]

$$\Gamma_{\text{tot}} = \Gamma_{\text{rad}} + \Gamma_{\text{nr}} = \frac{\rho_{\text{slot}}}{\rho_{\text{ref}}}\Gamma_{\text{ref}} + \Gamma_{\text{nr}} \ , \tag{4.42}$$

where Γ_{rad} is the radiative emission rate, which can be expressed in terms of the bulk radiative emission rate in a reference material, Γ_{ref}, and the LDOS enhancement in a slot structure relative to the reference bulk LDOS. The decay rate due to non-radiative processes, Γ_{nr}, includes effects such as dipole-dipole interactions and impurity quenching [30], which have been found not to depend on the local electromagnetic mode density [95].

The internal radiative quantum efficiency (QE) can then be defined as

$$\eta = \frac{\Gamma_{\text{rad}}}{\Gamma_{\text{rad}} + \Gamma_{\text{nr}}} = \frac{\Gamma_{\text{rad}}}{\Gamma_{\text{tot}}} \; . \tag{4.43}$$

Equation 4.43 clearly illustrates why it is easier to observe modifications of the LDOS with high quantum efficiency materials: changes in the radiative rate will result in larger changes in the total observed decay rate when $\Gamma_{\text{rad}} > \Gamma_{\text{nr}}$. However, if increases in Γ_{nr} can be minimized, enhancing the radiative emission rate will increase the value of η for the emitter, where the increase will be most pronounced for nominally inefficient active materials. This could prove to be important, for example, with silicon-nanocluster sensitized Er^{3+} materials [96], which are characterized by drastically increased effective excitation cross section, but typically exhibit reduced internal quantum efficiency [97, 98].

4.3.1 Structures with Sputtered Erbium-Doped Glass Active Layers

We fabricated erbium-doped multi-component glass (Er:glass) films by DC ion-beam sputtering from a custom-made target with argon source gas. The target was created by attaching erbium metal strips and fragments of soda-lime glass (Corning 2947) to a large SiO_2 disc, and the concentrations of erbium and soda-lime impurities in the sputtered films were controlled by adjusting the position of the attached pieces relative to the argon beam. The films were annealed in a rapid thermal annealing (RTA) furnace at 850 °C for 5 min in an O_2 ambient. The films producing the brightest photoluminescence (PL) near 1.54 μm wavelength with the longest PL lifetimes were analyzed by Rutherford backscattering spectroscopy (RBS) and found to contain 1.1 ± 0.1 atomic % erbium and less than 1.0 atomic % calcium and other soda-lime components. This erbium concentration is within the regime where energy migration between Er^{3+} ions typically leads to reduced PL lifetimes (concentration quenching) [30] but is comparable to concentrations reported in the literature for multicomponent glass exhibiting similarly long lifetimes [90]. We note that, although the optimized films were almost pure Er:SiO_2, the PL characteristics were greatly diminished if the small concentration of soda-lime glass was not added. Previous work suggests that, especially for larger concentrations of erbium, non-bridging oxygen sites created by the soda-lime impurities reduce the aggregation of erbium atoms, resulting in a greater number of optically active erbium ions [99].

To analyze the PL characteristics of the films, we employed top-down optical pumping and collection using the setup depicted in Fig. 4.7. Two excitation sources were implemented: An argon ion laser tuned to its emission line at $\lambda_0 = 488$ nm and a fiber-coupled diode laser emitting near $\lambda_0 = 980$ nm. These pump wavelengths are resonant with the Er^{3+} energy levels shown in Fig. 4.6. The argon laser (Coherent Innova 70C) was focused into a TeO_2 acousto-optic modulator with a measured response time of < 50 ns, and one of the first-order diffracted beams was isolated with an aperture. The modulated beam was then focused onto the sample, which was mounted vertically on an adjustable vacuum stage. Light from the 980-nm diode laser (Seastar Optics BFSWA0980) was coupled into free space with a fiber-coupled collimator and then focused onto the sample at a different angle than the argon laser beam, so that both sources could be used without rearranging optics. The diode laser was driven by an external laser diode controller (ILX Lightwave LDC-3722), which could be externally modulated to drive the laser from below threshold to near-maximum current with a measured response time better than 10 μs.

PL from Er:glass samples was collected using a lens with a large numerical aperture ($f/1$) and focused into a computer-controlled visible/IR grating monochromator (Oriel MS257) through a 1000-nm optical longpass filter. The diffracted light from the monochromator was detected using a liquid-nitrogen cooled near-IR photomultiplier tube (Hamamatsu) with an InGaAs photocathode and a response time of less than 1 ns. The detector signal was then either conditioned with a lock-in amplifier (Stanford Research Systems SR830) for spectrally resolved PL intensity measurements or sent to a multichannel scaler (Stanford Research SR430) for time-resolved measurements. A function generator was used to drive the modulation of the laser sources and sync them to the lock-in amplifier and multichannel scaler, which were interfaced to a computer for data collection.

Time-resolved PL measurements from an optimized 45-nm thick Er:glass film

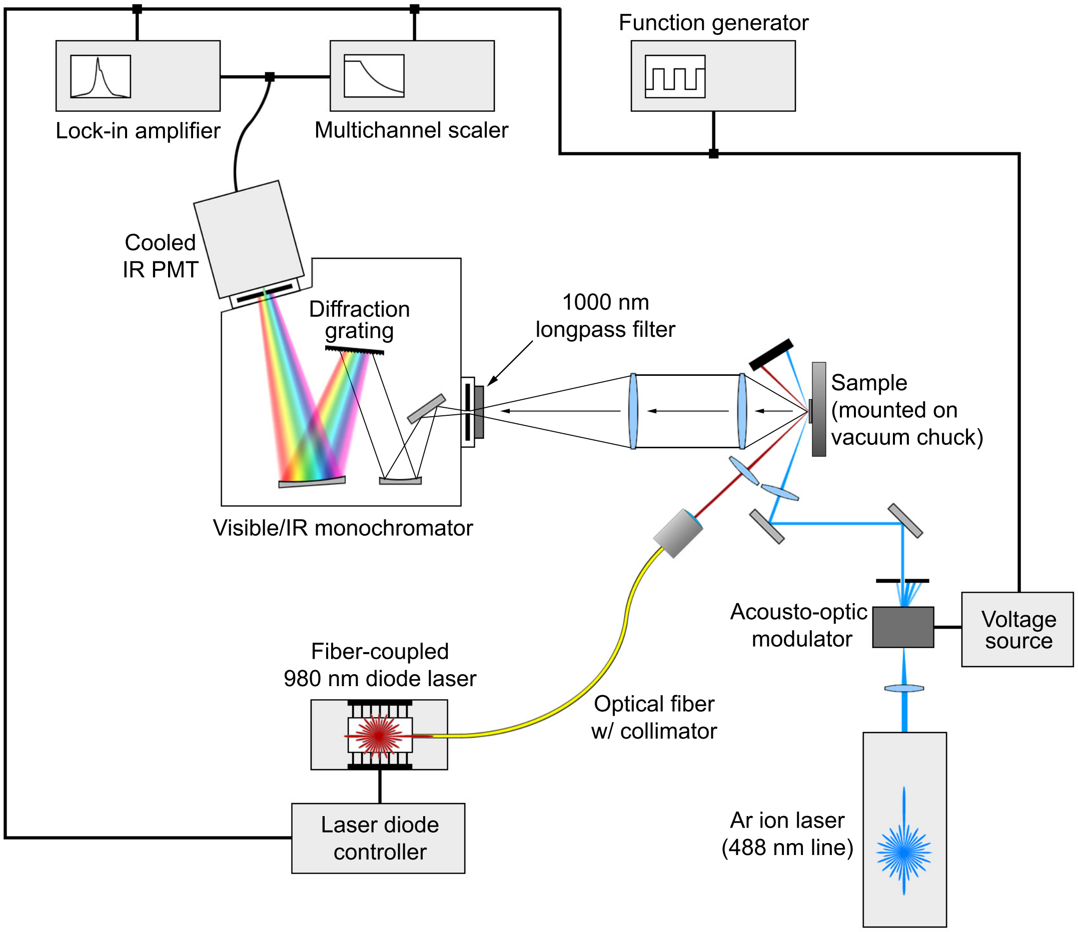

Figure 4.7. Layout of the optical setup used to measure photoluminescence spectra and decay times for erbium-doped films. The system allows for optical pumping at $\lambda_0 = 488$ or 980 nm with time resolution limited by the modulation response of the pump laser sources.

deposited on SiO_2 are shown in Fig. 4.8, where the erbium-doped film thickness was verified by RBS. The sample was pumped at 488 nm with a modulation rate of 9 Hz. The decay of the PL intensity exhibits single-exponential behavior with a characteristic lifetime, τ, that can be related to the total decay rate simply by $\Gamma_{\text{tot}} = 1/\tau$. A PL spectrum collected from the sample is shown in the inset of Fig. 4.8(b), where the peak PL intensity is observed at $\lambda_0 = 1537$ nm. For the pumping conditions used, the PL intensity was found to scale linearly with laser power. This indicates that the Er^{3+} emitters are far from saturation and the PL lifetime is independent of pump power.

As previously shown [72, 95], covering the surface of a thin film of active material with a high-index fluid provides a reversible means of perturbing the LDOS. Indeed, after covering the Er:glass sample with microscopy immersion oil with an index of 1.518, we observed a substantially reduced PL lifetime near $\lambda = 1537$ nm. The original lifetime was recovered after washing away the oil with isopropanol. By averaging the calculated LDOS, shown in Fig. 4.8(a), over the thickness of the 45-nm Er:glass film, we find two distinct values of the LDOS enhancement with and without the cover fluid. Using Eq. 4.42 to relate each of these calculated enhancements to the corresponding measurements of Γ_{tot}, we are able to solve for the unknown parameters Γ_{ref} and Γ_{nr}. From the lifetimes shown in Fig. 4.8, we find $\Gamma_{\text{ref}} = \Gamma_{\text{SiO}_2} = 65\ \text{s}^{-1}$ and $\Gamma_{\text{nr}} = 38\ \text{s}^{-1}$, which corresponds to an internal radiative QE of $\eta = 0.63$.

The same sputtering conditions were used to deposit Er:glass films onto silicon-on-insulator pieces with a 3-μm buried-oxide layer and single crystal silicon (c-Si) device layers of varying thickness. The c-Si device layers were thinned using thermal oxidation and HF etching, and the final thicknesses were measured by multiple-angle spectroscopic ellipsometry. After depositing the Er:glass layers and annealing the samples in O_2, additional ellipsometry measurements revealed that $\sim$6 nm of SiO_2 had grown under the sputtered active layers. Finally, silicon layers of uniform thickness were deposited atop the Er:glass layers and the samples were annealed at 700 °C for 5 min in N_2 in order to form silicon slot waveguide structures with polycrystalline silicon (poly-Si) top layers.

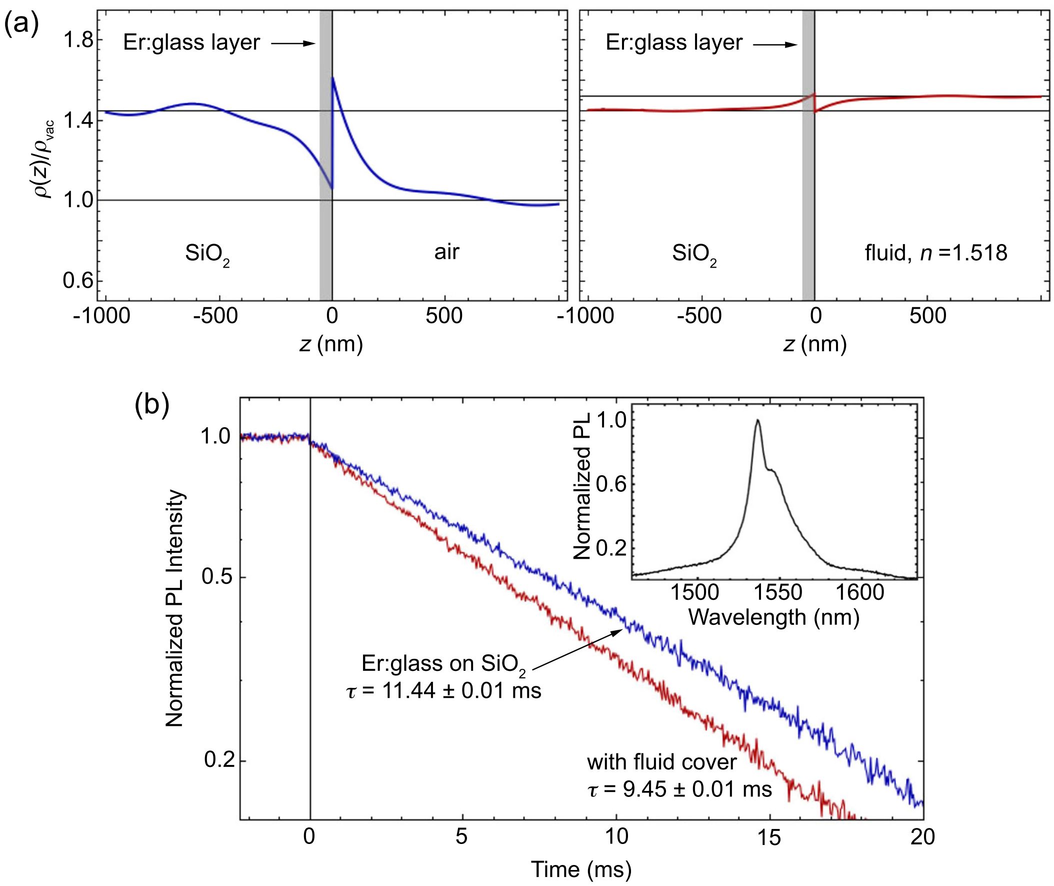

Figure 4.8. Measured photoluminescence spectrum and decay lifetime for an optimized sputtered erbium-doped glass film deposited on $\mathrm{SiO_2}$. (a) The calculated LDOS within the 45-nm thick Er:glass layer is significantly affected when the index of the cover layer is increased from 1 (air) to 1.518 (immersion oil). (b) When optically pumped at 488 nm, the measured PL lifetime reflects the change in the LDOS that occurs after oil is placed atop the sample. The increase in the total decay rate can be used to determine the radiative quantum efficiency of the $^4I_{13/2}$ to $^4I_{15/2}$ transition, which is found to be 0.63 for this sample. The PL spectrum (inset) peaks at $\lambda_0 = 1537$ nm.

For the fabricated waveguide geometry, the calculated average LDOS for the slot region is plotted in Fig. 4.9 for different thicknesses of the c-Si layer beneath the Er-doped film, where the top poly-Si layer thickness is held constant at 73 nm. The slot layer is 51-nm thick with the top 45 nm containing Er emitters. As the c-Si layer becomes thicker, the waveguide begins to support additional guided modes; however, as each guided mode is born, there is a slope discontinuity in the radiative mode contribution. The net effect is that the LDOS for all modes is a smoothly varying function. The contribution from the first-order TM mode is strongly dependent on the c-Si layer thickness, resulting in a factor of three change in ρ_{slot} for c-Si thicknesses between 0 and 200 nm. Consequently, one can expect large changes in the observed emission rate for changes in the waveguide geometry over this range.

Figure 4.10 shows PL lifetime measurements collected from three slot waveguides with the indicated lower silicon layer thicknesses. After the SOI substrates were thinned, the samples were processed simultaneously so that the slot and top silicon layers are identical and the local environment around the Er^{3+} emitters should not change from sample to sample. Consequently, any observed changes in the non-radiative decay rate is expected to be common to all three structures. Compared with the Er:glass films sputtered onto SiO_2, the PL intensity was low due to interference and absorption of the 488-nm pump in the silicon layers, but we also expect increased coupling of spontaneous emission into guided waveguide modes, resulting in less emission into radiative modes that can be collected from above the waveguide. We emphasize that the measured spontaneous emission lifetime is a function of the total mode density at the emitter position, so it is the same for all photons, independent of the mode into which the photons are emitted.

The non-radiative decay rate, Γ_{nr}, was used as a single constant fitting parameter to match the measured total decay rates to the calculated trend in emission rate plotted in Fig. 4.9. The deviation between the measured and calculated values is minimized for $\Gamma_{\text{nr}} = 320\ \text{s}^{-1}$, indicating a nearly order-of-magnitude enhancement of the non-radiative decay rate of Er^{3+} in the slot structures. This is consistent with observations reported for similar structures by Creatore, *et al.* [84], and will be

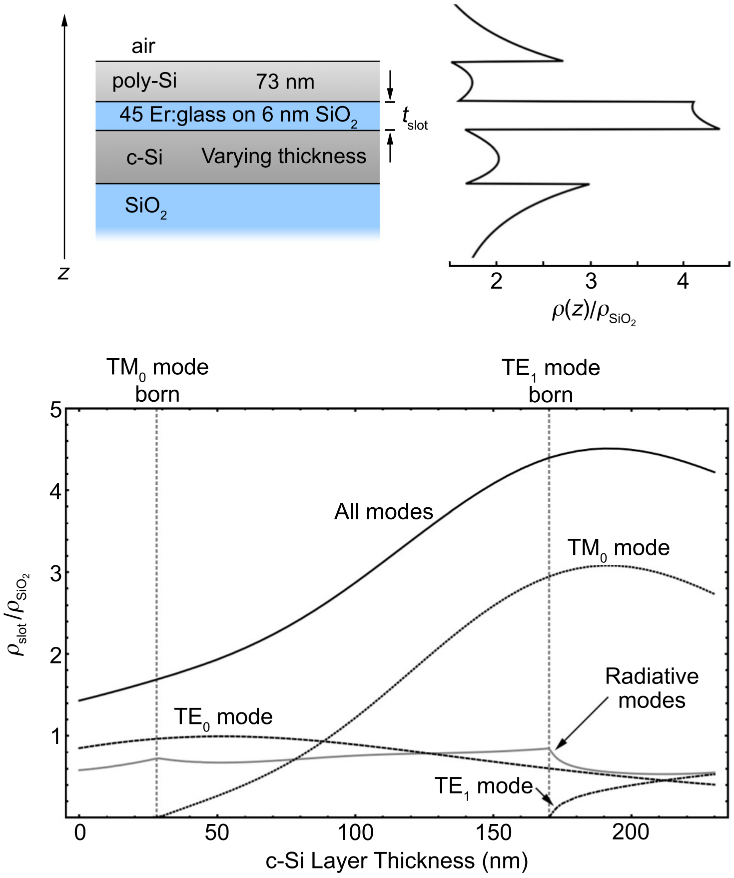

Figure 4.9. Calculated average LDOS for the active slot region of a silicon slot waveguide as a function of the lower silicon layer thickness. The top polycrystalline silicon layer thickness as well as the thickness of the slot are kept constant. As the lower silicon layer becomes thicker, the increase in the overlap of the fundamental TM mode with the slot region results in significant modification of the predicted radiative emission rate.

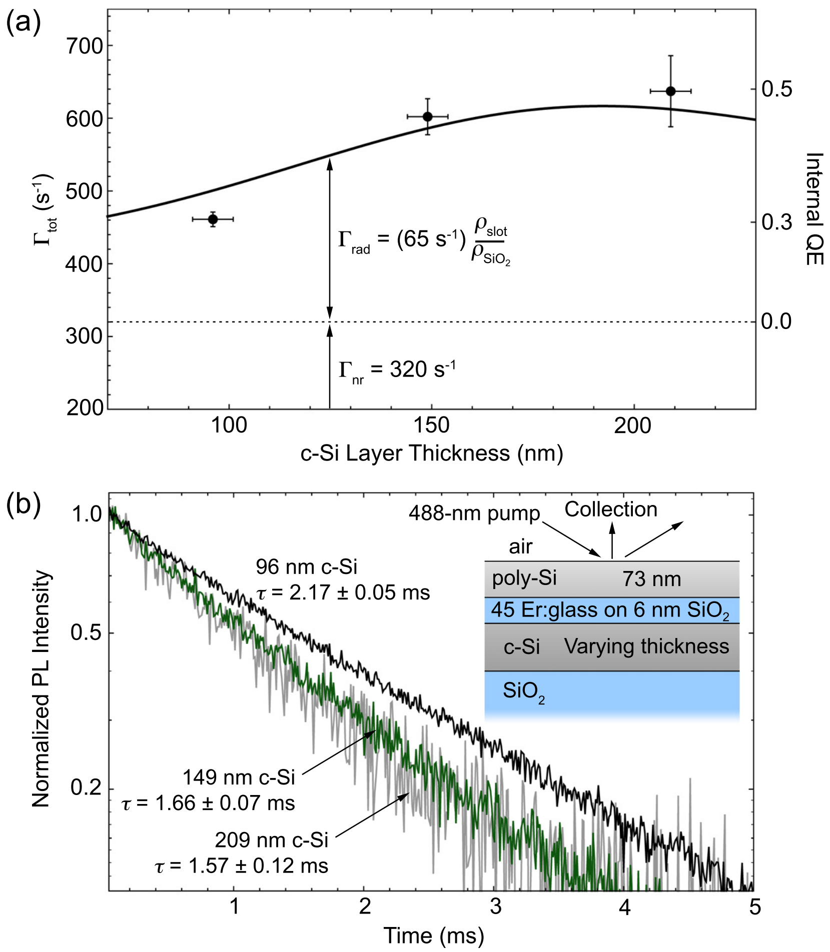

Figure 4.10. Measured total decay rate of Er^{3+} emitters embedded in slot waveguide structures with varying lower silicon-layer thickness. (a) The deviation between the calculated radiative spontaneous emission rate (solid line) and the measured decay rates is minimized for a constant non-radiative decay rate of $\Gamma_{nr} = 320\ s^{-1}$. (b) The experimental decay rates are extracted from PL lifetime measurements at $\lambda_0 = 1537$ nm. The errors in the measured values arise from exponential fits to the time-resolved PL and ellipsometry measurements of the silicon layer thicknesses.

addressed further in the following sections. Assuming a constant Γ_{nr}, the observed trend for Γ_{tot} for the different waveguide geometries in Fig. 4.9 suggests that the radiative emission rate is also significantly enhanced, as expected.

Taking the measured values of Γ_{tot} and the fitted value of Γ_{nr}, we can estimate the internal QE for emitters in the slot waveguide structures. In particular, η increases from 0.31 for the slot waveguide with thinnest c-Si layer to nearly 0.50 for the thicknest c-Si layer. This represents an overall decrease in η relative to the value of 0.63 measured for Er:glass on SiO_2; however, the enhancement of the radiative emission rate at least partially recovers the quantum efficiency lost to enhanced non-radiative decay.

The promising result from the measurements shown in Fig. 4.10 is that one can indeed enhance the spontaneous emission rate of dipole emitters in a slot waveguide and significantly affect the degree of enhancement by adjusting the waveguide layer dimensions. However, the significant enhancement of the non-radiative rate presents a significant practical barrier to exploiting changes in the LDOS in order to increase the radiative QE. One obvious culprit for non-radiative decay enhancement is energy transfer to free carriers and defects in the silicon layers; however, previous studies have found characteristic interaction distances between Er^{3+} ions and nearby silicon nanocrystals [100] and amorphous silicon layers [101] to be on the order of 1 nm. Consequently, we would expect only a small fraction of the Er^{3+} emitters in the Er:glass films to be affected. In the next section, we further study the influence of silicon layers on Er^{3+} emitters and show evidence for an apparently long-range interaction.

4.3.2 Non-Radiaitve Decay near a Single Silicon Layer

The same sputtering and annealing conditions were used to deposit Er:glass layers onto SOI substrates with a wider range of c-Si layer thicknesses, but no poly-Si top layers were deposited. The total decay rates for these samples are plotted in Fig. 4.11 along with the calculated radiative emission rate as a function of the c-Si layer thickness. The LDOS enhancement for an Er:glass layer on a single silicon

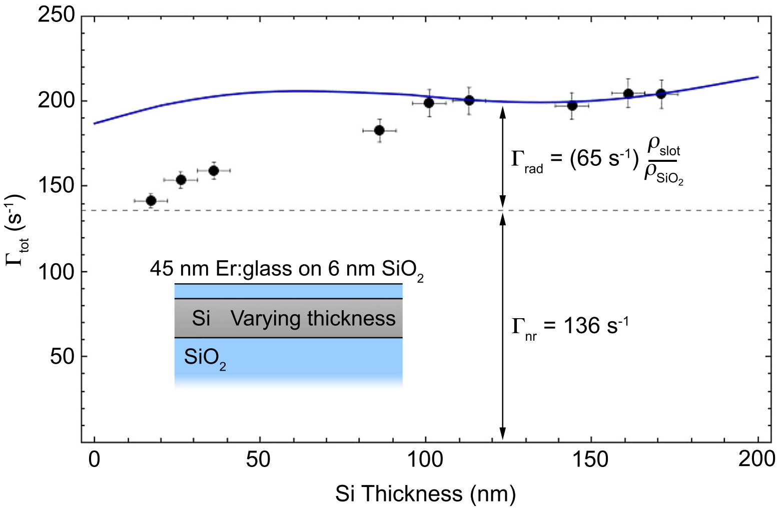

Figure 4.11. Total PL decay rate at $\lambda_0 = 1537$ nm measured from Er:glass films deposited on single-layer silicon waveguides of varying thickness. The blue solid line represents the calculated spontaneous emission rate assuming a constant non-radiative decay rate of $\Gamma_{nr} = 136\ \text{s}^{-1}$. The measured rates deviate from the predicted ones for silicon thicknesses below ~100 nm, indicating reduced non-radiative decay for thin waveguide structures. The samples were optically pumped at $\lambda_0 = 488$ nm.

waveguiding layer is minimal, since there is no slot confinement effect; however, there is some weak dependence on the silicon layer dimensions. Assuming a constant non-radiative decay rate of 136 s^{-1}, the calculated emission rate agrees with the measured values for silicon layers thicker than ~100 nm. This is still a significant increase in Γ_{nr} compared to Er:glass sputtered on SiO$_2$, indicating that the non-radiative decay observed for slot structures is due to both the c-Si and poly-Si layers.

For thinner silicon layers (< 100 nm), the assumption that Γ_{nr} is constant becomes dubious. In this regime, not only do the predicted values of the total decay rate begin to deviate from the measured values, but the estimated QE approaches zero, which is inconsistent with the significant PL intensities measured for these samples. One way to resolve these discrepancies is to assume that Γ_{nr} decreases for thin silicon waveguide layers. As previously mentioned, interactions with carriers and/or defects in the silicon would be expected to occur over length scales of ~1 nm, and the samples studied here have an undoped 6-nm SiO$_2$ spacer layer beneath the Er:glass resulting from high-temperature annealing in O_2. Therefore, it is probable that Γ_{nr} depends on another non-radiative effect that extends over several tens of nanometers. A possible explanation is strain introduced in the Er:glass film during annealing as a result of thermal mismatch with the SOI device layer. Strain could lead to enhanced erbium diffusion and, ultimately, erbium clustering; however, whether this hypothesis is viable remains an open question. Evidence that strain may cause degradation of Er^{3+} luminescence was observed by Borselli [31], who saw improved performance for Er:glass-clad silicon microdisk lasers with thick SiO_2 spacer layers. A careful study of strain in thermally mismatched silicon/glass layers and the resulting effect on the radiative efficiency of Er^{3+} would be a interesting (and very relevant) topic for future research.

4.3.3 Waveguides with Erbium-Implanted Silica Slots and Amorphous Silicon Top Layers

As a comparison to the sputtered Er:glass layers, we also studied erbium-implanted thermal oxide layers (Er:SiO_2) on SOI. A 6-in. SOI wafer with a 3-μm buried-oxide layer and a 220-nm silicon device layer was oxidized at 1000 °C for 3 h to grown ~100-nm of oxide. The wafer was then implanted with 1.28×10^{15} Er^{+} ions/cm^2 at 180 keV. Using the SRIM software package [102], these parameters were found to produce an erbium distribution centered 73 nm below the surface of the thermal oxide with a peak concentration of 3.2×10^{20} cm^{-3} (0.5 atomic %). As samples were needed, they were cleaved from the wafer and annealed in O_2 in the RTA at 1000 °C for 6 min, which was found to produce the longest PL lifetime without reducing the PL intensity near $\lambda_0 = 1535$ nm. The samples were then etched in buffered HF solution for 20 s to thin the erbium-implanted oxide layer to ~50 nm, and the RTA process was repeated to remove any water from the film. Spectroscopic ellipsometry measurements showed a final silicon device layer thickness of 165 nm beneath the 50-nm active layer.

A PL spectrum for an Er:SiO_2 film on SOI is shown in Fig. 4.12(a), with a peak in PL intensity at $\lambda_0 = 1535$ nm. The associated PL lifetime, under 980-nm optical pumping, was measured to be 5.31 ± 0.02 ms. Using immersion oil to perturb the index of the cover layer, as with the sputtered Er:glass layers, the internal radiative QE of the Er:SiO_2 was found to be $\eta = 0.39$, with $\Gamma_{SiO_2} = 75$ s^{-1} and $\Gamma_{nr} = 119$ s^{-1}.

To create slot waveguide structures, amorphous silicon (a-Si) top layers were deposited atop the Er:SiO_2 films by plasma-enhanced chemical vapor deposition (PECVD). As a waveguide material, a-Si has been shown to exhibit reasonably low optical loss at wavelengths near $\lambda_0 = 1550$ nm. Single layer devices have been demonstrated with propagation losses of 2.5 dB/cm [103] and slot waveguides with single-crystal silicon bottom layers and a-Si top layers have been shown to have overall losses of less than 2 dB/cm [45]. For the samples fabricated here, a-Si deposition was performed in an Oxford Instruments Plasmalab 100 chamber using 5% SiH_4 in helium as a precursor gas with 7 W forward power and a substrate temperature of 350 °C, as described in Appendix A. Depositions at this temperature produced films with an index of 3.55 near $\lambda_0 = 1535$ nm, indicating a high film density and providing high index contrast for improved slot confinement of the fundamental TM mode.

Although a-Si is very absorbing at wavelengths near 488 nm (a bulk absorption length of just 51 nm was determined for our films from ellipsometry data), we were able to excite PL using the 980-nm pump laser, as shown in Fig. 4.12(a). For increasing a-Si layer thickness, the calculated average slot LDOS enhancement, relative to bulk oxide, for the fabricated geometry increases from near unity for no a-Si layer to $\rho_{slot}/\rho_{SiO_2} = 6.5$ for an a-Si layer 180-nm thick. As shown in Fig. 4.12(b), the measured PL lifetime was indeed shorter for a slot structure with a near optimal a-Si layer thickness of 182 nm compared to a structure with just 26 nm of a-Si; however, the measured lifetimes for both samples (and samples with intermediate top layer thicknesses that are not represented in the figure) were much lower than expected relative to reference samples with no a-Si layer. In fact, the measured lifetimes indicate a non-radiative decay rate of $\Gamma_{nr} > 900$ s^{-1} and a maximum radiative QE of $\eta = 0.33$ for an optimal slot geometry. The apparent degradation of the Er:SiO_2 films is likely due to reduction of Er^{3+} ions during the hydrogen-rich PECVD process [104] and might be mitigated with a suitable diffusion barrier layer.

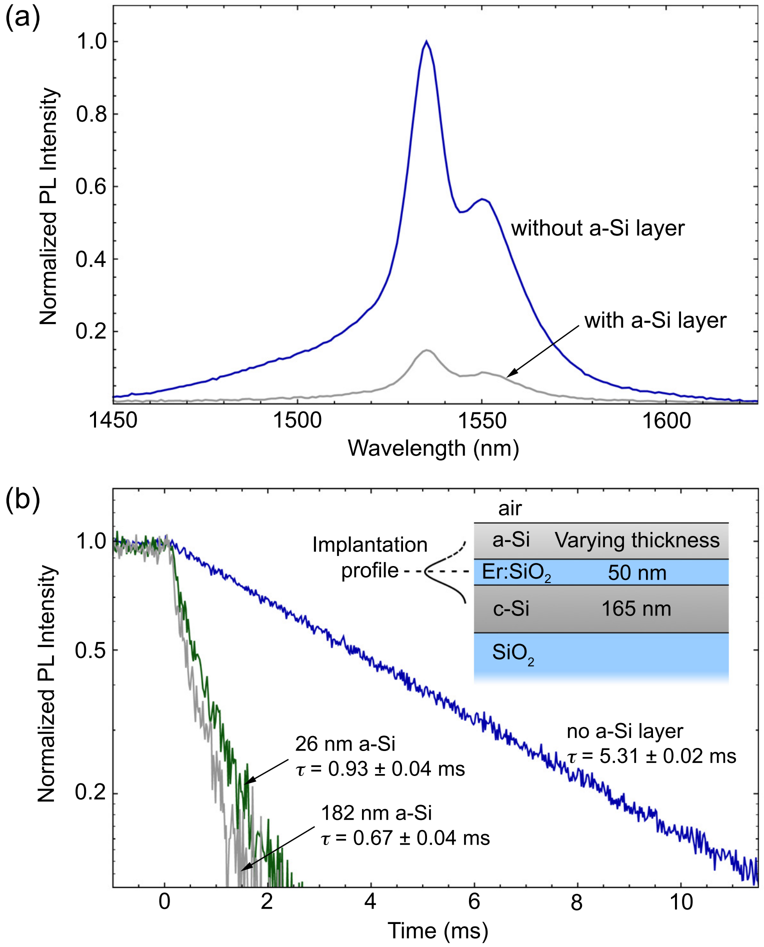

Figure 4.12. PL spectra and lifetime measurements for erbium-implanted SiO_2 films on SOI with and without an amorphous silicon top layer. (a) At a pump wavelength of 980 nm, the a-Si is transparent, allowing for top-down excitation of the buried Er:SiO_2 layer; however, the PL intensity collected from above the waveguide is reduced due to reflection of the pump beam from the a-Si and coupling of emission into slot waveguide modes. (b) The total decay rate is reduced for slot structures as a result of enhancement of both radiative and non-radiative processes.

4.4 Realizing Practical Silicon Slot Waveguide Devices with Erbium-Doped Active Layers

The realization of optimized active silicon slot waveguide devices could lead to a new class of on-chip light sources based on fast, efficient spontaneous emission. As shown here by calculations of the local density of optical states, the radiative rate of spontaneous emission from erbium-based active layers in slot waveguides can be enhanced over a broad spectral range by more than an order of magnitude relative to bulk emission rates, and emission can be preferentially coupled into a single guided mode. Combined with a phase-insensitive optical modulator, such a light source could be used, for example, to encode optical data for on-chip data transmission.

Practically, the integration of erbium-based active layers with silicon waveguides is nontrivial. We have examined the integration of sputtered and implanted erbium-doped films with single-crystal, polycrystalline, and amorphous silicon waveguide layers and have observed, consistent with the work of others, overall decreases in Er^{3+} quantum efficiency due to enhanced non-radiative decay. We acknowledge that the existing body of work, including our own studies, is by no means exhaustive, and there are many more paths to be explored. For example, in addition to the work presented in detail here, we attempted the integration of sputtered and implanted erbium-doped films with the wafer-bonded slot waveguides described in Chapter 3. Although it unfortunately became obvious only after several fabrication attempts, low-temperature wafer bonding of hydrophilic silica surfaces necessarily introduces an abundance of OH^- impurities at the bonding interface [64], creating quenching sites for Er^{3+} luminescence [30]. Future wafer bonding studies could implement a high-temperature (> 800 °C) process to bond hydrophobic erbium-doped silica surfaces while allowing the silica to flow and form a complete bond [66].

Overall, while there remain engineering challenges associated with the integration of erbium-based light sources on the silicon photonics platform, the potential benefits of deposited or implanted light-emitting layers in terms of cost and scalability should prompt continued research into erbium-related devices. For waveguide-integrated structures, and particularly for designs with high modal confinement, spontaneous emission rate enhancement will likely be an important, if not essential, factor in the device design.

Chapter 5

Vanadium Dioxide-Based Waveguide Modulators

This chapter summarizes the integration of silicon-on-insulator waveguides and ring resonators with lithographically patterned vanadium dioxide thin-film structures to demonstrate a compact in-line absorption modulator for use in photonic circuits. We employ simple substrate heating to induce an insulator-to-metal phase transition in the patterned VO_2 elements, which is accompanied by drastic changes in optical properties at near-infrared wavelengths and thus transmission modulation in the integrated SOI waveguides. Our proof-of-principle experiments are intended to demonstrate the viability of VO_2 as an active, switchable material compatible with the silicon photonics platform, but they also illustrate the utility of photonic waveguides for studying fundamental material properties. We hope to pave the way for future waveguide-integrated devices that employ phase switching induced by localized thermal stimulus or even optical and electrical stimuli, which have the potential to enable efficient, ultra-fast active photonics.

5.1 VO_2 for Active Integrated Photonics

The thermochromic phase transition of crystalline VO_2 occurring near 68 °C [105] has been of interest in recent years for its potential applications in active electrical and optical devices. Monophase VO_2 can be transformed from a relatively transparent insulating state with monoclinic crystal structure to a metallic state associated with a tetragonal (rutile) phase, as shown in Fig. 5.1, upon application of thermal [106], optical [107, 108], or electrical [109, 110] stimulus. Changes in the properties of VO_2 have been reported to occur on a time scale of 10 ns under an applied electric field or by direct heating [109, 111] and down to 100 fs using ultrafast optical pumping [107]. Furthermore, recent evidence obtained by femtosecond electron diffractometry suggests that the phase transition occurs in multiple stages: deformation of vanadium dimers in the monoclinic phase can occur on a sub-picosecond timescale, while the full structural transition to tetragonal symmetry occurs over a longer period of time [112]. This supports previous evidence that changes in optical and electrical properties can be induced independently from a structural transition [108], and suggests that ultrafast changes in the optical properties of VO_2 are, in fact, associated with distortions of the electronic structure in the monoclinic phase [107]. It remains an open question whether similarly fast modulation might be induced using an externally gated electric field, but evidence of field-induced switching, independent of heating beyond the phase transition temperature, has been reported [110, 113]. When the full structural transition does occur, the rate of switching back to the insulating phase depends on the dissipation of heat within the particular structure, but VO_2 films have been observed to regain their insulating-phase properties over time scales on the order of 10 ns [107, 109].

Given the drastic changes in optical properties associated with the VO_2 phase transition and the evidence of ultrafast switching, VO_2 is a very attractive material for active photonic devices. To date, there have been demonstrations of VO_2-based free-space optical modulators at infrared [111] and visible [114] wavelengths, where direct heating was employed to induce the phase transition. While these studies show promising results, many of the potential applications of a modulator operating at telecommunications wavelengths require compact integration of waveguide-coupled devices on a silicon chip.

Several silicon-based waveguide modulator designs have been investigated to compete with more conventional III-V semiconductor and $LiNbO_3$-based modulators. Prime examples of this technology take advantage of small changes in the refractive index of silicon due to voltage-induced variations in charge density. When in-

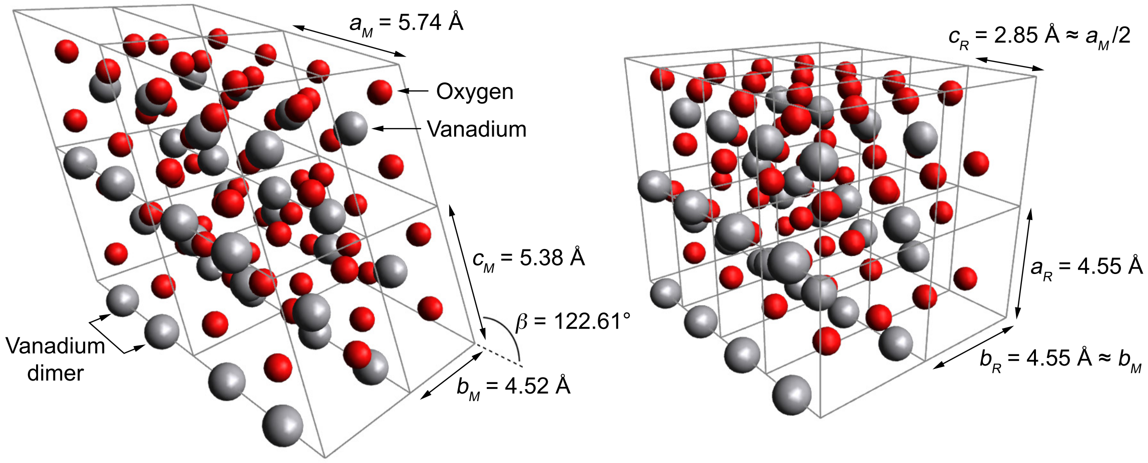

VO$_2$(M): Insulating monoclinic phase

VO$_2$(R): Metallic tetragonal (rutile) phase

Figure 5.1. Atomic structure of the monoclinic and tetragonal phases of VO$_2$. The monoclinic phase exhibits insulating optical and electrical properties at room temperature, while the tetragonal (rutile) phase, which becomes stable above 68 °C, has high DC conductivity and metallic optical properties at near-infrared wavelengths.

tegrated with a high-quality cavity [19] or Mach-Zehnder interferometer (MZI) [20], such perturbations of the index can result in greater than 15 dB modulation of a single wavelength with modulation frequencies in excess of 1 GHz; however, in order to accommodate interferometric structures, these devices have linear dimensions greater than 10 μm and are limited to a narrow spectral range. In comparison, LiNbO$_3$-based modulators can produce greater than 20 dB modulation at frequencies above 10 GHz [115], but they often employ MZI schemes and are relatively large. Compound-semiconductor electro-absorption waveguide modulators have been shown to be competitive with LiNbO$_3$ devices and have the advantage of broader wavelength operation; however, such devices often require propagation distances on the order of 100 μm [116] due to limited absorption modulation and modal overlap.

Future scalable on-chip optical modulators are expected to operate with switching energies on the order of 10^{-14} J [117]. For small volumes and short time scales, the thermal energy density required to induce the VO$_2$ phase transition in a thermally isolated device is approximately $c_p \rho_m \Delta T$, where $c_p = 690$ J/(kg·K) is the heat capacity of insulating VO_2, $\rho_m = 4.3 \times 10^{-3}$ kg/cm^3 is the material density, and ΔT is the required temperature increase [113, 118]. For a device initially at room temperature, this energy density is $\sim 10^2$ J/cm^3, and a typical thin film device with a thickness of less than 100 nm and a footprint of 1 μm^2 will have a switching energy on the order of 10^{-11} J. In comparison, for electrically driven VO_2 devices with switching times on the order of 10 ns, the field required to induce the VO_2 phase transition has been reported to be $\sim 10^5$ V/cm [110], and the leakage current at the transition is $\sim 10^4$ A/cm^2 [109, 113]. The corresponding switching energy is 10^{-12} J, indicating that field-induced switching can potentially be more efficient than thermal switching. To achieve even lower switching energies, it is feasible to envision device designs that, for example, further decrease the required volume of VO_2 or reduce the leakage current through a VO_2 film while still achieving the critical electric field required for the phase transformation.

As a step toward integrating VO_2-based devices into a Si photonics platform, we have fabricated compact, lithographically defined VO_2 modulators on SOI. We use substrate heating to thermally induce the VO_2 phase transition, and by demonstrating the efficacy of these devices as integrated absorption modulators, we intend to motivate future work to develop devices that operate on fundamentally faster time scales using localized electrical or optical stimuli. For a modulator with an active device length of 2 μm, we observe thermally induced optical modulation of a confined waveguide mode in excess of 6.5 dB at $\lambda = 1550$ nm, with 2 dB insertion loss. A 16-fold increase in VO_2 absorption across the phase transition allows the modulator to function as an effective single-pass device that is compact and broadband, in contrast to MZI and resonator-based designs. Electromagnetic simulations indicate that even deeper modulation is possible with modified device geometries. We also show that waveguide-based devices can be used to probe fundamental phase transition properties, including hysteresis and anomalous dielectric effects.

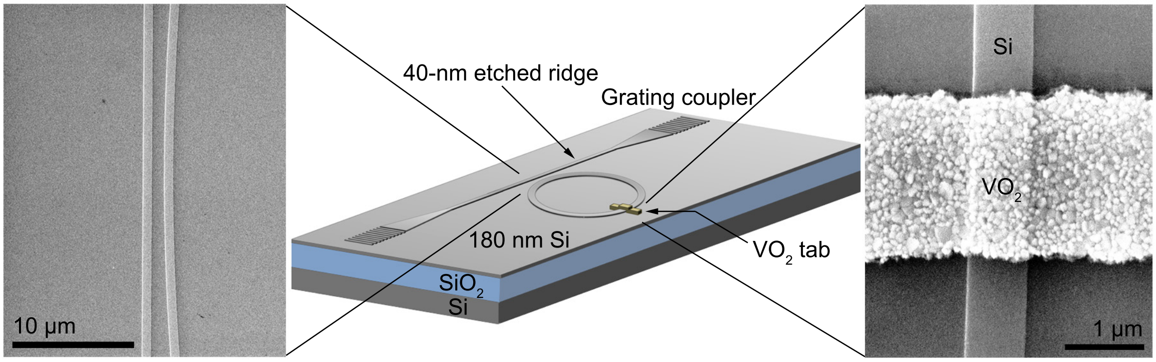

Figure 5.2. Schematic of the VO_2 modulator test bed, with a grating-coupled through-port waveguide and an evanescently coupled ring resonator. The scanning electron micrographs show the 1-μm coupling gap between the through-port waveguide and the 400 μm-diameter ring resonator (left) and a lithographically defined 2 μm-long polycrystalline VO_2 tab (right).

5.2 VO_2 Device Fabrication

To measure the optical loss induced by integrated VO_2 modulator devices, we first fabricated SOI test bed structures consisting of through-port waveguides evanescently coupled to large-diameter ring resonators, as shown in Fig. 5.2. The resonators are not fundamental to the modulator design, but they facilitate loss measurements independent of temperature-related changes in the amount of optical power coupled into the SOI waveguides. We used SOI with a lightly doped p-type ($\sim 10^{15}$ cm^{-3}) 220-nm silicon device layer on a 3-μm buried oxide, and patterns were defined using Micro Resist Technology ma-N 2403 resist with high-resolution electron-beam exposure. A waveguide width of 720 nm was chosen so that only the fundamental TE and TM modes are supported at $\lambda = 1550$ nm, while minimizing leakage loss from the TM mode [44]. To couple light into and out of the through-port waveguides, we defined symmetrical pairs of 30 μm-wide, 50 μm-long diffraction gratings with a 685-nm pitch, connected to linear waveguide sections via 500 μm linear tapers. Finally, 400 μm-diameter rings, which exhibit negligible bending loss, were patterned alongside the through-port waveguides, with a 1-μm coupling gap.

The waveguide pattern was transferred into the SOI to a depth of 40 nm by C_4F_8/O_2 plasma etching, and the resist was removed along with residual polymer etch products in a 3:1 Piranha solution of H_2SO_4 and 30 % H_2O_2 at 100 °C. After removing residual surface oxide in buffered HF, the resonators were characterized using the fiber-coupled waveguide testing platform described in Chapter 3 in order to obtain a baseline measurement of ring resonator quality factor.

5.2.1 Deposition and Characterization of VO_2 on SOI Devices

After optical characterization, the native oxide from testing in air was removed from the waveguides with another HF dip, and the samples were immediately inserted into a vacuum chamber for pulsed-laser deposition (PLD) of VO_2. Samples were heated to 500 °C, and deposition was performed by ablating a vanadium metal target with 300-mJ pulses from an excimer laser at a rate of 10 Hz in 12 mTorr O_2. For the devices considered here, VO_2 layers were deposited to an average thickness of 65 nm, which was verified by AFM. To pattern the VO_2 tabs, waveguide samples were again coated with resist, and tabs were patterned by electron beam lithography. The pattern was transferred into the VO_2 using chromium etchant (Sigma-Aldrich 651826) containing dilute ceric ammonium nitrate, $(NH_4)_2Ce(NO_3)_6$, and nitric acid, HNO_3, and the resist was removed in acetone. The VO_2 film was removed from control resonators, which were tested again in the fiber-coupling setup, and it was found that the resonator quality factor was not impacted by VO_2 deposition and etching.

In order to characterize the VO_2 films independently of waveguide measurements, thin films were deposited onto high-resistivity Si(001) substrates at the same time as the SOI devices, and the samples were analyzed by multiple-angle spectroscopic ellipsometry and x-ray diffractometry (XRD). Figure 5.3 shows the real and imaginary parts of the index of refraction, n and κ, of a 65-nm VO_2 film, as extracted from the ellipsometry amplitude and polarization parameters, Ψ and Δ. As shown in Fig. 5.3(a), three sets of Ψ and Δ spectra were collected at reflection angles of 60°, 65°, and 70° from the surface normal.

To obtain the complex index, the VO_2 film was modeled as a dispersionless but lossy material over wavelength windows of 50 nm. With the thickness fixed at the value measured by AFM, the values of n and κ were optimized by a minimization

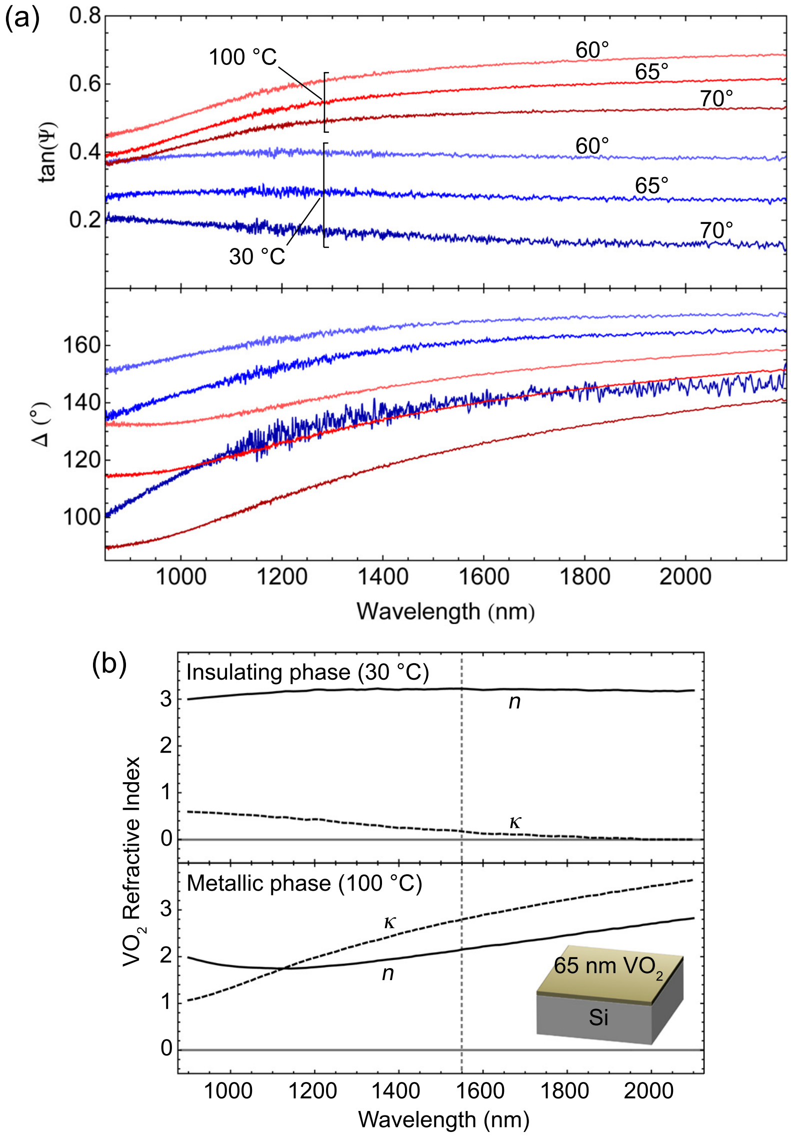

Figure 5.3. Optical properties of both phases of VO_2 in the near infrared, as measured by multiple-angle spectroscopic ellipsometry. (a) The ellipsometry amplitude and polarization parameters, Ψ and Δ, were collected at three different reflection angles and temperatures of 30 and 100 °C for a 65-nm thick VO_2 film on silicon. (b) The real, n, and imaginary, κ, parts of the VO_2 index extracted from the ellipsometry measurements in (a) show a clear transition from insulating to metallic optical properties, with a 16-fold increase in absorption at $\lambda = 1550$ nm.

algorithm to achieve the smallest error between the modeled and measured values of Ψ and Δ at all three reflection angles simultaneously. The fitting process was repeated as the 50-nm wavelength window was moved along the measured spectrum in increments of 10 nm. This interval fitting method functions as a running average filter to reduce noise in the extracted index values, and it allows for material dispersion to be determined without having, *a priori*, a phenomenological model of the material's optical properties. The method is acceptable for both phases of VO_2 in the near infrared since the index varies slowly with wavelength.

At $\lambda = 1550$ nm, the complex index of VO_2 is $3.21 + 0.17i$ near room temperature and $2.15 + 2.79i$ when heated to 100 °C, which indicates a clear transition from a nearly transparent state to a phase with metallic optical properties. In particular, the more than 16-fold increase in absorption is the basis for our optical modulator. Also, the optical properties for each phase are nearly constant over the telecommunications C-band (1530 to 1565 nm), making VO_2 a suitable material for broadband devices.

As shown in Fig.5.4(a), the XRD spectrum of the 65-nm VO_2 film produces a strong peak at a 2θ diffraction angle of 28°, corresponding to the (011) plane of VO_2. The spectrum does not show any peaks related to other stoichiometries of vanadium oxide, which would appear over this range of diffraction angles, indicating single-phase crystalline growth [119]. The scanning electron micrograph in the inset shows an average crystal grain size of nearly 100 nm. In terms of crystallinity and morphology, our films resemble previously reported ones deposited at low temperature and subsequently oxidized at 450 °C [119], indicating that our *in-situ* oxidation process is comparably effective at producing monophase VO_2 on silicon.

We also measured the electrical resistivity of VO_2 on a small chip of SOI using the four-point van der Pauw method [120]. The temperature was changed in increments of 1 °C at a rate of less than 1 °C/min to ensure thermal equilibrium, and the resistivity was measured for all the various source-probe configurations possible with four symmetric points. At each temperature, all resistivity measurements agreed to within 5%, and the averaged values of resistivity are plotted in Fig.5.4(b). Near room temperature, the measured resistivity is nearly equal to that of the underlying

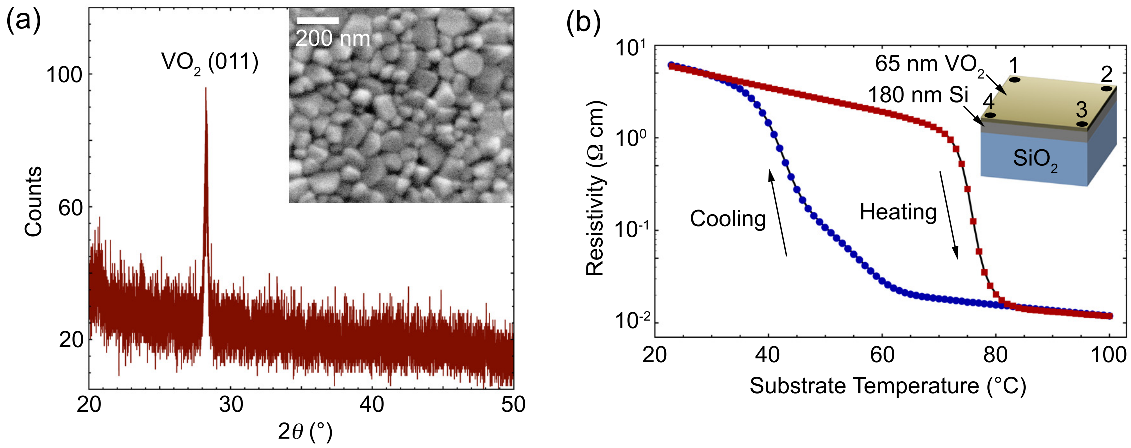

Figure 5.4. Structural and electrical properties of a 65-nm thick polycrystalline VO_2 film deposited on silicon. (a) The x-ray diffraction spectrum shows just one vanadium oxide-related peak, corresponding to VO_2, and the scanning electron micrograph (inset) shows the coarse polycrystalline structure. (b) The electrical resistivity versus temperature of the same 65-nm thick VO_2 film on SOI was measured using the four-point van der Pauw method.

SOI layer, indicating that the VO_2 is not significantly more conductive than lightly doped silicon; however, upon heating above 70 °C, we observe an abrupt transition to the significantly more conductive metallic phase. Upon cooling, the film regains its insulating-phase properties, but with a less abrupt transition with respect to temperature. In particular, the VO_2 does not completely switch back to its insulating phase until it has cooled to nearly 40 °C. As previously reported by Suh, *et al.* [119], such broad hysteresis is indicative of films with the coarse-grain microstructure observed here, since there is a lower density of nucleation sites for the metal-to-insulator transition compared with smaller-grained microstructure.

5.2.2 VO_2 Deposited on SiO_2

To further characterize the transport properties of the VO_2 deposited by PLD, we studied thin films on insulating substrates. Figure 5.5 shows a 50-nm thick VO_2 film deposited onto a 1-μm thick thermal oxide layer on silicon. Rather than cleave a small piece to obtain accurate four-point measurements, as was done for the films on SOI, the VO_2 was lithographically patterned in a cloverleaf shape. Unlike the films

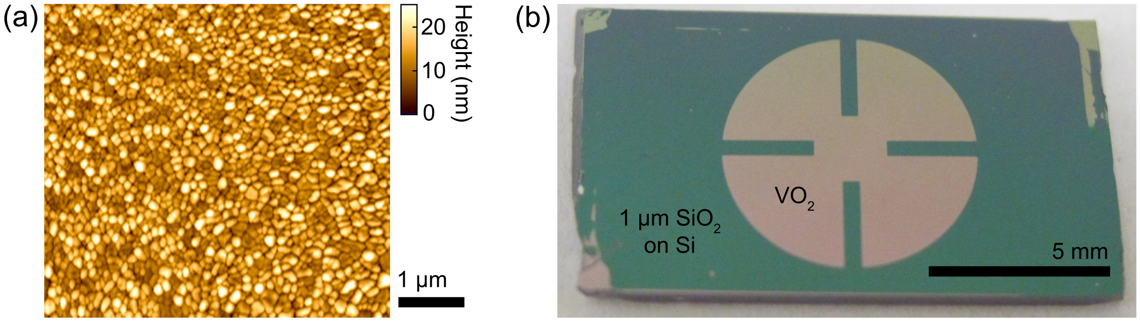

Figure 5.5. 50-nm thick VO_2 film deposited on SiO_2 for optical and electrical characterization. (a) An AFM scan of the VO_2 surface reveals polycrystalline structure similar to films deposited on silicon and a root-mean square surface roughness of 4.4 nm. (b) The VO_2 film was patterned in a cloverleaf shape for accurate four-point probe measurements.

on SOI, where the silicon device layer was nearly as conductive as the VO_2, the VO_2 is electrically isolated on the thermally grown SiO_2.

Using the same four-point van der Pauw configuration that was used for the previous resistivity measurements, the room-temperature VO_2 carrier concentration and mobility were measured in a Hall probe system using the patterned sample shown in Fig. 5.5. Accounting for the film thickness, the VO_2 was found to have a resistivity of $\rho = 15 \pm 3$ Ω·cm, which is slightly higher than the room-temperature resistivity shown in Fig. 5.4(b) for VO_2 on SOI, likely because there is no contribution from the SOI device layer. Conduction was found to be dominated by electron transport, with a carrier concentration of $n_e = (3 \pm 1) \times 10^{18}$ cm^{-3}. Monoclinic $VO_2(M)$ has a relatively narrow bandgap of ~ 0.7 eV, but electrical transport is thought to be dominated by a polaron hopping conduction mechanism with an activation energy significantly smaller than the bandgap energy [121]. Consistent with the measured carrier concentration, the number of carriers contributing to electrical conduction can be much higher with a hopping model than would be expected assuming only thermal excitation of carriers into the conduction band. The Hall mobility is $\mu_{\mathrm{H}} = 1/(en_e\rho) = 0.14 \pm 0.05$ cm^2/(V·s), which is the same order of magnitude as Hall mobilities previously measured for single-crystal VO_2 [122].

Temperature-dependent ellipsometry measurements were performed on the VO_2

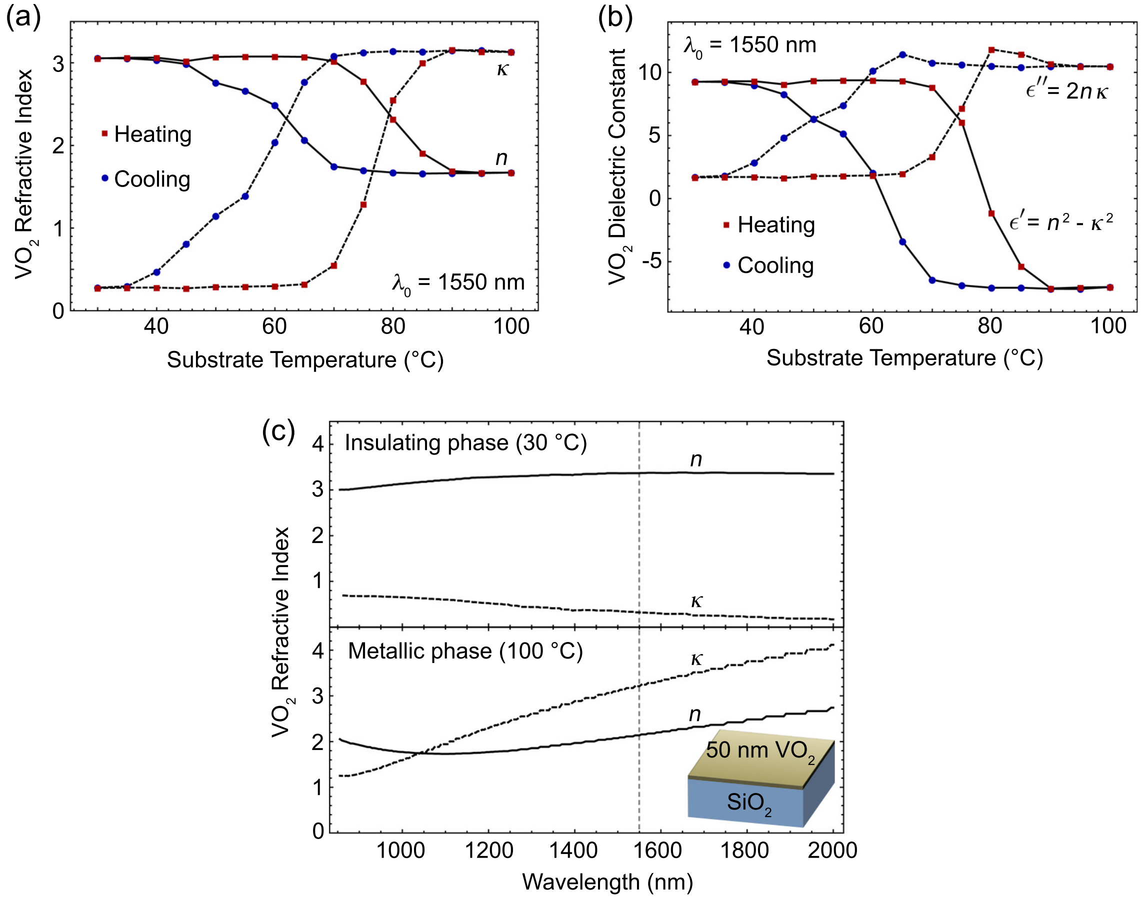

Figure 5.6. Temperature-dependent optical properties of VO_2 deposited on SiO_2, measured by ellipsometry. (a) The complex index of refraction is comparable to that measured for VO_2 deposited on silicon, except that the absorption is slightly larger for both phases. (b) The complex dielectric constant, extracted directly from the index, reveals local maxima in the imaginary part near the phase transition temperature. (c) The wavelength dependence of the complex refractive index is shown at 30 and 100 °C.

films deposited on SiO_2 in the the same manner as the measurements of films deposited on silicon. Figure 5.6 shows the complex dielectric constant, $\epsilon/\epsilon_0 = \epsilon' + i\epsilon''$, and refractive index for a 50-nm thick VO_2 film. The real part of the index spectra in Fig. 5.6(c) agrees very well with results obtained for films deposited on silicon; however, the material absorption is higher for VO_2 deposited on SiO_2 for both phases. This likely reflects slight differences in the microstructure resulting from the different deposition substrate and the shorter deposition time. We also note that a local maximum appears in the temperature dependence of the imaginary part of the dielectric constant, $\epsilon'' = 2n\kappa$, near the phase transition temperature. We attribute this to the coexistence of the $VO_2(M)$ and $VO_2(R)$ phases, as will be discussed in further in Section 5.3.

5.3 Modulator Characterization

We probed the loss induced by waveguide-integrated VO_2 tabs by measuring the linewidth of TE-mode resonances supported by the SOI ring-resonator test bed structures depicted in Fig. 5.2. Using the waveguide coupling setup described in Chapter 3, laser light near λ =1550 nm was coupled into and out of the through-port waveguides using surface relief grating couplers. Maximum coupling efficiency was achieved for an angle of $\sim 30°$ between the waveguide surface normal and the optical axis of the fiber focusers. The through-port transmission was measured as the input wavelength was swept from 1550 to 1551 nm at a sweep rate of 1 nm/s. This wavelength range was sufficient to consistently capture at least one resonance, since the free-spectral range (FSR) of ring-resonator modes of adjacent azimuthal order for our device geometry is approximately 0.5 nm.

5.3.1 Reference SOI Resonator Measurements

As a baseline reference, the through-port transmission for a bare 400-μm diameter ring resonator from which all VO_2 was removed is shown in Fig. 5.7(a). At 30 °C, the resonance at $\lambda_0 = 1550.706$ nm has a linewidth, $\delta\lambda$, of 14.1 pm and a FSR, $\Delta\lambda$, of 0.510 nm. By the relation $Q = \lambda_0/\delta\lambda$ (valid since $\delta\lambda << \lambda_0$), this corresponds to a loaded quality factor $Q_{\mathrm{ref}} = 110,000$. Since $\Delta\lambda << \lambda_0$, the group index is approximately $n_{\mathrm{g}} = {\lambda_0}^2/(L_{\mathrm{c}}\Delta\lambda) = 3.75$, where $L_{\mathrm{c}} = 400\pi$ μm is the round-trip length of the ring resonator.

Since the resonance linewidth is significantly larger than the FSR, we can fit the through-port transmission, $T(\lambda)$, to the form given in Eq. 2.37:

$$T(\lambda) = \frac{(t-a)^2 + (2\pi n_{\mathrm{g}} L_{\mathrm{c}})^2 at \frac{(\lambda-\lambda_0)^2}{{\lambda_0}^4}}{(1-at)^2 + (2\pi n_{\mathrm{g}} L_{\mathrm{c}})^2 at \frac{(\lambda-\lambda_0)^2}{{\lambda_0}^4}} \ . \tag{5.1}$$

We obtain $a = 0.951$ and $t = 0.964$, corresponding to an intrinsic loss per unit length of $\alpha_{\mathrm{prop}} = -2\ln(a)/L_{\mathrm{c}} = 0.800$ cm^{-1} = 3.47 dB/cm. This corresponds to an intrinsic quality factor of $Q_{\mathrm{int}} = 2\pi n_{\mathrm{g}}/(\alpha_{\mathrm{prop}}\lambda_0) = 190,000$. We assume the observed Q_{ref} to be a result of both propagation loss and loss due to the through-port coupler, represented here by the coupler quality factor, Q_{coup}, where

$$\frac{1}{Q_{\mathrm{ref}}} = \frac{1}{Q_{\mathrm{int}}} + \frac{1}{Q_{\mathrm{coup}}} \ . \tag{5.2}$$

The value of Q_{coup} is therefore 261,000, which corresponds to a fractional coupler loss of $l_{\mathrm{coup}} = 2\pi n_{\mathrm{g}} L_{\mathrm{c}}/(Q_{\mathrm{coup}}\lambda_0) = 0.073 = 0.32$ dB per pass in the resonator. The same value can be obtained from the fitted parameter t, where $l_{\mathrm{coup}} = -2\ln(t)$.

As shown in Fig. 5.7(a), the spectral response of the bare reference resonator was again measured with the waveguide sample heated to 100 °C using a substrate heater. The resonator quality factor was unaffected, which is expected since, even at 100 °C, free-carrier absorption is on the order of 10^{-2} dB/cm [5], and the propagation loss is dominated by scattering from the etched waveguide edges [55]. Furthermore, with a thermal expansion coefficient of just 2.6×10^{-6} °C^{-1}, the coupling gap and waveguide width change by a negligible amount for a temperature increase of 70 °C. However, due to the thermo-optic effect in the Si waveguide layer, the Si index changes by 5.2×10^{-5} °C^{-1} [123]. This results in an increase of the modal effective index, n_{eff}, and the group index with temperature, which redshifts each resonance by 0.08 nm/°C and slightly increases the FSR, as shown in Fig. 5.7.

We also observe that the off-resonance transmission for the reference devices is decreased when the sample is heated. Changes in the silicon refractive index shift the ideal coupling angle of the grating couplers, resulting in decreased coupling efficiency of our devices when the angle is fixed. This illustrates the advantage of using resonator linewidth to probe attenuation: as long as the optical power is low enough that nonlinear effects are negligible, the linewidth provides an intensive measure of loss that is independent of coupled power. Consistent with the assumption of linearity, we measured no change in linewidth with input power for the laser intensities used here.

5.3.2 VO_2-Clad Resonator Measurements

We next characterized ring resonators with VO_2 tabs patterned opposite the though-port coupler. Tabs with a 2-μm device length in the propagation direction proved most conducive to the measurement technique employed here, as they were long enough to significantly perturb the ring resonator modes, but not so long as to absorb more light than was needed to reliably measure linewidth. The spectral response, shown in Fig. 5.7(b), was measured in the same manner as the reference resonator, and the substrate temperature was increased by 5 °C between measurements (for brevity, not all temperatures are shown in the figure). The sample was allowed to thermally stabilize for several minutes between measurements to eliminate transient effects in the VO_2. As expected, based on the VO_2 refractive index, the presence of the tab significantly decreases the loaded quality factor, Q_{load}, of the TE resonator modes. Using the loaded quality factor of the otherwise identical reference resonator, Q_{ref}, we can isolate the effect of the tab by the relation

$$\frac{1}{Q_{\mathrm{load}}} = \frac{1}{Q_{\mathrm{int}}} + \frac{1}{Q_{\mathrm{coup}}} + \frac{1}{Q_{\mathrm{tab}}} = \frac{1}{Q_{\mathrm{ref}}} + \frac{1}{Q_{\mathrm{tab}}} \ . \tag{5.3}$$

The single-pass loss induced by the tab is therefore $l_{\mathrm{tab}} = 2\pi n_{\mathrm{g}} L_{\mathrm{c}}/(Q_{\mathrm{tab}}\lambda_0)$, where n_{g} is assumed to be unchanged from the reference resonator, as the tab length is just a small fraction of L_{c}.

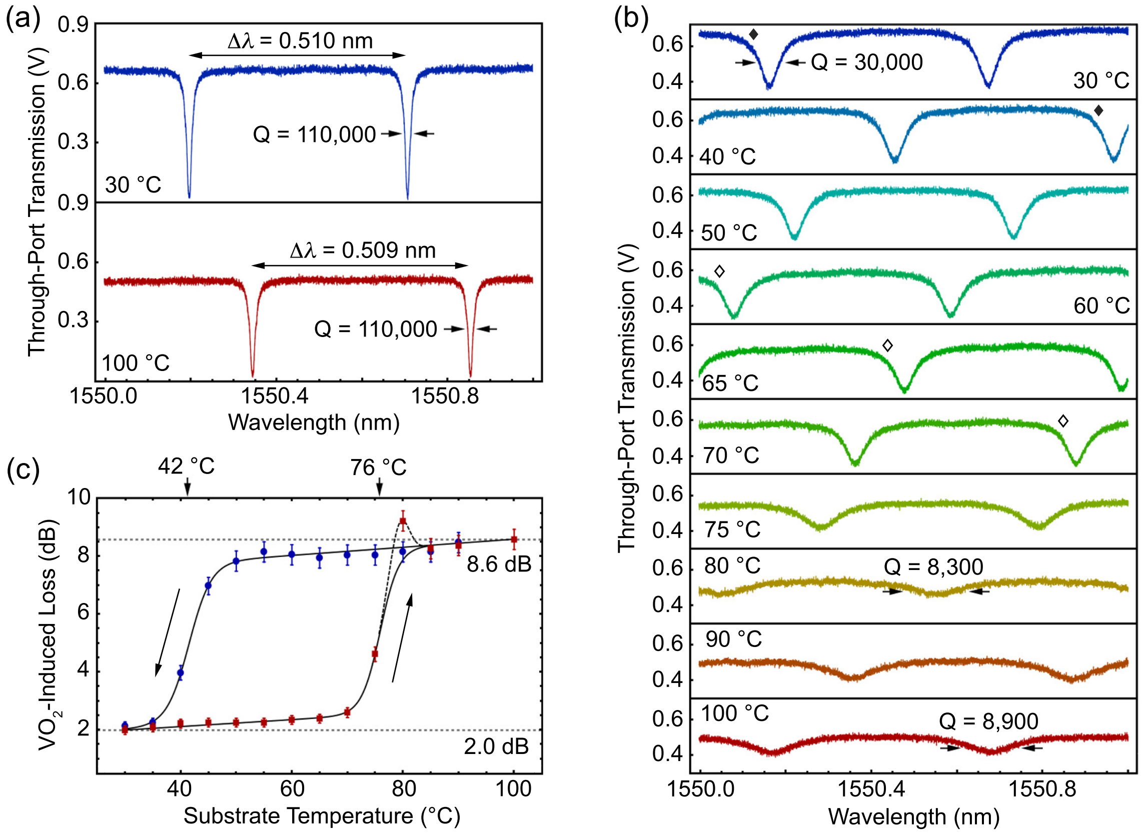

Figure 5.7. (a) TE-polarized through-port transmission spectra of a critically coupled SOI waveguide ring resonator without a VO_2 tab. The resonator Q is unchanged for substrate temperatures between 30 and 100 °C; however, the grating coupling efficiency is impacted by the thermo-optic effect in the silicon, resulting in lower off-resonance transmission. (b) Through-port transmission spectra for increasing substrate temperature with the same resonator geometry, but with a 2-μm long VO_2. Modes of the same azimuthal order are indicated with diamond-shaped markers, revealing a thermally induced redshift of 0.08 nm/°C. (c) Round-trip resonator loss near $\lambda = 1550$ nm due to the VO_2. Upon cooling, thermal hysteresis of over 30 °C is observed.

At 30 °C, we observe $Q_{\text{load}} = 30,000$, and the quality factor decreases rapidly near the VO_2 phase transition temperature at 68 °C, ultimately falling to $Q_{\text{load}} = 8,900$ at 100 °C. These values of Q_{load} correspond to a modulator loss of 2.0 dB when the VO_2 is in its insulating phase and 8.6 dB for the metallic phase, as shown in Fig. 5.7(c), which is a 78% decrease in transmission. We define a modulator figure of merit (FOM) as the ratio of the modulation depth to the insulating-phase insertion loss, equal to 3.3 in this case.

At 80 °C, we also see a repeatable decrease in Q_{load} to 8,300, corresponding to a loss of over 9 dB. We attribute this anomalous increase in loss to the coexistence of VO_2 domains in both insulating and metallic phases. As previously observed by Choi, *et al.* for mid-infrared wavelengths, the real part of the dielectric constant, $\epsilon' = n^2 - \kappa^2$, can become larger than the bulk insulating-phase during the insulator-to-metal transition prior to becoming negative in the metallic phase. This behavior was explained in terms of a percolation threshold, where isolated metallic domains are nucleated and become increasingly capacitively coupled as they expand toward one another with increasing temperature, resulting in a divergence of the effective dielectric constant. The anomalous increase in ϵ' was diminished, however, as the frequency was increased, becoming nearly zero at a wavelength of 2500 nm.

At even shorter wavelengths near 1550 nm, we indeed see no significant increase in ϵ' at intermediate temperatures, as shown in the ellipsometry measurements in Fig. 5.6(b). However, as the temperature approaches 80 °C, n does not decrease as rapidly as κ increases. Consequently, the imaginary part of the dielectric constant, ϵ'', which is proportional to the product of the real part of the index and the absorption, exhibits a local maximum during the insulator-to-metal transition. For our layered structure, a large VO_2 index will pull the mode into the VO_2 layer, exposing the mode to the increased material absorption. As the phase transition progresses with increasing temperature, the VO_2 assumes metallic dielectric properties, and the mode is pushed further down into the transparent Si layer, as shown in Fig. 5.8(a).

We observe that as the sample is cooled from 100 °C, the VO_2 tab exhibits enhanced absorption down to nearly 40 °C, which matches our previous observations of the electrical and optical properties versus temperature. Thermal hysteresis can be undesirable in certain applications and could be reduced by preparing films with smaller crystal grains at lower temperatures [119], but broad hysteresis could be useful, for example, in optical memory devices [124]. We note that there is a small increase in VO_2-induced loss at the onset of the metal-to-insulator transition during cooling, but it is not as pronounced as the local maximum observed during heating, possibly indicative of a subtle non-reciprocity in the phase-transition dynamics.

Finally, as our SOI waveguides also support a TM mode, we attempted to characterize the VO_2-induced loss for TM modes in the devices described above. Interaction of TM resonator modes with the VO_2 tab was found to create additional spectral features that obfuscate the resonances. As a result, measurements of the linewidth were unreliable. These spectral features are likely due to substrate leakage, since the TM-mode is close to cutoff, as well as mode conversion to TE-polarized modes via scattering [44]. Nevertheless, as described in the next section, electromagnetic simulations show that TM-mode operation absent these effects still leads to inferior modulator performance compared with TE-mode operation.

5.3.3 Comparison with Calculated Modal Loss

Figure 5.8(a) shows the optical power of the TE mode supported by our VO_2-clad waveguide geometry, as calculated using finite-element analysis in COMSOL. Assuming the insulating-phase dielectric properties measured for VO_2 deposited on silicon, 13.3% of the power lies in the VO_2 layer. For a metallic-phase VO_2 layer, the optical mode is squeezed toward the Si-SiO_2 interface, resulting in a decreased real part of the modal effective index, n_{eff}. Although the power confinement in the VO_2 is reduced to 4.6% in the metallic phase, the 16-fold increase in absorption results in an increase in the imaginary part of n_{eff} by a factor of 4.5. Assuming loss is due only to material absorption, the modal loss coefficient is $4\pi\ \text{Im}[n_{\text{eff}}]/\lambda$. Over a 2-$\mu$m device length, the predicted losses at $\lambda = 1550$ nm for the insulating and metallic phases are therefore 1.8 dB and 7.9 dB, respectively, in good agreement with the measured values. The calculated values are each approximately 10% less than the measured losses for each

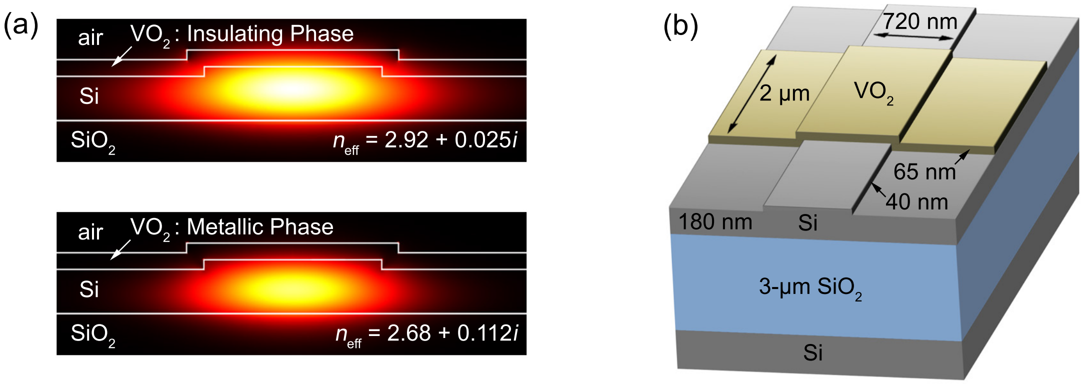

Figure 5.8. (a) Calculated modal effective index and power distribution of the TE mode supported by a VO_2-clad SOI waveguide at λ =1550 nm. The imaginary part of the effective index, n_{eff}, indicates the substantially enhanced modal absorption in metallic-phase VO_2. (b) Schematic of the structure used in FDTD calculations, shown with the experimentally realized dimensions.

phase of VO_2, suggesting that scattering from the VO_2 tab may account for a small fraction of the loss, while material absorption is dominant.

5.4 Optimization of Modulator Geometry

For the waveguide geometry shown in Fig. 5.8, we performed three-dimensional full-field finite-difference time-domain (FDTD) calculations using the Lumerical software package. Our idealized structure resembles the fabricated one except for the roughness of the polycrystalline VO_2; however, agreement of calculated modal loss with experiments suggests that surface scattering is negligible compared with material absorption. To obtain modulator loss with the FDTD simulations, we used the fundamental TE mode of the bare silicon waveguide at 1550 nm as an input source and recorded the normalized reflected and transmitted power. The reflected power was found to be less than 0.2% for all tab geometries considered here, so excess loss beyond that due to VO_2 absorption can be attributed to scattering into unguided modes. Consistent with the assertion that material loss is dominant for both VO_2 phases, loss increases linearly with device length, as seen in Fig. 5.9(a), and loss is minimal as the device length approaches zero. For a modulator with the experimental geometry, the insulating-phase transmission loss is 2.1 dB and the metallic-phase loss

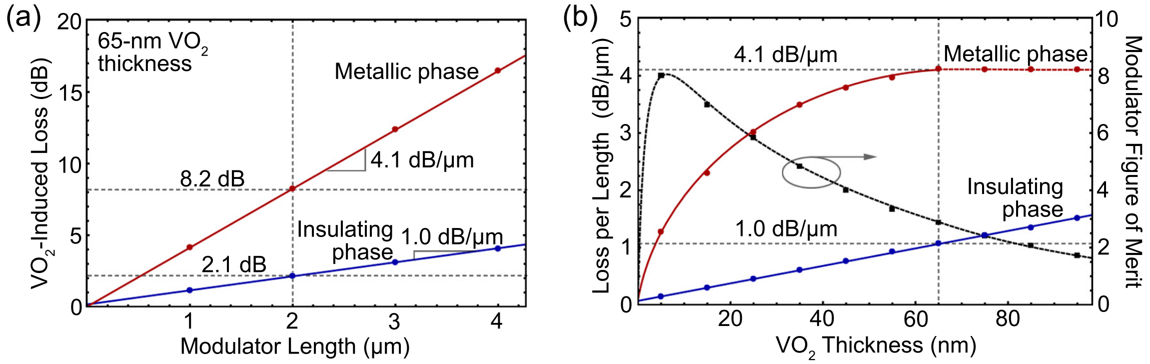

Figure 5.9. Calculated VO$_2$-induced transmission loss in waveguide devices as a function of VO$_2$ tab geometry, calculated using full-field FDTD simulations. The points are calculated values, while the curves are plotted as guides for the eye. (a) The TE-mode loss induced by a 65-nm thick VO$_2$ tab scales linearly with tab length for both phases of VO$_2$, and the predicted losses for a 2-μm tab are within 5% of the measured values. (b) The colored curves show the calculated loss per unit length as a function of VO$_2$ film thickness for each phase, while the dashed black curve is the modulator figure of merit, defined as the ratio of the modulation depth to the insertion loss.

is 8.2 dB, which agrees to within 5% of the measured values for both phases of VO$_2$.

In Fig. 5.9(b), we show the calculated losses for a modulator layer of varying thickness. For VO$_2$ in its insulating phase, the loss per unit length scales linearly with VO$_2$ thickness, due to the increasing modal overlap of the fundamental TE mode with the VO$_2$ layer. For the metallic phase, the enhanced absorption leads to a sharp increase in loss versus thickness for thin VO$_2$ layers, but the loss saturates since the mode extends a limited distance into the layer. We find that the experimental thickness of 65 nm is almost exactly at the point where the metallic VO$_2$ layer completely extinguishes the mode on the topside of the modulator. Also plotted is the previously defined modulator FOM as a function of thickness, where we see the largest ratio of modulation depth to insulating-phase loss for very thin VO$_2$ layers. For example, it is predicted that an 8 μm-long modulator composed of a 5-nm thick VO$_2$ film would exhibit 15.0 dB loss in the metallic state and just 1.6 dB in the insulating state. It is difficult to produce continuous films of VO$_2$ with such small layer thicknesses by PLD, as shown by Suh, *et al.* [119]; however, our films were observed to be continuous thicknesses as small as 50 nm and could likely be made somewhat thinner.

In the absence of clear loss measurements for the TM-polarized mode supported by our Si waveguides, we used FDTD to predict TM-mode modulator performance. The TM mode exhibits increased modal overlap with the VO_2 cladding since it is less confined in the Si layer, suggesting enhanced sensitivity to VO_2 index. Indeed, we calculate 16.8 dB loss for the experimental VO_2 tab geometry when the VO_2 is in its metallic state; however, the insulating-state loss is even further enhanced, resulting in 5.4 dB insertion loss. The corresponding modulator FOM is just 2.1, approximately two-thirds of the TE-mode FOM.

5.5 Prospects for VO_2-Based Silicon Photonic Devices

We have demonstrated a compact VO_2-based waveguide absorption modulator operating at wavelengths near 1550 nm as a potential component for future integrated optical circuits. While large-diameter ring resonators were used to accurately probe modulator loss, we show that in-line modulator devices need only be a few microns long, due to a measured 16-fold increase in material absorption at the VO_2 insulator-to-metal phase transition. By directly heating an integrated 2-μm device, we measured a single-pass loss of 2 dB at 30 °C, where VO_2 is in its insulating phase, and 8.6 dB at 100 °C, where VO_2 has transformed to its metallic phase, corresponding to a 78% decrease in transmission. We note that, as confirmed by electromagnetic simulations, simply extending the device length to 5 μm would result in modulation in excess of 16 dB, which is competitive with MZI and electro-absorption modulators. Devices of this geometry could not be quantitatively characterized with the ring-resonator test bed used here, as the large metallic-phase VO_2 loss almost completely extinguishes the cavity resonances; however, we envision that future devices will utilize more localized means to induce the phase transition, eliminating the need for a resonator as an accurate probe of modulation.

Since the VO_2 phase transition can also be induced athermally, future devices can potentially use local optical or electrical stimulus to not only induce the dramatic shift in absorption observed in this work, but do so on extremely short time scales. In particular, using waveguide-integrated devices similar to those presented here, work is ongoing to employ tunable-wavelength ultrafast pulsed laser excitation to switch compact VO_2 tabs of varying size. These devices consist of straight probe waveguides so that time-resolved measurements will not be impeded by the cavity lifetime of a ring resonator, but will be limited by detection speed. Time- and wavelength-resolved studies of optical switching on a waveguide platform has the potential to not only supply insight for future all-optical modulator devices but also provide an integrated testbed for characterizing ultrafast optical properties that are of interest from a fundamental scientific perspective.

Chapter 6

Efficient Coupling to Propagating Surface-Plasmon Modes

In this chapter, we demonstrate a silicon-waveguide-based platform for efficiently coupling light into and out of guided plasmonic modes supported at the surface of a metal film. The potential of plasmonic devices for on-chip telecommunication applications and signal processing has generated increasing interest in recent years [125, 126]. Since they can be excited at optical frequencies, propagating surface plasmon polaritons are capable of supporting higher bandwidths than electrical signals carried by conventional metal wires. Furthermore, in contrast to dielectric waveguides, plasmonic devices confine light to a surface, which can enhance interactions with matter for sensing [127] and light emission applications [128, 129] and allows for device dimensions below the diffraction limit [37, 130]. Finally, the ability to transmit light and electricity in the same component simultaneously opens up interesting possibilities for hybrid electrical-optical integration [126], and might also allow for optical devices with new functionalities. For example, an in-line optical power monitor has been recently demonstrated that measures changes in the temperature-dependent electrical resistivity of a metallic element, which can be correlated with the amount of power propagating in a plasmonic mode at the element's surface [131].

Due to absorption in the metal, guided-wave plasmonic devices suffer from substantial attenuation. Plasmonic waveguides with integrated gain media have recently been shown to exhibit reduced loss at telecommunication wavelengths [132, 133] and net gain closer to visible wavelengths [134, 135]. However, the impact of signal propagation loss on cm^2-scale integrated photonic chips can also be minimized by using an architecture featuring short plasmonic waveguides coupled to longer dielectric waveguides. This design approach significantly reduces overall chip-level waveguide losses relative to all-plasmonic networks, but the development of low-loss transitions between plasmonic and dielectric waveguides becomes critical. Here, we report on low insertion loss for polymer-on-gold dielectric-loaded plasmonic waveguides end-coupled to silicon-on-insulator waveguides, with a coupling efficiency of $79 \pm 2\%$ per photonic-plasmonic waveguide transition at telecommunication wavelengths. We also demonstrate efficient coupling to resonances in plasmonic ring cavities with an average intrinsic quality factor of 180 ± 8.

6.1 Propagating Surface Plasmon Polaritons

Plasmonics encompasses the application of propagating surface-plasmon polaritons and localized surface plasmon resonances to create structures exhibiting optical properties not observed with conventional dielectric components. Fundamentally, surface plasmons arise due to the coupling of a photon field to free-electron oscillations near the surface of a metal, or any other material with a sufficiently high concentration of free-carriers [136, 137]. Bulk plasmons are collective electron oscillations characterized by a distinct plasma frequency that depends on the electronic potential-energy landscape and dielectric environment. In a thin metal film, the plasma frequency can be modified by the presence of a non-absorbing dielectric near the film's surface, resulting in a somewhat lower *surface* plasma frequency [138]. Unlike bulk plasmons, surface plasmon polaritons (SPPs) can be excited at energies below the plasma frequency, where free electrons near the surface oscillate at the photon frequency but also modify the photon's dispersion characteristics.

Armed with accurate empirical values of the complex refractive index of a metal, Maxwell's equations can be solved to determine the field distribution and dispersion properties of SPP modes supported at a metal-dielectric interface. Consider the dielectric material to be medium 1, with dielectric constant $\epsilon_1/\epsilon_0 = {\epsilon_1}' = {n_1}^2$, and the metal to be medium 2, with dielectric constant $\epsilon_2/\epsilon_0 = {\epsilon_2}' + i{\epsilon_2}''$. The complex dielectric constant in the metal is expressed in terms of the complex index, $n_2 + i\kappa_2$, by the relations ${\epsilon_2}' = {n_2}^2 - {\kappa_2}^2$ and ${\epsilon_2}'' = 2n_2\kappa_2$. For the geometry shown in Fig. 6.1, and assuming monochromatic light with frequency ω propagating in the x-direction, we expect bound modes to have a magnetic field

$$\mathbf{H}(\mathbf{r}) = \mathbf{H}(z)e^{i\beta x} \ , \tag{6.1}$$

where β is the propagation constant. In order to satisfy the Helmholtz equation,

$$\frac{d^2\mathbf{H}}{dz^2} + \left(\frac{\epsilon(z)}{\epsilon_0}\frac{\omega^2}{c^2} - \beta^2\right)\mathbf{H}(z) = 0 \ , \tag{6.2}$$

but also have a solution that decays to zero far from the interface, we assume TM-mode solutions of the form

$$\mathbf{H}(z) = \begin{cases} A_1 e^{-k_{1z}z}\ \hat{\mathbf{y}} & \text{, for } z > 0 \\ A_2 e^{k_{2z}z}\ \hat{\mathbf{y}} & \text{, for } z < 0 \ . \end{cases} \tag{6.3}$$

By imposing continuity of the magnetic field at $z = 0$, we get $A_1 = A_2 = A$. We can find the electric field by the relation $\mathbf{E}(\mathbf{r}) = \frac{i}{\omega\epsilon(\mathbf{r})}\nabla \times \mathbf{H}(\mathbf{r})$, which yields

$$\mathbf{E}(z) = \begin{cases} \frac{A}{\epsilon_1\omega}e^{-k_{1z}z}(ik_{1z}\ \hat{\mathbf{x}} - \beta\ \hat{\mathbf{z}}) & \text{, for } z > 0 \\ -\frac{A}{\epsilon_2\omega}e^{k_{2z}z}(ik_{2z}\ \hat{\mathbf{x}} + \beta\ \hat{\mathbf{z}}) & \text{, for } z < 0 \ . \end{cases} \tag{6.4}$$

By imposing continuity of the in-plane component of the electric field, we obtain

$$\frac{k_{1z}}{\epsilon_1} = -\frac{k_{2z}}{\epsilon_2} \ , \tag{6.5}$$

and, by applying Eq. 6.2 in medium j, we find $k_{jz}^2 = \beta^2 - k^2\epsilon_j/\epsilon_0$,[†] where $k = \omega/c$.

[†] Unlike the previously considered solutions to the wave equation for dielectric waveguides, where $k_{jz}^2 = k^2\epsilon_j/\epsilon_0 - \beta^2$ only in the waveguiding layer, the momentum of a bound SPP mode is larger than the that of light freely propagating in either medium, analogous to a waveguide of zero thickness.

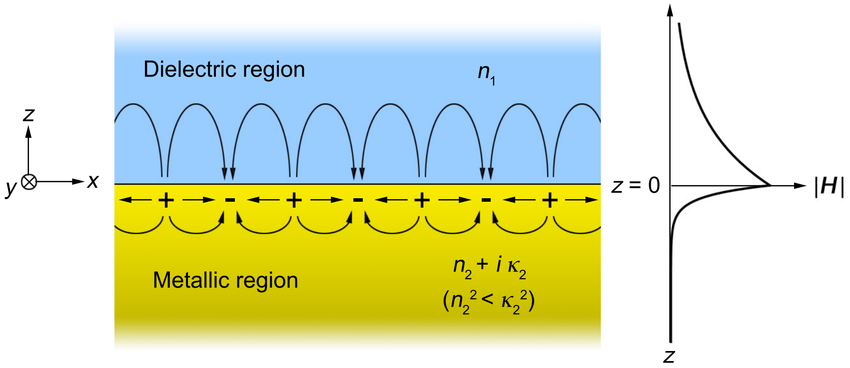

Figure 6.1. Layout of a single metal-dielectric interface supporting a TM-polarized propagating surface plasmon mode. Assuming the mode propagates in the x-direction, the magnetic field, $\mathbf{H}(z)$, is oriented along the y-direction and decays away exponentially from the interface in both regions.

By combining these results, we obtain the SPP dispersion relation:

$$\beta^2 = \frac{k^2}{\epsilon_0}\left(\frac{\epsilon_1\epsilon_2}{\epsilon_1+\epsilon_2}\right) \ . \tag{6.6}$$

We note that there can only be guided TM modes since TE modes have the boundary condition that the electric field *and* its first derivative must be continuous at the conductor-dielectric interface. Slope continuity is impossible to reconcile with the requirement that we have a solution that decays away exponentially on both sides of the interface.

From Eq. 6.6 we see that, because k_{jz} must be real for $j = 1, 2$ in order to have a guided mode, the real part of the dielectric constants in each medium need to have opposite sign. Since we assume that medium 1 is a non-absorbing dielectric with a positive real dielectric constant, medium 2 must have metallic optical properties with ${\kappa_2}^2 > {n_2}^2$, so that ${\epsilon_2}' = {n_2}^2 - {\kappa_2}^2 < 0$. When ${n_1}^2 = {\kappa_2}^2 - {n_2}^2$, we see that β diverges, which is characteristic of the surface plasma frequency.[‡] For typical metals [139, 140], the surface plasma frequency is in the visible or ultraviolet part of the spectrum when n_1 is relatively small (i.e. $n_1 \leq 2$). Consequently, we can expect to find guided SPP modes at longer near-infrared wavelengths. However, for real metals with $n_2 \neq 0$,

---

[‡] In real metals, damping of the oscillating free carriers prevents the propagation constant from diverging to ∞ [36].

SPP modes exhibit significant loss because κ_2 is large.

In this work, we are interested in coupling light into SPP modes at telecommunications wavelengths. We chose to use gold as the metal layer because it can be deposited as a high-quality, corrosion-resistant thin film using evaporation techniques and it exhibits relatively low SPP losses near $\lambda = 1550$ nm when $n_1 \sim 1.5$. From the complex index of gold measured by Johnson and Christy [139] and $n_1 = 1.5$, the condition ${n_1}^2 \approx {\kappa_{\mathrm{Au}}}^2 - {n_{\mathrm{Au}}}^2$ is met at a free-space wavelength of $\lambda \approx 500$ nm. At longer wavelengths, Eq. 6.6 can be used to find the complex propagation constant, which is related to the complex effective mode index as $n_{\mathrm{eff}} = \beta/k$. The $1/e$ decay length in the propagation direction is identified as the SPP propagation length, given by $L_{\mathrm{SPP}} = 1/(2\ \mathrm{Im}[\beta]) = \lambda/(4\pi\ \mathrm{Im}[n_{\mathrm{eff}}])$.

For the example of a gold-dielectric interface, we have $n_{\mathrm{Au}} = 0.515$ and $\kappa_{\mathrm{Au}} = 10.737$ at a free-space wavelength $\lambda = 1550$ nm. Assuming $n_1 = 1.5$, there is a SPP mode with $\mathrm{Re}[n_{\mathrm{eff}}] = 1.515 > n_1$, indicating that the mode is indeed guided, and $L_{\mathrm{SPP}} = 85.7\ \mu$m. While this characteristic SPP propagation length, which is typical of metal-dielectric SPP modes in the near infrared, is extremely short compared to the loss in dielectric waveguide modes, it can be a price worth paying in applications requiring strong field enhancement at a surface and/or the ability to propagate both light and electricity in a single element. In addition, overall loss can be reduced by designing compact devices with high in-coupling efficiency, as will be shown in the following sections.

6.2 Integrating Plasmonics with Silicon Photonics

Since the SOI photonics platform is emerging as the standard technology for optical systems on a chip, the viability of plasmonic components may depend as much on how easily the components can be integrated with silicon waveguides as it does on the functionality of the components themselves. Researchers have recently demonstrated important optical components on SOI, including lasers [25] and photodetectors [27] operating near $\lambda = 1550$ nm. Thus, while the tremendous potential of all-plasmonic circuitry has been touted, integration with SOI can facilitate the realization of plasmonic devices that take advantage of components already developed for silicon photonics, such as waveguide-integrated lasers [25] and photodetectors [27] operating near $\lambda = 1550$ nm. Furthermore, SOI waveguides can serve as low-loss interconnects for moving light between miniaturized plasmonic devices, minimizing overall on-chip losses.

Plasmonic waveguides have been previously demonstrated on SOI with lateral confinement achieved by patterning a metal film, and coupling efficiencies between 30 to 40% per transition were observed [141, 142, 143]. Metal slot waveguides have also been fabricated using Si wires as a mold for defining the waveguide shape [144, 145], and coupling efficiencies as high as 56% have been reported for devices supporting a single plasmonic mode. However, in all cases, these metal strip and slot waveguide designs have exhibited plasmon propagation lengths of less than 6 μm, limiting their utility in resonators and other interferometric devices. Very recently, Delacour *et al.* reported directional coupling to metal slot waveguides with predicted efficiencies comparable to those reported here; however, the exact efficiency is uncertain since the loss due to coupling and propagation were not measured independently [146].

6.3 SOI-Integrated Dielectric-Loaded SPP Waveguides

In contrast to patterned metal structures that often include fabrication-induced roughness, dielectric-loaded surface plasmon polariton (DLSPP) waveguides confine surface plasmons laterally using a dielectric wire patterned on a flat metal film. Typical absorption-limited plasmon propagation lengths for DLSPP waveguides are on the order of 10 to 100 μm for $\lambda \sim 1550$ nm [147, 148]. As optical components, DLSPP waveguides exhibit low enough propagation loss to be implemented in devices that require coherent propagation over many microns, such as ring resonators [39, 149] and Bragg gratings [150]. Furthermore, for operation at telecommunication wavelengths, DLSPP devices can be fabricated using standard lithography processes, as opposed to, for example, V-groove plasmonic waveguides that can have similarly low losses but

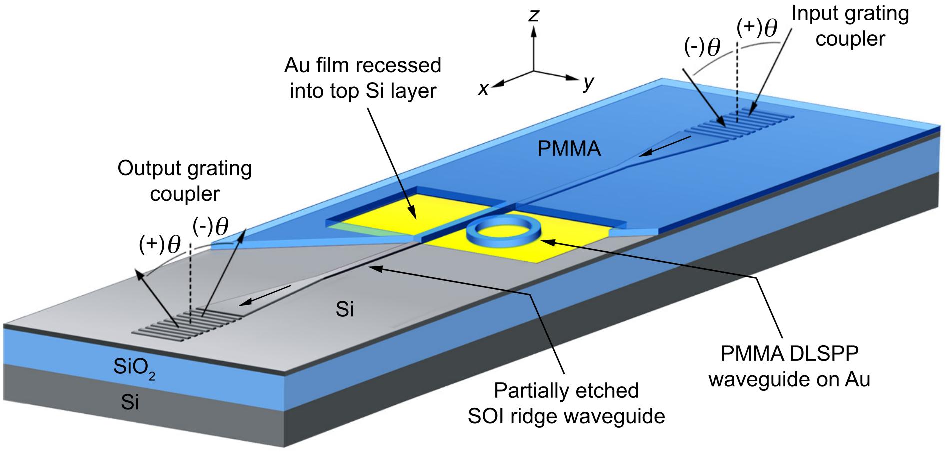

Figure 6.2. Schematic of a SOI-integrated dielectric-loaded SPP waveguide and ring resonator (not to scale). For clarity, the PMMA layer, which acts as both the dielectric load and a cover for the SOI waveguides, is shown partially removed from the output SOI waveguide.

require advanced focused ion-beam fabrication [151]. To date, conventional methods for coupling light into DLSPP waveguides have employed external laser sources with off-chip optics (e.g., using the Kretschmann-Raether configuration [137]), which limits miniaturization at the system level. In a significant step toward integration with telecommunication technology, Gosciniak, *et al.* recently demonstrated in- and out-coupling of light guided by DLSPP waveguides using single-mode optical fibers [152], similar to schemes used to couple to weakly confined long-range surface plasmons [153]. However, there remains a need for integration of DLSPP waveguides on a photonics platform compatible with on-chip light sources and detectors.

Here, we demonstrate DLSPP waveguides and ring resonators composed of polymethylmethacrylate (PMMA) patterned on gold, which are integrated with low-loss SOI photonic circuits, as shown schematically in Fig. 6.2. While we employ silicon diffraction gratings to interface the plasmonic devices with an external laser source and detector, we point out that, by utilizing SOI input/output waveguides, the devices demonstrated here are automatically compatible with SOI-integrated on-chip sources and detectors. Furthermore, the DLSPP-waveguide design can be implemented in a low-temperature back-end wafer process.

We first analyze the transmission through SOI-waveguide-coupled DLSPP waveguides of varying length and find that the DLSPP transmission decreases exponentially with a decay length of 51 ± 4 μm at $\lambda = 1550$ nm. This propagation length is reproducible at multiple grating coupling angles and wavelengths and is consistent with modal effective index calculations. Accounting for propagation loss, the coupling loss is found to be 1.0 ± 0.1 dB per transition between the SOI and DLSPP waveguides, in close agreement with full-field electromagnetic finite-difference time-domain (FDTD) simulations for the fabricated waveguide dimensions. Finally, we analyze the spectral response of 10-μm diameter DLSPP ring resonators and find an average intrinsic resonator quality factor of 180 ± 8 near $\lambda = 1524$ nm, where the resonator propagation length is limited by bending loss in the curved waveguide geometry.

6.3.1 Aligned Photonic-Plasmonic Waveguide Fabrication

SOI-waveguide-coupled DLSPP structures were fabricated on SOI wafer pieces with a lightly doped p-type ($\sim 10^{15}$ cm^{-3}) 220-nm silicon device layer on a 2-μm BOX layer. Arrays of 100-μm wide Au pads of varying length, L, were defined by electron-beam lithography using PMMA resist (MicroChem), where the polymer was used both as a mask for plasma etching of the top silicon layer and as a lift-off layer for metallization. We employed a cryogenic SF_6/O_2 etching process to achieve high etch selectivity of silicon over SiO_2, where the BOX layer functions as an etch stop (see Appendix A). A 5-nm titanium adhesion layer and an 80-nm gold layer were deposited into the etched regions by electron-beam evaporation, as shown in Fig. 6.3. This gold film is thick enough to eliminate coupling of surface plasmons on the top surface into radiation modes in the underlying BOX layer [154]. In addition, since titanium absorbs more strongly than gold near $\lambda = 1550$ nm [140], the adhesion layer extinguishes unwanted surface plasmons on the bottom surface of the metal. The silicon etch also consumed approximately 10 nm of the BOX layer, so that the top surface of the gold was recessed a depth $d_{\text{offset}} = 145$ nm below the surrounding silicon without additional etching of the SiO_2. We also fabricated samples using buffered HF to remove approximately 150 nm of additional SiO_2 from the BOX layer prior to metallization, resulting in a vertical silicon-gold offset close to $d_{\text{offset}} = 300$ nm.

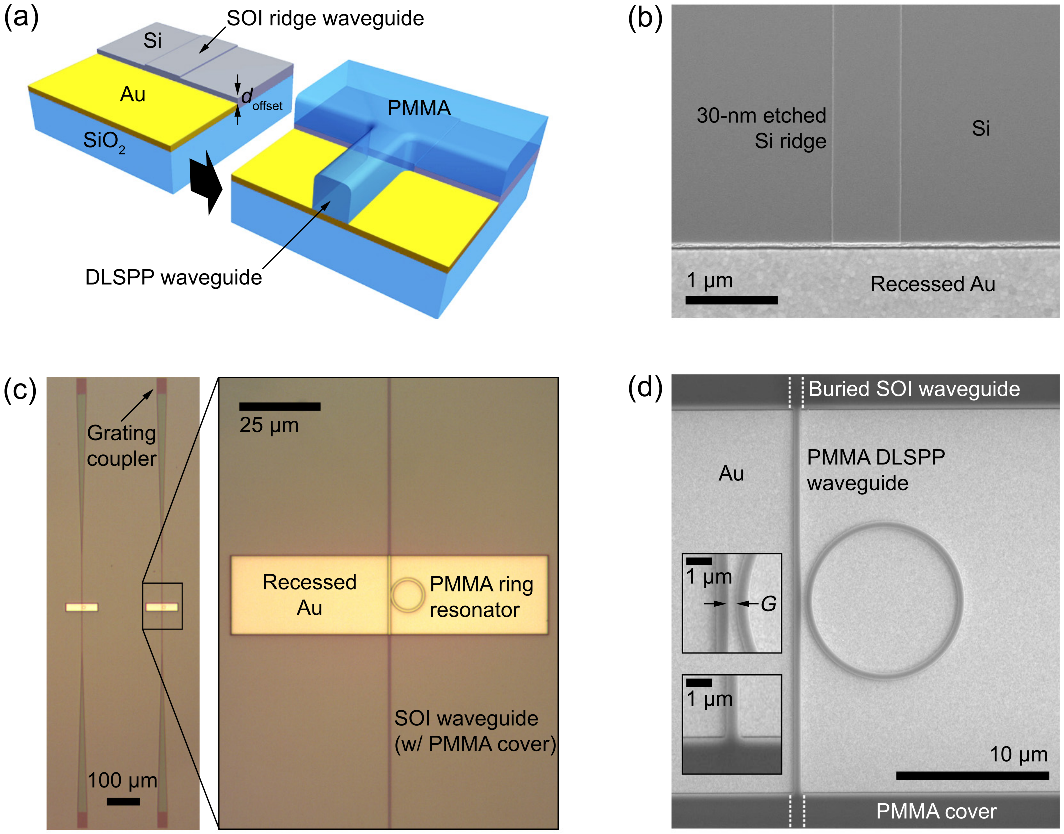

Figure 6.3. Fabricated DLSPP waveguide and ring resonator devices end-coupled to SOI ridge waveguides. (a) Scale representation of the coupling region between end-coupled SOI and DLSPP waveguides before and after spinning and patterning of the PMMA cover layer. (b) Scanning electron micrograph of an etched silicon ridge waveguide at the boundary of a recessed gold pad before coating with PMMA. (c) Optical micrographs of completed SOI-waveguide-coupled DLSPP devices. (d) Scanning electron micrograph of a DLSPP waveguide and ring resonator (coupling gap $G = 300$ nm) with buried SOI input/output waveguides.

Ridge waveguides were patterned on the silicon surrounding the gold pads using ma-N 2403 negative-tone electron-beam resist (Micro Resist Technology), and the exposed silicon was partially etched to a depth of 30 nm with by C_4F_8/O_2 plasma etching. The SOI waveguides were fabricated with a ridge width of 740 nm, as shown in Fig. 6.3(b), so that only the fundamental TE and TM modes are supported at the wavelengths of interest in this work. The waveguide dimensions were also chosen to fulfill the magic-width condition to minimize leakage loss from the TM mode [44]. To couple light into and out of the SOI waveguides, we defined symmetrical pairs of 30-μm wide, 50-μm long etched diffraction gratings with a 650-nm grating pitch, connected to the waveguides via 500 μm linear tapers.

The surface of the samples were coated with 560 nm of PMMA, cured for 5 min at 180 °C, and patterned to define single-mode, 500-nm wide DLSPP waveguide straights on the gold pads end-coupled to the SOI waveguides, as shown schematically in Fig. 6.3(a). The 500×560-nm DLSPP waveguide cross section supports only the fundamental TM_{00} plasmonic mode, with near-optimal modal confinement at $\lambda = 1550$ nm [133, 147, 154]. Devices were also fabricated with 10-μm diameter PMMA rings patterned alongside the straight DLSPP waveguides with a variable edge-to-edge separation gap, G. The PMMA was left on top of the SOI waveguides to serve as a dielectric cover. Micrographs of completed SOI and DLSPP waveguides are shown in Fig. 6.3(c) and (d).

6.3.2 Verifying the Fabricated Waveguide Geometry

The geometries of the SOI and DLSPP waveguides were verified using atomic-force microscopy (AFM). The AFM image in Fig. 6.4(a) shows the topography of an etched SOI ridge waveguide. A cross section from the image indicates that the waveguide width is close to the lithographically defined dimension of 740 nm, and the etch depth is 30 nm. Figure 6.4(b) shows the topography of a PMMA wire on Au from one of the SOI-waveguide-coupled DLSPP devices. The PMMA wire is nearly 500 nm wide at its top surface and approximately 560 nm tall. The AFM images of both the SOI and DLSPP waveguides were collected in non-contact mode, and the scanning parameters had to be carefully optimized to avoid damaging the soft, high aspect-ratio PMMA wires. Even so, the DLSPP waveguide scan shows edge roughness that was not clearly visible in electron microscope images, suggesting that the AFM tip slightly deformed the polymer. Nevertheless, the DLSPP waveguide geometry represented in Fig. 6.4(b) is consistent with measurements from electron micrographs of the patterned structures as well as film thickness measurements of unpatterned PMMA layers.

To obtain accurate measurements of the fabricated dimensions of the devices at the SOI-DLSPP coupling region, we used further AFM analysis to determine the topography of the spin-coated PMMA at the silicon-gold interfaces. An essential feature of our waveguide design is the vertical offset of between the silicon waveguiding layer and the gold surface that supports the DLSPP mode; however, this leads to varying topography on the top surface of the spin-coated PMMA layer. The scanning electron micrograph in Fig. 6.4(c) shows a recessed Au region on an SOI sample without a PMMA cover layer. The actual width of the recessed area is very close to the lithographically defined dimension of 20 μm. The contact-mode AFM image shows a feature fabricated in the same manner that has been subsequently coated with PMMA and baked at 180 °C for 5 min. We observe that the polymer conforms to the topography of the recessed structure (vertical offset $d_{\text{offset}} \approx 300$ nm), leading to a uniform height along the entire 20-μm wide recessed Au region. Furthermore, the vertical offset in the PMMA layer across the silicon-gold interface is close to the 300-nm offset between the underlying silicon and gold surfaces. From this analysis, we conclude that the PMMA uniformly covers the recessed gold, and there is an approximately 2-μm wide vertical taper in the polymer at the edges of the silicon layer, as depicted schematically in Fig. 6.4(d).

6.3.3 Calculated DLSPP Loss

Before discussing measurements of the coupling efficiency between SOI and DLSPP waveguides, we first characterize the modes supported in the DLSPP structure using electromagnetic eigenmode caculations. As with the etched SOI ridge waveguides, the modes of the laterally confined DLSPP structures cannot be found analytically, al-

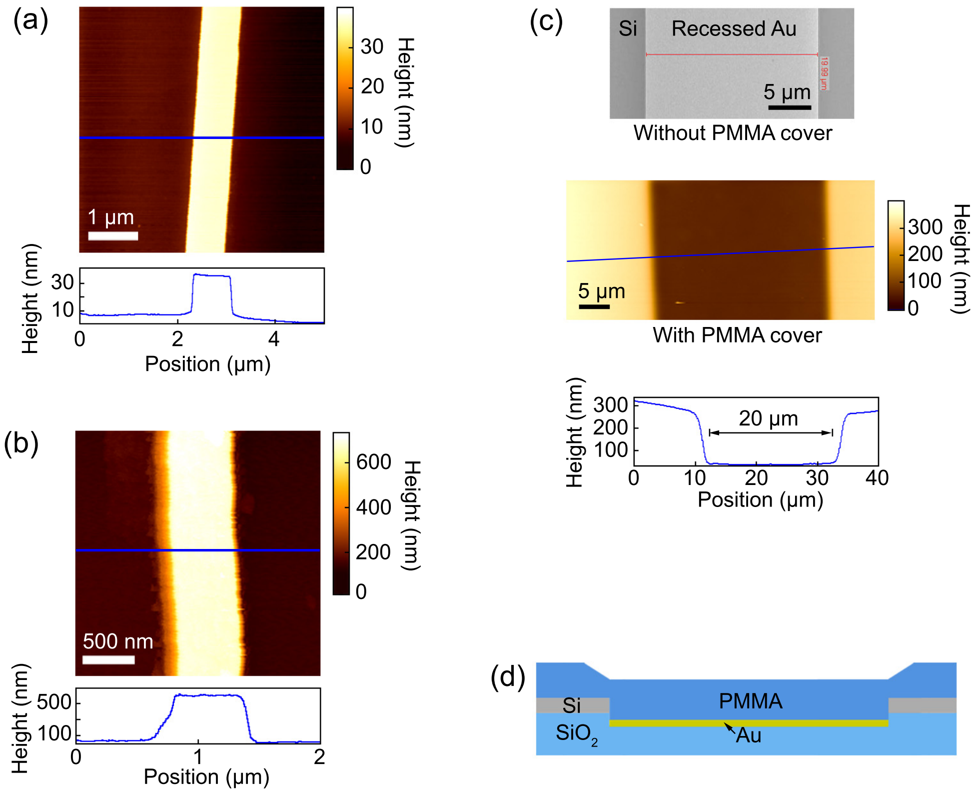

Figure 6.4. AFM analysis of fabricated SOI and DLSPP waveguides used to verify the device dimensions. (a) AFM image of an etched SOI waveguide prior to coating with PMMA. A cross-section of the topography is shown in blue. (b) AFM image of a PMMA-on-gold DLSPP waveguide. (c) Scanning electron micrograph of a 20-μm wide recessed gold feature prior to coating with PMMA. The AFM image below the electron micrograph shows the topography of a feature of identical width after being coated with PMMA. The recessed region is 20 μm wide, indicating that the polymer coats the recessed Au with a uniform thickness. (d) A schematic cross-section of the PMMA-coated feature, showing that the polymer is tapered at the edges of the silicon layer surrounding the gold region, as observed in (c).

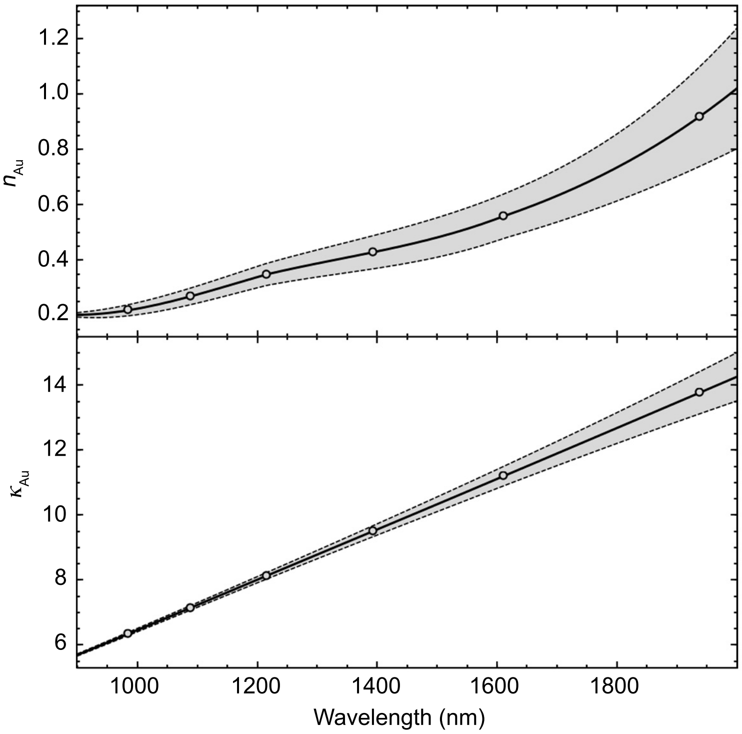

Figure 6.5. Real, n, and imaginary, κ, parts of the index of refraction of gold used in numerical calculations. The data points are from Johnson and Christy [139], and the curves are Hermite interpolations between the data points and their associated error bars.

though approximation methods have been used in the literature [147, 154]. To obtain accurate values of the complex modal index, we used the two-dimensional electromagnetic finite-element method (FEM) in COMSOL to find the modes numerically. Assuming light propagates only in the fundamental mode of the polymer-on-gold waveguide (an assumption that will be shown to be accurate near $\lambda = 1550$ nm), the theoretically predicted propagation loss is obtained from the imaginary part of the numerically calculated modal effective index. We assume an index of 1.49 for PMMA (as reported by the resist manufacturer, MicroChem) and an index of gold obtained by interpolating between the values measured by Johnson and Christy [139]. To obtain a continuous function for the real and imaginary parts of the index of gold, we fit Hermite interpolation functions between the measured data points as well as between the reported error bars, as plotted in Fig. 6.5.

In Fig. 6.6(a), we show the real part of the effective index for the modes supported by a DLSPP waveguide with the fabricated dimensions. A TE-polarized dielectric mode is supported by the polymer wire for wavelengths shorter than $\lambda = 1300$ nm, but the structure supports only the fundamental TM plasmonic mode for the wavelength range of interest in this work. As with the SPP mode supported at an infinite metal-dielectric interface, the DLSPP mode decays exponentially away from the surface in the vertical direction.

For wavelengths between $\lambda = 1500$ and 1600 nm, Fig. 6.6(b) shows the real part of the calculated DLSPP modal effective index and the propagation loss per length, given by $\alpha_{\text{prop}} = 1/L_{\text{SPP}} = 4\pi\ \text{Im}[n_{\text{eff}}]/\lambda$. In addition to the nominal effective index and loss, we show the range of calculated values corresponding to the uncertainty in the gold index reported by Johnson and Christy. While the uncertainty in the gold index does not lead to a significant spread in the calculated real effective index values, the modal loss is more sensitive. For $\lambda = 1500$ to 1600 nm, the modal effective index varies approximately linearly with a slope of $-0.27\ \mu\text{m}^{-1}$. The modal group index is calculated according to $n_{\text{g}}(\lambda) = n_{\text{eff}}(\lambda) - \lambda(\partial n_{\text{eff}}/\partial\lambda)$, which gives a value of $n_{\text{g}} \approx 1.6$ for this wavelength range.

6.4 Characterizing SOI-DLSPP Waveguide Loss

We experimentally determined the plasmon propagation loss on a sample with a silicon-gold vertical offset of $d_{\text{offset}} = 300$ nm by measuring the transmission through devices with DLSPP sections of varying length. The transmission for each device was normalized to the average transmission through a set of SOI reference waveguides that were patterned on the same sample and tested under the same coupling conditions. To probe a particular device with the setup described in Section 3.2, the swept laser source was focused onto the devices SOI input grating using a lensed fiber focuser at an angle θ relative to the sample surface normal. Light was collected by the focuser positioned above the output grating at the same angle, and the overall device transmission was measured with either the calibrated power meter or, for spectrally resolved measurements, the high-speed photoreceiver. As for previous devices, the

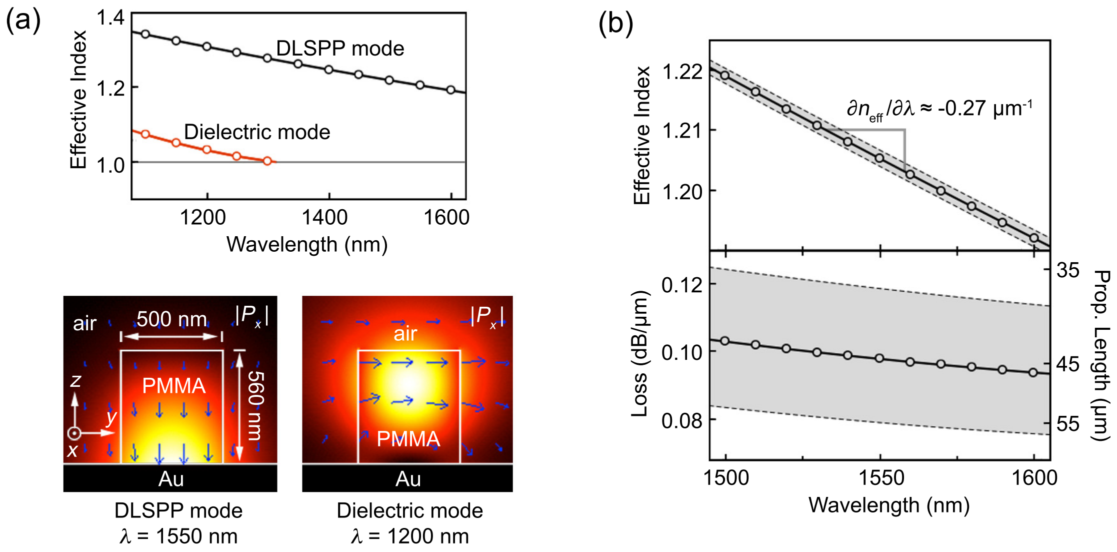

Figure 6.6. Calculated effective modal index and propagation loss for a DLSPP waveguide with the fabricated dimensions. (a) As seen in the modal dispersion, a TE-polarized dielectric mode is supported at wavelengths shorter than $\lambda \approx 1300$ nm, but only the fundamental TM-polarized DLSPP mode is supported at longer wavelengths. The density plots show the power in the propagation direction for each mode at the indicated wavelength, while the arrows represent the intensity and orientation of the transverse component of the electric field. (b) Dispersion of the DLSPP mode over the wavelength range of interest in this work, where the loss is obtained from the imaginary part of the modal effective index. The gray bands represent the range of predicted values resulting from the uncertainty in the refractive index of gold.

silicon gratings were designed to selectively couple light from free space to the forward-propagating fundamental TM mode of the SOI waveguides at $\theta \sim -30^\circ$ and to the forward-propagating TE mode at $\theta \sim 30^\circ$ within the wavelength range of the laser, although the coupling angle had to be adjusted slightly to correct for the effect of the PMMA covering the gratings.

To couple light into the TM-polarized DLSPP mode, we excited the TM SOI-waveguide mode near $\theta = -30^\circ$ and adjusted the polarization controller on the input fiber to maximize transmission. Because the SOI gratings exhibit a limited bandwidth of approximately 25 nm, we made additional adjustments to the coupling angle to achieve maximum transmission at different wavelengths within the tuning range of the laser source. At a coupling angle of $\theta = -26.5^\circ$, which was found to correspond to maximum transmission at $\lambda =$1550 nm, we measured the transmission through ten devices with DLSPP sections varying in length from $L = 10$ to 50 μm, with two nominally identical devices of each length. The transmission is plotted as a function of device length in the right panel of Fig. 6.7, where the transmission values are normalized to the average transmission through a set of three reference waveguides with no DLSPP section. For a laser power of 1 mW at the input fiber, we measured an average transmitted power of 24.6 ± 2.2 μW at $\lambda = 1550$ nm for the reference devices, where the loss is assumed to be due predominantly to the lensed fibers and grating couplers. By normalizing the DLSPP transmission by this value, we account for the expected fiber and grating-coupling loss in the SOI-DLSPP devices. In Fig. 6.7, the standard deviation of the average reference device transmission gives rise to the error bars for the normalized DLSPP-waveguide transmission values.

The transmission through the DLSPP waveguides decreases exponentially with increasing device length with a fitted propagation length of $L_{\mathrm{SPP}} = 51 \pm 4$ μm. Extrapolating to a DLSPP waveguide length of $L = 0$, we find a total coupling loss of 2.0±0.2 dB relative to the reference devices, or 1.0±0.1 dB per SOI-DLSPP waveguide transition, where the uncertainty arises from the fit to the measured transmission values. We repeated the transmission measurements on the same devices at $\lambda =$ 1520 nm for a grating coupling angle of $\theta = -22.5^\circ$, as shown in the left panel of

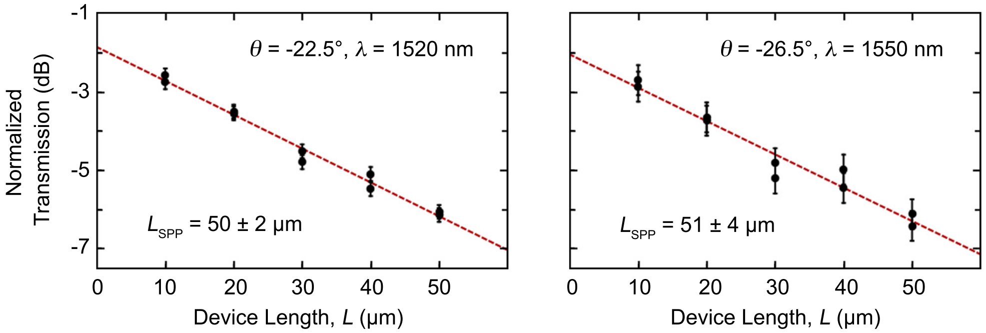

Figure 6.7. Measured TM-mode transmission through ten SOI-waveguide-coupled devices with DL-SPP sections of varying length, L, (two devices of each length) normalized to the average transmission through a set of three SOI reference devices. The error bars represent the uncertainty in the reference device measurements. The left panel shows the transmission at a grating coupling angle of $\theta = -22.5°$, corresponding to maximum transmission at $\lambda = 1520$ nm, while the right panel shows the transmission at $\lambda = 1550$ nm and a coupling angle of $\theta = -26.5°$. By extrapolating to a device length of $L = 0$, the total coupling loss at $\lambda = 1550$ nm is 2.0 ± 0.2 dB, or 1.0 ± 0.1 dB per SOI-DLSPP transition.

Fig. 6.7. We observe small differences in the relative transmission of some of the devices, but we find values for the propagation length and coupling loss that fall within the uncertainty of the values measured at $\lambda = 1550$ nm. This demonstrates that the measured coupling efficiency is reproducible despite inevitable variations in optical alignment between measurements. Furthermore, we note that the propagation length of $L_{\text{SPP}} \approx 50$ μm falls within the range predicted by the FEM calculations.

6.4.1 Verifying Transmission Exclusively via the DLSPP Mode

We also performed transmission measurements on devices from a second sample, also with a silicon-gold offset of $d_{\text{offset}} = 300$ nm, that was fabricated simultaneously with the previously characterized sample except that the final PMMA coating step was excluded. Without a PMMA dielectric load, light can only couple from the input SOI waveguide to the output via radiation modes or surface plasmons propagating along the gold-air interface. While we expect coupling to these modes, we also expect the power to disperse radially from the end of the SOI input waveguide and therefore not couple significantly into the SOI output waveguide. Indeed, the lowest loss we measured relative to the SOI reference waveguides was 17.4 ± 0.4 dB for a device with just a 10-μm long gold section, which is nearly six times greater loss than measured for DLSPP waveguides of the same length. Transmission via radiation and gold-air plasmon modes is likely even lower for DLSPP waveguide devices since coupling to those modes is impeded by the polymer wire. This finding supports the assumption that, for the DLSPP devices, light is transmitted to the SOI output waveguide almost exclusively through the single DLSPP mode.

In the top panel of Fig. 6.8, we show transmission spectra for one of the SOI reference waveguides as well as for DLSPP waveguides of each fabricated length, where light was coupled from the laser source into the TM-polarized SOI-waveguide mode. Other than the spectral lineshape characteristic of the SOI gratings, the DLSPP devices do not exhibit strong wavelength-dependent behavior over the wavelength range of interest. In the lower panel of Fig. 6.8, we show the spectral response of the same reference waveguide when light was coupled into the TE-polarized SOI-waveguide mode at a grating coupling angle $\theta = +26°$. Despite the higher transmission in SOI reference waveguides for the TE configuration due to greater grating efficiency for that polarization, we observed very little transmission through even the shortest DLSPP devices. Compared with a measured reference device transmission of 30.1 μW at $\lambda = 1550$ nm, we measured less than 50 nW of transmitted power for both DLSPP devices with $L = 10$ μm. This polarization dependence indicates that there is negligible TE-to-TM mode conversion, and it further corroborates the assertion that light traverses the gold film only in the TM-polarized DLSPP mode and not through coupling to radiation modes.

6.4.2 Comparison with SOI-Waveguide Loss

We note that measurements were also performed on 400-μm diameter SOI ring resonators patterned on the same samples as the DLSPP devices. The waveguide rings were fabricated with a cross section identical to the SOI waveguides used for coupling light into the DLSPP waveguides and were evanescently coupled to a grating-

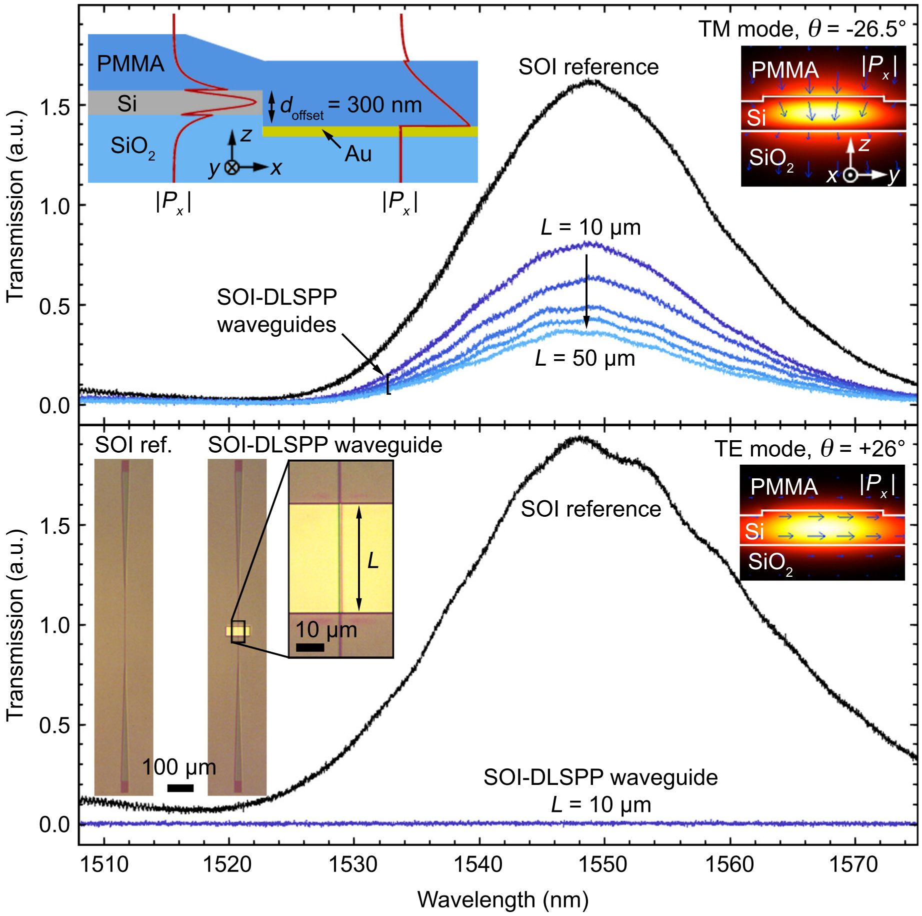

Figure 6.8. Transmission spectra for coupling from the TM SOI-waveguide mode at a grating coupling angle of $\theta = -26.5°$ (top panel) and for coupling from the TE mode at $\theta = +26°$ (lower panel). The density plots show the calculated power distribution in the SOI-waveguide modes, where the arrows represent the transverse component of the electric field. A cross-section of the SOI-DLSPP structure is depicted in the inset in the top panel, while the inset in the lower panel shows optical micrographs of a SOI reference device and a SOI-DLSPP device with $L = 40$ μm.

terminated bus waveguide across a 1-μm gap. Transmission spectra for TE- and TM-polarized modes for one such device are actually presented in Fig. 3.6 of Chapter 3 because these rings were found to have some of the highest TM-mode resonator quality factors observed with our SOI waveguide platform. Since TM-polarized SOI modes have a high field concentration at the top silicon surface, we suspect that the higher-index PMMA cover layer reduces surface scattering and, consequently, modal loss.

In any case, the SOI ring resonator measurements allowed us to verify that we could couple exclusively to the TE or TM mode for coupling angles of $\theta = +26°$ and $-26.5°$, respectively, since we observed only one characteristic free-spectral range for the ring resonances in each case. Furthermore, the resonance linewidths were used to determine the SOI-waveguide propagation loss. The intrinsic loss, independent of coupling to the bus waveguide, was found to be 3.7 dB/cm for TE modes and 5.5 dB/cm for TM modes near $\lambda = 1550$ nm. Because the waveguide width was designed to meet the magic-width criterion (with a PMMA cover) at $\lambda = 1550$ nm, the TM-mode loss was increased somewhat for different wavelengths within the laser tuning range; however, as seen in Fig. 3.6, the loss was increased by no more than a factor of 3 between $\lambda = 1530$ and 1575 nm. Ultimately, we see that the SOI-waveguide loss is approximately two orders of magnitude lower than the measured DLSPP waveguide loss, which clearly illustrates the utility of SOI-waveguide interconnects between plasmonic components.

6.4.3 Near-Field Microscopy Measurements of DLSPP Attenuation

To corroborate the surface plasmon propagation length obtained from variable-length waveguide transmission measurements, we analyzed the same DLSPP devices using near-field scanning optical microscopy (NSOM). NSOM/AFM measurements were performed with a tuning-fork based Nanonics MultiView 2000 scanning probe microscope in contact mode using a 200-nm diameter aperture probe in collection mode. Light was coupled into the SOI input waveguide of each device at a wavelength of 1520 nm using an identical lensed-fiber arrangement as used for the waveguide trans-

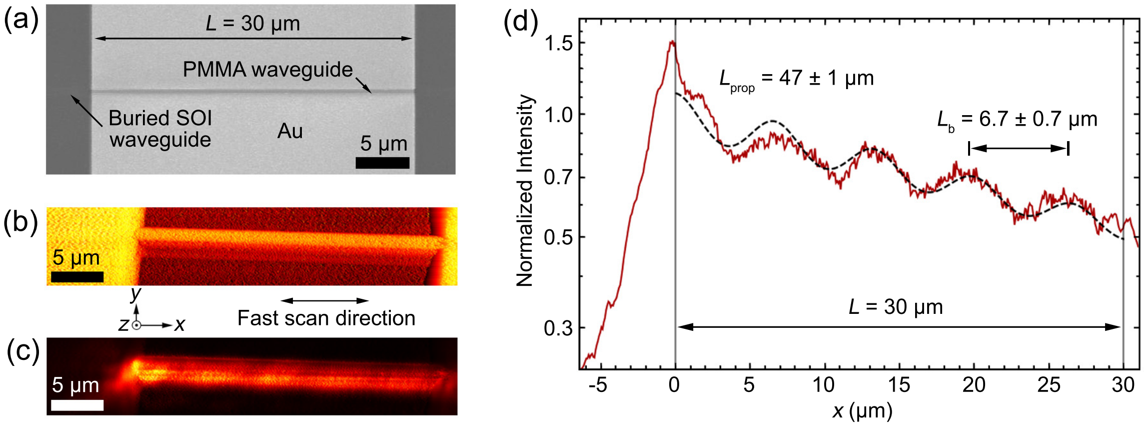

Figure 6.9. (a) Scanning electron micrograph of a 30-μm long DLSPP waveguide device. (b) AFM and (c) NSOM images collected simultaneously for a device with the same geometry, where light was coupled into the plasmonic section from a buried SOI waveguide lying to the left of the DLSPP device at $\lambda = 1520$ nm. (d) Total collected intensity from the NSOM image integrated along the y-direction as a function of position in the propagation direction. The measured intensity exhibits a characteristic decay length of 47 μm.

mission measurements, and light collected by the scanning probe was detected using an InGaAs avalanche photodiode.

An NSOM scan for one of the 30-μm long DLSPP waveguides used for transmission measurements is shown in Fig. 6.9. The AFM and NSOM images in Fig. 6.9(b) and (c) were collected simultaneously using a high gain setting for the tip deflection signal, which minimized damage to the polymer waveguide but led to a noticeable increase in the noise associated with the measured topography. Qualitatively, there is significant collected intensity only along the length of the polymer waveguide in the NSOM image, indicating that optical power is preferentially coupled into the DLSPP mode as opposed to air-Au surface plasmons, which would be expected to spread out from the sides of the waveguide. We also see reduced intensity at the surface of the PMMA covering the SOI input/output waveguides because the SOI waveguide mode is largely confined to the buried Si layer and not accessible to the NSOM probe.

Comparing the scanning electron micrograph in Fig. 6.9(a) with the AFM image in Fig. 6.9(b), we observe that the size and shape of the NSOM tip affects the apparent width of the DLSPP waveguide in the y-direction; however, we are primarily interested in decay of the DLSPP mode along the propagation (x) direction. Consequently, the intensity in the NSOM image was integrated along the y-direction and plotted on a normalized logarithmic scale in Fig. 6.9(d) as a function of propagation distance along the x-direction.

Other than an initial jump in intensity at the input SOI-DLSPP transition due to scattering at the SOI-DLSPP junction, the collected intensity plotted in Fig. 6.9(d) decays exponentially, but with an even oscillation period. Fitting the intensity profile to a model for a Fabry-Pérot cavity with loss, we find the non-physical result that the oscillation period corresponds to an intracavity mode index significantly less than 1. If we instead consider the oscillations to be the result of two modes with different effective wavelengths beating against one another, the beat period, $L_\mathrm{b} = 6.7\ \mu$m, corresponds to an effective index difference of $\lambda/L_\mathrm{b} = 0.23$ for $\lambda = 1520$ nm. This is very close to the difference between the DLSPP-mode effective index of 1.21 and the index of a radiative mode propagating in same direction in air (i.e. unity). It is therefore plausible that the observed oscillation is a result of near-field interference between the propagating DLSPP mode and scattered light propagating in free space along the x-direction.

Independent of the oscillation, the exponential decay in the intensity profile in Fig. 6.9(d) suggests a propagation length of $L_\mathrm{prop} = 47\ \mu$m. This is in agreement with the DLSPP-mode propagation length of $L_\mathrm{SPP} \approx 50\ \mu$m extracted from the variable-length waveguide transmission measurements and therefore supports our quantitative analysis of the SOI-DLSPP waveguide coupling loss.

6.4.4 Calculated SOI-DLSPP Insertion Loss

To further verify the measured coupling efficiency, the SOI-DLSPP waveguide structures were modeled with three-dimensional full-field finite-difference time-domain (FDTD) calculations using the Lumerical software package. Figure 6.10(b) shows the simulated structure, including input/output SOI waveguides and a 20-μm long DLSPP section. At the waveguide transitions, we modeled the PMMA layer with a 2-μm long linear taper at the edge of the silicon layer, in accord with AFM measurements of the fabricated topography. The calculated TM mode supported by the input SOI waveguide at $\lambda = 1550$ nm, plotted in Fig. 6.10(a), was used as the FDTD source, and we monitored the power transmitted through the output SOI waveguide 10 μm from the output transition. The monitor position was varied to ensure that it captured only power coupled into the (loss-less) output waveguide and not power scattered from the DLSPP-SOI transitions. The simulation boundaries were defined as perfectly matched layers and positioned far enough away from the waveguide so as to minimally impact the effective index of the calculated input mode. To ensure stability, the input source was defined temporally as a single pulse, and the field amplitudes were allowed to decay to 0.001% of their initial values. Spectral filtering was used to extract the power transmission associated with the input wavelength.

In Fig. 6.10(c), we show the total transmission calculated for different values of the silicon-gold offset, d_{offset}. The power profiles plotted in Fig. 6.10(b) indicate that light is coupled predominately into the DLSPP mode, supporting the assumption that light reaching the output monitor has traversed the gold region only through that mode. From FEM calculations at $\lambda = 1550$ nm using the gold index from Johnson and Christy [139], the propagation loss for the DLSPP mode, plotted in Fig. 6.10(a), is 0.10 dB/μm. Given the total calculated transmission of 43.2% (3.65 dB loss) for $d_{\text{offset}} = 300$ nm, we therefore estimate an attenuation of 2.0 dB for $L = 20$ μm. The modeled coupling loss is thus approximately 0.8 dB per SOI-DLSPP transition, just slightly lower than the experimentally measured value of 1.0 ± 0.1 dB.

6.5 Integrated DLSPP Ring Resonators

In addition to being potential building blocks for devices such as filters and modulators [39, 149, 155], ring resonators provide a means for further characterizing the DLSPP waveguide mode supported in our structures. On a sample with a smaller silicon-gold offset of $d_{\text{offset}} = 145$ nm, we fabricated 10-μm diameter DLSPP rings with a 500×560-nm cross-section, with each ring evanescently coupled to a straight 25-μm long DLSPP bus waveguide across a narrow coupling gap, G, as shown in Fig. 6.3(d). From the

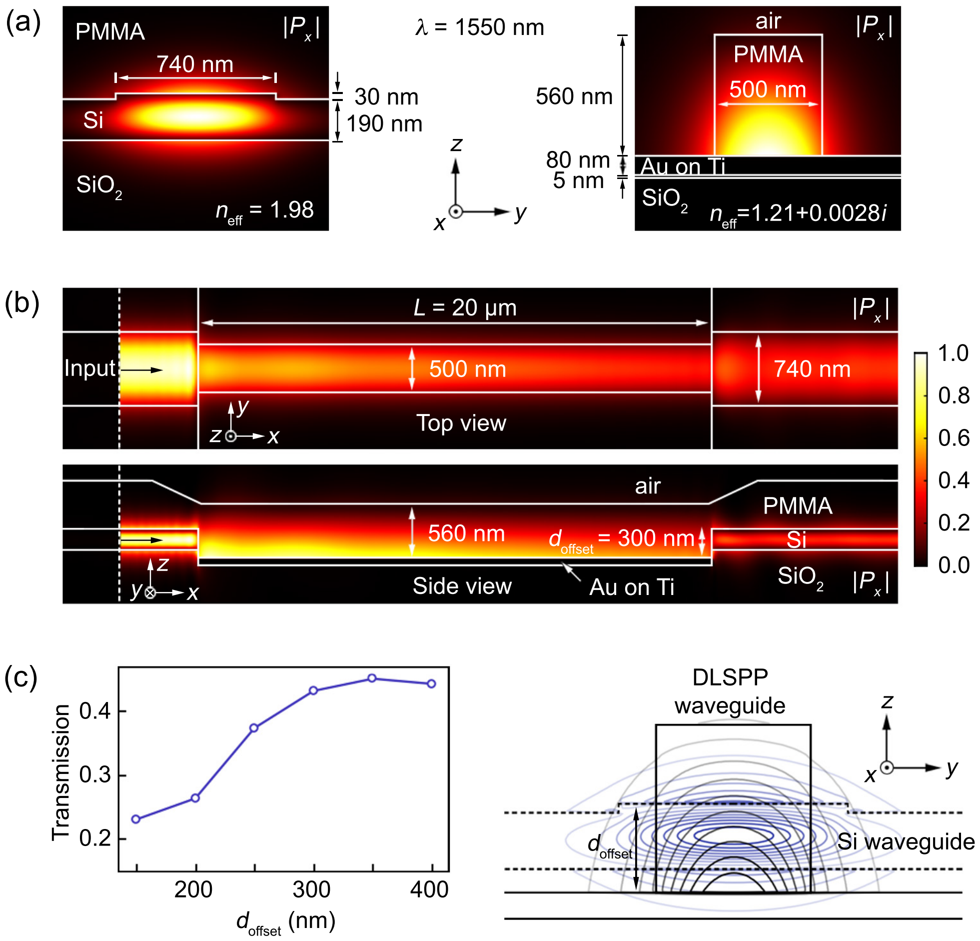

Figure 6.10. (a) Power distribution in the propagation direction for the TM SOI-waveguide mode and the DLSPP mode at $\lambda = 1550$ nm. (b) Finite-difference time-domain (FDTD) simulations showing the power in the propagation direction in a 20-μm long DLSPP waveguide with input/output SOI waveguides, where the input power was launched in the TM SOI-waveguide mode at the indicated position. The top view corresponds to a plane cutting through the center of the silicon waveguide perpendicular to the y-direction, 190 nm above the gold surface, and the side view corresponds to a plane bisecting the waveguide in the x-direction. (c) Total transmission through the DLSPP waveguide as a function of the vertical offset, d_{offset}. The contour plot shows the TM SOI-waveguide mode (blue) overlaid with the DLSPP mode (gray) for $d_{\text{offset}} = 300$ nm.

transmission spectra for the straight waveguides, we observe coupling to plasmonic ring resonances; however, as the linewidth of the resonances is a significant fraction of the SOI grating bandwidth, we must account for the grating response. Upon identifying the spectral position of the ring resonator modes within the laser tuning range, we adjusted θ to maximize the grating efficiency near the central wavelength of each resonance. In the top panel of Fig. 6.11, we show the raw transmission spectrum of a SOI-waveguide-coupled DLSPP reference waveguide (not coupled to any ring) for grating coupling angles of $\theta = -22.5°$ and $-33°$. Due to angle-dependent interference within the PMMA/Si/SiO_2 dielectric stack, we find that the grating efficiency is significantly higher for $|\theta| = 22.5°$ than for $|\theta| = 33°$, resulting in higher peak transmission at the smaller absolute coupling angle. Also shown in the top panel of Fig. 6.11 are the raw transmission spectra for three DLSPP waveguides, each coupled to a resonator across a different coupling gap, G.

The lower panel of Fig. 6.11 shows the corrected resonator transmission spectra, $T(\lambda)$, which are simply the raw transmission spectra divided by the reference device transmission at each wavelength. By normalizing the resonator transmission in this manner, we correct for both the SOI grating response and the propagation loss in the bus waveguide. Some error is introduced from variations in device fabrication and optical alignment from one measurement to the next, as evidenced by the asymmetry in some of the corrected spectra; however, we still clearly see resonances, which can be fit to a theoretical transmission model.

Examining the normalized resonator spectra, reduced transmission due to coupling into the rings is clearly visible near $\lambda = 1524$ and 1571 nm. The depths of the transmission minima increase with decreasing G, indicating that the resonators are under-coupled. Additionally, the resonance wavelength is blue-shifted with decreasing G, consistent with the coupling-induced frequency shift theoretically predicted by Tsilipakos, *et al.* [39]. We fit the resonator spectra to the functional form give in Eq. 2.30, adapted from the expression derived by Yariv for transmission through a waveguide coupled to a ring resonator [51]:

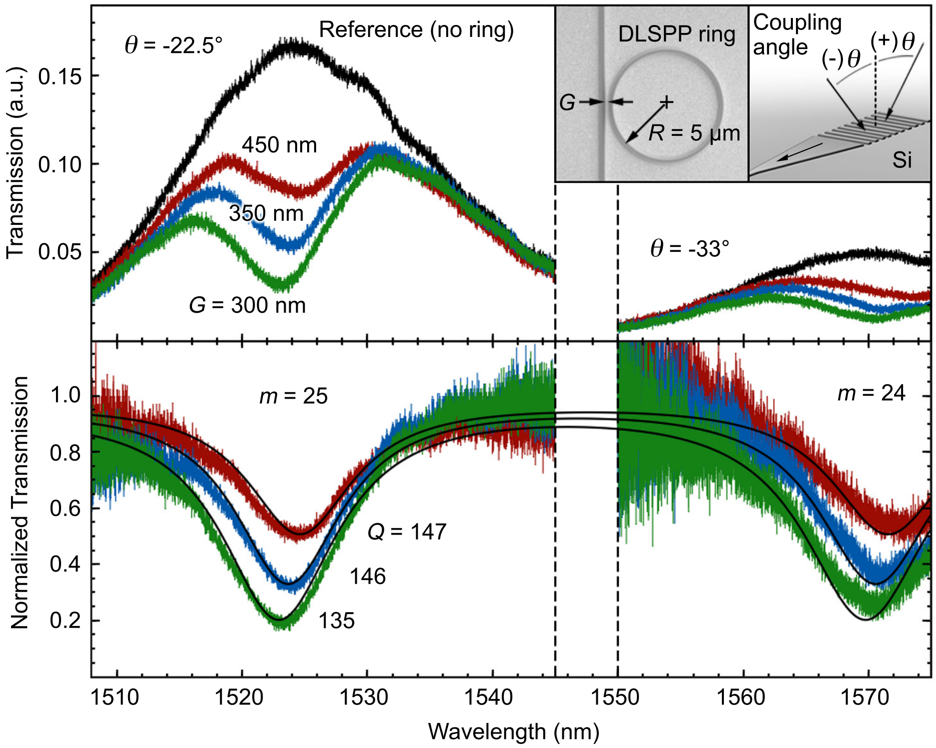

Figure 6.11. Transmission spectra of DLSPP waveguides evanescently coupled to ring resonators (radius $R = 5$ μm) with a varying separation gap, G, collected at the indicated grating coupling angles, θ. The raw spectra in the top panel show the effect of coupling into resonator modes (azimuthal order m) as well as the SOI grating response. The normalized spectra in the lower panel were obtained by dividing by the transmission spectrum of a reference device with no ring in order to correct for the grating response and the bus waveguide loss. Fitted transmission curves for each ring are shown in black, along with the loaded Q factors of the $m = 25$ resonances.

$$T(\lambda) = \frac{a^2 + |t|^2 - 2a|t|\cos\left(\frac{2\pi n_{\text{eff}}(\lambda)L_{\text{c}}}{\lambda} - \phi\right)}{1 + a^2|t|^2 - 2a|t|\cos\left(\frac{2\pi n_{\text{eff}}(\lambda)L_{\text{c}}}{\lambda} - \phi\right)}\ , \tag{6.7}$$

where $L_{\text{c}} = 10\pi\ \mu$m is the ring circumference at the waveguide centerline and $n_{\text{eff}}(\lambda)$ is the real part of the modal effective index, which we find to be negligibly different for the straight and curved waveguide geometries based on the resonator free-spectral range. The parameters a and $t = |t|e^{i\phi}$ are related to the field attenuation due to propagation and coupling, respectively, where $a < |t|$ for an under-coupled resonator. The propagation loss in the ring, α_{prop}, is due in general to a combination of absorption in the gold and bending loss. The phase factor, ϕ, accounts for the additional phase accumulation due to coupling, which is responsible for the observed coupling-induced shift of the resonance wavelength. At the m^{th}-order resonance wavelength, λ_m, the phase accumulated in one round trip around the ring obeys the relation

$$\frac{2\pi n_{\text{eff}}(\lambda_m)L_{\text{c}}}{\lambda_m} - \phi = 2\pi m, \quad m = 1, 2, 3... \tag{6.8}$$

Using the calculated $n_{\text{eff}}(\lambda)$ plotted in Fig. 6.6(b), we fit Eq. 6.7 to the measured ring resonator transmission spectra with a, $|t|$, and ϕ taken as the only fitting parameters. The best-fit values of $|t|$ are 0.81, 0.86, and 0.90 for $G =$ 300, 350, and 450 nm, respectively. The round-trip loss due to coupling, $l_{\text{coup}} = -2\ln|t|$, therefore decreases with increasing coupling gap. The best-fit values of a range between 0.54 and 0.57, and, as expected, there is no clear trend with coupling gap. The corresponding cavity propagation length is $L_{\text{prop}} = L_{\text{c}}/(-2\ln a) = 1/\alpha_{\text{prop}}$, which has an average value of $27 \pm 1\ \mu$m for the three resonator devices. We neglect the wavelength dependence of L_{prop} since the loss due to gold absorption varies by less than 3% over the range of our measurements. We can estimate the bending loss, α_{bend}, by assuming that the propagation length in the absence of bending effects is $L_{\text{SPP}} \approx 50\ \mu$m, as previously measured for the straight waveguides, yielding $\alpha_{\text{bend}} = \alpha_{\text{prop}} - 1/L_{\text{SPP}} \approx 0.074$ dB/μm, or 0.37 dB/rad. This bending loss agrees remarkably well with the value of 0.36 dB/rad measured by Holmgaard, *et al.* from NSOM measurements for DLSPP ring resonators of the same diameter [149]. Finally, we recall that the DLSPP ring resonators were patterned on a sample with a silicon-gold vertical offset of $d_{\text{offset}} = 145$ nm, and we note that the total loss measured for the 25-μm long DLSPP reference device was 7.1 ± 0.1 dB relative to SOI reference waveguides patterned on the same sample. For $L_{\text{SPP}} \approx 50$ μm, this indicates a coupling loss of 2.5 dB per transition, in fair agreement with the value of 1.9 dB estimated from the FDTD simulations for $d_{\text{offset}} = 150$ nm.

The quality factor for the m^{th}-order resonance is $Q = 2\pi c\tau_{\text{c}}/\lambda_m$, where $\tau_{\text{c}} = n_{\text{g}}L_{\text{c}}/(cl)$ is the cavity lifetime, defined in terms of the modal group index, n_{g}, and the round-trip loss, l. The previously calculated value of $n_{\text{g}} = 1.6$ for the DLSPP mode near $\lambda = 1550$ nm can be corroborated by measuring the free-spectral range between adjacent resonances, $\Delta\lambda = \lambda_m - \lambda_{m+1} = \lambda_{m+1}\lambda_m/(n_{\text{g}}L_{\text{c}})$. For the measured resonator spectra, we observe $\Delta\lambda \approx 47$ nm, which corresponds to $n_{\text{g}} = 1.62$. The good agreement with the value from two-dimensional FEM calculations supports the assumption that the real part of the DLSPP modal index corresponding to a bend radius of $R = 5$ μm is approximately equal the index of the straight-waveguide mode. The loaded Q factor of each $m = 25$ resonance is indicated in Fig. 6.11, which includes loss contributions from material absorption, coupling, and bending loss, so that $l = l_{\text{coup}} + \alpha_{\text{prop}}L_{\text{c}}$. Accounting only for absorption and bending loss, we define the intrinsic quality factor, Q_{int}, with $l = \alpha_{\text{prop}}L_{\text{c}}$. Since Q_{int} excludes loss due to coupling, it should be independent of G. Averaging over the measured devices, we find $Q_{\text{int}} = 180 \pm 8$ for the $m = 25$ resonance.

6.6 Summary and Outlook

In summary, we have demonstrated efficient coupling of light in and out of polymer-on-gold DLSPP waveguides and ring resonators using low-loss SOI waveguides at telecommunication wavelengths. Accounting for propagation loss, we measured coupling loss of 1.0 ± 0.1 dB per SOI-DLSPP waveguide transition at $\lambda = 1550$ nm, corresponding to coupling efficiency of $79 \pm 2\%$. The devices demonstrated here show

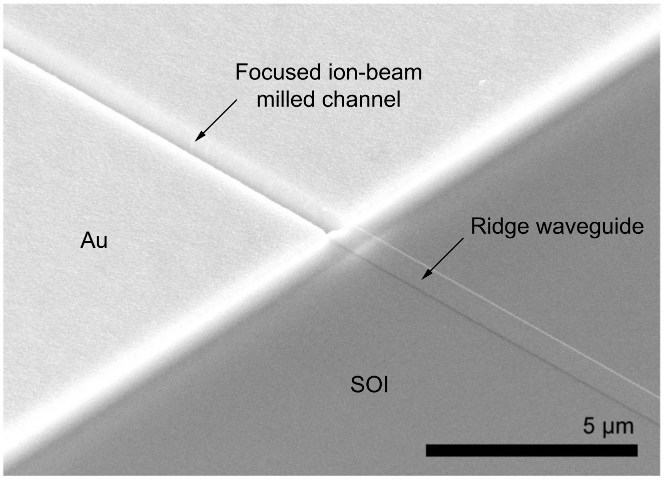

Figure 6.12. Scanning electron micrograph of a SOI ridge waveguide coupled to a plasmonic channel waveguide that has been milled into a thick gold layer.

that DLSPP waveguides can be efficiently interfaced with optical systems fabricated on SOI in order to combine the advantages of plasmonics with the low propagation loss of silicon photonic circuits.

Looking forward, there are other plasmonic waveguide geometries that could enable new functionality in photonic circuits but have yet to be demonstrated on an integrated platform. For example, metal channels that support a SPP mode between two vertical surfaces have been shown to be useful as compact wavelength-selective elements [151]. It has also been shown in theoretical studies that these structures can be used to form complex resonant waveguide networks that benefit from the unique confinement of the channel SPP mode [156], and work is ongoing to realize channel SPP waveguide networks on our SOI waveguide platform. Figure 6.12 shows a scanning electron micrograph of a structure fabricated with the same grating-coupled SOI waveguides that we used to couple light into DLSPP structures, except that the waveguides are coupled to air gaps milled into the surface of a thick gold layer.

The future of plasmonics for telecommunication applications will likely depend, in part, on how easily and efficiently plasmonic devices can be integrated with standard photonic components. As shown here, it is possible to integrate dielectric-loaded plasmonic waveguides onto the SOI platform with minimal insertion loss, and there are prospects for similar integration schemes with other plasmonic waveguide geometries. With the addition of SOI-integrated light sources and detectors, these plasmonic devices can become part of a compact, self-contained optical system on a chip.

Appendix A

Etching and Deposition Processes

We describe here the plasma-assisted etching and deposition processes that are referred to throughout this thesis. We note that the process recipes are tool-specific and are therefore likely to be helpful particularly for users of the Oxford Instruments etching and deposition tools in the Kavli Nanoscience Institute cleanroom facility at Caltech. However, we also hope to have provided sufficient detail for this information to be generally informative.

A.1 Silicon Etching

Four different silicon etching processes were developed for the Oxford Instruments Plasmalab System 100 ICP 380 etching tool. The system was equipped with a 5-kW inductively coupled plasma (ICP) generator operating at 2 MHz, and a sample-stage (table) electrode with a 600-W generator operating at 13.56 MHz. The etching chamber was load-locked and fitted with a turbo pump capable of maintaining a background pressure below 10^{-6} Torr. The sample stage temperature was regulated using a resistive heater and a liquid-nitrogen heat exchanger, and all samples were processed on 150-mm (6-in) diameter silicon carrier wafers. The wafers were secured on the adjustable-height table by a quartz clamp, and a flow of helium was used to ensure thermal conduction between the wafer and the sample stage. Smaller chips were mounted onto 150-mm silicon carrier wafers using Fomblin perfluorinated polyether vacuum fluid. The available etching process gases included SF_6, C_4F_8, and O_2.

Table A.1. Silicon etching processes for the Oxford Instruments Plasmalab System 100 ICP 380.

	C_4F_8/O_2 waveguide etch	C_4F_8/SF_6 pseudo-Bosch etch	SF_6/O_2 cryogenic etch
Table temperature (°C):	15	15	-110
Table height (mm):	20	20	20
Helium backing (Torr):	5 – 10	10	10
SF_6 flow (sccm):	—	33	50
C_4F_8 flow (sccm):	37.5	57	—
O_2 flow (sccm):	5	—	10
Process pressure (mTorr):	7	10	10
ICP power (W):	2100	1200	1000
Table electrode (W):	200	20	10
Silicon etch rate (nm/s):	~ 2	4 – 5	~ 10
Mask compatibility:	ma-N 2403	ma-N 2403, PMMA	PMMA
Additional information:	Etches SiO_2 faster than silicon; smooth partially etched surfaces	Etches SiO_2 more slowly than silicon; rough partially etched surfaces	Etches SiO_2 much more slowly than silicon ($> 10\times$)

Table A.1 lists the parameters for the two waveguide etch processes described in Chapter 2 and the cryogenic etch process referred to in Chapter 6. The C_4F_8/SF_6 "pseudo-Bosch" etch can be used to achieve vertical etching profiles [59]; however, the C_4F_8/O_2 etch was ultimately used to form waveguide structures because of the slower etch rate and the relative smoothness of silicon surfaces that had been partially etched using the process. The cryogenic silicon etch process was used to etch completely though the silicon device layer of SOI samples, using the SiO_2 BOX layer as an etch stop. The formation of a fluorinated glass passivation layer at cryogenic temperatures allows for highly directional and selective etching [157].

Table A.2. Additional etching processes for the Oxford Instruments Plasmalab System 100 ICP 380.

	SF_6 isotropic silicon etch	O_2 plasma clean
Table temperature (°C):	15	15
Table height (mm):	20	20
Helium backing (Torr):	10	5 – 10
SF_6 flow (sccm):	80	—
O_2 flow (sccm):	—	80
Process pressure (mTorr):	20	12
ICP power (W):	2000	2000
Table electrode (W):	50	40
Silicon etch rate (nm/s):	20 – 40	—
Additional information:	Silicon etch rate depends on silicon load (exposed area)	Chamber should be pre-cleaned; resist and etch residue fully removed after 60 s with minimal silicon etching

For completeness, Table A.2 lists the parameters for an isotropic SF_6-based silicon etch that was not used specifically for the work described in this thesis but was implemented elsewhere for through-wafer etching [158]. The etch rate of the isotropic etching process could be increased by reducing the amount of exposed silicon in the etching chamber, for example by using an oxidized carrier wafer. Table A.2 also describes an O_2-plasma cleaning process that was found to be effective for removing polymerized etching residue and plasma-hardened resist from SOI samples. Finally, we note that the pseudo-Bosch and isotropic silicon etching processes required a plasma strike step, where the ICP and table-electrode powers were increased for a few seconds at the beginning of the etch.

A.2 Dielectric and Amorphous Silicon PECVD

To deposit silicon oxide, silicon nitride, and amorphous silicon (a-Si) films, we used an Oxford Instruments Plasmalab System 100 plasma-enhanced chemical-vapor deposition (PECVD) chamber with a high-frequency (RF) generator operating at 13.56 MHz and a low-frequency generator operating at 50 kHz. The chamber was load-locked and fitted with N_2O, NH_3, and SiH_4 process gases. We used either 5% SiH_4 diluted in N_2 for the dielectric films or 5% SiH_4 diluted in argon for the a-Si films. The sample stage was equipped with a heater capable of reliably reaching temperatures up to 400 °C.

Table A.3. Dielectric and amorphous silicon deposition processes for the Oxford Instruments Plasmalab System 100 PECVD.

	SiO_2	SiN_x	a-Si
Table temperature (°C):	350	350	variable
Diluted SiH_4 flow (sccm):	170	400	280
N_2O flow (sccm):	710	—	—
NH_3 flow (sccm):	—	30	—
Process pressure (mTorr):	1000	1000	2000
High-frequency (RF) power (W):	20	20	7
Low-frequency (LF) power (W):	—	20	—
Deposition rate (nm/min):	64	15	see Fig. A.2
Index at $\lambda = 1550$ nm:	1.48	1.99	see Fig. A.2
Additional information:	Uses 5% SiH_4 diluted in N_2	Uses 5% SiH_4 diluted in N_2; 20 s plasma cycle: RF for 13 s, LF for 7 s	Uses 5% SiH_4 diluted in argon

The PECVD SiO_2 and SiN_x films were employed for the hardmask process described in Chapter 2. The deposition processes, as outlined in Table A.3, were adapted from recipes provided by Oxford Instruments, where the diluted SiH_4 flow was adjusted to achieve the desired refractive index. The film thickness and refractive index were determined using a Sentech SE 850 variable-angle spectroscopic ellipsometer in reflection mode over wavelengths from 400 to 2200 nm. The optical properties of the dielectric films were not critical for the hardmask process; however, the nitride films were also used as passivating anti-reflective coatings in another work [159], and a more detailed analysis of the refractive index can be found there.

The a-Si PECVD process given in Table A.3 was used to deposit high-index top layers for the erbium-doped slot waveguide structures described in Chapter 4. To accurately model the spontaneous emission rate enhancement for these structures, it is important to use accurate values of the a-Si optical properties. Figure A.1(a) shows ellipsometry spectra measured for a thin a-Si film deposited atop a 520-nm thick thermal oxide on a crystalline silicon substrate. The spectra measured at three different reflection angles were fit simultaneously to the model proposed by Forouhi and Bloomer for the optical dispersion of amorphous semiconductors [160]. By minimizing the deviation between the measured and modeled values of the ellipsometry amplitude and phase parameters, Ψ and Δ, the film thickness and complex refractive index were determined for a-Si films deposited a different substrate temperatures. Figure A.1(b) shows the best-fit complex refractive index, $n + i\kappa$, for an a-Si film deposited at 350 °C.

Figure A.2 shows the measured real part of the refractive index at a wavelength of $\lambda = 1550$ nm for a-Si films deposited at temperatures between 200 and 400 °C. The a-Si refractive index approaches its maximum value at the higher deposition temperatures, which suggests that lower deposition temperatures result in films with a less homogeneous silicon composition. The lower panel of Fig. A.2 shows the temperature dependence of the a-Si deposition rate, which increases monotonically with substrate temperature.

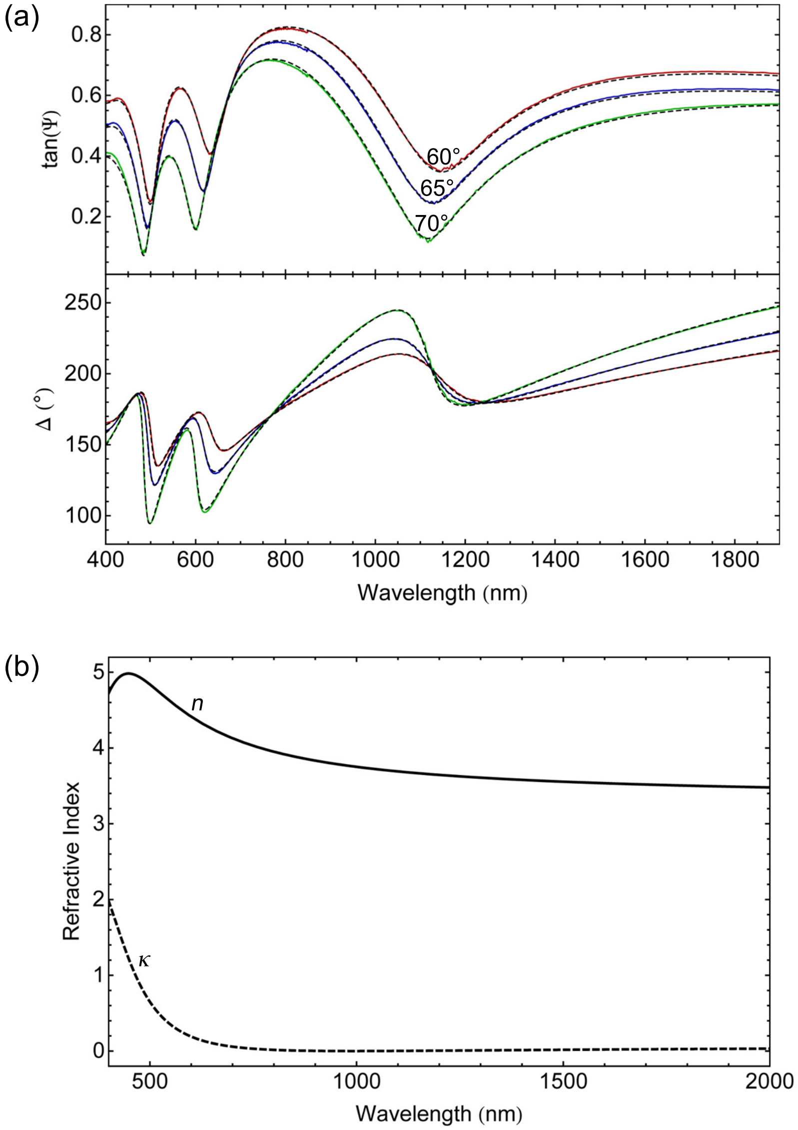

Figure A.1. (a) Ellipsometry spectra collected at three different reflection angles for a 53-nm thick a-Si film deposited by PECVD at 350 °C. The deposition substrate was a crystalline silicon wafer with a 520-nm thick thermally grown SiO_2 surface layer. The raw data are shown by the colored curves, while the dashed black curves represent a fit to the experimental spectra using the Forouhi-Bloomer model [160]. (b) Real, n, and imaginary, κ, parts of the refractive index of a PECVD a-Si film deposited at 350 °C, where the material dispersion was modeled from the ellipsometry data.

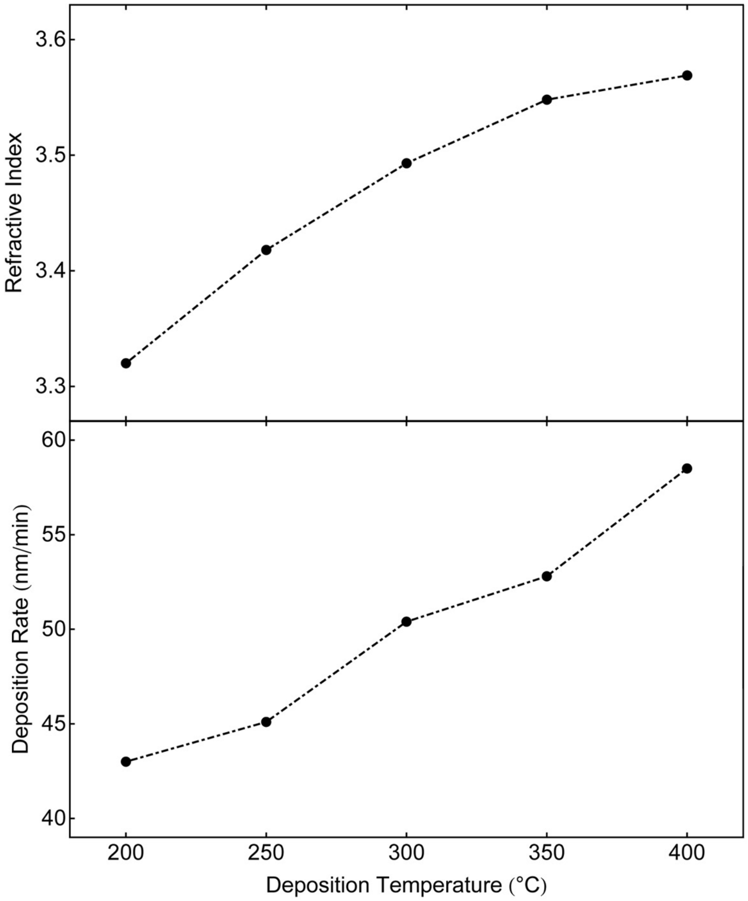

Figure A.2. Real part of the refractive index at $\lambda = 1550$ nm measured for PECVD a-Si films deposited at different substrate temperatures (upper panel). The film deposition rates are plotted in the lower panel.

References

[1] C. K. Cao and G. A. Hockham, "Dielectric-fibre surface waveguides for optical frequencies," Proc. IEE **113**, 1151–1158 (1966).

[2] C. K. Cao and T. W. Davies, "Spectroscopic studies of ultra low loss optical glasses," J. Sci. Instrum. **1**, 1063–1068 (1968).

[3] G. K. Teal, "Single crystals of germanium and silicon - basic to the transistor and integrated circuit," IEEE T. Electron Dev. **ED-23**, 621–639 (1976).

[4] R. A. Soref and B. R. Bennett, "All-silicon active and passive guided-wave components for $\lambda = 1.3$ and 1.6 μm," IEEE J. Quantum Electron. **QE-22**, 873–879 (1987).

[5] R. A. Soref and B. R. Bennett, "Electrooptical effects in silicon," IEEE J. Quantum Electron. **QE-23**, 123–129 (1987).

[6] J. B. Lasky, "Wafer bonding for silicon-on-insulator technologies," Appl. Phys. Lett. **48**, 78–80 (1986).

[7] W. P. Maszara, G. Goetz, A. Caviglia, and J. B. McKitterick, "Bonding of silicon wafers for silicon-on-insulator," J. Appl. Phys. **64**, 4943–4950 (1988).

[8] Y. A. Vlasov and S. J. McNab, "Losses in single-mode silicon-on-insulator strip waveguides and bends," Opt. Express **12**, 1622–1631 (2004).

[9] M. Bruel, "Application of hydrogen ion beams to silicon on insulator material technology," Nucl. Instrum. Meth. B **108**, 313–319 (1996).

[10] The Microphotonics Center at MIT, *Microphotonics: Hardware for the Information Age* (Mass. Inst. Technol., Cambridge, MA, 2005).

[11] R. Soref, "The past, present, and future of silicon photonics," IEEE J. Sel. Top. Quant. **12**, 1678–1687 (2006).

[12] C. Gunn, A. Narasimha, B. Analui, Y. Liang, and T. J. Sleboda, "A 40-gb silicon photonics transceiver," Proc. SPIE **6477**, 64770N (2007).

[13] A. Shacham, K. Bergman, and L. P. Carloni, "Photonic networks-on-chip for future generations of chip multiprocessors," IEEE T. Comput. **57**, 1246–1260 (2008).

[14] B. G. Lee, A. Biberman, J. Chan, and K. Bergman, "High-performance modulators and switches for silicon photonic networks-on-chip," IEEE J. Sel. Top. Quant. **16**, 6–22 (2010).

[15] G. Chen, H. Chen, M. Haurylau, N. A. Nelson, D. H. Albonesi, P. M. Fauchet, and E. G. Friedman, "On-chip copper-based vs. optical interconnects: delay uncertainty, latency, power, and bandwidth density comparative predictions," Proc. of the IEEE International Interconnect Technology Conference, pp. 39–41 (2006).

[16] A. Densmore, M. Vachon, D. X. Xu, S. Janz, R. Ma, Y. H. Li, G. Lopinski, A. Delâge, J. Lapointe, C. C. Luebbert, Q. Y. Liu, P. Cheben, and J. H. Schmid, "Silicon photonic wire biosensor array for multiplexed real-time and label-free molecular detection," Opt. Lett. **34**, 3598–3600 (2009).

[17] M. A. Green, J. Zhao, A. Wang, P. J. Reece, and M. Gal, "Efficient silicon light-emitting diodes," Nature **412**, 805–808 (2001).

[18] H. Rong, R. Jones, A. Liu, O. Cohen, D. Hak, A. Fang, and M. Paniccia, "A continuous-wave Raman silicon laser," Nature **433**, 725–728 (2005).

[19] Q. Xu, B. Schmidt, S. Pradhan, and M. Lipson, “Micrometre-scale silicon electro-optic modulator,” Nature **435**, 325–327 (2005).

[20] A. Liu, R. Jones, L. Liao, D. Samara-Rubio, D. Rubin, O. Cohen, R. Nicolaescu, and M. Paniccia, “A high-speed silicon optical modulator based on a metal-oxide-semiconductor capacitor,” Nature **427**, 615–618 (2004).

[21] F. Horst, W. M. J. Green, B. J. Offrein, and Y. A. Vlasov, “Wavelength division multiplexing based photonic integrated circuits on silicon-on-insulator platform,” IEEE Phot. Tech. Lett. **21**, 1743–1745 (2009).

[22] A. Liu, L. Liao, Y. Chetrit, J. Basak, H. Nguyen, D. Rubin, and M. Paniccia, “Wavelength division multiplexing based photonic integrated circuits on silicon-on-insulator platform,” IEEE J. Sel. Top. Quant. **16**, 23–32 (2010).

[23] P. H. Wendland and M. Chester, “Electric field effects on indirect optical transitions in silicon,” Phys. Rev. **140**, 1384–1390 (1965).

[24] K. Preston, Y. H. D. Lee, M. Zhang, and M. Lipson, “Waveguide-integrated telecom-wavelength photodiode in deposited silicon,” Opt. Lett. **36**, 52–54 (2011).

[25] A. W. Fang, H. Park, O. Cohen, R. Jones, M. J. Paniccia, and J. E. Bowers, “Electrically pumped hybrid AlGaInAs-silicon evanescent laser,” Opt. Express **14**, 9203–9210 (2006).

[26] X. Sun, A. Zadok, M. J. Shearn, K. A. Diest, A. Ghaffari, H. A. Atwater, A. Scherer, and A. Yariv, “Electrically pumped hybrid evanescent Si/InGaAsP lasers,” Opt. Lett. **34**, 1345–1347 (2009).

[27] D. Ahn, C. Y. Hong, J. Liu, W. Giziewcz, M. Beals, L. C. Kimerling, J. Michel, J. Chen, and F. X. Kärtner, “High performance, waveguide integrated Ge photodetectors,” Opt. Express **15**, 3916–3921 (2007).

[28] L. Chen, K. Preston, S. Manipatruni, and M. Lipson, "Integrated GHz silicon photonic interconnect with micrometer-scale modulators and detectors," Opt. Express **17**, 15248–15256 (2009).

[29] E. Desurvire, J. R. Simpson, and P. C. Becker, "High-gain erbium-doped traveling-wave fiber amplifier," Opt. Lett. **12**, 888–890 (1987).

[30] A. Polman, "Erbium implanted thin film photonic materials," J. Appl. Phys. **82**, 1–39 (1997).

[31] M. Borselli, "High-Q microresonators as lasing elements for silicon photonics," Ph.D. thesis, California Institute of Technology (2006).

[32] V. R. Almeida, Q. Xu, C. A. Barrios, and M. Lipson, "Guiding and confining light in void nanostructure," Opt. Lett. **29**, 1209–1211 (2004).

[33] Q. Xu, V. R. Almeida, R. R. Panepucci, and M. Lipson, "Experimental demonstration of guiding and confining light in nanometer-size low-refractive-index material," Opt. Lett. **29**, 1626–1628 (2004).

[34] C. A. Barrios and M. Lipson, "Electrically driven silicon resonant light emitting device based on slot-waveguide," Opt. Express **13**, 10092–10101 (2005).

[35] T. Baehr-Jones, M. Hochberg, G. Wang, R. Lawson, Y. Liao, P. A. Sullivan, L. Dalton, A. K. Y. Jen, and A. Scherer, "Optical modulation and detection in slotted silicon waveguides," Opt. Express **13**, 5216–5226 (2005).

[36] J. A. Dionne, L. A. Sweatlock, H. A. Atwater, and A. Polman, "Planar metal plasmon waveguides: Frequency-dependent dispersion, propagation, localization, and loss beyond the free electron model," Phys. Rev. B **72**, 075405 (2005).

[37] J. A. Dionne, L. A. Sweatlock, H. A. Atwater, and A. Polman, "Plasmon slot waveguides: Towards chip-scale propagation with subwavelength-scale localization," Phys. Rev. B **73**, 035407 (2006).

[38] J. A. Dionne, K. A. Diest, L. A. Sweatlock, and H. A. Atwater, “PlasMOStor: A metal-oxide silicon field effect plasmonic modulator,” Nano Lett. **9**, 897–902 (2009).

[39] O. Tsilipakos, T. V. Yioultsis, and E. E. Kriezis, “Theoretical analysis of thermally tunable microring resonator filters made of dielectric-loaded plasmonic waveguides,” J. Appl. Phys. **106**, 093109 (2009).

[40] K. K. Lee, D. R. Lim, L. C. Kimerling, J. Shin, and F. Cerrina, “Fabrication of ultralow-loss Si/SiO$_2$ waveguides by roughness reduction,” Opt. Lett. **26**, 1888–1890 (2001).

[41] M. A. Webster, R. M. Pafchek, G. Sukumaran, and T. L. Koch, “Low-loss quasi-planar ridge waveguides formed on thin silicon-on-insulator,” Appl. Phys. Lett. **87**, 231108 (2005).

[42] R. Pafchek, R. Tummidi, J. Li, M. A. Webster, E. Chen, and T. L. Koch, “Low-loss silicon-on-insulator shallow-ridge TE and TM waveguides formed using thermal oxidation,” Appl. Opt. **48**, 958–963 (2009).

[43] A. Yariv and P. Yeh, *Photonics: Optical Electronics in Modern Communications* (Oxford University Press, New York, NY, 2007).

[44] M. A. Webster, R. M. Pafchek, A. Mitchell, and T. L. Koch, “Width dependence of inherent TM-mode lateral leakage loss in silicon-on-insulator ridge waveguides,” IEEE Photon. Technol. Lett. **19**, 426–431 (2007).

[45] R. M. Pafchek, J. Li, R. S. Tummidi, and T. L. Koch, “Low loss Si-SiO$_2$-Si 8-nm slot waveguides,” IEEE Phot. Tech. Lett. **21**, 353–355 (2009).

[46] W. Streifer, D. R. Scifres, and R. D. Burnham, “Analysis of grating-coupled radiation in GaAs:GaAlAs lasers and waveguides,” IEEE J. Quant. Elect. **QE-12**, 422–428 (1976).

[47] W. Streifer, D. R. Scifres, and R. D. Burnham, "TM-mode coupling coefficients in guided-wave distributed feedback lasers," IEEE J. Quant. Elect. **QE-12**, 74–78 (1976).

[48] D. Pascal, R. Orobtchouk, A. Layadi, A. Koster, and S. Laval, "Optimized coupling of a Gaussian beam into an optical waveguide with a grating coupler: comparison of experimental and theoretical results," Appl. Opt. **36**, 2443–2447 (1997).

[49] M. Borselli, T. J. Johnson, and O. Painter, "Measuring the role of surface chemistry in silicon microphotonics," Appl. Phys. Lett. **88**, 131114 (2006).

[50] D. Marcuse, "Bend loss of slab and fiber modes computed with diffraction theory," IEEE J. Quantum Elect. **29**, 2957–2961 (1993).

[51] A. Yariv, "Universal relations for coupling of optical power between microresonators and dielectric waveguides," Electron. Lett. **36**, 321–322 (2000).

[52] A. Nitkowski, L. Chen, and M. Lipson, "Cavity-enhanced on-chip absorption spectroscopy using microring resonators," Opt. Express **16**, 11930–11936 (2008).

[53] V. R. Almeida, R. R. Panepucci, and M. Lipson, "Nanotaper for compact mode conversion," Opt. Lett. **28**, 1302–1304 (2003).

[54] B. G. Lee, F. E. Doany, S. Assefa, W. M. J. Green, M. Yang, C. L. Schow, C. V. Jahnes, S. Zhang, J. Singer, V. I. Kopp, J. A. Kash, and Y. A. Vlasov, "20-μm-pitch eight-channel monolithic fiber array coupling 160 Gb/s/channel to silicon nanophotonic chip," Proc. of the 2010 Conference on Optical Fiber Communication, pp. 1–3 (2010).

[55] M. Borselli, T. J. Johnson, and O. Painter, "Beyond the Rayleigh scattering limit in high-Q silicon microdisks: theory and experiment," Opt. Express **13**, 1515–1522 (2005).

[56] D. L. Flamm, V. M. Donnelly, and J. A. Mucha, "The reaction of fluorine atoms with silicon," J. Appl. Phys. **52**, 3633–3639 (1981).

[57] R. d'Agostino and D. L. Flamm, "Plasma etching of Si and SiO_2 in SF_6-O_2 mixtures," J. Appl. Phys. **52**, 162–167 (1981).

[58] M. Haverlag, D. Vender, and G. S. Oehrlein, "Ellipsometric study of silicon surface damage in electron cyclotron resonance plasma etching using CF_4 and SF_6," Appl. Phys. Lett. **61**, 2875–2877 (1992).

[59] M. D. Henry, S. Walavalkar, A. Homyk, and A. Scherer, "Alumina etch masks for fabrication of high-aspect-ratio silicon micropillars and nanopillars," Nanotechnology **20**, 255305 (2009).

[60] F. V. Laere, G. Roelkens, M. Ayre, J. Schrauwen, D. Taillaert, D. V. Thourhout, T. F. Krauss, and R. Baets, "Compact and highly efficient grating couplers between optical fiber and nanophotonic waveguides," J. Lightwave Technol. **25**, 151–156 (2007).

[61] M. Galli, D. Gerace, A. Politi, M. Liscidini, M. Patrini, L. Andreani, A. Canino, M. Miritello, R. L. Savio, A. Irrera, and F. Priolo, "Direct evidence of light confinement and emission enhancement in active silicon-on-insulator slot waveguides," Appl. Phys. Lett. **89**, 241114 (2006).

[62] T. Baehr-Jones, M. Hochberg, C. Walker, and A. Scherer, "High-Q optical resonators in silicon-on-insulator-based slot waveguides," Appl. Phys. Lett. **86**, 081101 (2005).

[63] K. Preston and M. Lipson, "Slot waveguides with polycrystalline silicon for electrical injection," Opt. Express **17**, 1527–1534 (2009).

[64] Q. Y. Tong, G. Fountain, and P. Enquist, "Room temperature SiO_2/SiO_2 covalent bonding," Appl. Phys. Lett. **89**, 042110 (2006).

[65] S. Lardenois, D. Pascal, L. Vivien, E. Cassan, S. Laval, and R. Orobtchouk, "Low-loss submicrometer silicon-on-insulator rib waveguides and corner mirrors," Opt. Lett. **28**, 1150–1152 (2003).

[66] Q. Y. Tong and U. Gösele, *Semiconductor Wafer Bonding: Science and Technology* (John Wiley and Sons, New York, NY, 1999).

[67] E. M. Purcell, "Spontaneous emission probabilities at radio frequencies," Phys. Rev. **69**, 681 (1946).

[68] S. Wang, A. Eckau, E. Neufeld, R. Carius, and C. Buchal, "Hot electron impact excitation cross-section of Er^{3+} and electroluminescence from erbium-implanted silicon metal-oxide-semiconductor tunnel diodes," Appl. Phys. Lett. **71**, 2824–2826 (1997).

[69] S. Yerci, R. Li, and L. D. Negro, "Electroluminescence from Er-doped Si-rich silicon nitride light emitting diodes," Appl. Phys. Lett. **97**, 081109 (2010).

[70] C. K. Carniglia and L. Mandel, "Quantization of evanescent electromagnetic waves," Phys. Rev. D **3**, 280–296 (1971).

[71] K. H. Drexhage, "Influence of a dielectric interface on fluorescence decay time," J. Lumin. **1-2**, 693–701 (1970).

[72] E. Snoeks, A. Lagendijk, and A. Polman, "Measuring and modifying the spontaneous emission rate of erbium near an interface," Phys. Rev. Lett. **74**, 24592462 (1995).

[73] E. Yablonovitch, T. J. Gmitter, and R. Bhat, "Inhibited and enhanced spontaneous emission from optically thin AlGaAs/GaAs double heterostructures," Phys. Rev. Lett. **61**, 2546–2549 (1988).

[74] R. J. Walters, J. Kalkman, A. Polman, H. A. Atwater, and M. J. A. de Dood, "Photoluminescence quantum efficiency of dense silicon nanocrystal ensembles in SiO_2," Phys. Rev. B **73**, 132302 (2006).

[75] H. Khosravi and R. Loudon, “Vacuum field fluctuations and spontaneous emission in a dielectric slab,” Proc. R. Soc. Lond. A **436**, 373–389 (1992).

[76] H. P. Urbach and G. L. J. A. Rikken, “Spontaneous emission from a dielectric slab,” Phys. Rev. A **57**, 3913–3930 (1998).

[77] J. T. Robinson, C. Manolatou, L. Chen, and M. Lipson, “Ultrasmall mode volumes in dielectric optical microcavities,” Phys. Rev. Lett. **95**, 143901 (2005).

[78] Y. C. Jun, R. M. Briggs, M. L. Brongersma, and H. A. Atwater, “Broadband enhancement of light emission in silicon slot waveguides,” Opt. Express **17**, 7479–7490 (2009).

[79] R. M. Briggs, G. M. Miller, and H. A. Atwater, “Modifying the radiative quantum efficiency of erbium-doped glass in silicon slot waveguides,” Proc. of the 6th IEEE International Conference on Group IV Photonics, pp. 223–225 (2009).

[80] Y. C. Jun, R. D. Kekatpure, J. S. White, and M. L. Brongersma, “Nonresonant enhancement of spontaneous emission in metal-dielectric-metal plasmon waveguide structures,” Phys. Rev. B **78**, 153111 (2008).

[81] A. C. Hryciw, Y. C. Jun, and M. L. Brongersma, “Plasmon-enhanced emission from optically-doped MOS light sources,” Opt. Express **17**, 185–192 (2009).

[82] Y. C. Jun, R. Pala, J. S. White, and M. L. Brongersma, “Strong modification of quantum dot spontaneous emission via gap plasmon coupling in metal nanoslits,” J. Phys. Chem. C **114**, 72697273 (2009).

[83] C. Creatore and L. C. Andreani, “Quantum theory of spontaneous emission in multilayer dielectric structures,” Phys. Rev. A **78**, 063825 (2008).

[84] C. Creatore, L. C. Andreani, M. Miritello, R. L. Savio, and F. Priolo, “Modification of erbium radiative lifetime in planar silicon slot waveguides,” Appl. Phys. Lett. **94**, 103112 (2009).

[85] M. O. Scully and M. S. Zubairy, *Quantum Optics* (Cambridge University Press, Cambridge, UK, 1997).

[86] R. Loudon, *The Quantum Theory of Light* (Oxford Science Publications, New York, NY, 1983).

[87] D. P. Nyquist, D. R. Johnson, and S. V. Hsu, "Orthogonality and amplitude spectrum of radiation modes along open-boundary waveguides," J. Opt. Soc. Am. **71**, 49–54 (1981).

[88] S. Hüfner, *Optical Spectra of Transparent Rare Earth Compounds* (Academic Press, New York, NY, 1978).

[89] T. Kitagawa, K. Hattori, M. Shimizu, Y. Ohmori, and M. Kobayashi, "Guided-wave laser based on erbium-doped silica planar lightwave circuit," Electron. Lett. **27**, 334–335 (1991).

[90] J. Shmulovich, A. Wong, Y. H. Wong, P. C. Becker, A. J. Bruce, and R.Adar, "Er^{3+} glass waveguide amplifier at 1.5 μm on silicon," Electron. Lett. **28**, 1181–1182 (1992).

[91] R. N. Ghosh, J. Shmulovich, C. F. Kane, M. R. X. de Barros, G. Nykolak, A. J. Bruce, and P. C. Becker, "8-mW threshold Er^{3+}-doped planar waveguide amplifier," IEEE Phot. Tech. Lett. **8**, 888–890 (1996).

[92] Y. C. Yan, A. J. Faber, H. de Waal, P. G. Kik, and A. Polman, "Erbium-doped phosphate glass waveguide on silicon with 4.1 dB/cm gain at 1.535 μm," Appl. Phys. Lett. **71**, 2922–2924 (1997).

[93] H. S. Han, S. Y. Seo, and J. H. Shin, "Optical gain at 1.54 μm in erbium-doped silicon nanocluster sensitized waveguide," Appl. Phys. Lett. **79**, 4568–4570 (2001).

[94] A. J. Kenyon, P. F. Trwoga, M. Federighi, and C. W. Pitt, "Optical properties of PECVD erbium-doped silicon-rich silica: evidence for energy transfer between

silicon microciusters and erbium ions," J. Phys.: Condens. Matter **6**, L319–L324 (1994).

[95] M. de Dood, J. Knoester, A. Tip, and A. Polman, "Förster transfer and the local optical density of states in erbium-doped silica," Phys. Rev. B **71**, 115102 (2005).

[96] G. M. Miller, R. M. Briggs, and H. A. Atwater, "Achieving optical gain in waveguide-confined nanocluster-sensitized erbium by pulsed excitation," J. Appl. Phys. **108**, 063109 (2010).

[97] G. Franzò, D. Pacifici, V. Vinciguerra, and F. Priolo, "Er^{3+} ions-Si nanocrystals interactions and their effects on the luminescence properties," Appl. Phys. Lett. **76**, 2167–2169 (2000).

[98] D. Pacifici, G. Franzò, F. Priolo, F. Iacona, and L. D. Negro, "Modeling and perspectives of the Si nanocrystals-Er interaction for optical amplification," Phys. Rev. B **67**, 245301 (2003).

[99] F. Enrichi, G. Mattei, C. Sada, E. Trave, D. Pacifici, G. Franzò, F. Priolo, F. Iacona, M. Prassas, M. Falconieri, and E. Borsella, "Study of the energy transfer mechanism in different glasses co-doped with Si nanoaggregates and Er^{3+} ions," Opt. Mater. **27**, 904–909 (2005).

[100] B. Garrido, C. García, P. Pellegrino, D. Navarro-Urrios, N. Daldosso, L. Pavesi, F. Gourbilleau, and R. Rizk, "Distance dependent interaction as the limiting factor for Si nanocluster to Er energy transfer in silica," Appl. Phys. Lett. **89**, 163103 (2006).

[101] J. H. Jhe, J. H. Shin, K. J. Kim, and D. W. Moon, "The characteristic carrier-Er interaction distance in Er-doped a-Si/SiO_2 superlattices formed by ion sputtering," Appl. Phys. Lett. **82**, 4489–4491 (2003).

[102] J. F. Ziegler, J. P. Biersack, and U. Littmark, *The Stopping and Range of Ions in Solids* (Pergamon Press, New York, NY, 1985).

[103] R. Sun, J. Cheng, J. Michel, and L. Kimerling, "Transparent amorphous silicon channel waveguides and high-Q resonators using a damascene process," Opt. Lett. **34**, 2378–2380 (2009).

[104] J. H. Shin, S. Y. Seo, and S. J. Lee, "Effect of hydrogenation on room-temperature 1.54 μm Er^{3+} photoluminescent properties of erbium-doped silicon-rich silicon oxide," Appl. Phys. Lett. **73**, 3647–3649 (1998).

[105] F. J. Morin, "Oxides which show a metal-to-insulator transition at the Neel temperature," Phys. Rev. Lett. **3**, 34–36 (1959).

[106] J. B. Goodenough, "The two components of crystallographic transition in VO_2," J. Solid State Chem. **3**, 490–500 (1971).

[107] A. Cavalleri, C. Tóth, C. Siders, J. A. Squier, P. F. F. Ráksi, , and J. C. Kieffer, "Femtosecond structural dynamics in VO_2 during an ultrafast solid-solid phase transition," Phys. Rev. Lett. **87**, 237401 (2001).

[108] H. T. Kim, Y. W. Lee, B. J. Kim, B. G. Chae, S. J. Yun, K. Y. Kang, K. J. Han, K. J. Yee, , and Y. S. Lim, "Monoclinic and correlated metal phase in VO_2 as evidence of the mott transition: coherent phonon analysis," Phys. Rev. Lett. **97**, 266401 (2006).

[109] B. G. Chae, H. T. Kim, D. H. Youn, and K. Y. Kang, "Abrupt metalinsulator transition observed in VO_2 thin films induced by a switching voltage pulse," Physica B **369**, 76–80 (2005).

[110] C. Ko and S. Ramanathan, "Observation of electric field-assisted phase transition in thin film vanadium oxide in a metal-oxide-semiconductor device geometry," Appl. Phys. Lett. **93**, 252101 (2008).

[111] S. Chen, X. Yi, H. Ma, H. Wang, X. Tao, M. Chen, , and C. Ke, "A novel structural VO_2 micro-optical switch," Opt. Quantum Electron. **35**, 1351–1355 (2003).

[112] P. Baum, D. S. Yang, and A. H. Zewail, “4D visualization of transitional structures in phase transformations by electron diffraction,” Science **318**, 788–792 (2007).

[113] G. Gopalakrishnan, D.Rezmetov, and S. Ramanathan, “On the triggering mechanism for the metal-insulator transition in thin film VO_2 devices: electric field versus thermal effects,” J. Mater. Sci. **44**, 5345–5353 (2009).

[114] L. Jiang and W. N. Carr, “Design, fabrication and testing of a micromachined thermo-optical light modulator based on a vanadium dioxide array,” J. Micromech. Microeng. **14**, 833–840 (2004).

[115] E. L. Wooten, K. M. Kissa, A. Yi-Yan, E. J. Murphy, D. A. Lafaw, P. F. Hallemeier, D. Maack, D. V. Attanasio, D. J. Fritz, G. J. McBrien, and D. E. Bossi, “A review of lithium niobate modulators for fiber-optic communications system,” IEEE J. of Select. Topics Quant. Electron. **6**, 69–82 (2000).

[116] T. Ido, S. Tanaka, M. Suzuki, M. Koizumi, H. Sano, and H. Inoue, “Ultra-high-speed multiple-quantum-well electro-absorption optical modulators with integrated waveguides,” J. Lightwave Technol. **14**, 2026–2034 (1996).

[117] D. A. B. Miller, “Device requirements for optical interconnects to silicon chips,” Proceedings of the IEEE **97**, 1166–1185 (2009).

[118] G. Stefanovich, A. Pergament, and D. Stefanovich, “Electrical switching and mott transition in VO_2,” J. Phys.: Condens. Matter **12**, 8837–8845 (2000).

[119] J. Y. Suh, R. Lopez, L. C. Feldman, and J. R. F. Haglund, “Semiconductor to metal phase transition in the nucleation and growth of VO_2 nanoparticles and thin films,” J. Appl. Phys. **96**, 1209–1213 (2004).

[120] L. J. van der Pauw, “A new method of measuring the resistivity and Hall coefficients on lamellae of arbitrary shape,” Philips Tech. Rev. **20**, 220–224 (1958).

[121] V. N. Andreev and V. A. Klimov, "Electrical conductivity of the semiconducting phase in vanadium dioxide single crystals," Phys. Solid State **49**, 2251–2255 (2007).

[122] A. S. B. Jr., H. W. Verleur, and H. J. Guggenheim, "Infrared optical properties of vanadium dioxide above and below the transition temperature," Phys. Rev. Lett. **17**, 1286–1289 (1966).

[123] J. A. McCaulley, V. M. Donnelly, M. Vernon, and I. Taha, "Temperature dependence of the near-infrared refractive index of silicon gallium arsenide, and indium phosphide," Phys. Rev. B **49**, 7408–7417 (1994).

[124] H. Coy, R. Cabrera, N. Sepúlveda, and F. E. Fernández, "Optoelectronic and all-optical multiple memory states in vanadium dioxide," J. Appl. Phys. **108**, 113115 (2010).

[125] R. Zia, J. A. Schuller, A.Chandran, and M. L. Brongersma, "Plasmonics: the next chip-scale technology," Mater. Today **9**, 20–27 (2006).

[126] T. Ebbesen, C. Genet, and S. I. Bozhevolnyi, "Surface-plasmon circuitry," Phys. Today **61**, 44–50 (2008).

[127] K. Kneipp, Y. Wang, H. Kneipp, L. T. Perelman, I. Itzkan, R. Dasari, and M. S. Feld, "Single molecule detection using surface-enhanced Raman scattering (SERS)," Phys. Rev. Lett. **78**, 1667–1670 (1997).

[128] R. F. Oulton, V. J. Sorger, T. Zentgraf, R.-M. Ma, C. Gladden, L. Dai, G. Bartal, and X. Zhang, "Plasmon lasers at deep subwavelength scale," Nature **461**, 629 (2009).

[129] C. E. Hofmann, F. J. G. de Abajo, and H. A. Atwater, "Enhancing the radiative rate in III-V semiconductor plasmonic core-shell nanowire resonators," Nano Lett. **11**, 372–376 (2011).

[130] H. T. Miyazaki and Y. Kurokawa, "Squeezing visible light waves into a 3-nm-thick and 55-nm-long plasmon cavity," Phys. Rev. Lett. **96**, 097401 (2006).

[131] A. Kumar, J. Gosciniak, T. B. Andersen, L. Markey, A. Dereux, and S. I. Bozhevolnyi, "Power monitoring in dielectric-loaded surface plasmon-polariton waveguides," Opt. Express **19**, 2972–2978 (2011).

[132] M. Ambati, S. H. Nam, E. Ulin-Avila, D. A. Genov, G. Bartal, and X. Zhang, "Observation of stimulated emission of surface plasmon polaritons," Nano Lett. **8**, 3998–4001 (2008).

[133] J. Grandidier, G. C. des Francs, S. Massenot, A. Bouhelier, L. Markey, J. C. Weeber, C. Finot, and A. Dereux, "Gain-assisted propagation in a plasmonic waveguide at telecom wavelength," Nano Lett. **9**, 2935–2939 (2009).

[134] I. D. Leon and P. Berini, "Amplification of long-range surface plasmons by a dipolar gain medium," Nat. Photonics **4**, 382–387 (2010).

[135] M. C. Gather, K. Meerholz, N. Danz, and K. Leosson, "Net optical gain in a plasmonic waveguide embedded in a fluorescent polymer," Nat. Photonics **4**, 457–461 (2010).

[136] K. L. Kliewer and R. Fuchs, "Collective electronic motion in a metallic slab," Phys. Rev. **153**, 498–512 (1967).

[137] H. Raether, *Surface Plasmons on Smooth and Rough Surfaces and on Gratings* (Springer, Berlin, 1988).

[138] R. H. Ritche, "Plasma losses by fast electrons in thin films," Phys. Rev. **106**, 874–881 (1957).

[139] P. B. Johnson and R. W. Christy, "Optical constants of the noble metals," Phys. Rev. B **6**, 4370–4379 (1972).

[140] E. Palik, ed., *Handbook of Optical Constants of Solids* (Academic Press, New York, 1985).

[141] M. Hochberg, T. Baehr-Jones, C. Walker, and A. Scherer, “Integrated plasmon and dielectric waveguides,” Opt. Express **12**, 5481–5486 (2004).

[142] J. Tian, S. Yu, W. Yan, and M. Qiu, “Broadband high-efficiency surface-plasmon-polariton coupler with silicon-metal interface,” Appl. Phys. Lett. **95**, 013504 (2009).

[143] Z. Han, A. Y. Elezzabi, and V. Van, “Experimental realization of subwavelength plasmonic slot waveguides on a silicon platform,” Opt. Lett. **35**, 502–504 (2010).

[144] L. Chen, J. Shakya, and M. Lipson, “Subwavelength confinement in an integrated metal slot waveguide on silicon,” Opt. Lett. **31**, 2133–2135 (2006).

[145] R. Yang, R. A. W. Z. Lu, and M. A. G. Abushagur, “Efficient light coupling between dielectric slot waveguide and plasmonic slot waveguide,” Opt. Lett. **35**, 649–651 (2010).

[146] C. Delacour, S. Blaize, P. Grosse, J. M. Fedeli, A. Bruyant, R. Salas-Montiel, G. Lerondel, and A. Chelnoko, “Efficient directional coupling between silicon and copper plasmonic nanoslot waveguides: toward metal-oxide-silicon nanophotonics,” Nano Lett. **10**, 2922–2926 (2010).

[147] T. Holmgaard and S. I. Bozhevolnyi, “Theoretical analysis of dielectric-loaded surface plasmon-polariton waveguides,” Phys. Rev. B **75**, 245405 (2007).

[148] T. Holmgaard, S. I. Bozhevolnyi, L. Markey, and A. Dereux, “Dielectric-loaded surface plasmon-polariton waveguides at telecommunication wavelengths: Excitation and characterization,” Appl. Phys. Lett. **92**, 011124 (2008).

[149] T. Holmgaard, Z. Chen, S. I. Bozhevolnyi, L. Markey, and A. Dereux, “Dielectric-loaded plasmonic waveguide-ring resonators,” Opt. Express **17**, 2968–2975 (2009).

[150] T. Holmgaard, Z. Chen, S. I. Bozhevolnyi, L. Markey, A. Dereux, A. V. Krasavin, and A. V. Zayats, “Wavelength selection by dielectric-loaded plasmonic components,” Appl. Phys. Lett. **94**, 051111 (2009).

[151] S. I. Bozhevolnyi, V. S. Volkov, E. Devaux, J. Y. Lalulet, and T. W. Ebbesen, "Channel plasmon subwavelength waveguide components including interferometers and ring resonators," Nature **440**, 508–511 (2006).

[152] J. Gosciniak, V. S. Volkov, S. I. Bozhevolnyi, L. Markey, S. Massenot, and A. Dereux, "Fiber-coupled dielectric-loaded plasmonic waveguides," Opt. Express **18**, 5314–5319 (2010).

[153] P. Berini, R. Charbonneau, N. Lahoud, and G. J. Mattiussi, "Characterization of long-range surface-plasmon-polariton waveguides," J. Appl. Phys. **98**, 043109 (2005).

[154] J. Grandidier, S. Massenot, G. C. des Francs, A. Bouhelier, J. C. Weeber, L. Markey, A. Dereux, J. Renger, M. U. Gonzalez, and R. Quidant, "Dielectric-loaded surface plasmon polariton waveguides: Figures of merit and mode characterization by image and Fourier plane leakage microscopy," Phys. Rev. B **78**, 245419 (2008).

[155] J. Gosciniak, S. I. Bozhevolnyi, T. B. Anderson, V. S. Volkov, J. Kjelstrup-Hansen, L. Markey, and A. Dereux, "Thermo-optic control of dielectric-loaded plasmonic waveguide components," Opt. Express **18**, 1207–1216 (2010).

[156] E. Feigenbaum and H. A. Atwater, "Resonant guided wave networks," Phys. Rev. Lett. **104**, 147402 (2010).

[157] M. J. de Boer, J. G. E. Gardeniers, H. V. Jansen, E. Smulders, M. J. Gilde, G. Roelofs, J. N. Sasserath, and M. Elwenspoek, "Guidelines for etching silicon MEMS structures using fluorine high-density plasmas at cryogenic temperatures," J. Microelectromech. S. **11**, 385–401 (2002).

[158] I. M. Pryce, K. Aydin, Y. A. Kelaita, R. M. Briggs, and H. A. Atwater, "Highly strained compliant optical metamaterials with large frequency tunability," Nano Lett. **10**, 4222–4227 (2010).

[159] M. D. Kelzenberg, S. W. Boettcher, J. A. Petykiewicz, D. B. Turner-Evans, M. C. Putnam, E. L.Warren, J. M. Spurgeon, R. M. Briggs, N. S. Lewis, and H. A. Atwater, “Enhanced absorption and carrier collection in Si wire arrays for photovoltaic applications,” Nat. Mater. **9**, 239–244 (2010).

[160] A. R. Forouhi and I. Bloomer, “Optical dispersion relations for amorphous semiconductors and amorphous dielectrics,” Phys. Rev. B **34**, 7018–7026 (1986).